

Experiment and Machine Protection from Fast Losses caused by Crab Cavities in the High Luminosity LHC

THÈSE N° 8533 (2018)

PRÉSENTÉE LE 28 MAI 2018

À LA FACULTÉ DES SCIENCES DE BASE
LABORATOIRE DE PHYSIQUE DES ACCÉLÉRATEURS DE PARTICULES
PROGRAMME DOCTORAL EN PHYSIQUE

ÉCOLE POLYTECHNIQUE FÉDÉRALE DE LAUSANNE

POUR L'OBTENTION DU GRADE DE DOCTEUR ÈS SCIENCES

PAR

Andrea SANTAMARÍA GARCÍA

acceptée sur proposition du jury:

Prof. C. Hébert, présidente du jury
Prof. L. Rivkin, Dr H. Burkhardt, directeurs de thèse
Dr D. Wollmann, rapporteur
Prof. . K. Oide, rapporteur
Prof. A. Bay, rapporteur



ÉCOLE POLYTECHNIQUE
FÉDÉRALE DE LAUSANNE

Suisse
2018



One never notices what has
been done; one can only see
what remains to be done.

Marie Skłodowska-Curie

Acknowledgements

First, I want to thank Leonid Rivkin for believing in our research topic and welcoming me into EPFL's doctoral program. I can say I have profited from EPFL's lectures, trainings, and events as much as time has allowed. It has been a wonderful experience!

Next, I want to warmly thank Helmut Burkhardt for taking me as his student and proposing such an interesting and challenging thesis topic. The topic is at the intersection of many areas of accelerator physics such as beam dynamics, collimation, machine protection, machine-experiment interface, and radiofrequency. Knitting these together is not an obvious task, but he always kept in mind the bigger picture.

I can say with absolute certainty that this thesis would not have been possible without the help of Kyrre Sjobak. He arrived as a fellow a few months after I started my Ph.D., and we have tightly worked together as a team ever since. I learned everything I know about RF from him, leading to endless discussions about crab cavity behavior that will, in the end, shape my understanding of the subject. He introduced me to the crazy world of Emacs (both a blessing and a curse) and helped me with all my computer and code-related issues, no matter how small. The effort and dedication that Kyrre put into debugging, developing, and maintaining SixTrack not only allowed me to focus on my simulations but has been fundamental to the success of the DYNK module, making it a standardized tool for failure simulations for everyone to use. Not only that but he read my thesis from cover to bottom, correcting the smallest of details several times. We have gone through some challenging moments research-wise together that we can laugh about now over a beer. A heartfelt *thank you* for accompanying me through my first years in research!

Big thanks to Daniel Wollmann, Matthieu Valette, and Bjorn Lindstrom, our machine protection team. Their interest in this research topic, our discussions, and the collaboration between both teams and other groups kept the topic moving forward and materialized in very interesting results.

During these years I've been knocking on many ABP-HSS doors looking for help, so thank you, guys! A very special thanks to the collimation team for their support, especially to Roderik Bruce who has followed my work since my arrival and has always provided constructive feedback. Another big *thank you* to Riccardo de Maria for all the help with SixTrack.

I would also like to thank Philippe Baudrenghien, Rama Calaga, Alejandro Castilla Loeza, Karim Gibrán Hernández Chahín, and Alick Macpherson for sharing their knowledge on the crab cavity prototypes and LLRF system with us.

The writing quality of this thesis will be considerably lower without the help of some friends! Huge thanks to Simon Albright, Alejandro Avilés del Moral, James Molson, Adrian Oeftiger, and Kyrre Sjobak for taking the time to have a look at the manuscript.

During my time here I embarked on other projects, such as replacing the old pictures hanging in the corridor from buildings 9 to 6 by new ones, and I want to thank everyone who got involved! Special thanks to Giovanna Campogiani for starting the project when she was here and to Kurt Hubner and Delphine Bail for their resolve to complete it. I would also like to thank Bernard Holzer for sponsoring the first meetings of the project with some pizza and keeping in touch with the student's initiatives.

Leaving work behind, I want to express my sincere gratitude to all my Geneva friends. Thank you guys for all the moments we have spent together, all the good laughs... those are the memories that I will fondly remember as being part of my Ph.D. years!

To the constants in my life, my family and friends in Spain, I have to thank for always believing in me. *¡Os quiero!*

Last but not least, I want to wholeheartedly thank Alejandro Avilés del Moral, better known as Ome. He has gone through the good times and difficult times with me, listened to my rants and concerns, challenged my ideas, laughed at my absurd jokes, and put up with my continuous teasing. For this time together, thank you!

Geneva, January 2018,
Andrea

Abstract

The High Luminosity Large Hadron Collider (HL-LHC) upgrade aims for a tenfold increase in integrated luminosity compared to the nominal Large Hadron Collider (LHC), and for operation at a leveled luminosity five times higher than the nominal LHC peak luminosity. In order to compensate the geometric luminosity loss due to the increased crossing angle, crab cavities will be used to transversely rotate the beam bunches, allowing quasi head-on collisions at the experiments.

Crab cavity failures can be very fast, having time constants similar to the reaction time of the machine protection system. In such a scenario the beams cannot be immediately extracted, making the protection of the accelerator fully rely on passive protection devices such as the collimation system. At the same time the energy stored in the HL-LHC beams will be doubled with respect to the LHC to more than 700 MJ, which increases the risk of damaging the accelerator and the experiments in case of failure. Crab cavity failures have the potential to displace the beam core and create considerable particle losses around the accelerator, posing a machine protection challenge. Any increase in failure rates will be difficult to compensate, affecting the performance of the HL-LHC and therefore the integrated luminosity goal. This is why it is important to correctly interlock the accelerator and make sure that certain types of failure never happen. In order to do this advanced simulations are needed well before the crab cavity prototypes can be tested in real operating conditions.

This thesis analyzes different failure scenarios for crab cavities installed around the ATLAS and CMS experiments. The selected failure scenarios are later simulated with the tracking code SixTrack thanks to a newly developed functionality. The distribution of the particle losses in space and time are analyzed for the different failure cases and a quantitative estimate of the impact in the collimation system is given. The results are analyzed from a machine protection point of view, where the time for the beam abort trigger

is calculated for each failure case and mitigation techniques are proposed. These results allow identifying corner cases corresponding to the most dangerous crab cavity failure scenarios, serving as input for the design of the future interlocking system.

Keywords: accelerator physics, HL-LHC, beam dynamics, crab cavities, collimation, machine protection, single particle tracking.

Contents

ACKNOWLEDGEMENTS	III
ABSTRACT	V
1. INTRODUCTION	1
1.1. Motivation for this work	4
1.2. Thesis structure	5
2. BEAM DYNAMICS	7
2.1. Introduction	7
2.1.1. The Frenet-Serret coordinate system	8
2.2. Transverse motion	9
2.2.1. Magnets	9
2.2.2. Motion through a quadrupole	11
2.3. The concept of emittance	14
2.3.1. Courant-Snyder or Twiss parametrization	14
2.3.2. The Root Mean Square emittance	17
2.3.3. Action-angle variables	18
2.4. Particle tracking	19
2.4.1. SixTrack	20
3. THE HIGH LUMINOSITY LHC	23
3.1. The LHC in a nutshell	24
3.1.1. The concept of luminosity	26
3.1.2. Luminosity production in the LHC	27
3.1.3. The collimation system	29
3.1.4. LHC Run 2	32
3.2. The High Luminosity LHC	33
3.2.1. The crab-crossing scheme	35
3.2.2. The insertion region for high luminosity experiments	39

3.2.3.	Detector upgrade	44
3.2.4.	Luminosity leveling	46
3.3.	Machine-detector interface	47
3.3.1.	Machine induced backgrounds	47
3.4.	Machine protection	48
3.4.1.	Performance and availability	48
3.4.2.	Hazards, risks and mitigation	50
3.4.3.	Challenges for the HL-LHC	50
3.5.	Summary	52
4.	UNDERSTANDING CRAB CAVITIES	53
4.1.	Historical introduction	53
4.2.	Cavity resonators	56
4.2.1.	Higher order modes	56
4.3.	Mechanical deformations	57
4.3.1.	Lorentz force detuning	57
4.3.2.	Mechanical model of a cavity	59
4.3.3.	The quality factor	60
4.3.4.	Power dissipation	60
4.3.5.	Resonant amplitude response	61
4.4.	Crab cavity design and schemes	63
4.4.1.	Crab cavities at KEKB	63
4.4.2.	Local and global crabbing schemes	64
4.4.3.	Crab cavities for the HL-LHC	65
4.5.	Crab cavity kick	66
4.6.	Crab cavity voltage	69
4.7.	Crab cavity failures	72
4.7.1.	The LLRF feedback system	72
4.7.2.	Power source failure	73
4.7.3.	LLRF malfunction	74
4.7.4.	Quenches	76
4.7.5.	Probability of failure	77
4.8.	Summary	80
5.	CRAB CAVITY FAILURE SIMULATIONS	81
5.1.	Crab cavity failures with SixTrack	82
5.1.1.	The dynamic kick module	82
5.1.2.	Collimation studies with SixTrack	83
5.2.	Simulation set-up	85
5.2.1.	Crab cavities	85
5.2.2.	Collimation	86
5.2.3.	Chosen failure cases	86
5.2.4.	Particle distribution	88
5.2.5.	Computational considerations	90

5.3. Results from SixTrack simulations	91
5.3.1. Single particle simulations	91
5.3.2. Collimation studies	93
5.3.3. Machine protection considerations	102
5.4. Analysis	106
5.4.1. Study of the asymmetry in beam losses	106
5.4.2. Phase advance optimization as mitigation	108
5.4.3. Impact on the experiments	110
5.5. Summary and discussion	112
6. SUMMARY, CONCLUSION, AND OUTLOOK	115
APPENDICES	119
A. MODES IN A CYLINDRICAL CAVITY	119
B. BEAM LOADING AND THE LUMPED CIRCUIT MODEL	123
B.1. Beam loading	123
B.2. The lumped circuit model	124
C. CRAB CAVITY AND COLLIMATOR CONFIGURATION	127
D. SIXTRACK FLOWCHARTS	131
E. PUBLICATIONS	137
E.1. Limits on Failure Scenarios for Crab Cavities in the HL-LHC .	138
E.2. General Functionality for Turn Dependent Element Properties in SixTrack	143
E.3. Machine Protection from Fast Crab Cavity Failures in the High Luminosity LHC	148
E.4. Time Scale of Crab Cavity Failures Relevant for High Lumi- nosity LHC	153
BIBLIOGRAPHY	

List of Figures

1.1	The Standard Model of Particle Physics.	1
1.2	The Globe of Innovation for the International Year of Light talks in 2015.	3
1.3	Stored beam energy as a function of beam momentum for several accelerators.	4
1.4	Baseline HL-LHC program.	5
2.1	The right handed, planar Frenet-Serret coordinate system. . .	8
2.2	Top: the magnetic field of a an upright dipole (black) and its equipotential lines (color) in arbitrary units. Bottom: the magnetic field of an upright focusing quadrupole. By conven- tion focusing quadrupoles focus in the horizontal plane. . . .	10
2.3	Representation of a FODO cell as optic lenses, where QF de- notes a focusing quadrupole and QD a defocusing one. . . .	10
2.4	Depiction of the betatron motion (red) in the vertical plane. .	12
2.5	Transformations of phase space for a focusing quadrupole (top left), defocusing quadrupole (top right) and drift space (bottom).	13
2.6	Phase space and the Twiss parameters, where $\gamma = \frac{1+\alpha^2}{\beta}$	14
2.7	A random sequence of magnetic elements (blue) and the ref- erence orbit (red).	15
3.1	The accelerator complex at CERN.	24
3.2	A schematic view of the LHC beam and its sectors.	25
3.3	The LHC optimal turnaround time [1, 2].	27
3.4	A particle beam of 10^5 particles modeled as a 2D double Gaus- sian distribution.	28
3.5	View along the beam path of a collimator and its RF contacts.	29

3.6	Scheme of the multistage collimation system at the LHC. The interaction with the collimator materials is itself a source of off-momentum and betatron halo. Electromagnetic and hadronic showers develop during the interaction with the collimator and carry an important fraction of the beam energy [3, Chapter 13].	30
3.7	Peak instantaneous luminosity delivered to A Toroidal LHC Apparatus (ATLAS) during stable beams.	32
3.8	The evolution of the peak luminosity with the β function at the IP (left), and the emittance (right), as described by Eq. (3.2). The black stars represent the working points for each machine.	33
3.9	Roadmap to the HL-LHC.	34
3.10	The different beam-beam effects and visualization of the beam sizes and crossing angle. The crossing angle serves to reduce head-on collisions to only one per Interaction Point (IP). . . .	35
3.11	Beam-beam force in a head-on collision, on a test particle as described by Eq. (3.9).	36
3.12	Illustration of a bunch crossing with parasitic collisions (left) and with an increased crossing angle (right).	37
3.13	The evolution of the geometrical reduction factor R_ϕ with β^* (left), and the total crossing angle (right). The working points of each machine are marked with a black star.	38
3.14	Schematic view of the kick imparted by the crab cavities. The <i>crabbing</i> compensates the crossing angle for the incoming beam just before collision and returns it to its original position after collision.	38
3.15	A D2 dipole magnet and drawing of an inner-triplet quadrupole. 39	
3.16	Simplified layout of one of the sides of the Insertion Region (IR), at a high luminosity experiment for High Luminosity (HL)-LHC. The layout of the other side is exactly symmetric. 41	
3.17	The IR for the two high luminosity experiments ATLAS and Compact Muon Solenoid (CMS), with HLLHCV1.2 optics. The closed orbit is shown as a black line, and the 5σ , 10σ envelopes in blue for beam 1, and in red for beam 2. The aperture is marked in gray, and the correspondent elements are depicted as rectangles at the top.	42
3.18	Close-up of the crossing planes shown in Fig. 3.17. Both experiments collide with the same crossing angles but in opposite transverse planes. The solenoid magnet is part of each detector and is used to sort particles by momentum. It is built to be transparent to the beam itself but constitutes a small source of coupling.	43

3.19	Representation of a primary vertex with only two associated tracks, its secondary vertices, a cone as used in some jet reconstruction algorithms and pile-up events.	44
3.20	Pile-up.	45
3.21	Luminosity leveling	46
3.22	Statistical definition of availability and reliability, with respect to observable parameters [4].	49
3.23	The Machine Protection System (MPS) response time at LHC.	49
4.1	R. B. Palmer showing the principle of the crab crossing scheme on the blackboard.	54
4.2	Main events in the history of crab cavities.	55
4.3	Stiffening structure in gray (left) and tuning system in a dressed cavity (right) for the Double Quarter Wave (DQW) crab cavity, one of the selected crab cavities for the HL-LHC.	59
4.4	Normalized resonant amplitude response for various Q_L factors.	62
4.5	KEKB crab cavity.	63
4.6	Left: global crabbing scheme. Right: local crabbing scheme. The black rectangles represent the crab cavities.	64
4.7	Crab cavities for the HL-LHC.	65
4.8	A Gaussian particle bunch at the IP, with (right) and without (left) a crab cavity kick, using HL-LHC parameters. The shape of the Radio-Frequency (RF) curvature can be observed.	68
4.9	Evolution of the crab cavity voltage depending on the β_{cc} function at their location and on the total crossing angle θ . The dashed line indicates the values for the HL-LHC.	70
4.10	Proposed crab cavity Low Level RF (LLRF) architecture for one IP and one beam. The local loop delay is estimated to be 1 μ s and the global multi-cavity loop delay 5 μ s.	72
4.11	Time evolution of the stored energy U and voltage V when the power source is switched off for $Q_{\text{ext}} = 5 \times 10^5$ and $f_0 = 400$ MHz, which gives $\tau_V \approx 400$ μ s ≈ 4 LHC turns.	73
4.12	Left: Normal operation. Right: a decrease in tilt induced by a decrease in voltage.	74
4.13	Left: Normal operation. Right: a change in phase, entailing a transverse kick of the bunch core.	75
4.14	Crab cavity breakdown at KEKB in 2008.	78
4.15	Trip rate of the crab cavity system at KEKB during its lifetime.	78
4.16	Yearly luminosity production as a function of average crab cavity downtime and MTBF.	79
5.1	A Double Quarter Wave (DQW) crab cavity on the test bench in the SM18 facility at CERN. Taken the 30 th of August, 2016.	81

5.2	Layout of the crab cavities used in the SixTrack simulations, for ATLAS (left) and CMS (right).	85
5.3	Initial particle distribution at IP1, where the gray ellipses indicate areas of constant sigma. We can observe a small, non-zero alpha in the horizontal plane.	89
5.4	Crab cavity parameters modified for each failure case. The phase remains constant at zero value in the V (voltage decay) scenario and the voltage remains constant in the PJ (phase jump) and PS (phase slip) scenarios.	91
5.5	Single particle tracking for the three selected failure scenarios, where each point corresponds to one turn. The failures happen in IP1 and the distribution is observed at a vertical primary collimator. The position of the collimator jaws is shown in gray color. In the legend CC stands for crab cavity.	92
5.6	Visual representation of the data given in Table 5.3 50 turns after the failure. The gray area represents the opening of the primary collimator.	94
5.7	Top: loss map for the phase slip of four crab cavities in IP1 for beam 1 (<u>PS IP1 4CC</u> failure case). Bottom: cumulative losses per turn grouped per collimator type for the same failure scenario. The legends show the fraction of beam lost 50 turns after the failure.	96
5.8	Top: loss map for the phase slip of four crab cavities in IP1 for beam 2 (<u>PS IP1 4CC</u> failure case). Bottom: cumulative losses per turn grouped per collimator type for the same failure scenario. The legends show the fraction of beam lost 50 turns after the failure.	97
5.9	Top: loss map for the phase slip of four crab cavities in IP5 for beam 1 (<u>PS IP5 4CC</u> failure case.) Bottom: cumulative losses per turn grouped per collimator type for the same failure scenario. The legends show the fraction of beam lost 50 turns after the failure.	98
5.10	Top: loss map for the phase slip of four crab cavities in IP5 for beam 2 (<u>PS IP5 4CC</u> failure case). Bottom: cumulative losses per turn grouped per collimator type for the same failure scenario. The legends show the fraction of beam lost 50 turns after the failure.	99
5.11	Cumulative losses per turn grouped per collimator type for ATLAS (top) and CMS (bottom) for the voltage decay of four crab cavities, beam 1 (<u>V 4CC</u> failure case). The legends show the fraction of beam lost 50 turns after the failure. . . .	100

5.12	Cumulative losses per turn grouped per collimator type for ATLAS (top) and CMS (bottom) for the voltage decay of four crab cavities, beam 2 (<u>V 4CC</u> failure case). The legends show the fraction of beam lost 50 turns after the failure. . . .	101
5.13	Limits on the number of 7 TeV protons impacting on TCP collimators as a function of BLM integration time.	102
5.14	Closed orbit calculated by MAD-X in the case of a phase jump of 60° of four crab cavities upstream of ATLAS (top row) and CMS (bottom row) in IR7.	107
A.1	The first 5 Bessel functions of the first kind.	120
A.2	Different magnetic and electric transverse modes in a cylindrical cavity with a radius of 0.5 m at a frequency of 0.5 GHz.	122
B.1	A positively charged bunch passing through a cavity. As the bunch passes it leaves a negative image current at the upstream end of the cavity gap. By charge conservation a positive image current is created downstream of the cavity gap, generating an electric field and, therefore, a beam-induced voltage. The energy change in the cavity ΔW is equal to the energy variation in the bunch.	124
B.2	A circuit model of a beam loaded cavity, where the <i>klystron</i> is the source of radio waves, the input coupler is represented by a transmitter of impedance Z , and the cavity resonator by an RLC circuit. The beam is represented by a source of current.	124
D.1	Program flow in SixTrack with DYNK, where <code>comdynk</code> contains all the variables needed for DYNK to run.	132
D.2	Details of program flow when running subroutine <code>thin6d</code>	133
D.3	Collimation version of SixTrack and collimation post-processing file flow chart. The green nodes represent external input files while the blue ones represent the relevant files produced in the process.	134

List of Tables

3.1	The injector chain of the LHC.	24
3.2	The LHC IRs.	25
3.3	Current LHC and HL-LHC luminosity goals at 25 ns operation.	33
3.4	Comparison of nominal and standard HL-LHC parameters for 25 ns bunch spacing operation	34
3.5	The LHC experiments, their crossing plane and their changes for HL-LHC, where the luminosity is given in $\text{cm}^{-2} \text{s}^{-1}$ and the inner pipe radii in mm.	45
3.6	Classification of failures by timescale for beam loss, where 270 μs is 3 LHC turns [5]. This corresponds to the reaction time of the MPS described in Fig. 3.23.	51
4.1	Working parameters of the DQW and RF Dipole (RFD) crab cavities	66
5.1	Voltage per crab cavity used in the simulations.	86
5.2	HL-LHC collimator openings in terms of σ for emittances of 2.5 μm and 3.5 μm	86
5.3	Losses in the collimation system 10 and 50 turns after the failure, given in fraction of beam lost, and the maximum dis- placement of the bunch observed in terms of sigma. In the table V stands for voltage decay, PJ for phase jump, PS for phase slip and CC for crab cavity.	94
5.4	Trigger of the beam abort for each failure case where V stands for voltage decay, PJ for phase jump, PS for phase slip and CC for crab cavity.	103
5.5	Number of protons lost in different scenarios for beam 1. . . .	104
5.6	Number of protons lost in different scenarios for beam 2. . . .	105
5.7	Orbit distortion created at the primary collimators from the kick of four crab cavities and the phase advance between them.	106

C.1	Position, phase advance, Twiss parameters and dispersion for the crab cavities used in the simulations.	128
C.2	Position, phase advance, Twiss parameters and dispersion for the primary and secondary collimators in IR7.	129

Chapter No.1

Introduction

The LHC is the largest and most powerful particle collider in the world, built beneath the Franco-Swiss border near Geneva at the European Organization for Nuclear Research (CERN) [6].

The LHC focuses on experimentally testing the *Standard Model* theory of particle physics and exploring the theories beyond it. The Standard Model classifies elementary particles, i.e. particles whose internal structure is unknown, into *leptons*, *quarks*, and *bosons*, as shown in Fig. 1.1.

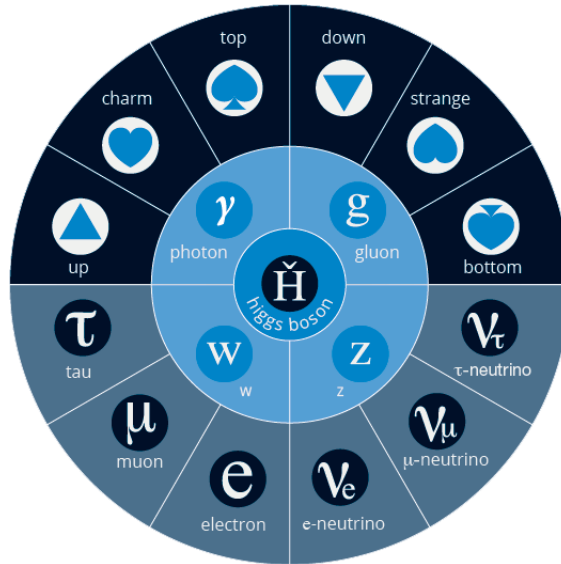


Figure 1.1. The Standard Model of Particle Physics. **Top rim:** quarks. **Bottom rim:** leptons. **Inner circle:** gauge bosons. **Central circle:** scalar boson [7].

Particle colliders have played an instrumental role in consolidating the Standard Model with the following discoveries:

Up, down, and strange quarks, 1968 observed at SLAC National Accelerator Laboratory [8, 9].

Charm quark, 1974 observed at SLAC National Accelerator Laboratory [10] and Brookhaven National Laboratory (BNL) [11].

Tau lepton, 1975 observed at SLAC National Accelerator Laboratory [12].

Gluon, 1978 first evidence at the PLUTO experiment [13] in DORIS and observation in 1980 at the PETRA storage ring (Deutsches Elektronen-Synchrotron (DESY)) [14].

Z^0 and W^\pm bosons, 1983 observed at the UA1 [15] and UA2 [16] experiments in the Large Electron-Positron Collider (LEP) (CERN).

Top quark, 1995 observed at the CDF [17] and DØ [18] experiments in Tevatron (Fermilab).

The Higgs boson, 2012 observed at the ATLAS [19] and CMS [20] experiments in the LHC (CERN).

Being the last part of the Standard Model to be experimentally verified, huge efforts were put into the search of the Higgs boson. The LHC started operating at 3.5 TeV of energy in 2010, followed in 2012 by the discovery of a new particle with mass between 125 and 127 GeV/c², tentatively confirmed to be the Higgs boson. A year later, two of the original researchers that postulated the Higgs mechanism in 1964 were awarded the Nobel Prize in Physics.

The predictions derived from the Standard Model have been continuously backed up by experimental results. However, the theory falls short in a number of ways. The Standard Model is inconsistent with the theory of general relativity used to describe the force of gravity in modern physics. Additionally, there is a variety of observed phenomena that cannot be explained by the Standard Model such as dark matter, dark energy, the existence of neutrino masses, or the matter-antimatter asymmetry. Furthermore, recent results from the LHCb experiment at CERN have hinted at possible Standard Model deviations [21]. Other open questions show the work that lies ahead of the particle physics community such as the hierarchy problem, the proton radius puzzle, or the strong CP problem. In order to answer these questions several theories have been developed in the area known as physics *Beyond the Standard Model*, such as string theory or supersymmetry. The experiments at the LHC have been performing a wide range of searches from supersymmetric and exotic particles to rare decays of the Higgs boson, although no solid evidence for new physics has been found so far. Nevertheless, constraints have been placed on models resulting in many supersymmetry

and exotic scenarios [22].

The exploratory potential of high energy hadron colliders allows accessing the highest mass scales of the energy frontier and will remain unchallenged for the foreseeable future. This is why the full exploitation of the LHC is the highest priority of the energy frontier, hadron collider program [23]. To this end, a new configuration of the LHC has been proposed under the name of HL-LHC. The HL-LHC will not only provide a better chance to see rare processes and to improve statistically marginal measurements, but can reveal to which level does the Higgs boson behave as predicted by the Standard Model [23]. Higgs couplings to the third generation fermions were well established in 2017, but the couplings to the second generation fermions through rare muon decays will only be accessible at HL-LHC [24]. The HL-LHC upgrade aims for a tenfold increase in the total number of collisions created, which can be achieved by a combination of measures. These include a change in the layout of the LHC and innovations that push accelerator technology beyond its present limits [25].



Figure 1.2. The Globe of Innovation for the International Year of Light talks in 2015 [26]

1.1 Motivation for this work

One of the novel technologies that will be used in the HL-LHC are *crab cavities*. Crab cavities are special superconducting radiofrequency cavities that will tilt the particle bunch transversely to achieve a higher rate of particle collisions. Additionally, the stored energy per proton beam will increase by a factor of two as compared to the nominal LHC. This means that an uncontrolled beam loss can severely damage the accelerator [25, Chapter 7].

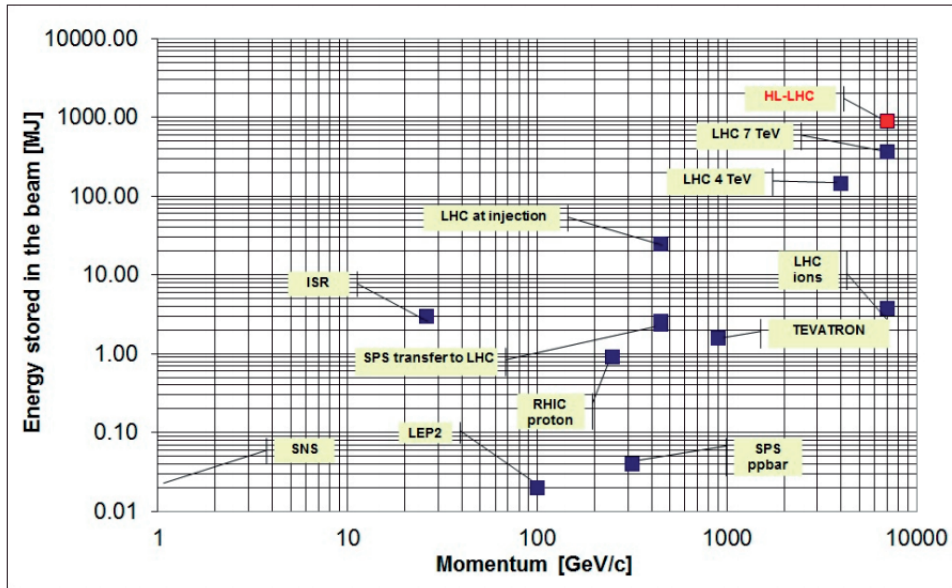


Figure 1.3. Stored beam energy as a function of beam momentum for several accelerators [3, Chapter 12].

New accelerator equipment like crab cavities might cause new failure modes, which are not sufficiently covered by the current machine protection system of the LHC [3, Chapter 12]. Moreover, crab cavity failures can be very fast, leaving no time for extraction in a controlled way. In this case the passive absorbers are the only protection for the accelerator [27]. Crab cavities have never been used in a hadron accelerator before, which further motivates the detailed study of crab cavity failures.

The time scale of the HL-LHC project is such that the writing of this thesis coincides with the freezing of basic design parameters. Critical decisions were taken, such as space requirements and positioning of the crab cavities. This was recently published in the first Technical Design Report (TDR) [25]. Crab cavities will be installed during the Long Shutdown 3 in 2025, so detailed simulations are key before the prototypes are tested in real operating conditions.

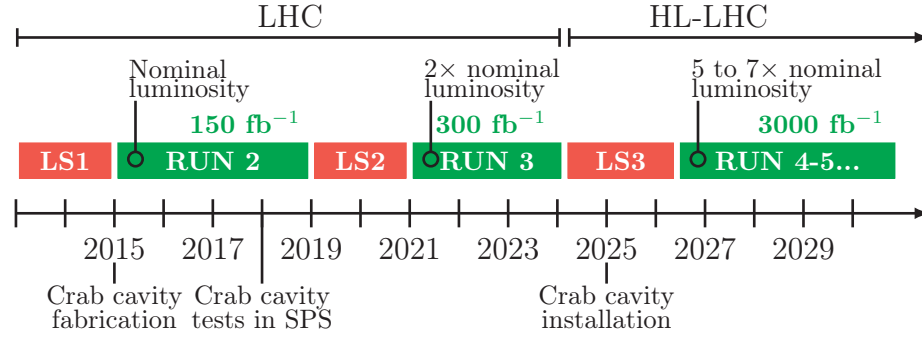


Figure 1.4. Baseline HL-LHC program, where the refurbishment of the accelerator is divided in two Long Shutdowns (LSs).

1.2 Thesis structure

The corpus of the thesis is structured in the following chapters:

Chapter 2, Beam dynamics introduces the basic theoretical concepts of accelerator physics that are used throughout the thesis.

Chapter 3, The High Luminosity LHC briefly introduces the LHC and the current status of the project. This is followed by a description of the High Luminosity upgrade in terms of goals and accelerator layout changes, such as the introduction of crab cavities. Machine protection challenges associated to these changes are discussed, as well as the role machine protection plays in maximizing the machine performance.

Chapter 4, Understanding Crab Cavities is a primer on crab cavities. It provides a historical introduction to crab cavities, an explanation of basic radiofrequency concepts, and the derivation of the relevant crab cavity parameters. With the theory laid out, the chapter then explores crab cavity failures in detail.

Chapter 5, Crab Cavity Failure Simulations describes the tracking program SixTrack and the new functionality that was added to it in the context of this thesis to simulate crab cavity failures in the HL-LHC. This chapter also presents the set-up, results, and analysis of the simulations carried out with SixTrack, where different crab cavity failures are taken into account and compared.

Chapter No.2

Beam Dynamics

This chapter is a brief introduction to transverse beam dynamics and describes fundamental concepts that are used throughout the thesis. Unless explicitly specified, the content of this chapter is based on well-known accelerator physics manuals [28] and lectures.

2.1 Introduction

The energy at collision in the nominal LHC and the standard HL-LHC is 7 TeV, from which we can obtain the following relativistic parameters:

$$\gamma_r = \frac{E}{m_p} = 7460.5 \quad \beta_r = \sqrt{1 - \frac{1}{\gamma_r^2}} = 0.999999991. \quad (2.1)$$

This means that the protons travel at practically the speed of light.

In accelerators charged particles are guided along a specific path with magnetic fields. Since the LHC is a circular collider we are interested in circular trajectories, i.e. trajectories where the Lorentz force and the centrifugal force compensate to maintain a constant radius. Since these particles are relativistic, the force seen by them will mostly come from the magnetic contribution

$$ev\vec{B} = \frac{m_0\gamma_r\vec{v}^2}{\rho} \quad \rightarrow \quad \vec{B}\rho = \frac{\vec{p}}{e}, \quad (2.2)$$

where e is the electric charge, \vec{v} is the speed of the particle, \vec{B} is the magnetic field, m_0 is the rest mass of the particle, \vec{p} is the momentum of the particle, and ρ denotes the local bending radius of the trajectory. The term $\vec{B}\rho$ is

called *beam rigidity*. We can also derive the revolution frequency of the particles around an orbit of circumference \mathcal{C}

$$f_r = \frac{\beta_r c}{\mathcal{C}}. \quad (2.3)$$

The circumference of the LHC is of ≈ 26658.864 m, obtaining a revolution frequency of $f_r = 11.245$ kHz.

2.1.1 The Frenet-Serret coordinate system

It is useful to describe the motion of the particles with respect to the orbit $\vec{\rho}(s)$ that we just introduced, called the *reference orbit*. A curvilinear coordinate system around this reference orbit is called the Frenet-Serret coordinate system, where $(\hat{x}, \hat{y}, \hat{s})$ form the orthonormal basis:

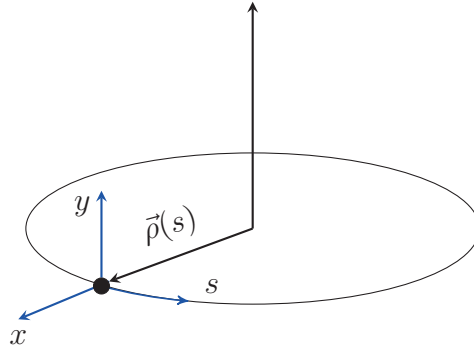


Figure 2.1. The right handed, planar Frenet-Serret coordinate system.

The motion of a particle can then be expressed as a perturbation around the reference orbit:

$$\vec{r}(s) = \vec{\rho}(s) + x\hat{x}(s) + y\hat{y}(s) \quad (2.4)$$

where the path length along the closed orbit s is the independent variable of the motion. It is important to note that the equations of motion in accelerator physics are solved with respect to s , not with respect to time.

2.2 Transverse motion

2.2.1 Magnets

Accelerators are mostly made up of magnets, which are designed to fulfill specific duties that depend on the number of magnetic poles they possess. A magnetic field is a function of space that can be expanded into a Taylor series, in this context called a *multipole expansion*. A general expression of a multipole expansion for magnetic fields can be encapsulated in the formula

$$B_y + iB_x = \sum_n (b_n + ia_n) (x + iy)^n, \quad (2.5)$$

where the multipole coefficients are given by:

$$b_n = \frac{1}{n!} \left. \frac{\partial^n B_y}{\partial x^n} \right|_{x=y=0} \quad a_n = \frac{1}{n!} \left. \frac{\partial^n B_x}{\partial x^n} \right|_{x=y=0}. \quad (2.6)$$

The b_n coefficients represent the normal components of the field, while a_n represents the skew ones. Different types of magnets correspond to a certain multipole order n , their magnetic poles being laid out $\frac{360^\circ}{2(n+1)}$ apart so that the other multipolar terms cancel out. The pole contours of the magnet follow the lines of equal potential.

Dipoles

Dipole magnets are the main components of a circular accelerator, since they bend the particle trajectory into a closed orbit. Applying equations (2.5) and (2.6) to a normal dipole ($n=0$, $a_n = 0$) we obtain:

$$B_y = 1 \quad B_x = 0. \quad (2.7)$$

Quadrupoles

Quadrupoles provide a magnetic field whose magnitude grows rapidly with the radial distance from its longitudinal axis. This is used for beam size control, i.e. to focus and defocus the beam.

$$B_y = \frac{\partial B_y}{\partial x} x \quad B_x = \frac{\partial B_y}{\partial x} y. \quad (2.8)$$

Remembering that $\vec{F} = e(\vec{v} \times \vec{B})$, we can see in the bottom plot of Fig. 2.2 that in the horizontal plane the forces applied to the particle will point to

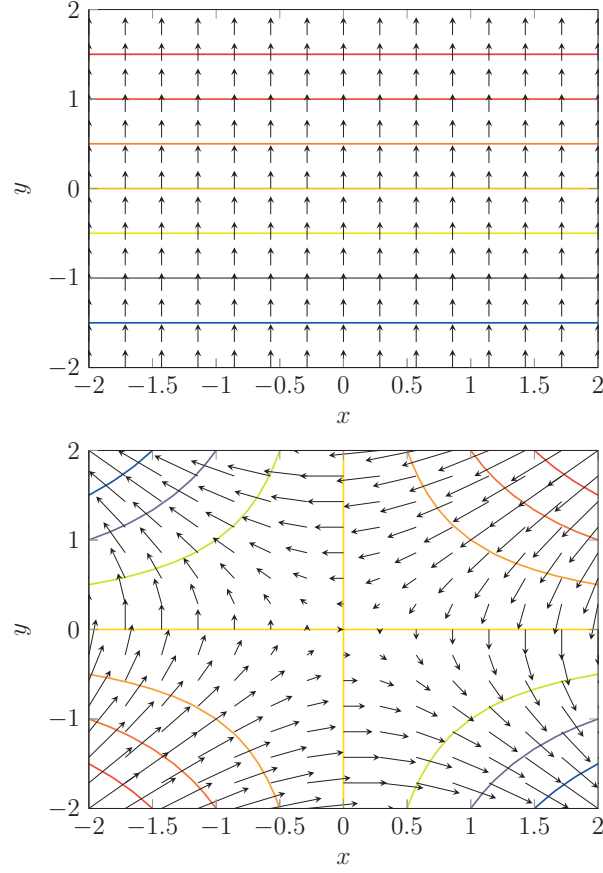


Figure 2.2. **Top:** the magnetic field of a an upright dipole (black) and its equipotential lines (color) in arbitrary units. **Bottom:** the magnetic field of an upright focusing quadrupole. By convention focusing quadrupoles focus in the horizontal plane.

the origin (focusing), while in the vertical plane they point outwards (defocusing). The LHC uses the *alternating-gradient focusing* principle or *strong focusing*. It consists on alternating focusing and defocusing quadrupoles, called *FODO cells* (Focusing - Drift Space - Defocusing - Drift Space), so that the net effect on the beam is convergent. This creates a transverse harmonic oscillation of the particles around the closed orbit, as shown in Fig. 2.3.

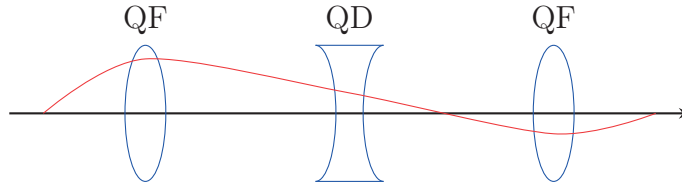


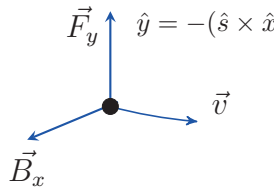
Figure 2.3. Representation of a FODO cell as optic lenses, where QF denotes a focusing quadrupole and QD a defocusing one.

2.2.2 Motion through a quadrupole

In order to study the particle motion through a quadrupole we change the independent variable from time to space in Newton's second law of motion:

$$F_y = m \frac{d^2 y}{dt^2} = m \frac{d^2 y}{ds^2} \left(\frac{ds}{dt} \right)^2 + m \frac{dy}{ds} \frac{d^2 s}{dt^2} = mv^2 y'' . \quad (2.9)$$

Considering the Lorentz force for relativistic particles and the expression of the magnetic field for a normal quadrupole given in Eq. (2.8) we obtain:



$$\vec{F}_y = e(\vec{E} + \vec{v} \times \vec{B}_x) = -evB_x = -evb_1 y \quad (2.10)$$

Equations (2.9) and (2.10) lead to the well-known harmonic oscillator

$$\begin{aligned} mv^2 y'' &= -evb_1 y \\ y'' &= -\frac{e}{p} b_1 y , \\ y'' + k_1 y &= 0 \end{aligned} \quad (2.11)$$

where:

$$k_1 = \frac{b_1}{B\rho} = \frac{e}{p} b_1 , \quad (2.12)$$

is the restoring force, or the *focusing strength* of the quadrupole.

The solutions for Eq. (2.11) are cosine-like C and sine-like S trajectories that propagate from the beginning s_0 to the end s of the magnet, which can be expressed in matrix notation as

$$\begin{pmatrix} y(s) \\ y'(s) \end{pmatrix} = \begin{pmatrix} C(s, s_0) & S(s, s_0) \\ C'(s, s_0) & S'(s, s_0) \end{pmatrix} \begin{pmatrix} y(s_0) \\ y'(s_0) \end{pmatrix} . \quad (2.13)$$

Assuming that the quadrupole strength k_1 is constant over the length of the magnet, the general solutions are:

$$\begin{pmatrix} C & S \\ C' & S' \end{pmatrix} = \begin{cases} \begin{pmatrix} \cos \sqrt{k_1} l & \frac{1}{\sqrt{|k_1|}} \sin \sqrt{k_1} l \\ -\sqrt{|k_1|} \sin \sqrt{k_1} l & \cos \sqrt{k_1} l \end{pmatrix} & \text{for } k_1 > 0 \\ \begin{pmatrix} \cosh \sqrt{k_1} l & \frac{1}{\sqrt{|k_1|}} \sinh \sqrt{k_1} l \\ -\sqrt{|k_1|} \sinh \sqrt{k_1} l & \cosh \sqrt{k_1} l \end{pmatrix} & \text{for } k_1 < 0 \\ \begin{pmatrix} 1 & l \\ 0 & 1 \end{pmatrix} & \text{for } k_1 = 0 \end{cases} \quad (2.14)$$

where $l = s - s_0$. The solutions can be uniquely determined by the initial conditions ($s = s_0$), which are often chosen to be:

$$\begin{aligned} C(s_0, s_0) &= 1 & S(s_0, s_0) &= 0 \\ C'(s_0, s_0) &= 0 & S'(s_0, s_0) &= 1 \end{aligned} \quad (2.15)$$

This leaves us with the general expression of the so-called *betatron motion*

$$y(s) = A \cos \sqrt{k_1} l, \quad (2.16)$$

where A is the amplitude of the motion.

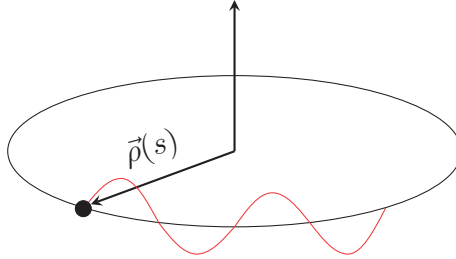


Figure 2.4. Depiction of the betatron motion (red) in the vertical plane.

The matrices obtained in Eq. (2.14) belong to the group of all real 2×2 matrices with determinant one, i.e. $\text{SL}_2(\mathbb{R})$. This is the group of all linear transformations that preserve the area in phase space, also called *symplectic*. It is important to note that when talking about phase space in this context it does not refer to the *canonical* phase space (x, p_x) , but to $(x, x' = \frac{dx}{ds})$, sometimes called *trace space*. The change of variables is

$$p_x = \gamma_r m_0 v = \gamma_r m_0 \frac{dx}{dt} = \gamma_r m_0 \frac{dx}{ds} \frac{ds}{dt} = x' p_s \quad (2.17)$$

The matrices obtained for $k_1 \neq 0$ in Eq. (2.14) are called elliptic elements of $\text{SL}_2(\mathbb{R})$ and correspond to a rotation of the trajectory in phase space. On the

other hand, in the absence of magnetic fields ($k_1 = 0$) we obtain a shearing of phase space, as shown in Fig. 2.5.

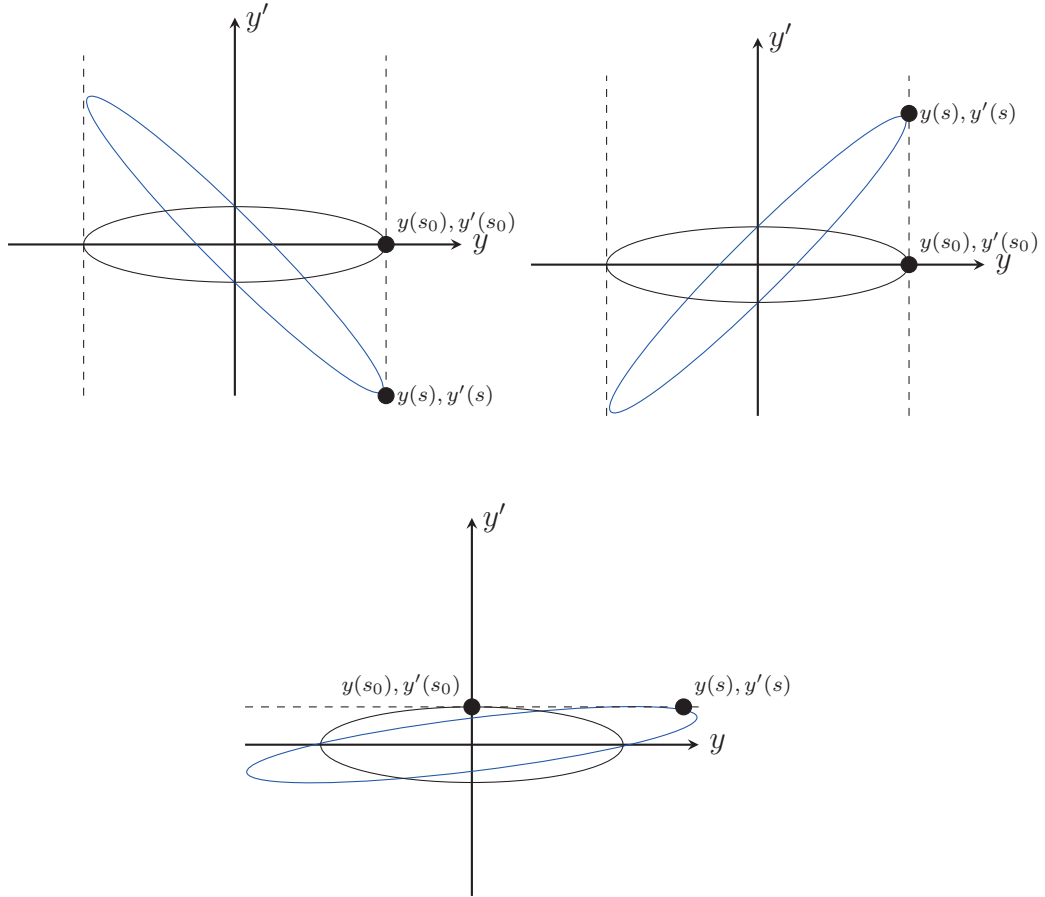


Figure 2.5. Transformations of phase space for a focusing quadrupole (top left), defocusing quadrupole (top right) and drift space (bottom).

2.3 The concept of emittance

2.3.1 Courant-Snyder or Twiss parametrization

The ellipses described by the particles in phase space are conventionally parametrized with the *Twiss* or *Courant-Snyder* parameters α and β , where the parametric equation in cartesian coordinates of the ellipse in the horizontal plane is [29]:

$$\epsilon_x = \gamma_x x^2 + 2\alpha_x x x' + \beta_x x'^2 \quad (2.18)$$

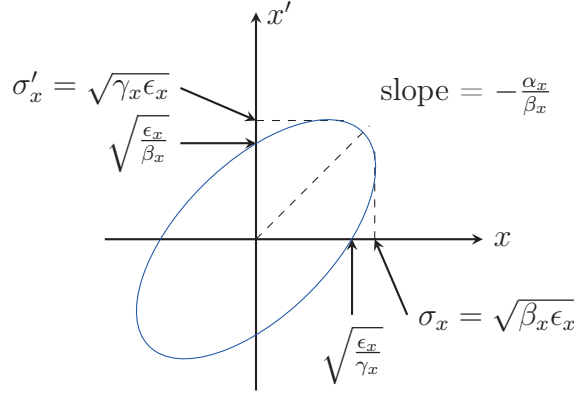


Figure 2.6. Phase space and the Twiss parameters, where $\gamma = \frac{1+\alpha^2}{\beta}$.

The parameter β determines the maximum local amplitude of the particle motion, while α is the correlation between x and x' , where:

$$\alpha \begin{cases} > 0 & \text{Beam converges} \\ = 0 & \text{Beam has a symmetry point} \\ < 0 & \text{Beam diverges} \end{cases} \quad (2.19)$$

We can calculate the area of the ellipse by setting $\alpha = 0$, which corresponds to an upright ellipse. In this case the semi axis will be the beam envelope σ_x and the beam divergence σ'_x , giving an area of:

$$\pi \sigma_x \sigma'_x = \pi \epsilon_x \quad (2.20)$$

We call ϵ the *emittance* of the beam, and it is measured in meters per radian. It is useful to also define an emittance that is energy independent, the so-called *normalized emittance*:

$$\epsilon_n = \beta_r \gamma_r \epsilon \quad (2.21)$$

In nominal LHC the normalized emittance has a value of $3.75 \mu\text{m}$, which will be reduced to $2.50 \mu\text{m}$ for HL-LHC in order to increase the number of collisions. It is important to realize that the Twiss parameters are properties of the *lattice* (i.e. given by the magnet configuration), and that the emittance is a property of the beam. More precisely, the emittance is a property of a distribution of particles, not a single particle. Considering Eq. (2.16) again, we can see that with the Twiss parametrization the amplitude of the motion is the beam envelope $A = \sigma_x = \sqrt{\epsilon_x \beta_x}$. Usually $\beta = \beta(s)$, which modulates the oscillation making it pseudo-harmonic.

The transfer matrix method

In the same way we derived the matrices appearing in Eq. (2.14) for a quadrupole magnet, we can derive a matrix for any other kind of magnet. This opens up the possibility of transporting a particle through an entire accelerator by multiplying the matrices of the elements it contains, also called *transfer matrices*.

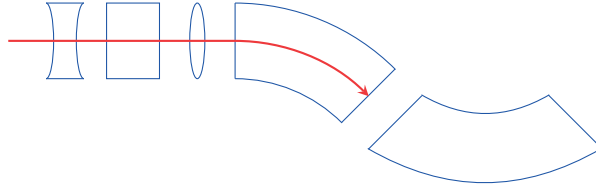


Figure 2.7. A random sequence of magnetic elements (blue) and the reference orbit (red).

In circular accelerators the particle orbit is periodic after one revolution. Additionally, they have an inner periodicity since the lattice cells are repeated several times. In this case, in order to compute the effect of N identical cells through k revolutions for a transfer matrix \mathcal{M} describing the cell, we need to multiply the matrix by itself the correspondent amount of times

$$[\mathcal{M}(s)]^{Nk}. \quad (2.22)$$

For the motion to be stable all the elements of the matrix $[\mathcal{M}(s)]^{Nk}$ must remain bounded as k increases indefinitely. To obtain the stability condition we consider the eigenvalues of the matrix \mathcal{M} :

$$X(s) = \begin{pmatrix} x(s) \\ x'(s) \end{pmatrix} = \mathcal{M} \begin{pmatrix} x(s_0) \\ x'(s_0) \end{pmatrix} = \lambda_1 \cdot x(s_0) + \lambda_2 \cdot x'(s_0). \quad (2.23)$$

Since we have seen that these matrices are linear canonical transformations, we can apply the condition that the determinant must be equal to one:

$$\text{Det}(\mathcal{M}) = 1 \quad \rightarrow \quad \lambda_1 \cdot \lambda_2 = 1. \quad (2.24)$$

We can then generally write

$$\lambda_1 = e^{i\mu} \quad \lambda_2 = e^{-i\mu}, \quad (2.25)$$

and the trace will be

$$\text{Tr}(\mathcal{M}) = \lambda_1 + \lambda_2 = e^{i\mu} + e^{-i\mu} = 2 \cos \mu. \quad (2.26)$$

For the movement to be bounded, μ needs to be real. If it were complex we would obtain an hyperbolic cosine which is not bounded, whereas $|\cos \mu| < 1$. The condition for stability is then:

$$|\text{Tr}(\mathcal{M})| < 2 \quad \mu \in \mathbb{R}. \quad (2.27)$$

Remembering the transfer matrix for a quadrupole given in Eq. (2.14), we see that $|\text{Tr}(M)| < 2$ corresponds to an elliptic element of $\text{SL}_2(\mathbb{R})$.

If we consider now the transfer matrix \mathcal{M} with $|\lambda_1 + \lambda_2| \neq 2$ and $\cos \mu \neq 1$, $\sin \mu \neq 1$ we can express \mathcal{M} in a more useful form, parametrizing it in terms of the Twiss parameters. It is often the case that the value of β is better known than the strength of the magnet. The transfer matrix \mathcal{M} can be generally expressed as

$$\mathcal{M} = \begin{pmatrix} a & b \\ c & d \end{pmatrix} = \mathcal{I} \cos \mu + \mathcal{J} \sin \mu \quad (2.28)$$

where

$$\mathcal{I} = \begin{pmatrix} 1 & 0 \\ 0 & 1 \end{pmatrix} \quad \mathcal{J} = \begin{pmatrix} \alpha & \beta \\ -\gamma & \alpha \end{pmatrix} \quad \text{and} \quad \mathcal{J}^2 = -\mathcal{I}, \quad (2.29)$$

from which we can deduce that:

$$\alpha = \frac{a - d}{2 \sin \mu} \quad \beta = \frac{b}{\sin \mu} \quad \gamma = -\frac{c}{\sin \mu}. \quad (2.30)$$

Since the determinant should be equal to one, we can derive the relation between the parameters

$$\beta\gamma - \alpha^2 = 1 \quad \rightarrow \quad \gamma = \frac{1 + \alpha^2}{\beta}, \quad (2.31)$$

obtaining

$$\mathcal{M} = \begin{pmatrix} \cos \mu + \alpha \sin \mu & \beta \sin \mu \\ -\gamma \sin \mu & \cos \mu - \alpha \sin \mu \end{pmatrix}, \quad (2.32)$$

where μ is the *phase advance*, corresponding to the number of betatron oscillations a particle undergoes in an accelerator segment. This is given by

$$\mu(s) = \oint \frac{ds}{\beta(s)}. \quad (2.33)$$

The total number of betatron oscillations in one revolution is called the tune Q , and is related to the phase advance

$$Q = \frac{\mu_{\text{tot}}}{2\pi}. \quad (2.34)$$

We can also build a transfer matrix that transports the particle between two arbitrary points in the machine

$$\mathcal{M}_{1 \rightarrow 2} = \begin{pmatrix} \sqrt{\frac{\beta_2}{\beta_1}}(\cos \Delta\mu + \alpha_1 \sin \Delta\mu) & \sqrt{\beta_1 \beta_2} \sin \Delta\mu \\ -\frac{(1 + \alpha_1 \alpha_2) \sin \Delta\mu + (\alpha_2 - \alpha_1) \cos \Delta\mu}{\sqrt{\beta_1 \beta_2}} & \sqrt{\frac{\beta_1}{\beta_2}}(\cos \Delta\mu - \alpha_2 \sin \Delta\mu) \end{pmatrix}. \quad (2.35)$$

2.3.2 The Root Mean Square emittance

The beam distribution can be characterized by its first and second moments. The first moments give the centroid motion. The second moments are combined in a *beam matrix* or *sigma matrix*, which is just a statistical way of parametrizing the phase space ellipse. The explicit sigma matrix for x , assuming that the horizontal and vertical plane are not coupled, is [29]

$$\Sigma_{\text{beam}}^x = \begin{pmatrix} \langle x^2 \rangle - \langle x \rangle^2 & \langle xx' \rangle - \langle x \rangle \langle x' \rangle \\ \langle x'x \rangle - \langle x' \rangle \langle x \rangle & \langle x'^2 \rangle - \langle x' \rangle^2 \end{pmatrix} = \begin{pmatrix} \sigma_{xx} & \sigma_{xx'} \\ \sigma_{x'x} & \sigma_{x'x'} \end{pmatrix}, \quad (2.36)$$

where

$$\begin{aligned}\langle x^2 \rangle &= \frac{\sum x^2}{n} - \left(\frac{\sum x}{n} \right)^2 \\ \langle x'^2 \rangle &= \frac{\sum x'^2}{n} - \left(\frac{\sum x'}{n} \right)^2, \\ \langle xx' \rangle &= \frac{\sum xx'}{n} - \left(\frac{\sum x \sum x'}{n^2} \right)\end{aligned}\quad (2.37)$$

and all sums are performed for the n particles in the distribution.

The beam matrix is related to the Twiss parameters by

$$\Sigma_{beam}^x = \epsilon_x \begin{pmatrix} \beta_x & -\alpha_x \\ -\alpha_x & \gamma_x \end{pmatrix}, \quad (2.38)$$

and the emittance is given by the square root of the determinant of the sigma matrix, called the Root Mean Square (RMS) emittance $\epsilon_x = \sqrt{\sigma_{xx}\sigma_{x'x'} - \sigma_{x'x}\sigma_{xx'}}$.

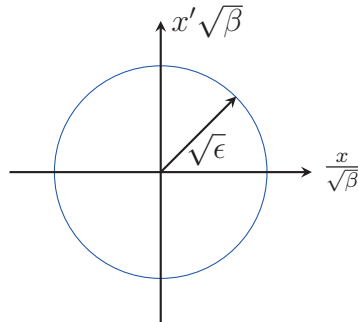
2.3.3 Action-angle variables

It is often useful to work on a normalized phase space, given by the Floquet transformation

$$\begin{pmatrix} v \\ v' \end{pmatrix} = \begin{pmatrix} \frac{1}{\sqrt{\beta}} & 0 \\ \frac{\alpha}{\sqrt{\beta}} & \sqrt{\beta} \end{pmatrix} \begin{pmatrix} u \\ u' \end{pmatrix} \quad \begin{cases} v = \frac{u}{\sqrt{\beta}} \\ v' = u \frac{\alpha}{\sqrt{\beta}} + u' \sqrt{\beta} \end{cases}. \quad (2.39)$$

The magnitude of the new vector will give us the radius of the phase space circle:

$$\sqrt{v^2 + v'^2} = \sqrt{\epsilon}. \quad (2.40)$$



In this case, the motion of the particle is better described by the canonical variables action J_x and angle μ_x

$$\begin{aligned} x &= \sqrt{2J_x\beta_x} \cos \mu_x \\ x' &= -\sqrt{\frac{2J_x}{\beta_x}} (\sin \mu_x + \alpha_x \cos \mu_x), \\ J_x &= \frac{1}{2}(\gamma x^2 + 2\alpha_x x' + \beta x'^2) \end{aligned} \tag{2.41}$$

where the angular position along the ring μ becomes the independent variable and the trajectory of a particle is now independent of the position s . The constant radius of the circle $\sqrt{2J}$ defines the action J , which is an invariant of the motion [30]. The emittance can now be defined as the average of the action of the particles $\epsilon = \langle J \rangle$. As an invariant of the motion, the emittance is the single most important concept used in accelerator physics to characterize the beam.

2.4 Particle tracking

An accelerator lattice is represented in code by a concatenation of its different components, such as drifts, magnets, and cavities. Tracking codes simulate the trajectory of a particle in an accelerator for many turns and are widely used to study a variety of phenomena. Each component type defines different equations of motion, which in tracking codes are approximated by transfer matrices as the ones studied in this chapter, also called *symplectic maps*.

The simplest form of a symplectic map is a square matrix \mathcal{S} of unit determinant that satisfies

$$\mathcal{S}^\top \mathcal{M} \mathcal{S} = \mathcal{M} \quad \text{where} \quad \mathcal{M} = \begin{pmatrix} 0 & \mathcal{I}_n \\ \mathcal{I}_n & 0 \end{pmatrix}, \tag{2.42}$$

\mathcal{I}_n being the $n \times n$ identity matrix. *Symplecticity* is a property of the Hamiltonian formalism, chosen generally in accelerator physics for its flexibility transforming between coordinate systems. Physically it is described by Liouville's theorem, which states that a volume in phase space will be conserved as long as the border points follow canonical (symplectic) transformations. This is a property of charged particles moving in electromagnetic fields in the absence of non-conservative forces, which in accelerator physics translates into the conservation of the particle's action J

$$\mathcal{S}J = J, \tag{2.43}$$

and therefore of the beam emittance $\epsilon = \langle J \rangle$.

The symplectic map of an element in an accelerator can be derived from the general form of the Hamiltonian describing the motion in an accelerator. It can be derived by taking the general form of a Hamiltonian for relativistic particles in an electromagnetic field in a curved system and changing the independent variable from time to arc length s , normalizing the canonical momenta by p_s , and transforming the canonical pair (E, t) to their deviations from a fixed reference [31], giving

$$\mathcal{H} = \frac{1 + \eta\delta}{\beta_r} \left(p_t + \frac{1}{\beta_r} \right) - (1 + hx) \frac{qA_s}{p_s} - (1 + hx) \sqrt{\left(1 + p_t - \frac{q\phi}{p_s} \right)^2 - \left(p_x - \frac{qA_x}{p_s} \right)^2 - \left(p_y - \frac{qA_y}{p_s} \right)^2 - \frac{1}{\beta_r^2 \gamma_r^2} \left(p_t - \frac{q\phi}{p_s} \right)^2}, \quad (2.44)$$

where $h = 1/\rho$ is the curvature of the reference system, $\eta = \alpha - 1/\gamma^2$ is the momentum compaction factor, $\delta = (p_s - p_0)/p_0$ is the momentum spread, p_0 is the design momentum, $p_s = p_0(1 + \delta)$ is the average momentum, β_r and γ_r are the relativistic factors, $p_t = \Delta E/p_s c$ is the normalized longitudinal momentum, q is the particle charge, p_x and p_y are the normalized canonical momenta ϕ is the scalar potential and A the vector potential.

2.4.1 *SixTrack*

Tracking codes such as SixTrack, used to carry out the simulations of this thesis, approximate \mathcal{H} to a second order expansion of the canonical momenta, obtaining finite power series maps. The power at which the series is truncated defines the order of the approximation to the particle motion, which introduces a symplectic error that will accumulate turn by turn. Nevertheless, this approximation has been found to be an adequate description for beam dynamics in the LHC [32, 33, 34].

Maps are used in SixTrack usually in the thin lens approximation, although thick tracking is also available. In the thin lens approximation a magnet of a specific length is divided in a certain amount of *slices* of zero length, separated by drifts. Each slice gives a kick to the particle, changing only its momentum. The amount of slices, drifts and their position is defined by several methods optimized to give the same result as the original thick element, such as the TEAPOT method [35]. SixTrack uses machine lattices as input, where the elements are already sliced. Specifically, SixTrack is normally used to read lattices generated by the Methodological Accelerator Design (MAD)-X program [36], which uses several slicing methods [37, 38].

Thin slicing is used to reduce the computing power needed for tracking.

It is important to note that SixTrack is a single particle dynamics code in which the interaction of a single particle with the rest of the particles of the beam is not considered, nor their interaction with the environment (impedance). Space charge effects decrease with the growth of the relativistic factors β_r and γ_r , so it is safe to assume that these forces will not affect the general trajectory of LHC's ultrarelativistic particles.

Chapter No.3

The High Luminosity LHC

The future configuration of the LHC, called the High Luminosity LHC (HL-LHC), will use crab cavities to modulate luminosity and reach its design peak luminosity. The peak luminosity represents the potential rate of collisions per square centimeter, an essential parameter to extend the discovery potential of the LHC. Apart from a higher peak luminosity, a good performance is also needed to maximize the amount of recorded collisions. This is achieved by having very reliable systems and small downtimes after equipment failures. Crab cavities are relatively new devices that will operate with a high energy beam very near the experiments, which have the potential of affecting their performance. This motivates the detailed study of crab cavity behavior during failure. This chapter serves as an introduction to the LHC machine and the HL-LHC upgrade, where different machine protection concerns are discussed.

3.1 The LHC in a nutshell

The Large Hadron Collider (LHC) is the last ring in a series of injectors that accelerate the particles to increasingly higher energies (see Table 3.1). Hydrogen atoms are stripped of their electrons to yield protons, which are then accelerated by the Linear Accelerator (LINAC) 2, the Proton Synchrotron Booster (PSB), the Proton Synchrotron (PS), the Super Proton Synchrotron (SPS), finally arriving at the LHC.

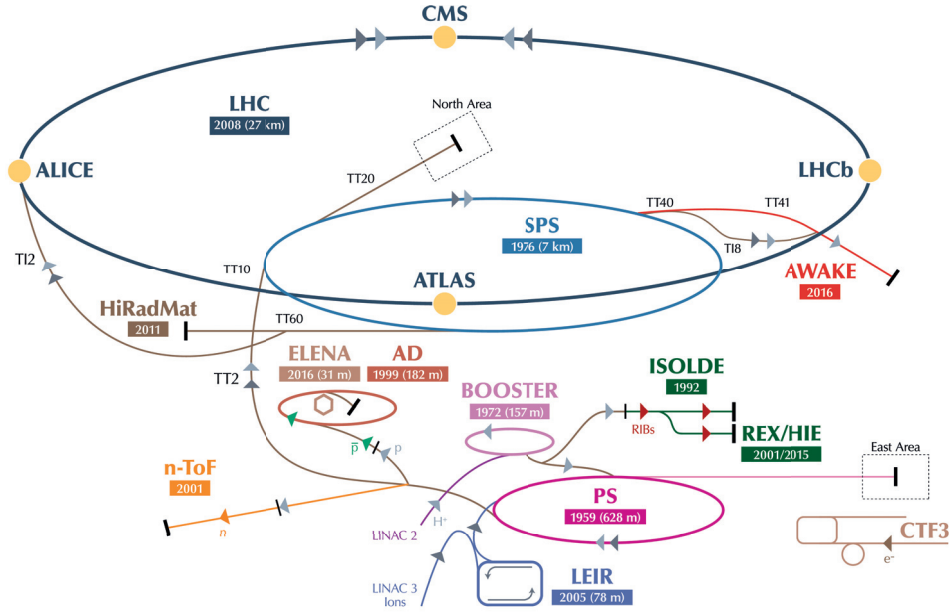


Figure 3.1. The accelerator complex at CERN [39].

Table 3.1. The injector chain of the LHC.

Name	Top energy (GeV)	Circumference (m)
LINAC 2	0.050	—
PSB	1.4	157
PS	25	628.32
SPS	400	6911.56
LHC	7000	26658.88

The LHC is a synchrotron accelerator, a storage ring, and a collider. It is composed of two rings where the beams travel in opposite directions and collide at the Interaction Points (IPs). There are four IPs in the LHC, which are located at the center of each particle detector: A Toroidal LHC Apparatus (ATLAS), A Large Ion Collider Experiment (ALICE), the Compact Muon Solenoid (CMS), and LHC-beauty (LHCb). The beam travelling

clockwise is conventionally named *beam 1*, and the beam travelling counter-clockwise *beam 2*. Both rings have separate vacuum chambers except in the area around the IPs, where both beampipes merge to allow the collision of both beams.

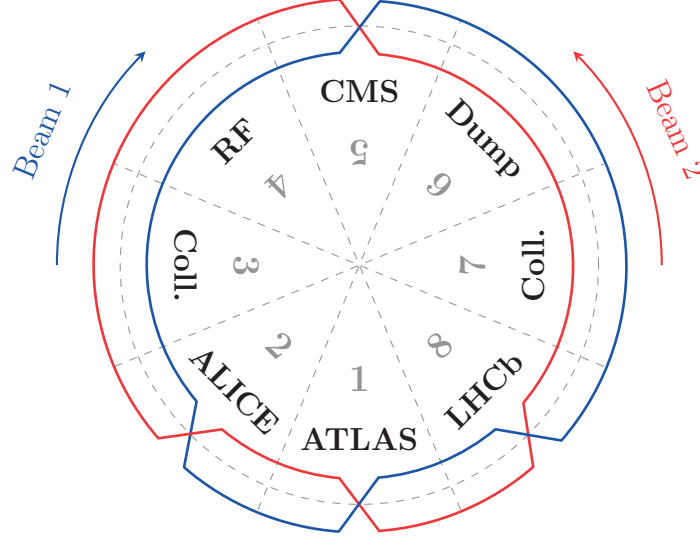


Figure 3.2. A schematic view of the LHC beam and its sectors.

The LHC follows the LEP tunnel geometry, which is composed of eight arcs and eight Long Straight Sections (LSSs), rather than being a perfect circle as shown in Fig. 3.2. Each LSS has an IR, where the experiments and four different utility systems are located, as described in Table 3.2.

Table 3.2. The LHC IRs.

Region	Name	Function
IP1	ATLAS	Detector
IP2	ALICE	Detector
IR3	Collimation	Off-momentum cleaning
IR4	RF	Beam acceleration and dedicated beam instrumentation
IP5	CMS	Detector
IR6	Beam dump	Beam extraction
IR7	Collimation	Betatron cleaning
IP8	LHCb	Detector

3.1.1 The concept of luminosity

The energy at collision and the number of useful interactions are the most important figures of merit of particle physics experiments, the latter being especially important in the study of rare events with small production cross sections σ_p , where the cross-section represents the probability for any given physics process to occur. Luminosity \mathcal{L} is defined as the proportionality factor between the number of interactions per second dN/dt and the cross-section

$$\frac{dN}{dt} = \mathcal{L} \sigma_p, \quad (3.1)$$

and is given in units of $\text{cm}^{-2} \text{s}^{-1}$. By adding the cross-sections for all possible processes and knowing the luminosity we obtain that dN/dt is equal to the total number of collisions. This is why luminosity is used as a parameter to measure the ability of a collider to produce the required interactions. We often find in the literature a simplified expression of the luminosity that considers identical, round Gaussian beams, and neglects factors that reduce luminosity such as collision offsets, the hourglass effect or non-zero dispersion at the IP, given by

$$\mathcal{L} = \frac{E n_b N^2 f_{rev}}{4\pi m_p \epsilon_n \beta^* c^2}, \quad (3.2)$$

where E is the particle energy, n_b the number of bunches per beam, N the bunch population, f_{rev} the revolution frequency, m_p the proton mass, ϵ_n the normalized emittance and β^* the beta function at the IP. The luminosity \mathcal{L} in Eq. (3.2) represents the instantaneous number of interactions per second, i.e. the *peak luminosity*. While the achievable peak luminosity represents the discovery potential of an accelerator, it is the total accumulation of recorded data that ultimately describes its performance. The *integrated luminosity* represents the number of collisions, or data, recorded by the experiments in a certain amount of time.

$$\mathcal{L}_{\text{int}} = \int_0^T \mathcal{L}(t) dt, \quad (3.3)$$

and colliders such as the LHC are designed and operated to maximize it.

3.1.2 Luminosity production in the LHC

Beams are put in collision during the *stable beams* or *physics* phase of the LHC operational cycle, shown in Fig. 3.3. The operational cycle starts when the beams are transferred from the SPS to the LHC at 450 GeV during the *injection* phase, after verifying the correct behavior of the machine with a safe beam probe. The magnet strengths, proportional to the longitudinal momentum as shown in Eq. (2.2), are then *ramped-up* in order to accelerate the beams to top energy. This is followed by a *squeeze* in beam size and adjustment for collision [1]. The time between beam dump and stable beams, also called the *turnaround time*, was on average 8.8h in 2015 [2].

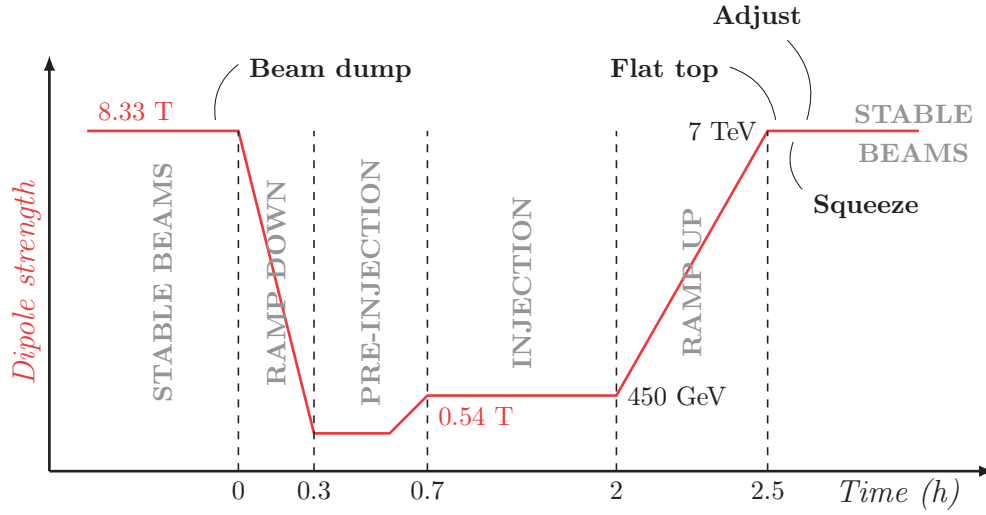


Figure 3.3. The LHC optimal turnaround time [1, 2].

Luminosity is not constant during a physics run but decays due to the degradation of intensities and emittances of the circulating beams [40, Chapter 3.1.3]. The main cause for luminosity decay are the collisions themselves or *burn-off*, where the number of particles starts decreasing due to the inelastic interactions that take place. We can see from Eq. (3.1) that, indeed, the luminosity is proportional to the variation of the number of particles over time. The luminosity decay due to burn-off can be modeled as

$$\mathcal{L}(t) = \frac{\mathcal{L}(0)}{(1 + t/\tau)^2}, \quad (3.4)$$

where τ is the *luminosity lifetime*.

Beam halo

The beam lifetime is not constant through the operational cycle due to different sources of beam loss such as collision with residual gas molecules in the beampipe, intrabeam scattering, beam instabilities, synchrotron radiation damping, beam-beam effects and dynamic changes during the operational cycle. These diffusion mechanisms migrate particles from the bunch core to higher amplitudes, populating what is known as the beam *halo*. We can distinguish between the *betatron* and *off-momentum* halo, created by deviations in transverse amplitude or energy, respectively. We can generally model the core of a LHC proton bunch in the transverse plane as a four-dimensional (x, x', y, y') Gaussian distribution. In order to account for the halo particles we also consider a second Gaussian distribution, or *tail*, that will have a larger standard deviation σ and a smaller number of particles than the core, as depicted in Fig. 3.4. Generally, it is considered that the particles with an amplitude beyond 3σ constitute the beam halo and below 3σ the core. The core contributes to 99% of the luminosity [41].

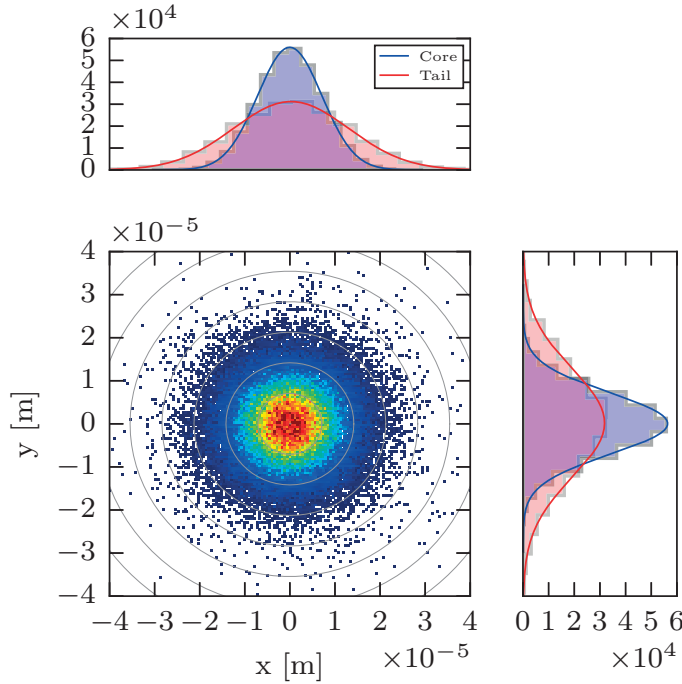


Figure 3.4. A particle beam of 10^5 particles modeled as a 2D double Gaussian distribution. Here, $\sigma_{\text{tail}} = 1.8\sigma_{\text{core}}$, where the core makes up 95% of the beam, and the tail 5% [42]. The gray circles have a radius of $n\sigma$, where $n = 1, 2, 3, \dots$. The top and right plots show the histogram of the distribution, and the probability density function divided into core (blue) and tail (red).

3.1.3 The collimation system

The magnets produced to guide and control the beam through the machine are not perfect and exhibit nonlinearities that grow transversely with the distance from their longitudinal axis. This is why particles that go beyond a certain amplitude, called the *dynamic aperture*, can become unstable during the beam lifetime. The unstable motion of the particles can make them reach amplitudes higher than the geometric aperture of the machine, where they are lost. The halo is populated by particles beyond the dynamic aperture and increases the particle losses around the machine. Uncontrolled particle losses can quench superconducting magnets and cause irreparable damage to the machine. Additionally, continuous particle losses on equipment reduces its lifetime and can produce events from particle-matter interactions that contribute to the machine background (further explored in Section 3.3.1). Since the addition of particles to the halo during operation is continuous and unavoidable, a multistage collimation system was deployed in the LHC to protect the regions with sensitive equipment [3, Chapter 13]. The collimation system also protects the machine from losses that cannot be managed by an active protection system, such as the ones caused by ultrafast failures.

Collimators constitute the limiting aperture of the machine and are made of two parallel, movable jaws of special materials, allowing the beam core to pass through the gap between them while intercepting the beam halo (see Fig. 4.5).

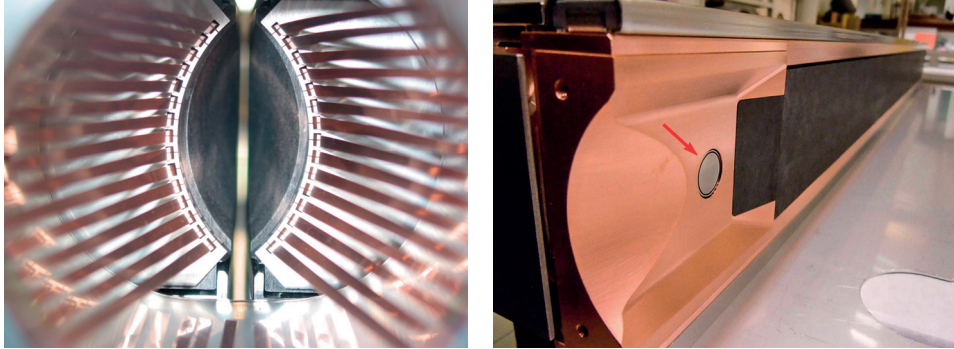


Figure 3.5. **Left:** view along the beam path of a collimator and its RF contacts, with a 2 mm gap. The collimator can open up to 60 mm [43]. **Right:** one of the jaws of a carbon collimator with a copper support, featuring a 10 cm tapering at both ends to avoid geometrical impedance effects, and an embedded Beam Position Monitor (BPM) button (see red arrow) [44].

The collimator openings are conventionally expressed in units of the local betatron RMS beam size

$$\sigma = \sqrt{\beta \epsilon_g}, \quad (3.5)$$

where β is the beta function at the position of the collimator, $\epsilon_g = \epsilon_n / \beta_r \gamma_r$ is the geometrical emittance and β_r, γ_r the relativistic factors. The two jaws are transversely positioned around the beam center at a distance of $\pm n\sigma$, n depending on the collimator family. The openings must respect a predefined hierarchy to ensure an efficient cleaning, as illustrated in Fig. 3.6.

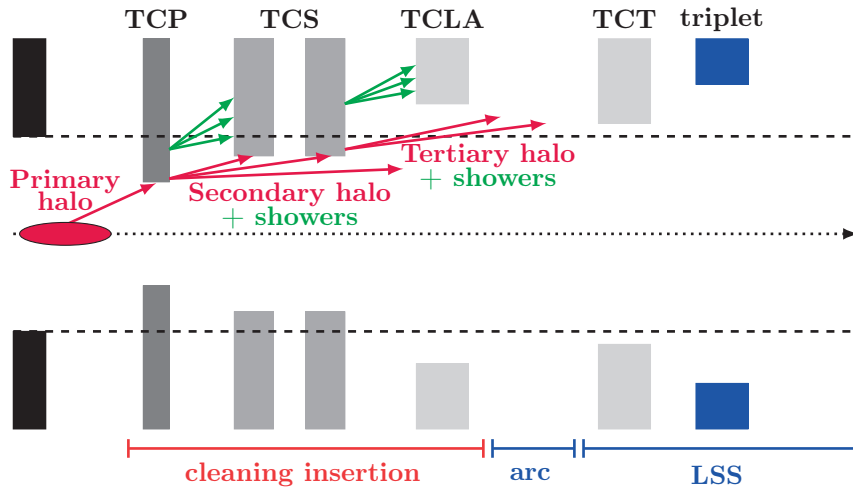


Figure 3.6. Scheme of the multistage collimation system at the LHC. The interaction with the collimator materials is itself a source of off-momentum and betatron halo. Electromagnetic and hadronic showers develop during the interaction with the collimator and carry an important fraction of the beam energy [3, Chapter 13].

The majority of the collimators are spread out among two warm insertions dedicated to clean the off-momentum halo (IR3) and the betatron halo (IR7), shown in Fig. 3.2. We can find three families of collimators in these areas: the Target Collimator Primary (TCP), the Target Collimator Secondary (TCS), and the Target Collimator Long Absorber (TCLA). The TCPs have the smallest aperture and are therefore the first collimators to intercept the halo particles. The particles that manage to escape and the showers created in the impact with the TCPs are then intercepted by the TCSs followed by the TCLAs to absorb any remnants. The Target Collimator Tertiaries (TCTs) are located upstream of the IPs to protect the final focusing system, and therefore constitute the smallest aperture restriction in the LSS around the experiments. Both TCPs and TCSs take the majority of the losses, so they need to be built with a robust material that limits the energy absorption in the jaws such as Carbon Fiber Composite (CFC). The TCLAs and TCTs, on

the other hand, are made of tungsten alloy since they intercept the tertiary halo and need to absorb as much as possible. While the TCPs and TCSs can withstand the impact of several bunches without damage, the TCLAs and TCTs should never intercept large losses. The rest of the collimators protect the injection and extraction transfer lines [3, Chapter 13].

Cleaning performance

The cleaning performance of the collimation system is measured by the *local cleaning inefficiency* $\tilde{\eta}_c$, defined as the number of protons lost in the machine aperture N_{lost} per unit length Δs at a longitudinal position s in the ring, normalized by the total losses in the machine N_{abs} :

$$\tilde{\eta}_c = \frac{N_{\text{lost}}(s \rightarrow s + \Delta s)}{N_{\text{abs}}} \frac{1}{\Delta s}. \quad (3.6)$$

The cleaning inefficiency represents the fraction of protons lost at a certain location, so it depends on the longitudinal position $\tilde{\eta}_c = \tilde{\eta}_c(s)$.

The collimation system should have a cleaning inefficiency low enough to avoid quenching superconducting magnets. This means that the proton loss rate R_{loss} needs to be below the quench limit R_{quench}

$$R_{\text{loss}} \tilde{\eta}_c < R_{\text{quench}}. \quad (3.7)$$

The design proton loss rate R_{loss} for the LHC collimators is of 4.3×10^{11} protons per second. The intensity of the beam N will decay with the proton loss rate, which sets a certain beam lifetime τ_{beam}

$$\tau_{\text{beam}} \approx \frac{N}{R_{\text{loss}}}. \quad (3.8)$$

From Eq. (3.7) and Eq. (3.8) we can see that the collimation inefficiency sets a limit on the beam intensity: if the inefficiency is very high, i.e. if the collimation system is not cleaning the beam properly and there is a leakage of halo particles, the number of particles circulating needs to be reduced to avoid quenches [40, Section 18.2.1].

3.1.4 LHC Run 2

Run 2 denotes the LHC operation between 2015 and 2019 (see Fig. 3.9).

In the year 2016, the number of collisions in the LHC was 60% higher than anticipated, collecting more data than the three previous runs combined ($\sim 40 \text{ fb}^{-1}$). Additionally, a record number of bunches circulating was achieved, as well as a record beam lifetime, making 2016 an exceptional year for the LHC. In the year 2017 the LHC far exceeded its target for that year, collecting 50 fb^{-1} of data and reaching a record peak luminosity of $2.06 \times 10^{34} \text{ cm}^{-2} \text{ s}^{-1}$, which is twice the nominal value [45].

This performance was possible thanks to the flexibility of the injector chain. The ultimate peak luminosity goal was reached in 2016 thanks to the implementation of a new bunch-production scheme called Batch Compression Merging and Splitting (BCMS) [46]. This scheme allows reducing the beam size considerably, which in turn produces more collisions. Additionally, a new bunch scheme was developed in 2017 to reduce the interaction of the beam with an increased density of macroparticles due to a vacuum incident, called the *8b4e beam* [47]. Using this beam resulted in a smoother operation that allowed reaching the 50 fb^{-1} of recorded data in 2017.

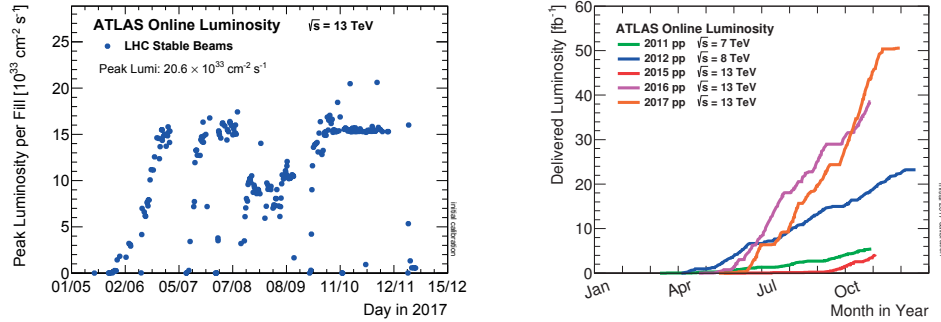


Figure 3.7. **Left:** the peak instantaneous luminosity delivered to ATLAS during stable beams for proton-proton (pp) collisions at 13 TeV centre-of-mass energy for each LHC fill as a function of time in 2017. **Right:** integrated luminosity per year recorded in ATLAS during stable beams for high energy proton-proton (pp) collisions [48].

3.2 The High Luminosity LHC

The HL-LHC aims at a tenfold increase of the LHC annual integrated luminosity (shown in Table 3.3), which would provide the High Energy Physics (HEP) community with an unprecedented data sample that will be key to tackling some of the most important open questions in particle physics [23].

Table 3.3. Current LHC and HL-LHC luminosity goals at 25 ns operation.

	LHC 2017	HL goal	HL ultimate goal
$\mathcal{L}_{\text{peak}} (10^{34} \text{ cm}^{-2} \text{ s}^{-1})$	2.06	5.0 ¹	7.5 ¹
$\mathcal{L}_{\text{int}} (\text{fb}^{-1}/\text{year})$	50	250	320
$\mathcal{L}_{\text{int}} (\text{fb}^{-1})$	123 ²	3000	4000

¹ Leveled (see Section 3.2.4).

² The data was not recorded at the same energy.

In order to achieve the ambitious goals described above, we must first define the strategy to increase the luminosity. The luminosity is inversely proportional to the β function at the IP (see Fig. 3.8), which means that one can maximize the luminosity by operating with β^* as low as possible. This method contributed significantly to the performance of the LHC during Run 1 [49] and has been chosen as one of the mechanisms to increase the luminosity in HL-LHC. Other methods include an increase in the number of particles per bunch N and a reduction of the emittance ϵ_n , as shown in Table 3.4.

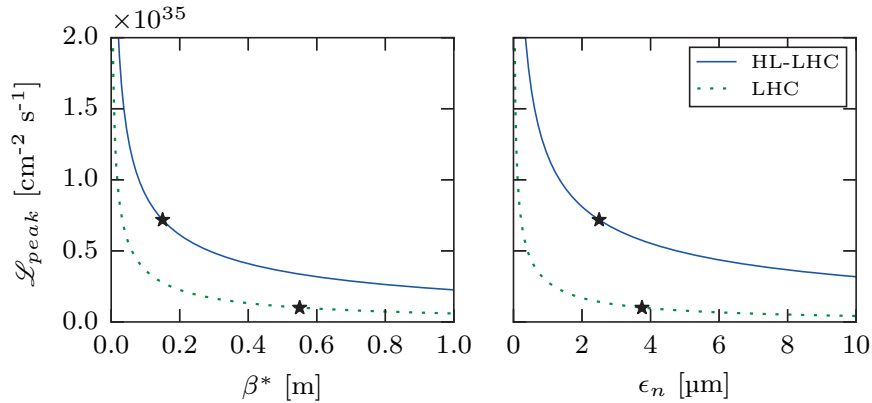


Figure 3.8. The evolution of the peak luminosity with the β function at the IP (left), and the emittance (right), as described by Eq. (3.2). The black stars represent the working points for each machine.

Table 3.4. Comparison of nominal and standard HL-LHC parameters for 25 ns bunch spacing operation [50].

Parameter	LHC	HL-LHC
Beam energy in collision [TeV]	7	7
Particles per bunch, N [10^{11}]	1.15	2.2
Number of bunches per beam, n_b	2808	2748
Number of collisions (IP1, IP5)	2808	2736
Crossing angle (IP1, IP5) [μrad]	285	590
Minimum β^* [m]	0.55	0.15
Normalized emittance ϵ_n [μm]	3.75	2.50
RMS energy spread [10^{-4}]	1.13	1.13 ¹
RMS bunch length [cm]	7.55	7.55 ²
Piwinski parameter, ϕ	0.65	3.14
Total loss factor without CC, R_0	0.836	0.305
Total loss factor with CC, R_1	–	0.829
Pile up without CCs and leveling ³	27	198
Pile up with CCs and leveling	–	138
Peak luminosity without CCs [$10^{34} \text{ cm}^{-2} \text{ s}^{-1}$]	1.00	7.18
Virtual luminosity with CCs [$10^{34} \text{ cm}^{-2} \text{ s}^{-1}$] ⁴	–	19.54
Levelled luminosity [$10^{34} \text{ cm}^{-2} \text{ s}^{-1}$]	1.5	5

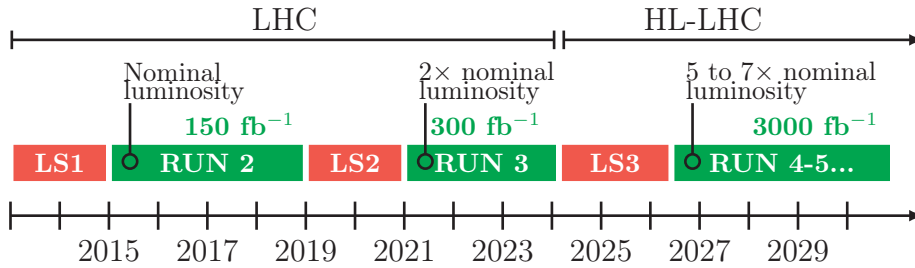
¹ Changed to 1.08×10^{-4} for V6.1.0 of the HL-LHC parameters (Oct. 2016).

² Changed to 8.1 cm for V6.1.0 of the HL-LHC parameters (Oct. 2016).

³ Calculated with an inelastic cross-section of 85 mb.

⁴ $\mathcal{L}_{peak} R_1/R_0$, with no limit in the event pile-up.

The baseline program for the upgrade spans over more than twenty years, including building and scientific exploitation (see Fig. 3.9). The refurbishment of the machine will be divided in two LSs. LS2 will tackle the upgrade of the injectors, among others, and LS3 the final HL configuration.

**Figure 3.9.** Roadmap to the HL-LHC.

The HL-LHC upgrade poses exceptional technical challenges and will rely on a series of innovative technologies such as Nb_3Sn magnets or the use of crab cavities in a crab-crossing scheme, further described in the next section.

3.2.1 The crab-crossing scheme

In a proton storage ring such as the LHC the two beams repeatedly cross each other in the common vacuum chamber areas, which are found around the IPs and span ~ 130 meters in both directions. During their trajectory, both towards and outwards the IP, the positively charged beams interact electromagnetically with each other via the *beam-beam effect*. The beam-beam effect is divided between *head-on* and *long-range*, depending on the distance between beams (see Fig. 3.10).

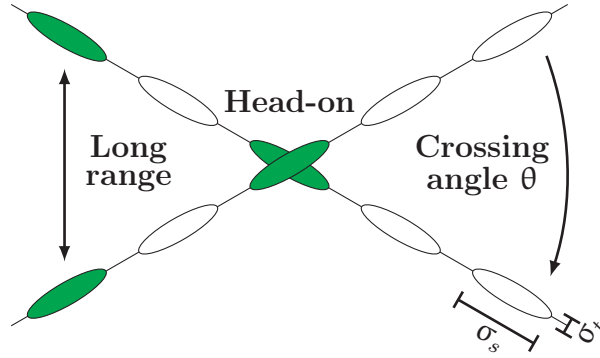


Figure 3.10. The different beam-beam effects and visualization of the beam sizes and crossing angle. The crossing angle serves to reduce head-on collisions to only one per IP.

The particles from both beams see the electromagnetic force from the oppositely moving bunch, called the beam-beam force. Assuming that only one of the oppositely moving bunches is affected and changed by the beam-beam interaction (the so-called *weak beam*) and that both bunches are frozen in time at a certain distance, we can model the deflection θ of the particles within the weak beam by

$$\vec{\theta} = -\frac{2Nr_0}{\gamma_r} \frac{\vec{r}}{|\vec{r}|^2} \left[1 - \exp\left(-\frac{\vec{r}^2}{2\sigma_t^2}\right) \right], \quad (3.9)$$

where N is the number of particles in the bunch, r_0 is the classical particle radius, γ_r is the relativistic gamma factor, \vec{r} is the distance of the particle to the bunch center and σ_t is the transverse beam size. Eq. (3.9) is valid for equally charged, round Gaussian beams.

We can see from Fig 3.11 that the beam-beam force acts linearly over small particle amplitudes, but that it is strongly nonlinear at larger amplitudes. The beam-beam effect is, in fact, the strongest nonlinearity present in a particle collider that is unavoidable.

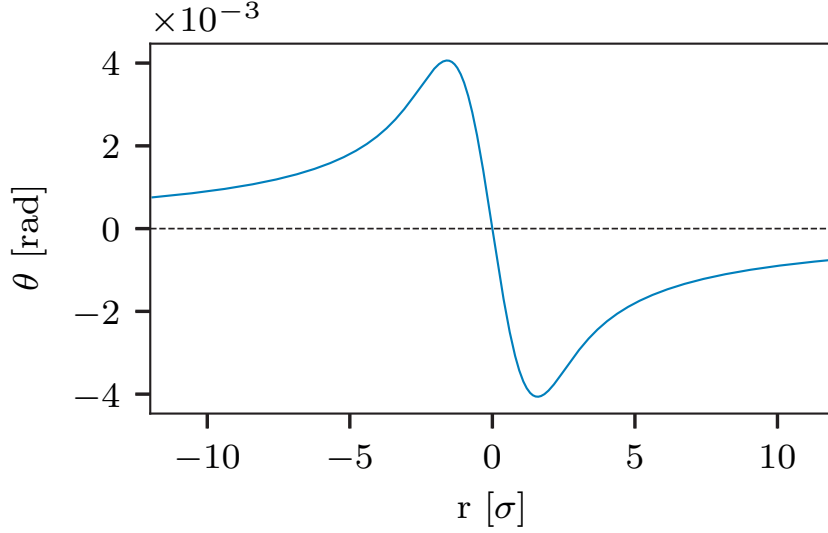


Figure 3.11. Beam-beam force in a head-on collision, on a test particle as described by Eq. (3.9).

Parasitic collisions among the counter-rotating beams happen in long-range encounters, creating beam losses. In [51] it was found that these losses have a significant impact on the beam lifetime in the LHC, and therefore on the machine performance. The amount of parasitic collisions depends on the separation between the beams, which in turn depends on the crossing angle and beam size.

The beta function, and therefore the beam size, evolve around the IP following

$$\beta(s) = \beta^* + \frac{s^2}{\beta^*}. \quad (3.10)$$

As shown in Table 3.4, β^* will be greatly reduced in the HL-LHC. Following Eq. (3.10) this will induce a fast growth in beam size with the distance from the IP. Bigger beams will generate additional parasitic collisions, impacting the HL-LHC performance. Furthermore, beam-beam effects increase with the intensity of the beams as seen in Eq. (3.9), leading to unprecedented beam-beam parameters in the HL-LHC. In order to mitigate parasitic collisions, the crossing angle will be doubled for the HL-LHC. Nevertheless, this introduces an additional problem, namely a luminosity loss due to the reduction of the overlapping area of the bunches (illustrated in Fig 3.12).

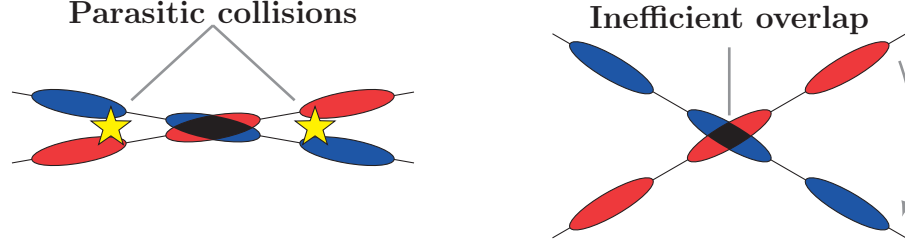


Figure 3.12. Illustration of a bunch crossing with parasitic collisions (left) and with an increased crossing angle (right).

Taking the crossing angle into account, the *reduced luminosity* \mathcal{L}_ϕ can be expressed as

$$\mathcal{L}_\phi = \mathcal{L} R_\phi, \quad (3.11)$$

where R_ϕ the geometrical loss factor

$$R_\phi = \frac{1}{\sqrt{1 + \phi^2}}, \quad (3.12)$$

ϕ is the Piwinski parameter

$$\phi = \frac{\theta \sigma_s}{2 \sigma_t}, \quad (3.13)$$

and θ the total crossing angle. We can see from Fig. 3.13 that for the LHC, the crossing angle reduces the luminosity to 80% of the original value, while for HL-LHC is reduced to 30% of the original value.

The use of crab cavities has been chosen as the baseline scenario to suppress the luminosity loss due to the crossing angle in the HL-LHC. Crab cavities are superconducting RF cavities that can rotate the beam very precisely to compensate for the geometrical luminosity loss (see Fig. 3.14). These devices have never been used in a hadron machine before, and therefore requires to be studied in detail. The current areas of crab cavity research at CERN include, among others, impedance effects such as transverse instabilities, the effects of phase and amplitude noise on beam quality, identification of failure modes, their mitigation, and prototype characterization. Crab cavity prototypes will be installed in the SPS and tested with LHC beams during 2018, which will allow validating their operation modes and cavity control systems [52]. A more detailed description of crab cavities can be found in Chapter 4.

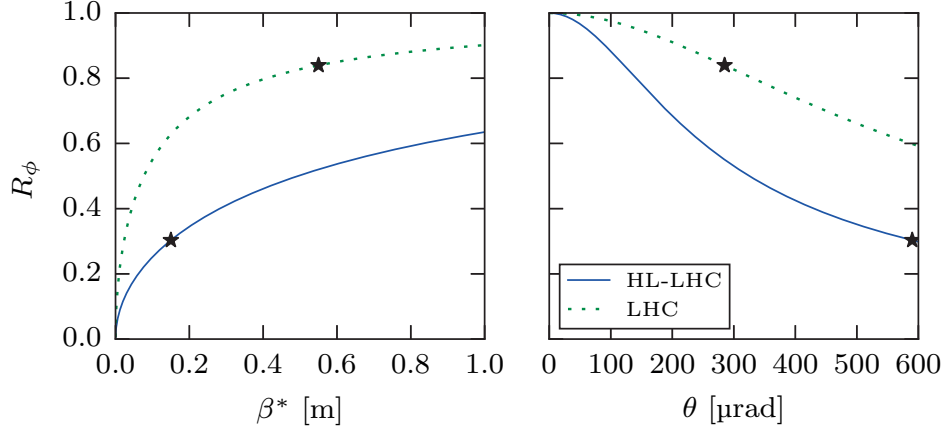


Figure 3.13. The evolution of the geometrical reduction factor R_ϕ with β^* (left), and the total crossing angle (right). The working points of each machine are marked with a black star.

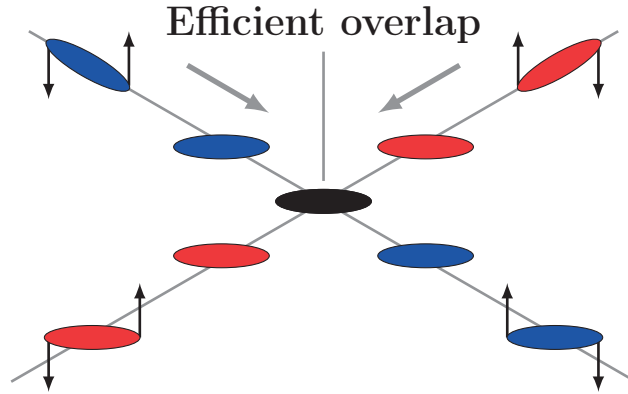


Figure 3.14. Schematic view of the kick imparted by the crab cavities. The *crabbing* compensates the crossing angle for the incoming beam just before collision and returns it to its original position after collision.

3.2.2 The insertion region for high luminosity experiments

The IRs around the IPs 1, 2, 5, and 8 house the experiments and span 300 meters from the IP in both directions until the arcs. Fig. 3.16 shows the components in one of the sides of an IR, where we distinguish between the *incoming* and *outgoing* beam. The beam orbit in these areas is mainly defined by the following magnetic elements:

The triplet (Q1 to Q3) is the final focusing system, which focuses the incoming beams before collision. It is composed of 3 quadrupole magnets with alternating polarities called Q1, Q2, and Q3, where Q2 is split into two modules. Due to the alternating polarities, the beam size grows considerably in Q2 before being focused (see Fig. 3.17), becoming an aperture bottleneck. With the reduction of β^* for the HL-LHC, the beam size will grow even more at this location. For this reason, the triplet will be replaced by new Nb₃Sn magnets with an aperture of 150 mm, instead of the current 70 mm. The triplet is superconducting, operated at 1.9 K, and therefore susceptible to quench.

Separation/recombination dipoles (D1 and D2) dipole magnets that guide the outgoing beams and the charged collision debris into two separated vacuum chambers. The D1 dipole is a warm magnet, while the D2 is a superconducting module operated at 4.5 K. They will both be replaced for HL-LHC, D1 becoming superconducting and both featuring larger apertures in IPs 1 and 5.

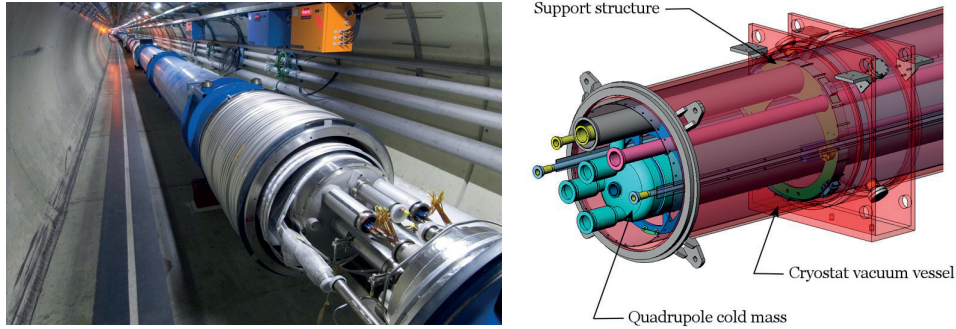


Figure 3.15. **Left:** a D2 dipole magnet in the LHC tunnel, before being connected [53]. **Right:** drawing of an inner-triplet quadrupole showing the cold mass and cryostat vacuum vessel [54].

After the recombination dipoles, we find the matching section (Q4 to Q7) and the dispersion suppressor (Q8 to Q11). Apart from the magnets described above, the experimental IRs also contain other types, such as orbit

correctors that create an orbit bump for the crossing angle or sextupoles. In order to protect the accelerator elements from collision debris carried along with the outgoing beam, several passive protection devices exist for the high luminosity experiments, ATLAS and CMS:

Target Absorber Secondaries (TAS) charged particle absorber, positioned immediately after the detector to shield the triplet from secondary particles produced in collision. It will be replaced by an absorber with with increased aperture called TAXS (from 30 mm to 60 mm).

Target Absorber Neutral (TAN) neutral particle absorber, positioned between D1 and D2 to intercept the neutral collision debris. The transition from a common vacuum chamber to separate ones happens inside this absorber. It will be replaced by an absorber with with increased aperture called TAXN (from 52 mm to 85 mm).

Physics debris collimator (TCLX, TCL5, TCL6) the TCLX is a collimator designed to protect the D2 from the debris of the outgoing beam. Other debris collimators are located further down the matching section (TCL5, TCL6).

The TAN and TAS protect sensitive equipment downstream of the outgoing beam, but they can also have a secondary role as shields from failures affecting the incoming beam. This is of special relevance for HL-LHC since their apertures will double.

Dedicated protection from the incoming beam also exists:

Tertiary collimators (TCT4s, TCT6s) The vertical and horizontal TCT4 protect the triplet and the D1 from regular losses of the incoming beam. Both TCT4s also provide shielding from accidental losses happening upstream, but they risk being damaged in the case of very fast failures [55].

Finally, the crab cavities are located between D2 and Q4, as shown in Fig. 3.16.

The beam can be manipulated in many ways, depending on the position and strength of the magnets. Each designed set of magnet strengths, element choice, and position, or configuration, is called *optics*. Several optics are currently under study for the HL-LHC [25, Chapter 2].

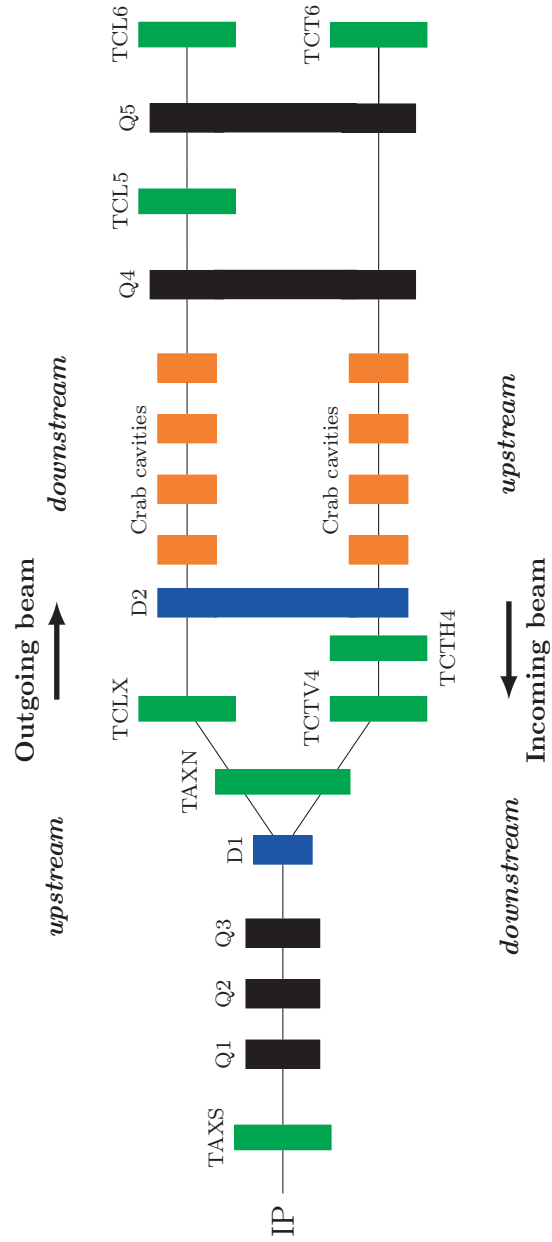


Figure 3.16. Simplified layout of one of the sides of the IR, at a high luminosity experiment for HL-LHC. The layout of the other side is exactly symmetric.

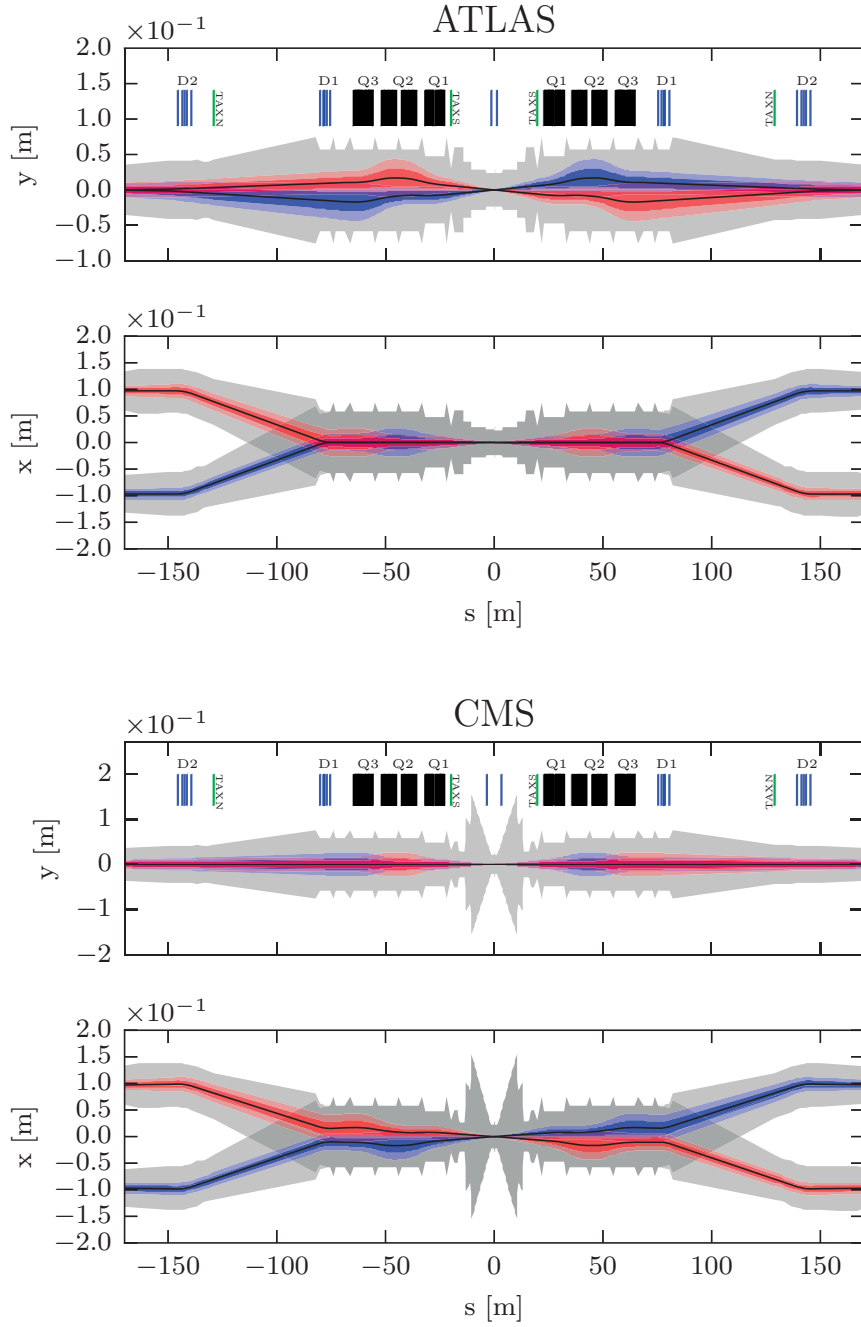


Figure 3.17. The IR for the two high luminosity experiments ATLAS and CMS, with HLLHCv1.2 optics. The closed orbit is shown as a black line, and the 5σ , 10σ envelopes in blue for beam 1, and in red for beam 2. The aperture is marked in gray, and the correspondent elements are depicted as rectangles at the top.

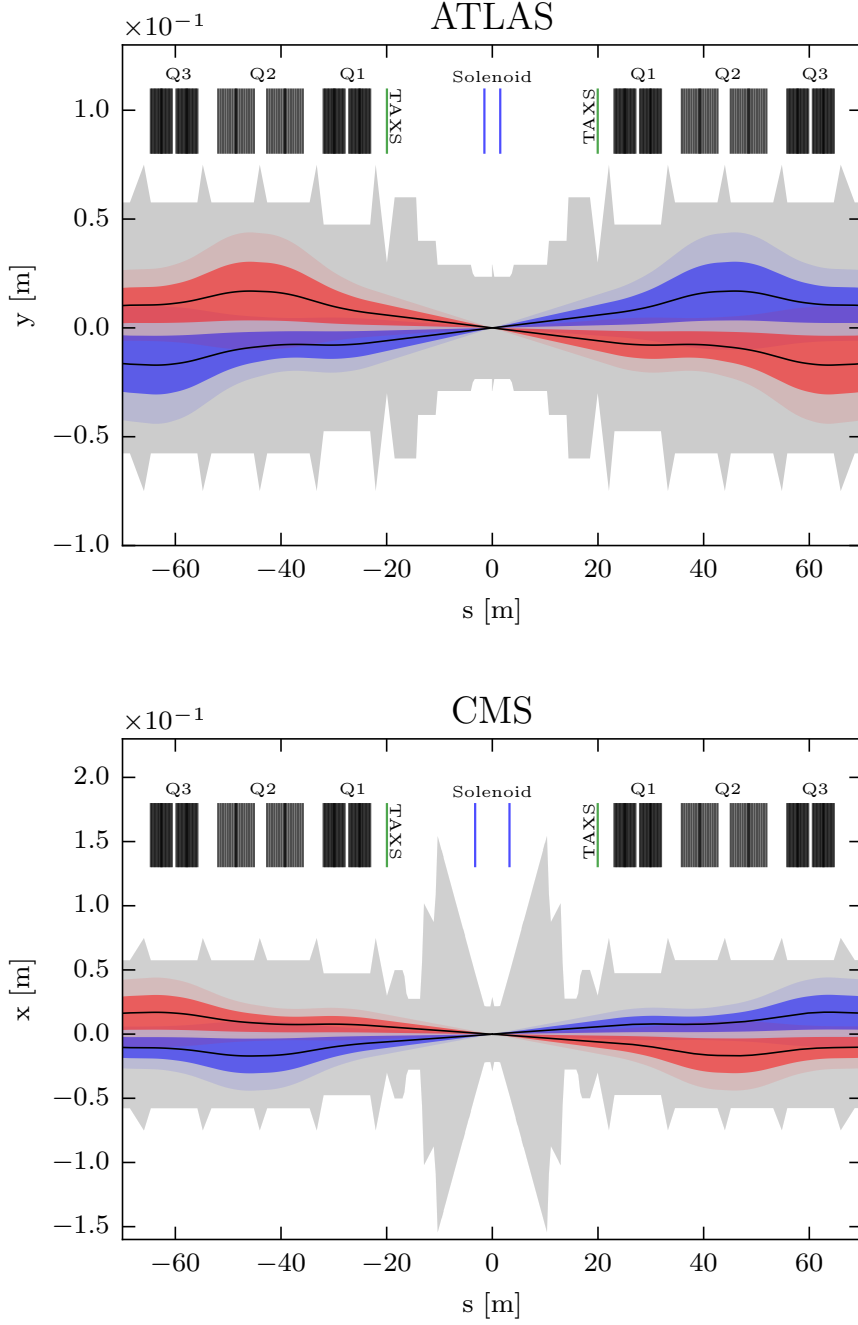


Figure 3.18. Close-up of the crossing planes shown in Fig. 3.17. Both experiments collide with the same crossing angles but in opposite transverse planes. The solenoid magnet is part of each detector and is used to sort particles by momentum. It is built to be transparent to the beam itself but constitutes a small source of coupling.

3.2.3 Detector upgrade

The study of hard scattering processes at the LHC is key for exploring physics beyond the Electroweak Symmetry Breaking (EWSB) scale. Both hard and soft scattering processes occur at collision, and the detector distinguishes between them by reconstructing only the most energetic events, which come from the so-called *primary vertices*. Primary vertices are selected by looking at the collisions that happen within a predefined area near the detector and have a certain number of tracks associated with them. If several events fulfill these requirements, the one with the highest number of associated tracks will be considered the primary vertex and will be further analyzed. The rest of the collisions that happen in each bunch crossing that are not a primary vertex are called *pile-up* events. The amount of expected pile-up μ is related to the peak luminosity \mathcal{L} by

$$\mu = \frac{\mathcal{L} \sigma_{\text{inelastic}}}{n_b f_{\text{rev}}}, \quad (3.14)$$

where $\sigma_{\text{inelastic}}$ is the pp inelastic cross section and n_b the number of bunches that collide [56].

Pile-up affects the reconstruction of physical objects such as jets (narrow cones of hadrons and other particles produced in the interaction), electrons, muons, or photons. This decreases the quality of the data by reducing the energy resolution in the calorimeters and making track-vertex association more difficult. This is why the high luminosity experiments, ATLAS and CMS, prefer to take data at a reduced luminosity. The method to achieve it is called *luminosity leveling* and is introduced in the next chapter.

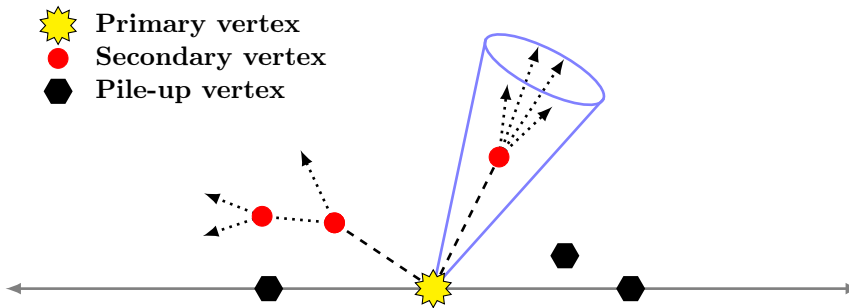


Figure 3.19. Representation of a primary vertex with only two associated tracks, its secondary vertices, a cone as used in some jet reconstruction algorithms and pile-up events.

In the HL-LHC the integrated radiation dose to the HL experiments will increase roughly by a factor 10 and pile-up will increase by a factor 5, presenting a very challenging environment for the experiments that is well beyond their current capabilities. This dense pile-up environment and high radiation levels require, among others, the development of new technologies for high

bandwidth data transmission and radiation hard sensors [57]. The upgrade of the experiments will be done progressively during the shutdown periods LS2 and LS3, also called Phases I and II, that will focus first on the trigger and detection systems and later on the inner tracker.

The pixel detectors are crucial in the reconstruction of primary and secondary vertices, so their good functioning will be key in a high pile-up environment. In order to improve their resolution they will be placed closer to the IP by reducing the experimental beampipe, as described in Table 3.5.

Table 3.5. The LHC experiments, their crossing plane and their changes for HL-LHC, where the luminosity is given in $\text{cm}^{-2} \text{s}^{-1}$ and the inner pipe radii in mm.

Name	IP	Plane	Design \mathcal{L}		Pile-up		Beampipe	
			HL-LHC	LHC	HL-LHC	LHC	HL-LHC	LHC
ATLAS	1	V	5×10^{34}	2×10^{34}	138	40	23.5	27
ALICE	2	V	1×10^{31}	1×10^{31}	0.06	0.02	18.2	27
CMS	5	H	5×10^{34}	2×10^{34}	138	40	21.7	27
LHCb	8	H	2×10^{33}	4×10^{32}	8	2	3.5	5

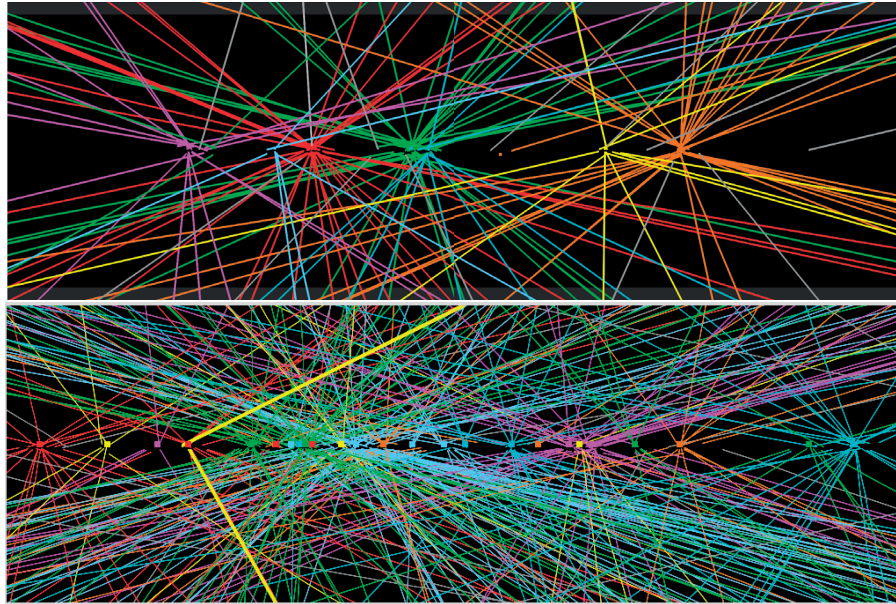


Figure 3.20. **Top:** a collision event from the first 2011 fill with stable beams, showing seven pile-up vertices. **Bottom:** a candidate Z boson event in the dimuon decay with 25 reconstructed vertices. The image shows the high pileup environment during Run I in 2012 when β^* was reduced to 0.6m [58]. Around 138 vertices are expected to be produced at the HL-LHC within a similar space.

3.2.4 Luminosity leveling

The pile-up needs to be controlled in order to keep the data quality at an appropriate level and to reduce the energy deposition from the physics debris in the IR magnets [25, Chapter 1.2.3]. This is done through *luminosity leveling*, where the pile-up events are controlled by deliberately reducing the peak luminosity (see Eq. (3.14)). Luminosity leveling provides the experiments with very stable operating conditions [59], which is achieved by compensating the decay of the beam intensity due to proton burn-off via a parameter that controls luminosity (e.g. β^* , crossing angle, offset at the IP).

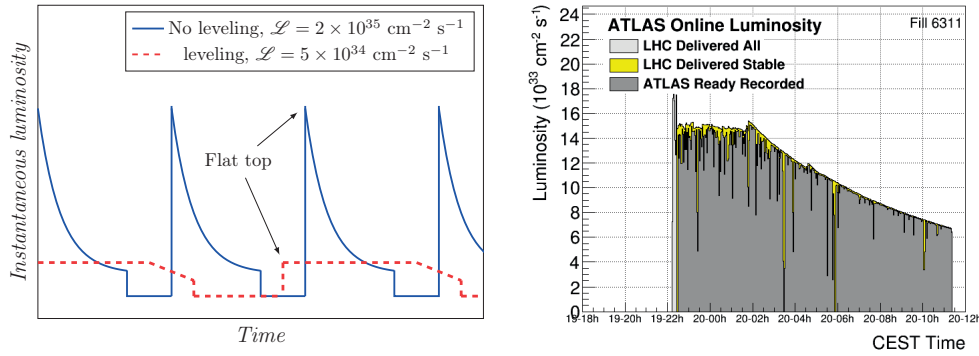


Figure 3.21. **Left:** Luminosity profile with and without leveling [3, Chapter 1]. **Right:** ATLAS luminosity for the fill 6311 with luminosity leveling [60].

The preferred method to level luminosity in the HL-LHC is β^* *leveling*, in which the beam size at the IP is changed through β^* during stable beams (see Eq. (3.2)). Other alternatives exist, such as managing pile-up with a *crab kissing* scheme [61]. The right-side plot of Fig. 3.21 shows an example of luminosity leveling in the LHC. The fill starts at high luminosity, which is leveled with beam separation for three hours. The luminosity is then increased by reducing the crossing angle before luminosity production starts decaying. Crab cavities will allow extending the leveling time in the same way, resulting in an increased production of integrated luminosity.

3.3 Machine-detector interface

Machine-detector interface refers to the transitioning area between the experiments and the rest of the accelerator. It is often the case that the detectors and the surrounding area have conflicting requirements in terms of machine and experiment protection, so it is important to plan their upgrade together [3, Chapters 5 and 7]. In the case of the HL-LHC the experimental beampipes are reduced by 50%, while the aperture at the triplet magnets and the passive absorbers will be increased by a factor 2. The opening of the passive absorbers will leave the experimental beampipe unprotected from potential fast crab cavity failures, which are located near the IP. Taking into account that stored energy in the beams will be doubled in HL-LHC, the machine-detector interface configuration poses some machine protection concerns (further explored in Chapter 3.4). It should also be considered that if the collimators were to intercept strongly populated tails in the case of failure, the secondary particles scattered from collimators could quench the magnets in the downstream section [41]. Furthermore, if the number of tertiary halo particles is big enough, the quaternary halo could still shower from the TCTs to the experimental cavern through the more open beampipe, contributing to the *machine induced background*. These scenarios are further explored in Chapter 5.

3.3.1 Machine induced backgrounds

The beam not only interacts with itself (e.g.: space charge, intra-beam scattering) or with the other beam (beam-beam effects), but also interacts with its environment through different mechanisms. The beam can interact with the electromagnetic fields induced by the beam in the vacuum chamber, creating instabilities or electron cloud. It can also create particle showers by colliding with residual gas molecules or by hitting an aperture limitation. The collision residues that reach the experimental cavern are called *machine induced background*, or just background. Background affects the quality of the data recorded by increasing trigger rates, processing time and by decreasing the detector resolution. The background rates increase linearly with intensity and slightly with energy. Efforts have been put into improving the understanding of background sources at the LHC in order to minimize them and prepare for the HL-LHC. It has been found that *beam-gas* (beam colliding with rest gas in the vacuum chamber) is the main source of background at the LHC, while *beam halo* is far less important. It can, nevertheless, become a relevant source of background during an ultrafast failure [62].

3.4 *Machine protection*

The uncontrolled release of a fraction the stored energy of the beam can damage the machine. Reducing the risk of this happening is, therefore, essential for the safety and sustainability of any accelerator facility. This is especially relevant for future high intensity and high energy machines. Machine Protection Systems (MPSs) limit the damage to equipment and reduce risks, either by preventing a failure from occurring or by mitigating the consequences of a failure.

The energy stored in the the HL-LHC beam will be approximately 700 MJ, which is double the energy stored per beam currently in the LHC. Both quantities are several orders of magnitude above the quench limit of the superconducting magnets used to guide the beam, which could cause the simultaneous failure of various magnets and constitute a harmful event for the machine. Paired with the appearance of new fast failure scenarios, such as crab cavity failures, the HL-LHC poses a machine protection challenge.

In order to understand the impact that fast failures might have on the machine performance we must first know how the MPS at the LHC works, what constitutes a hazard for the machine, and what are the timescales for these failures.

3.4.1 *Performance and availability*

We can assess the level of performance of an accelerator by looking at how much data was gathered during its lifetime, i.e. by looking at the integrated luminosity. The integrated luminosity depends, in turn, on how much time the beams are colliding and the experiments recording the data from the collisions. Equipment damage due to an accidental release of energy entails a downtime period for repair operations which directly impacts the availability of the machine and therefore its performance. The term *availability* loosely refers to the probability of an accelerator being operational at a certain time. *Operational* may refer to the machine functioning without beam (e.g. for commissioning and tests), with beam (also called beam availability), or with useful beam for the experiments (called physics availability) [63]. We will only use the last definition as it directly affects the integrated luminosity. A more rigorous definition of availability is used for statistical failure behavior predictions, tightly related to *reliability*, as shown in Fig. 3.22. Reliability is usually defined as the total relative amount of beam time made available to machine users within the scheduled time period [64].

In order to maximize operational availability and minimize downtime, as well as avoiding expensive equipment repair and irreparable damage, a MPS exists in LHC. The MPS monitors the relevant beam and equipment param-

$$\left. \begin{aligned}
\text{Availability} &= \frac{\text{MTBF}}{\text{MTBF} + \text{MTTR}} \\
\text{Reliability} &= \frac{\text{MTTR}}{\text{MTBF} + \text{MTTR}}
\end{aligned} \right\}
\begin{aligned}
&\text{Mean Time Between Failures} \\
&\text{"Average time between two failures of a repairable system"} \\
&\text{Mean Time To Repair} \\
&\text{"Average time to recover from a failure"}
\end{aligned}$$

Figure 3.22. Statistical definition of availability and reliability, with respect to observable parameters [4].

eters through different types of instrumentation, and takes action when a value is out of a predefined range through the Beam Interlock System (BIS). The BIS is part of the MPS and is connected to roughly 20 subsystems that, based on the global information of the beam, can inhibit operation by transmitting beam dump requests.

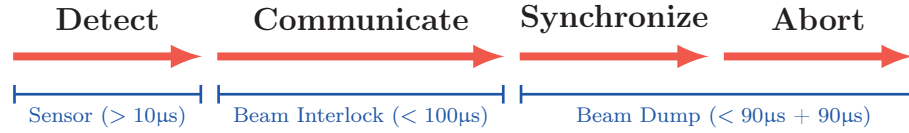


Figure 3.23. The MPS response time at LHC, from failure detection to completion of beam dump. This reaction time is sufficient for failures occurring on timescales above 3 LHC turns [3, Chapter 12].

The beam dumping system extracts the beam from the ring and dumps it into an external absorber, called the Dump for Ejected Beam (TDE), that is positioned sufficiently far away to allow for some energy dilution and emittance blow-up. The TDE is made of graphite, and is the only element that can withstand the impact of a full beam. A safe extraction of the beam to the TDE must be ensured in order to avoid damage to equipment.

If the interlocks cause beam dumps too often the research programme will be disrupted, affecting the availability of the machine. On the other hand, under-protecting will result in damage, which will also impact availability. This is why, in order to maximize availability, a balance between machine protection and operation must be kept.

3.4.2 Hazards, risks and mitigation

A hazard is a set of conditions that, together with a particular worst-case scenario, will lead into an accident. Some common hazards in accelerators include the energy stored in superconducting magnets, the power in normal conducting magnets, the energy stored in RF systems, high voltage systems (e.g. kickers), and powering systems. Hazards become accidents due to equipment failure and result in beam losses that risk damaging and irradiating the accelerator components [65]. Other sources of beam loss, not related to failures, are inelastic collisions at the IPs (burn-off), the interaction of the beam particles with residual gas, intra-beam scattering, beam instabilities, and dynamic changes during the operational cycle.

The system described in Fig. 3.23 is an *active* protection system, which detects failures through the fast monitoring of hardware parameters, and allows stopping operation before the beam is affected. Nevertheless, for very fast failures there is not enough time for detection and mitigation, so the protection of the machine relies on a *passive* protection system. This system is composed of collimators that intercept the beam losses until the failure is detected and the beam dumping system is activated.

3.4.3 Challenges for the HL-LHC

Considering the luminosity leveling needed due to the pile-up limitation in the HL-LHC, it is clear that in order to reach the goal of 300 fb^{-1} of recorded data per year the beams will have to be in collision for as long as possible. Since availability directly impacts the luminosity production, an availability-driven design is key in order to reach such an ambitious goal. There are two factors that together can hugely impact the availability at the HL-LHC: the stored beam energy and the appearance of new failure scenarios [27], as previously described.

The stored energy in the beam can be calculated considering the energy of each particle

$$E_{\text{stored}} = E \cdot N \cdot n_b, \quad (3.15)$$

where E is the particle energy, N the number of particles per bunch and n_b the number of circulating bunches per beam. For HL-LHC, with 2.2×10^{11} particles per bunch and 2748 bunches, we obtain $\sim 700 \text{ MJ}$ for each beam. This is double the energy stored in LHC beams.

The introduction of new elements such as the crab cavities will inevitably lead to new failure scenarios. In order to study failures it is useful to characterize them by their time constant for beam loss: from slow and manageable by the active protection system to very fast, completely relying on the robustness of the passive protection absorbers. Failures classified by timescale are described in Table 3.6.

Table 3.6. Classification of failures by timescale for beam loss, where $270\ \mu\text{s}$ is 3 LHC turns [5]. This corresponds to the reaction time of the MPS described in Fig. 3.23.

Type	Timescale	Examples	Protection
Slow	$> 1\ \text{s}$	Transverse beam instabilities Failure of orbit or tune feedback Cryogenics	Active & manual
Fast	$> 10\ \text{ms}$	Powering failures Superconducting magnet quench RF trip	Active
Very fast	$> 270\ \mu\text{s}$	Normal-conducting magnet trip Transverse damper failure Dust particle in the beam (UFO) crab cavity failure	Active & passive
Ultrafast	$\leq 270\ \mu\text{s}$	Injection and extraction failure crab cavity failure	Passive

Failures can also be characterized by the risk they pose, defined as [4]

$$\text{Risk} = \text{Probability} \times \text{Consequences},$$

where *probability* stands for the statistical probability of the failure happening, and *consequences* refer to its damage potential.

This thesis focuses on assessing only the consequences crab cavity failures can have on the machine. Currently, an accurate estimation of the probability of failure is premature since the crab cavity prototypes are still under development and cannot be tested in the conditions of their final setup. Nevertheless, some estimations have been made in [66], further commented in Chapter 4, Section 4.7.5.

3.5 *Summary*

The HL-LHC is an ambitious project that aims at a tenfold increase in integrated luminosity compared to the LHC. To achieve this the number of particles per bunch will be doubled and the beta function at the IP will be considerably reduced. Nevertheless, this poses several implementation challenges.

On the one hand, the reduction in beta function at the IP will make the beam sizes grow faster with the distance from the IP. This increases the probability of long-range encounters, creating additional beam losses and affecting the beam lifetime. In order to avoid this the beams are further separated by doubling the crossing angle. However, the increase in crossing angle reduces the overlapping area of the bunches at collision and therefore reduces the peak luminosity. To solve this, crab cavities were proposed to compensate the crossing angle and allow quasi head-on collisions.

On the other hand, an increase in the number of particles and a reduction of beam size leads to an increase in pile-up events at the detectors, which greatly affects the quality of the data and increases the energy deposition in the neighboring regions. For this reason the HL-LHC operation will rely on luminosity leveling, where the peak luminosity is kept at a constant and reduced level, for as long as possible.

Machine protection challenges also appear for the HL-LHC. The doubling of the number of particles will double the energy stored per beam, increasing the probability of damage to the accelerator. Additionally, new fast failure scenarios happening near the experiments appear due to the presence of crab cavities. Both factors can hugely impact the machine availability, which motivates the detailed study of crab cavity failures well before tests with prototypes can be performed.

Chapter No.4

Understanding Crab Cavities

Crab cavities are a novel type of cavities designed to transversely rotate the beam. They have only been used in one e^+e^- collider so far (The High Energy Accelerator Research Organization (KEK)), under conditions which were very different from the needs of the HL-LHC. This chapter takes a theoretical approach to studying crab cavity failures by providing an overview of mechanical deformations in RF cavities (Sections 4.2, 4.3), introducing the new HL-LHC crab cavity prototypes (Section 4.4), deriving relevant quantities (Sections 4.5, 4.6) and describing the failure modes considered in this thesis (Section 4.7).

4.1 Historical introduction

A *crab-wise crossing* was first proposed as a mechanism of increasing the luminosity in a e^+e^- linear collider, with the help of RF deflectors, by R. B. Palmer at the Stanford Linear Accelerator Center (SLAC) in 1988 [67]. One year later it was shown by K. Oide and K. Yokoya, from KEK, that the crab crossing scheme is also applicable to circular colliders [68]. In particular, it was shown that the *synchrotron-betatron* coupling terms that usually appear in a normal crossing angle scheme disappear with the crab crossing.

When two beams collide with a crossing angle, the beam-beam forces will generate synchro-betatron resonances, also called satellite resonances, as shown by A. Piwinski in 1977 [69]. Synchro-betatron resonances can also be generated by non-zero dispersion at the Interaction Point (IP). Additionally, it was shown in [70] that the synchrotron tune is comparable to the linear beam-beam tune shift and can provide Landau damping. The existence of synchrotron-betatron resonances in the LHC was studied in [71] and

found to be generally small and well tolerable. This could change for the HL-LHC which will need larger crossing angles at reduced β^* . The compensation of large crossing angles using crab cavities should help to keep synchro-betatron resonances at low levels also for HL-LHC.

The RF deflector devised to tilt the bunches was later called a *crab cavity*. The main development of crab cavities came from KEK, where they designed and developed the first prototypes as shown in Fig 4.2. Furthermore, KEKB was the first and only accelerator to operate with crab cavities (see Sections 4.4.1 and 4.7.5 for more information), achieving the world record luminosity of $2.11 \times 10^{34} \text{ cm}^{-2} \text{ s}^{-1}$. In parallel to the developments in KEK, crab cavities started to be studied as an option for the LHC and later for the HL-LHC. This triggered new designs and pushed forward the study of these devices.

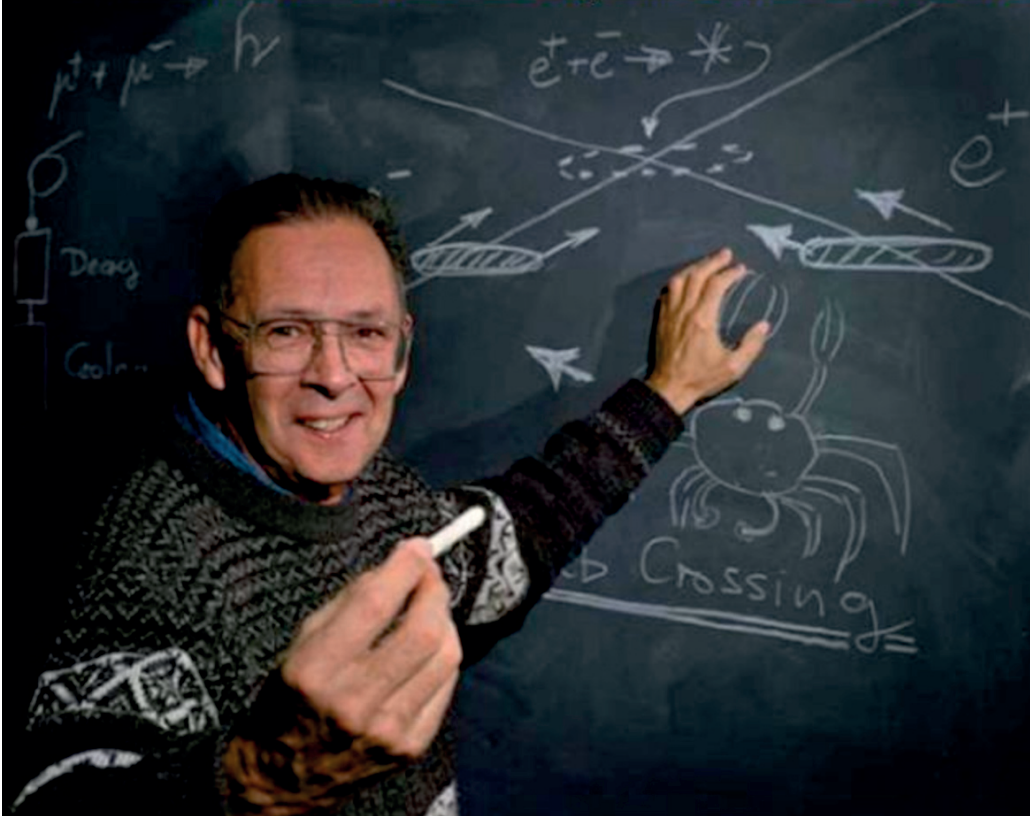


Figure 4.1. R. B. Palmer showing the principle of the crab crossing scheme on the blackboard. The picture was taken in February of 2008 during the first session of the *Joint BNL/US-LARP/CARE-HHH Mini-Workshop on Crab Cavities for the LHC* [72].

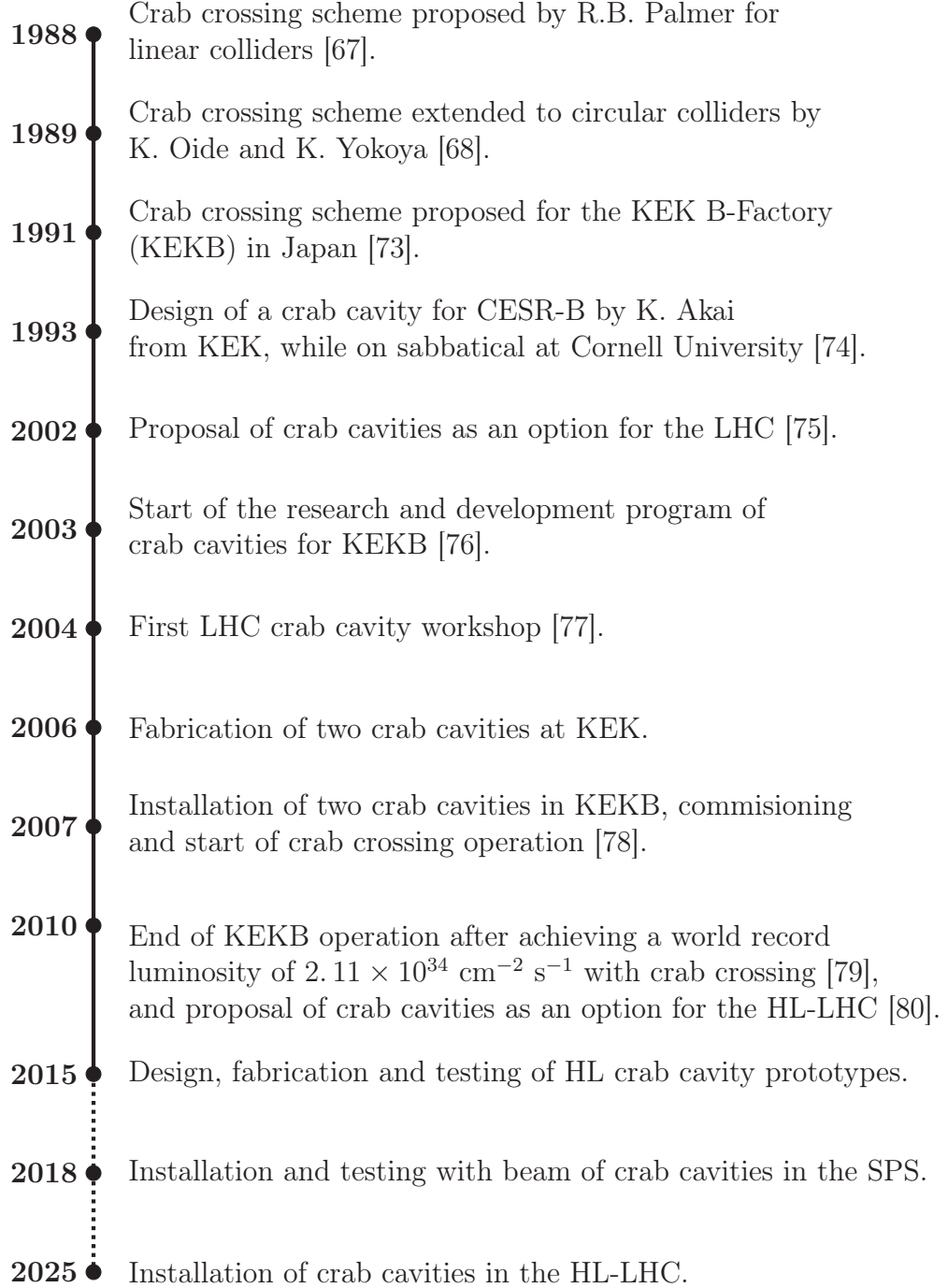


Figure 4.2. Main events in the history of crab cavities.

4.2 *Cavity resonators*

A cavity is a hollow, closed conductor that is driven by an external force. A source of RF waves, also called *klystron*, is coupled to the cavity via an *input coupler* which efficiently transfers the RF power to the cavity. When the source is coupled to the cavity the transmitted Electromagnetic (EM) waves excite the resonant modes of the cavity (see Appendix A). The EM waves will be reflected back and forth in the cavity walls creating standing waves that store energy. This stored energy may be transmitted to the beam or dissipated as loss.

In the steady-state case, the time-average stored electric and magnetic energy in a simple lossless isotropic, homogeneous, linear medium (such as vacuum) of volume V is given by

$$U_{\text{tot}} = \frac{1}{2} \int_V \left(\mu |\vec{H}|^2 + \epsilon |\vec{E}|^2 \right) dv, \quad (4.1)$$

where ϵ is the medium's permittivity and μ the permeability. The stored energy continuously swaps between electric and magnetic energy such that \vec{E} and \vec{H} are always 90 degrees out of phase. This means that on average both energies must be equal, and that the stored energy is constant in time in the absence of dissipation sources.

4.2.1 *Higher order modes*

Cavities are designed to work at a specific resonant frequency, but when the beam passes through the cavity it can excite a wide spectrum of other modes that can be higher in frequency. These are called Higher Order Modes (HOMs), lower called Lower Order Modes (LOMs), or very near the working frequency called Same Order Modes (SOMs). These modes are detrimental since they can cause heating and instabilities in the beam, especially if beam-deflecting modes are excited, such as the dipole, quadrupole or sextupole modes. In order to avoid the interaction of the beam with the most easily excited modes, cavities are designed with special shapes and equipped with additional couplers. If the cavity is misaligned or the beam not centered, other modes can still be excited and affect the beam. In general, cavities are designed such that the nearest detrimental mode is as far as possible from the working resonant frequency.

4.3 Mechanical deformations

Cavities are subject to forces that can deform the cavity walls and, therefore, change their fundamental resonant frequency. These mechanical deformations can come from changes in the EM field of the cavity, called *ponderomotive effects*, or from the cavity's environment called *microphonics*. Microphonics usually have a frequency higher than 1 Hz and happen due to ground vibrations or pressure fluctuations around the cavity. Ponderomotive effects are usually referred as *Lorentz force detuning*. Additionally, fabrication imperfections and thermal effects can be a source of errors.

4.3.1 Lorentz force detuning

We saw in Eq. (4.1) that the electric and magnetic fields are in equilibrium for a cavity in resonance, i.e. the electric and magnetic stored energies are equal. If the geometry of the cavity is perturbed the equilibrium between fields will be broken and the resonant frequency of the cavity will automatically shift in order to restore the balance. If the perturbation takes place at a sufficiently slow rate, i.e. at a rate that is slow compared to the oscillation of the system, an invariant of the system exists. The invariant I , also called the *adiabatic invariant*, is expressed in Hamiltonian mechanics in terms of the canonical coordinates (q, p) as

$$I \equiv \oint \frac{p dq}{2\pi}, \quad (4.2)$$

where q denotes the displacement and p the momentum. Approximating the behavior of our resonant cavity to the one of a harmonic oscillator the invariant of the system is given by

$$I = \frac{U}{\omega_0}, \quad (4.3)$$

where ω_0 is the resonant angular frequency and U the total stored energy [81, Chapter 5, Section 12]. Eq. (4.3) is often found in the RF literature as

$$\frac{\Delta f}{f} = \frac{\Delta U}{U}, \quad (4.4)$$

where ΔU is the work done on the RF field of the cavity and Δf is the resonant RF frequency shift due to ΔU . This is known as the *Boltzmann-Ehrenfest theorem*, which in this context describes the coupling of mechanical deformations to the RF field of the cavity. Combining Eqs. 4.1 and 4.4 we can obtain *Slater's theorem*

$$\Delta f \propto (\epsilon_0 E^2 - \mu_0 H^2) \Delta V, \quad (4.5)$$

which describes the change in the resonant frequency Δf when some small volume ΔV is removed from the total cavity volume.

The deformation of the cavity structure usually comes from the stored EM fields via the *radiation pressure*. The photons circulating in the cavity hit the cavity walls and change their propagation direction, transferring momentum to the structure of the cavity [82]. This creates a radiation pressure that can induce a mechanical deformation of the cavity, putting the cavity out of resonance as shown by Eq. (4.5). The radiation pressure can be expressed as:

$$P_{rad} = \frac{1}{4}(\mu_0 H^2 - \epsilon_0 E^2). \quad (4.6)$$

We can see that the pressure is inwards in the regions with dominant electric energy and outwards in the regions with dominant magnetic energy density, being zero only in areas with perfectly balanced fields. The change in frequency of a cavity due to the radiation pressure is called the *Lorentz force detuning*, which can be induced by small field amplitude errors. When this happens the cavity is driven out of resonance, losing the coupling to the power source and starting to reflect power back through the coupler. The fields will then decay, making the radiation pressure decrease and the structure of the cavity relax. If the power is not cut, the fields will build up again inside the cavity and later decay, creating self-sustained ponderomotive oscillations of the cavity structure [83, Chapter 2.6.3]. This effect can be counteracted passively by increasing the stiffness of the cavity, or actively with a *tuning system*. Tuning systems mechanically correct the geometry variation of the cavity in order to match its resonant frequency to the operating frequency. Fast tuners can compensate for Lorentz force detuning as well as for microphonics, thermal contractions, or manufacturing shape errors [84]. Tuning systems are always part of a superconductive cavity setup since it is practically impossible to produce a cavity with a net frequency change equal to zero. Normal conducting cavities are tuned once after fabrication.

The Lorentz force detuning is usually characterized by the *Lorentz force coefficient*, which represents the coupling between the RF field and the mechanical mode

$$\Delta f = k_L V^2, \quad (4.7)$$

where k_L is the Lorentz force coefficient, V the voltage of the fundamental mode and Δf the shift in frequency.

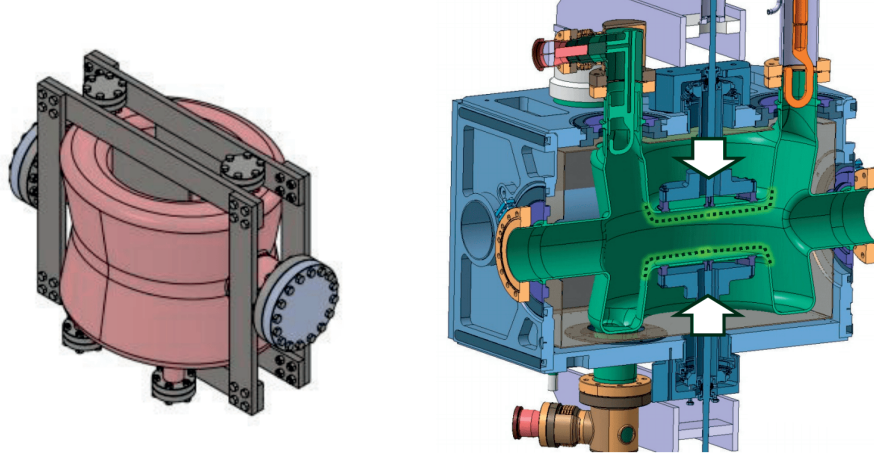


Figure 4.3. Stiffening structure in gray (left) and tuning system in a dressed cavity (right) for the Double Quarter Wave (DQW) crab cavity, one of the selected crab cavities for the HL-LHC, further described in Section 4.4.3 [85, 86]. The white arrows represent the direction of the force applied by the tuner, and the input coupler is shown in orange.

4.3.2 Mechanical model of a cavity

The ponderomotive oscillations induced in the structure of the cavity by the Lorentz force detuning can be modelled by a damped, driven harmonic oscillator. In this model, the deformation of the cavity is driven by the radiation pressure while the damping term represents the mechanical damping of the system

$$\overbrace{\frac{d^2x}{dt^2} + \omega_0^2 x}^{\text{Harmonic oscillator}} + \underbrace{\xi \omega_0 \frac{dx}{dt}}_{\text{Damping term}} = \overbrace{\omega_0^2 k_L V^2}^{\text{Driving term}}, \quad (4.8)$$

where x is the displacement of the cavity surface, ξ is a dimensionless damping coefficient, ω_0 is the resonant angular frequency of the cavity, k_L is the Lorentz force coefficient, and V the voltage of the fundamental mode [87, 88]. This model can be used to study the coupling of the cavity to a single mechanical mode. In reality the cavity couples to several mechanical modes simultaneously with different strengths.

4.3.3 The quality factor

An equivalent equation to Eq. (4.8) can be used to describe the behavior of the electromagnetic waves inside the cavity too, since they are also both driven by the power source and damped by dissipative effects. In this case it is usual to express the damping coefficient ξ_{RF} as its inverse

$$Q \equiv \frac{1}{\xi_{\text{RF}}}, \quad (4.9)$$

which is known as the *quality factor* or *Q factor*. Cavities are usually characterized by their *Q factor*, which describes how underdamped the waves in the resonator are. A high *Q* indicates a low rate of energy loss relative to the stored energy of the resonator

$$Q \equiv 2\pi f_0 \times \frac{\text{Energy stored}}{\text{Energy lost per cycle}}, \quad (4.10)$$

where f_0 is the resonant frequency of the cavity. The *Q factor* can be interpreted as roughly 2π times the number of RF cycles it takes to dissipate the energy stored in the cavity.

4.3.4 Power dissipation

The stored energy of the cavity can be lost through various mechanisms, one of them being ohmic losses. Ohmic losses are due to the surface resistance of the cavity walls, existent even if the cavity is superconducting [83, Chapter 3], which entails energy dissipation through heating. Considering a quality factor Q_0 that characterizes the rate of energy loss only from ohmic losses, we can express that rate as the power P_0 dissipated in the cavity walls

$$\frac{dU}{dt} = -P_0 = -\frac{\omega_0}{Q_0}U, \quad (4.11)$$

which has the solution:

$$U(t) = U(0) e^{-\omega_0 t/Q_0} = U(0) e^{-t/\tau_U}. \quad (4.12)$$

From Eq. (4.12) we can see that the energy of the cavity decays exponentially with a time constant τ_U

$$\tau_U = \frac{Q_0}{\omega_0}. \quad (4.13)$$

Apart from ohmic losses, energy can be also dissipated through the input coupler. Couplers are designed to allow an energy exchange with the modes

of the cavity and, while they usually replenish the energy of the cavity, they can also receive energy back if the cavity is not in resonance or the beam not aligned with the longitudinal axis of the cavity. The quality factor that characterizes the energy dissipation through the coupler is called the external Q factor or Q_{ext} . The same relations derived for Q_0 can be derived for Q_{ext} , being both quantities generally expressed as

$$Q_0 = \frac{\omega_0 U}{P_0} \quad \text{and} \quad Q_{\text{ext}} = \frac{\omega_0 U}{P_{\text{ext}}}, \quad (4.14)$$

where U denotes the stored energy of the cavity, P_0 the power lost in the cavity walls, and P_{ext} the power lost through the coupler when the RF sources are turned off. Both types of energy losses are usually considered together in the so-called *loaded quality factor* Q_L , which can be derived from the total dissipated power

$$P_L = P_0 + P_{\text{ext}}, \quad (4.15)$$

obtaining the loaded Q factor

$$\frac{1}{Q_L} = \frac{1}{Q_0} + \frac{1}{Q_{\text{ext}}}. \quad (4.16)$$

Usually, the dissipation in the cavity walls is much smaller than the dissipation through the coupler, making the loaded quality factor practically equal to the external quality factor.

4.3.5 Resonant amplitude response

A damped oscillator does not resonate at a pure frequency ω_0 , but is instead made up of a superposition of frequencies centered on $\omega = \omega_0 + \Delta\omega$, where $\Delta\omega$ is called the *bandwidth*. Any frequency detuning bigger than the cavity's bandwidth will detune the cavity, so the tuners need to be able to compensate for any frequency variation happening within that range. We can use the resonant amplitude response of a cavity to derive an expression for the frequency bandwidth. For this we will first consider the time dependency of the EM fields, which can be expressed as

$$E(t) = E_0 e^{-\omega_0 t/2Q_L} e^{-i(\omega_0 + \Delta\omega)t}, \quad (4.17)$$

as described in Eq. (4.12) and remembering that $U \propto E^2$ from Eq. (4.1). We can apply a Fourier transform to the function given by Eq. (4.17), which is continuous in the time domain, in order to obtain it in frequency domain

$$E(t) = \frac{1}{\sqrt{2\pi}} \int_{-\infty}^{\infty} E(\omega) e^{-i\omega t} d\omega, \quad (4.18)$$

where:

$$E(\omega) = \frac{1}{\sqrt{2\pi}} \int_0^{\infty} E_0 e^{-\omega_0 t/2Q_L} e^{-i(\omega+\omega_0+\Delta\omega)t} dt. \quad (4.19)$$

We can immediately deduce how the amplitude will change with frequency:

$$|E(\omega)|^2 \propto \frac{1}{(\omega - \omega_0 - \Delta\omega)^2 + (\omega_0/2Q)^2}. \quad (4.20)$$

Eq. (4.20) is commonly known as a *Lorentzian function* (or a *Cauchy-Lorentz distribution*), which is the solution to the differential equation describing a forced resonance.

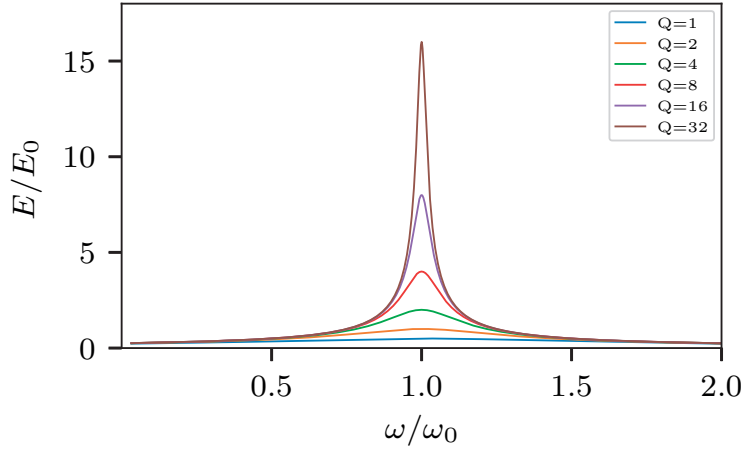


Figure 4.4. Normalized resonant amplitude response for various Q_L factors.

We can see in Fig. 4.4 that the amplitude is indeed maximal at the resonant frequency ω_0 and that higher amplitudes are reached for less damped resonators. For sufficiently large Q_L factors ($Q_L \gg 1$), i.e. when the oscillator is only weakly damped ($\xi_{\text{RF}} \ll 1$), the resonant curve has a full width at half maximum of

$$\Delta\omega = \frac{\omega_0}{Q_L}, \quad (4.21)$$

from where $Q_L = \omega_0/\Delta\omega$. Superconducting cavities have usually very high Q_L factors so, most of the time, Q_L also characterizes a resonator's bandwidth relative to its center frequency. In the case of the HL-LHC crab cavities, $Q_L = 5.3 \times 10^5$ and $f = 400$ MHz. Considering that $f = \Delta\omega/2\pi$, we obtain a frequency bandwidth of $\Delta f \approx 756$ Hz.

4.4 Crab cavity design and schemes

From the big, elliptical KEKB crab cavities to the new compact ones for the HL-LHC, the design of crab cavities has evolved and improved over more than two decades.

4.4.1 Crab cavities at KEKB

KEKB is an e^-e^+ collider located at the KEK accelerator laboratory in Tsukuba, Japan. KEKB produces copious amounts of B-mesons to study CP-violation at the Belle experiment. It is composed of two rings, one for the electrons, at 8 GeV of energy called the High Energy Ring (HER) and one for the positrons, at 3.5 GeV of energy called the Low Energy Ring (LER). KEKB was the first accelerator to ever use crab cavities. Crab cavities were installed in 2007 after 14 years of research and development and they were used in operation until the end of KEKB in 2010, as shown in Fig. 4.2 [89].

KEKB crab cavities have a squashed, elliptical shape designed to damp HOMs while maintaining a high Q value for the crabbing mode.

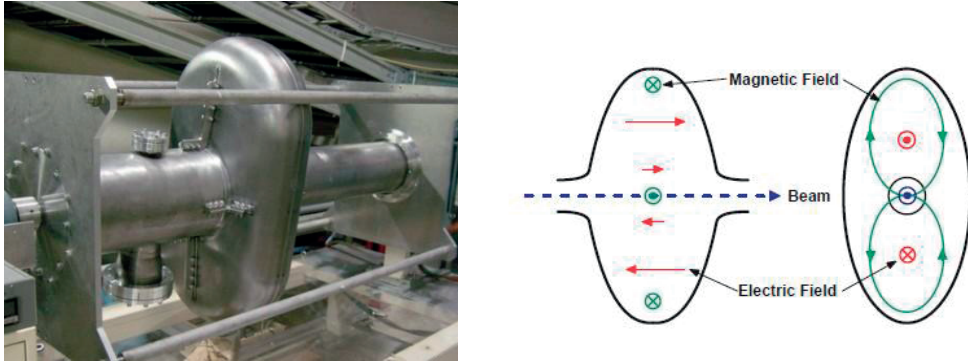


Figure 4.5. **Left:** KEKB crab cavity during its fabrication in 2005, during the barrel polishing process [90]. **Right:** the crabbing mode TM_{110} of the KEKB crab cavity, where the magnetic field gives the transverse kick to the beam [91].

4.4.2 Local and global crabbing schemes

The crab cavities at KEKB were installed in a *global crabbing scheme*, i.e. only one set of crab cavities exist per ring. This means that the *crabbing* (or tilt of the bunch) is not compensated, so the beam oscillates as it travels around the ring. On the other hand, a *local scheme* needs two sets of crab cavities, one to rotate the bunch and one to undo the rotation, per IP and per beam. The possibility of a global crabbing scheme was studied for the HL-LHC [80, Section 3.2] but was rejected due to its inability to provide crabbing for both ATLAS and CMS, where the beam collides in different transverse planes.

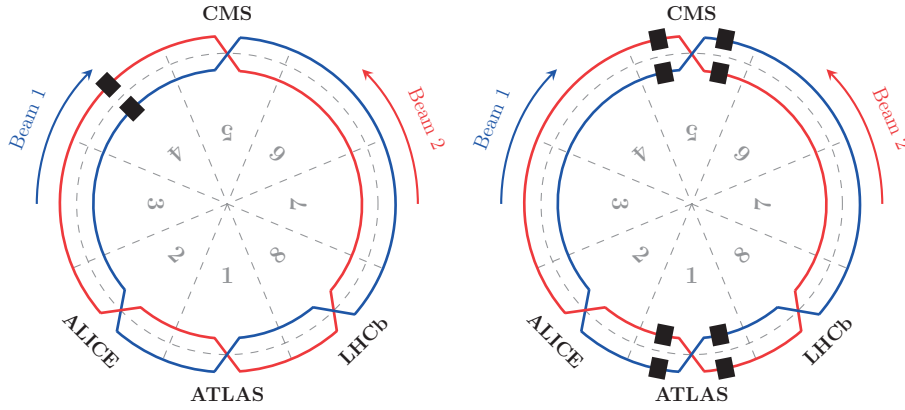
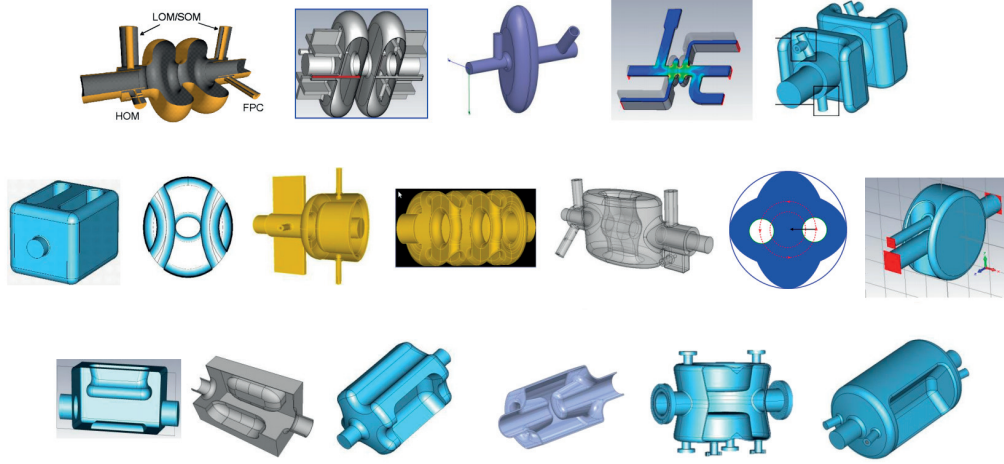


Figure 4.6. Left: global crabbing scheme. Right: local crabbing scheme. The black rectangles represent the crab cavities.

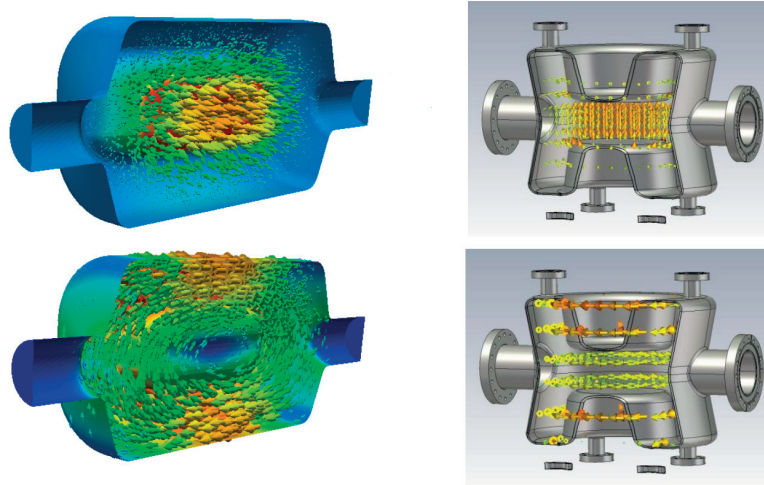
A local scheme for each HL experiment implies placing the crab cavities near each side of the correspondent IPs, where the incoming beam needs to be *crabbed* and the outgoing beam *uncrabbed*. A set of crab cavities is therefore needed for each beampipe. Nevertheless, the separation between beampipes in the LHC tunnel is too small for a conventional KEKB-like cavity. In order to solve this problem, the development of compact "TEM-like" and "TE-like" crab cavity designs blossomed between 2009 and 2012 as described in the next Section.

4.4.3 Crab cavities for the HL-LHC

Due to the space limitations of the LHC tunnel the HL-LHC crab cavities need to be compact, working at a lower resonant frequency compared to the KEKB ones. Many conceptual designs were proposed between 2009 and 2012, as shown in Fig. 4.7, but only two of them were downselected: the RF Dipole (RFD) and the Double Quarter Wave (DQW) crab cavities. Both cavities are made of bulk niobium sheets welded together, cooled with superfluid helium.



(a) Different geometries of crab cavities designed for the HL-LHC [92]. The last two cavities are the DQW and the RFD, respectively.



(b) The RFD (left column) and DQW (right column) crab cavity prototypes for the HL-LHC. The top row shows the electric field, while the bottom row shows the magnetic field [93, 94].

Figure 4.7. Crab cavities for the HL-LHC.

The DQW has a coaxial geometry with a gap to allow the passage of the beam, crabbing with a “TEM-like” mode which is also the first eigenmode. The RFD has a double ridged cylindrical structure. Its first eigenmode is very effective for accelerating particles but not for deflecting them, so a higher “TE₁₁-like” mode is used for crabbing (see Appendix A for more information on cavity modes). The RFD prototype was jointly developed by Old Dominion University and SLAC, while the DQW was developed by BNL, both under the support of the Research and Development program US LARP for the LHC HiLumi upgrade.

Table 4.1. Working parameters of the DQW and RFD crab cavities [95, 25].

	DQW	RFD
Resonant frequency (MHz)	400.79	400.79
Nearest HOM (MHz)	579	634
Deflecting voltage (MV)	3.4	3.4
Stored energy (J)	10.9	10.7
External quality factor Q_{ext}	$3 - 5 \times 10^5$	$3 - 5 \times 10^5$
Lorentz force coefficient k_L (Hz/MV ²)	-206	-114
R/Q (Ω)	~ 400	~ 400

4.5 Crab cavity kick

The transverse kick of the cavity will be imparted by its transverse voltage \vec{V}_\perp

$$\vec{V}_\perp = V_x \hat{e}_x + V_y \hat{e}_y, \quad (4.22)$$

where \hat{e} is the unit vector. We can find an expression for the voltage of the cavity by first considering the electrostatic potential energy

$$U_e = - \int_{r_0}^r qE(r') \, dr', \quad (4.23)$$

which is defined as the negative work done by the electrostatic force \vec{F} to bring a point charge from r_0 to r . In our case we are interested in the work done by the electromagnetic fields on the point charge along its trajectory through the cavity. Remembering that the electrostatic potential energy can be also expressed with respect to the associated voltage as

$$U_e = qV, \quad (4.24)$$

we can express the transverse voltage of the cavity by integrating the transverse electromagnetic force, i.e. the Lorentz force, along the cavity's length L .

$$mq\vec{V}_\perp = - \int_0^L \vec{F}_\perp dz, \quad (4.25)$$

where \perp denotes the transverse coordinates x, y . The cavity's voltage is a function of space and time $F(z(t), t(z))$ where $z(t) = z_0 + \beta ct'$ and $t(z) = t_0 + t'z/\beta c$, t' denoting the time it takes to traverse the cavity. We change the independent variable from space to time, obtaining

$$mq\vec{V}_\perp = -\beta c \int_0^{L/\beta c} \vec{F}_\perp dt' = -\beta c \int_0^{t_{\max}} m \frac{d\vec{p}_\perp}{dt'} dt' = -m\beta c \Delta\vec{p}_\perp. \quad (4.26)$$

As discussed in Chapter 2, we know that $p_x = p_s x'$, allowing us to express the change in angle due to the transverse kick as

$$x' = -\frac{qV_x}{\beta c p_s} = -\frac{qV_x}{E}, \quad (4.27)$$

where E is the beam energy. As we saw in this chapter, crab cavities contain oscillatory fields. For the case of a crab cavity, the voltage will behave as

$$V_x = V_0 \sin(\phi_{cc} + \omega_{cc}t), \quad (4.28)$$

obtaining the full expression for the transverse kick

$$x' = -\frac{qV_0}{E} \sin(\phi_{cc} + \omega_{cc}t), \quad (4.29)$$

which is equivalent for the y coordinate. It is important to note that the crab cavity kick is in the (x', z) plane, or (y', z) for a vertical crossing angle, not in the (x, z) or (y, z) . It is only after the passage through the triplet that the kick is transformed from (x', z) to (x, z) . After collision a second set of crab cavities uncrab the beam, returning it to its original shape.

Another way of deriving the crab cavity kick is from the crab cavity Hamiltonian, given by

$$\mathcal{H}_{cc} = \frac{qV_0}{E} \sin(\phi_{cc} + \omega_{cc}t)x, \quad (4.30)$$

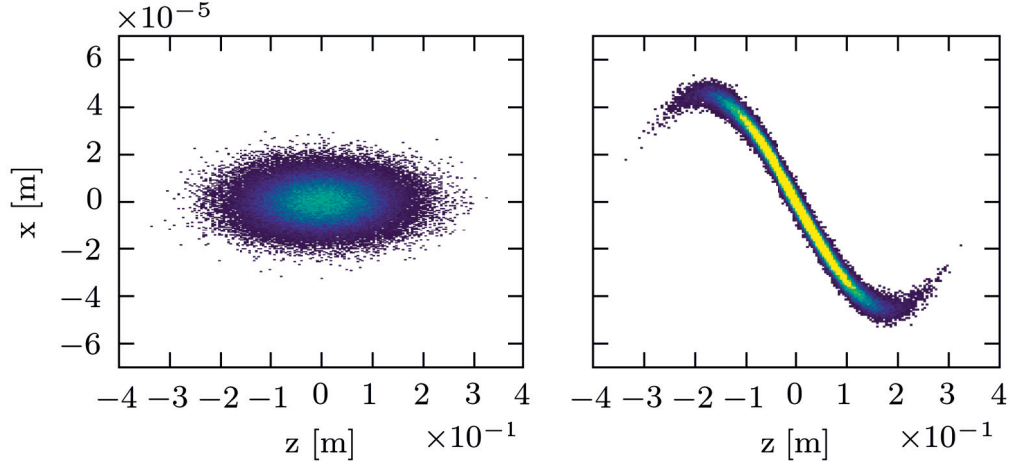


Figure 4.8. A Gaussian particle bunch at the IP, with (right) and without (left) a crab cavity kick, using HL-LHC parameters. The shape of the RF curvature can be observed.

which can be derived with the formulas given in [96]. Applying Hamilton's equations we obtain

$$\Delta p_x \approx -\frac{\partial \mathcal{H}}{\partial x} = -\frac{qV_0}{E} \sin(\phi_{cc} + \omega_{cc}t), \quad (4.31)$$

which is the same kick as the one derived in Eq. 4.29. A longitudinal kick also exists and is given by

$$\Delta p_z \approx -\frac{\partial \mathcal{H}}{\partial z} = -\frac{qV_0}{E} \frac{\omega_{cc}}{c} \cos\left(\phi_{cc} + \frac{\omega_{cc}z}{c}\right)x. \quad (4.32)$$

4.6 Crab cavity voltage

The crab cavity voltage needed to tilt the bunch sufficiently to fully compensate the crossing angle depends on the characteristics of the lattice, i.e. the optics parameters at the relevant locations. In order to find the optimal location for the crab cavities in the lattice it is important to know the exact relation between the cavity's voltage and the optics. To find it we will start by looking at how the position of a particle changes while traveling from the crab cavity to the IP. For this we can use the generic translation matrix $M_{1 \rightarrow 2}$ that translates a position vector in phase space from point 1 to point 2 in terms of the Twiss functions in both points:

$$M_{1 \rightarrow 2} = \begin{pmatrix} \sqrt{\frac{\beta_2}{\beta_1}}(\cos \Delta\mu + \alpha_1 \sin \Delta\mu) & \sqrt{\beta_1 \beta_2} \sin \Delta\mu \\ -\frac{(1 + \alpha_1 \alpha_2) \sin \Delta\mu + (\alpha_2 - \alpha_1) \cos \Delta\mu}{\sqrt{\beta_1 \beta_2}} & \sqrt{\frac{\beta_1}{\beta_2}}(\cos \Delta\mu - \alpha_2 \sin \Delta\mu) \end{pmatrix}. \quad (4.33)$$

In our case, point 1 will be the crab cavity and point 2 the IP. Applying $M_{1 \rightarrow 2}$ to the position vector in the crab cavity we can obtain the final position at the IP

$$\begin{pmatrix} x_{\text{IP}} \\ x'_{\text{IP}} \end{pmatrix} = \begin{pmatrix} M_{11} & M_{12} \\ M_{21} & M_{22} \end{pmatrix} \begin{pmatrix} x_{\text{cc}} \\ x'_{\text{cc}} \end{pmatrix} \rightarrow \begin{cases} x_{\text{IP}} = M_{11}x_{\text{cc}} + M_{12}x'_{\text{cc}} \\ x'_{\text{IP}} = M_{21}x_{\text{cc}} + M_{22}x'_{\text{cc}} \end{cases}, \quad (4.34)$$

where we can replace the angle x'_{cc} by the crab cavity kick derived in Eq. (4.29):

$$x_{\text{IP}} = M_{11}x_{\text{cc}} + M_{12} \frac{qV_0}{E} \sin(\phi_{\text{cc}} + \omega_{\text{cc}}t). \quad (4.35)$$

We want to relate the expression we just obtained to the crossing angle θ . Crab cavities need to tilt the bunch by only half of the crossing angle $\theta/2$, so assuming that the crossing angle is in the horizontal plane, we can express this angle by the slope it defines:

$$\tan \frac{\theta}{2} = \frac{\Delta x}{\Delta s} \approx \frac{dx}{ds}. \quad (4.36)$$

Combining Eqs. 4.35 and 4.36 we obtain:

$$\tan \frac{\theta}{2} = \frac{d(M_{11}x_{\text{cc}} + M_{12} \frac{qV_0}{E} \sin(\phi_{\text{cc}} + \omega_{\text{cc}}t))}{ds}. \quad (4.37)$$

We can express the time t as $z/\beta c$ where $z = s - s_0$, s_0 being the position of the reference particle. Considering the small angle approximation and seeing that the only dependency with s is in the second term, we obtain

$$\tan \frac{\theta}{2} = \frac{qV_0\omega_{cc}M_{12}}{\beta cE} = \frac{qV_0\omega_{cc}\sqrt{\beta_{IP}\beta_{cc}}\sin\Delta\mu}{\beta cE}, \quad (4.38)$$

from where we can isolate the voltage:

$$V_{cc} = \frac{\beta cE \tan \frac{\theta}{2}}{q\omega_{cc}\sqrt{\beta_{IP}\beta_{cc}}\sin\Delta\mu}. \quad (4.39)$$

The voltage given by Eq. (4.39) is the total voltage needed to fully compensate the crossing angle but it can be divided by the number of crab cavities installed, as shown in Fig. 4.9.

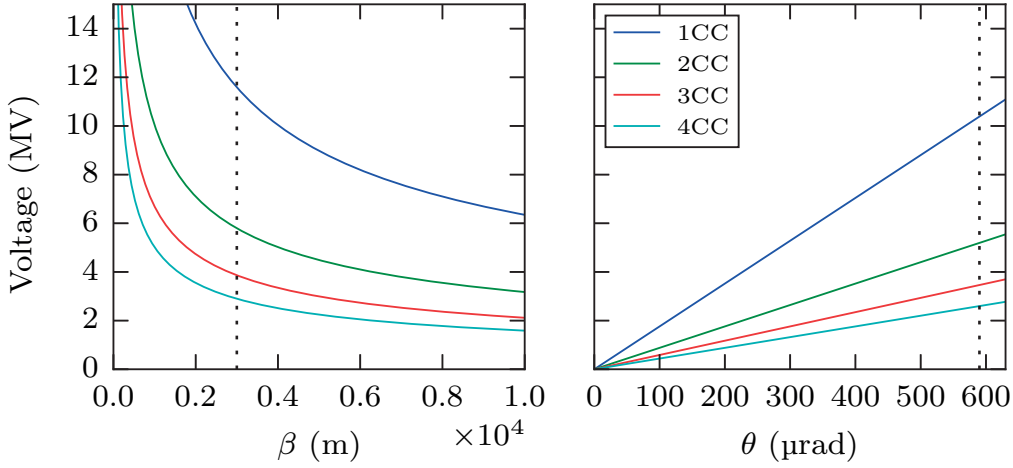


Figure 4.9. Evolution of the crab cavity voltage depending on the β_{cc} function at their location and on the total crossing angle θ . The dashed line indicates the values for the HL-LHC.

The voltage we just calculated corresponds to the voltage for the upstream cavities, i.e. the ones that *crab* the beam before collision. For the effect of the crab cavities to remain local the beam must be *uncrabbed* at the downstream cavities. We calculate the voltage for the downstream cavities using Eq. (4.33) to transport the position vector from the upstream to the downstream crab cavities. To simplify the equation we can assume that the phase advance between the upstream and downstream cavities is 180° . Indeed, the phase advance between the crab cavities and the IP is optimized to be 90° so that the particles with higher amplitude at the crab cavity arrive with minimum amplitude at the IP. Since the beta function is very small at the IP and so is the beam size $\sigma = \sqrt{\beta\epsilon}$, the particles with lowest amplitude at the crab cavity will not reach very big amplitudes at the IP. Another simplification can be made assuming the alpha functions at both locations are equal, yielding the following set of equations:

$$\begin{cases} x_{\text{ccdown}} = M_{11}x_{\text{ccup}} \\ x'_{\text{ccdown}} = M_{22}x'_{\text{ccup}} \end{cases} . \quad (4.40)$$

We can write down explicitly the kick $\Delta x'_{\text{ccup}}$ given by the upstream crab cavity:

$$x'_{\text{ccdown}} = M_{22} \left(x'_{\text{ccup}} + \Delta x'_{\text{ccup}} \right) . \quad (4.41)$$

We can also write down the kick $\Delta x'_{\text{ccdown}}$ given by the downstream cavities explicitly, setting the final total angle equal to the one before the kick of the upstream cavities:

$$x'_{\text{ccdown}} + \Delta x'_{\text{ccdown}} = M_{22}x'_{\text{ccup}} . \quad (4.42)$$

Substituting Eq. (4.41) in Eq. (4.42)

$$M_{22} \left(x'_{\text{ccup}} + \Delta x'_{\text{ccup}} \right) + \Delta x'_{\text{ccdown}} = M_{22}x'_{\text{ccup}} , \quad (4.43)$$

obtaining:

$$\Delta x'_{\text{ccdown}} = -M_{22}\Delta x'_{\text{ccup}} . \quad (4.44)$$

From Eq. (4.29) we can see that $x' \propto V$, allowing us to write

$$V_{\text{ccdown}} = -M_{22}V_{\text{ccup}} . \quad (4.45)$$

Considering equations 4.39 and 4.44, and applying the HL-LHC parameters given by the HLLHCV1.2 optics we obtain the following values for the total voltage of the upstream and downstream crab cavities:

$$V_{\text{ccup}} = 10.61 \text{ MV} \quad \text{and} \quad V_{\text{ccdown}} = 10.38 \text{ MV} . \quad (4.46)$$

In reality the phase advance between the crab cavities and the IP is never exactly 90° , and the alpha function is not the same for the upstream and downstream cavities (see Table C.1). In this case the equations cannot be solved analytically, but can be approximated computationally (see Table 5.1).

4.7 Crab cavity failures

Crab cavity failures can be very fast and induce large coherent betatron oscillations, generating beam losses before the beam can be properly dumped. Furthermore, the effect of the failure is cumulative with the number of crab cavities failing. We want to study exactly how fast crab cavity failures can be, what kind of failures we can expect, and the impact that very fast failures can have on beam dynamics and beam loss. For this, we first need to understand how crab cavities will be controlled once installed.

4.7.1 The LLRF feedback system

Crab cavity operation will be controlled by the LLRF feedback system. The LLRF ensures the correct and safe operation of the crab cavities by maintaining them tuned at their resonant frequency, keeping the deflecting field at the demanded value and by synchronizing the phase of the RF kicks with the passage of the bunches for both beams. The LLRF also fulfills other tasks such as compensating for beam loading when the bunch is not perfectly centered and reducing the impedance of the fundamental mode of the cavity to avoid beam instabilities. To achieve this, the LLRF system needs to measure the variations of the correspondent parameters, process the signal, and send the response back to the controller. The time needed for this process is called the *loop delay* and is the main performance limitation of the LLRF feedback system.

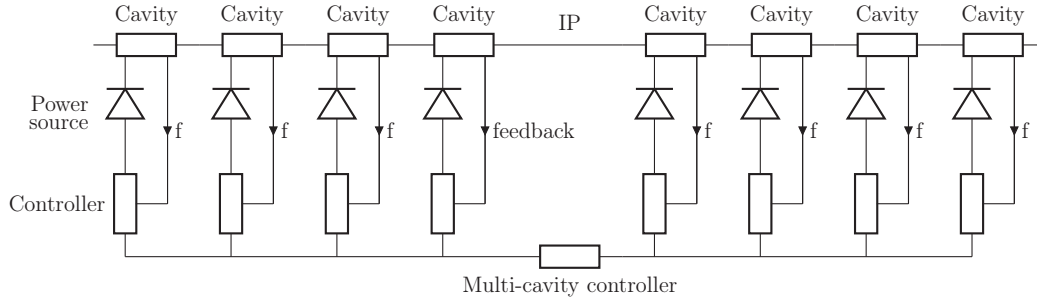


Figure 4.10. Proposed crab cavity LLRF architecture for one IP and one beam. The local loop delay is estimated to be $1 \mu\text{s}$ and the global multi-cavity loop delay $5 \mu\text{s}$ [97].

Each crab cavity will have their own powering system, regulated by a cavity controller. Having an individual power supply for each crab cavity reduces the loop delay and allows fast and independent control of the cavity's voltage and phase. Additionally, a central multi-cavity controller receives measurements from all the cavities and adjusts the fields at both sides of the IP such that the orbit distortions remain local. This is of special relevance during crab cavity failures since it could mitigate the losses during the turns needed to dump the beam.

4.7.2 Power source failure

When the power source of the crab cavity is abruptly switched off, the stored energy U of the cavity exponentially decays with the characteristic time constant, as derived in Eq. (4.12). Taking into account that for the HL-LHC crab cavity prototypes the quality factor values are $Q_0 \sim 10^{10}$ and $Q_{\text{ext}} \sim 10^5$, we can conclude from Eq. (4.14) that $Q_L \approx Q_{\text{ext}}$, obtaining the following time constant:

$$\tau_U = \frac{Q_{\text{ext}}}{\omega_0}. \quad (4.47)$$

We can also derive the time constant for the voltage decay knowing that $U \propto V^2$ (Eq. (4.1)), obtaining

$$V = V_0 \cdot e^{-\frac{\omega_0 t}{2Q_{\text{ext}}}}, \quad (4.48)$$

from where:

$$\tau_V = \frac{2Q_{\text{ext}}}{\omega_0}. \quad (4.49)$$

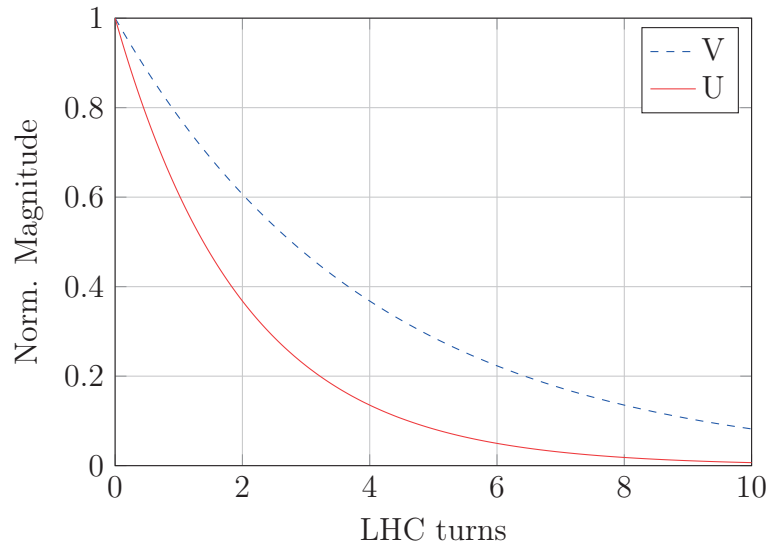


Figure 4.11. Time evolution of the stored energy U and voltage V when the power source is switched off for $Q_{\text{ext}} = 5 \times 10^5$ and $f_0 = 400$ MHz, which gives $\tau_V \approx 400 \mu\text{s} \approx 4$ LHC turns.

As discussed in Subsection 4.3.1, any change in the cavity fields will cause a mechanical deformation of the cavity structure due to the radiation pressure Eq. (4.6), which will entail a detuning in frequency Eq. (4.5). In the case of an exponential voltage decay and the tuners not managing to compensate for the induced detuning, a change in frequency could happen before the voltage has completely decayed. Nevertheless, it is possible that the time the cavity structure needs to contract and relax is significantly longer than the voltage decay time. In that case, the phase and frequency would remain approximately constant for the time it takes the cavity voltage to decay.

In terms of beam dynamics, a decrease in voltage will induce a change in the tilt imparted to the bunch by the crab cavity, as illustrated in Fig. 4.12. A fluctuation in voltage adds a residual tilt that will result in a not fully compensated crossing angle at the IP. This effect can be countered by adjusting the voltage of the downstream crab cavity so that it fully removes the tilt of the bunch.

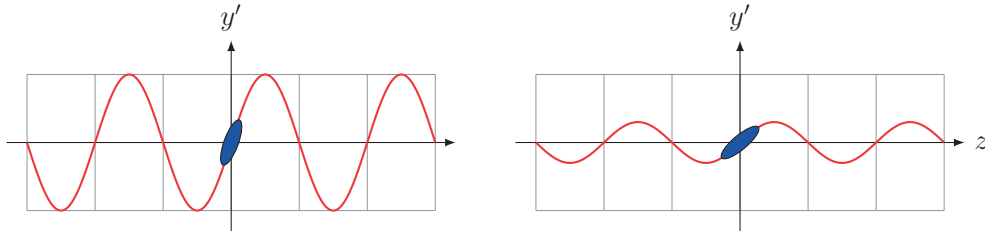


Figure 4.12. **Left:** Normal operation. **Right:** a decrease in tilt induced by a decrease in voltage.

The effects that an abrupt cut in the power source can have on beam dynamics and overall losses are explored in Chapter 5, with the help of tracking codes and the HL-LHC lattice.

4.7.3 LLRF malfunction

If the crab cavity phase is not synchronized to be zero at bunch arrival, the center of the bunch will see a non-zero voltage. This failure case is critical since, if the change in phase is big enough, the bunch core could reach the collimators, damaging them and putting the protection of the machine at risk. The LLRF will control this phase, synchronized with the phase of the RF accelerating cavities. The reference signal to synchronize both accelerating and crab cavities is generated above ground in IP4. It is also foreseen to include a local pick-up for more accurate adjustments of the crab cavities' phase [97].

We want to assess how much the phase of the crab cavity can change in one turn if the wrong signal was fed by the LLRF, with the available power.

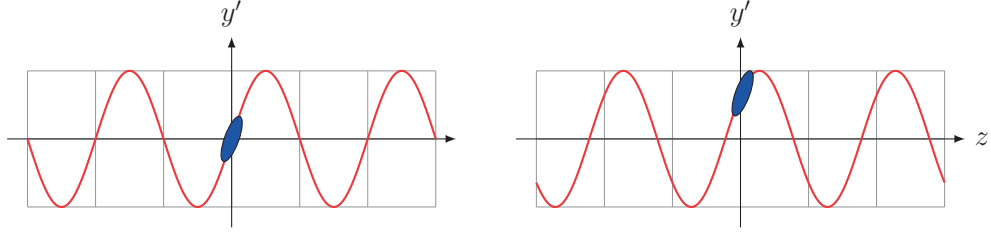


Figure 4.13. **Left:** Normal operation. **Right:** a change in phase, entailing a transverse kick of the bunch core.

For this, we can use the beam-cavity-transmitter relations derived for crab cavities in [98, 99], where the generator power is expressed as

$$P_g(t) = \left(\frac{R}{Q} \right)_\perp Q_L |I_g(t)|^2, \quad (4.50)$$

using the Linac impedance definition as the crab cavity parameters are usually given following that convention, where R/Q_\perp is the transverse geometric shunt impedance (see Appendix B), Q_L is the loaded Q factor, and $I_g(t)$ is the generator current for an on-tune cavity ($\Delta\omega$) and a centered bunch (no offset)

$$I_g(t) = \frac{V_\perp(t)}{2 \left(\frac{R}{Q} \right)_\perp Q_L} + \frac{dV_\perp(t)}{dt} \frac{1}{\omega \left(\frac{R}{Q} \right)_\perp}, \quad (4.51)$$

where V_\perp is the deflecting voltage. Let's assume a phase variation of the cavity voltage adding a phasor to the amplitude

$$V_\perp = V_0 e^{i\phi(t)}, \quad (4.52)$$

from where:

$$\frac{dV_\perp(t)}{dt} = \frac{dV_0(t)}{dt} e^{i\phi(t)} + V_0 \frac{d\phi(t)}{dt} i. \quad (4.53)$$

Assuming that the field amplitude V_0 is constant in time, replacing Eq. (4.53) in Eq. (4.51) we obtain:

$$\begin{aligned} I_g(t) &= \frac{V_0 e^{i\phi(t)}}{2 \left(\frac{R}{Q} \right)_\perp Q_L} + \frac{V_0 e^{i\phi(t)}}{\omega \left(\frac{R}{Q} \right)_\perp} \frac{d\phi(t)}{dt} i \\ &= \frac{V_0 e^{i\phi(t)}}{2 \left(\frac{R}{Q} \right)_\perp Q_L} \left(1 + \frac{2Q_L}{\omega} \frac{d\phi(t)}{dt} i \right). \end{aligned} \quad (4.54)$$

Remembering that $|z_1 z_2|^2 = |z_1|^2 |z_2|^2$, $|x + iy|^2 = x^2 + y^2$ and $|re^{i\phi}|^2 = |r|^2$:

$$|I_g(t)|^2 = \frac{V_0^2}{4 \left(\frac{R}{Q}\right)_\perp Q_L^2} \left[1 + \left(\frac{2Q_L}{\omega} \frac{d\phi(t)}{dt} \right)^2 \right]. \quad (4.55)$$

Substituting Eq. (4.55) in Eq. (4.50) yields

$$P_g(t) = \frac{1}{4} \frac{V_0^2}{\left(\frac{R}{Q}\right)_\perp Q_L} \left[1 + \left(\frac{2Q_L}{\omega} \frac{d\phi(t)}{dt} \right)^2 \right], \quad (4.56)$$

from where we can isolate the maximum phase change per time interval:

$$\left. \frac{d\phi(t)}{dt} \right|_{\max} = \frac{\omega}{2Q_L} \sqrt{\frac{4(R/Q_\perp)Q_L P_{\max}}{V_0^2} - 1}, \quad (4.57)$$

Considering the following values for the crab cavity parameters:

$Q_L = 3 \times 10^5$, $R/Q_\perp = 500 \, \Omega$, $P_{\max} = 100 \, \text{kW}$, $V_0 = 3.4 \, \text{MV}$ and $f = 400 \, \text{MHz}$, we obtain a maximum phase change per turn of

$$\left. \frac{d\phi(t)}{dt} \right|_{\max} = 44^\circ, \quad (4.58)$$

which has the potential of producing big losses in the collimation system. This scenario will be further explored in Chapter 5.

4.7.4 Quenches

A *quench* is a thermal breakdown of superconductivity in the cavity during normal operation, usually caused by surface defects or multipacting [84, Chapters 10 and 11]. In the case of surface defects, RF currents flow through it causing Joule heating. If the defect is heated beyond the critical temperature of the superconducting material the region around the defect becomes normal conducting, dissipating much more power than before. This can turn a larger portion of the cavity normal conducting, in which case the coupling with the power source is lost and all the power is reflected back through the coupler. The fields of the cavity will then abruptly drop and the cavity will start cooling down again until it recovers superconductivity. The cavity may continue jumping between superconducting and quenched states, provided that the power is being supplied during this time. This phenomenon works with the same mechanism as the self-sustained ponderomotive oscillations described in Section 4.3.1, only that in this case superconductivity is lost and

recovered along the process. In multipacting processes the RF power is absorbed by an electron current generated in a chain reaction inside the cavity, leading to the quenching process we just described.

The drop in voltage observed during a quench is much faster than the decay dominated by the characteristic time constant, as described in Subsection 4.7.2. Tests on the DQW crab cavity prototypes in the SM18 facility at CERN revealed that the quenches happen faster than $25\ \mu\text{s}$ [100], although the time constant will be measured with more precision in the SPS tests in 2018. Any change in voltage that happens faster than the characteristic time constant τ will require additional power input. This suggests that by monitoring the changes in the input power we can predict the onset of a quench.

4.7.5 *Probability of failure*

As discussed in Chapter 3, knowing the probability of a failure happening and its consequences helps us understand the risk that a certain failure poses to the machine. In the case of the HL-LHC, that probability will only be known after the crab cavities are tested in real conditions, i.e. fully set up in the tunnel, with beam, and a feedback system. We can, nevertheless, make an estimation considering the failure rate of the LHC accelerating cavities and of the KEKB crab cavities. Indeed, crab cavity quenches were observed in KEKB during operation [101]. When the quench was detected, the klystron power was increased to compensate for the induced power dissipation until it was turned off. After that, the voltage of the cavity decayed as expected, but the cavity phase lost synchronization with the reference signal and started oscillating without control, as shown in Fig. 4.14. A change of phase of 50° was observed to happen in $50\ \mu\text{s}$ after the RF power was switched off, kicking the beam horizontally. It was then concluded that the beam should be aborted before the RF is turned off in order to avoid losing control of the crab cavity phase.

During the lifetime of KEKB's crab cavities, it was observed that they failed on average 1.3 times per day for HER and 0.5 times per day for LER, as shown in Fig. 4.15, which translates into 18 and 24 hours of MTBF respectively.

On the other hand, the accelerating cavities in the LHC have been very reliable with only 12 faults over 45 days of operation in the summer of 2016, with a MTBF of 90 hours and a downtime of 0.7 hours. As a preliminary estimation, it is reasonable to assume that the MTBF of the future HL-LHC crab cavities can lie between the MTBF of the KEK crab cavities and the MTBF of the LHC accelerating cavities. Some availability studies have simulated the impact of crab cavity failures on the HL-LHC luminosity

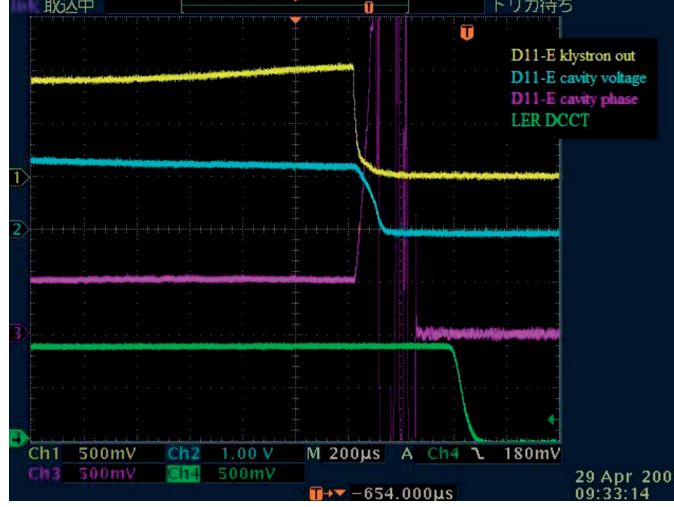


Figure 4.14. Crab cavity breakdown at KEKB in 2008, where the yellow plot represents the klystron power, the blue plot the cavity voltage, the purple plot the cavity phase and the green plot the beam current [101].

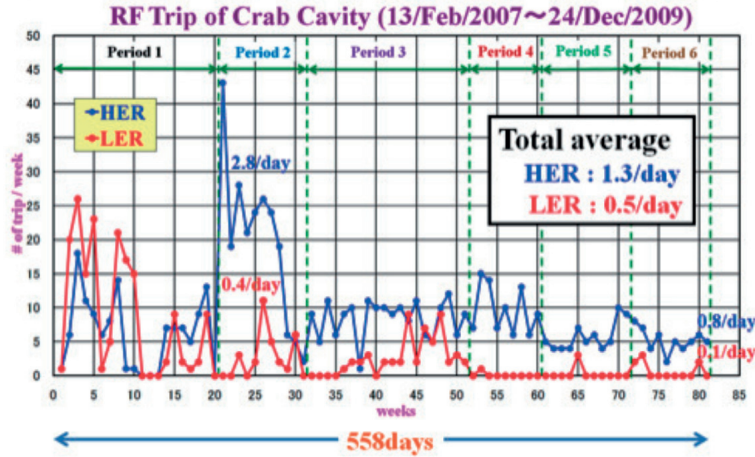


Figure 4.15. Trip rate of the crab cavity system at KEKB during its lifetime. We can observe that the trip rate was higher during the commissioning period (Period 2) [102].

production using a Monte Carlo model taking these two cases into account [66]. It was shown that even with a very short MTBF, such as the one of the KEKB crab cavities in the HER ring, we would still gain 25% of integrated luminosity. It is still worth noting that these results are strongly dependent on the downtime induced by the failures. For example, if every crab cavity failure would lead to a magnet quench, the downtime will increase to 8 hours. In this case, a gain in luminosity will only be observed if the MTBF was greater than 15 hours. The criticality of crab cavity failures greatly affects the potential gain in luminosity production, which is why understanding crab

cavity failures is a necessary task. An advanced interlock system as well as mitigation strategies are needed in order to reduce the consequences of crab cavity failures, and therefore their downtime [66].

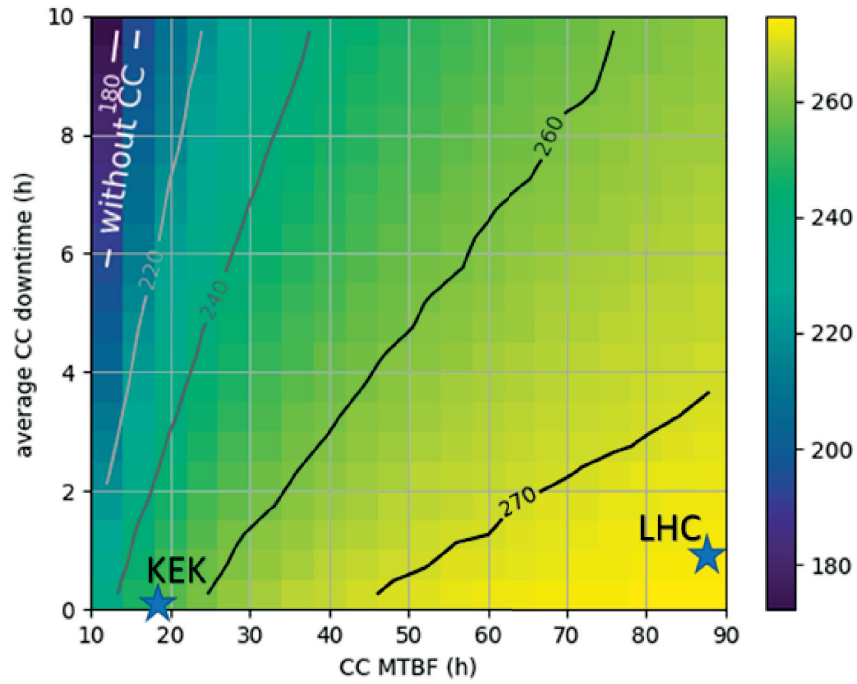


Figure 4.16. Yearly luminosity production as a function of average crab cavity downtime and MTBF [66].

4.8 *Summary*

Imbalances in the EM field of the crab cavity cause radiation pressure, which can change the cavity's shape and, therefore, its resonant frequency. If the deformation is significant and cannot be compensated by the tuning system, the coupling with the power source will be lost and the crab cavity power will start being reflected back through the coupler, entailing an exponential decay in the cavity voltage. This *detuning* of the cavity is a relatively slow process because it is dictated by the timescale of the mechanical deformation of the cavity. We are interested in faster failure scenarios during which the machine protection system cannot actively protect and mitigate. For example, a power source failure happens in timescales of the order of only a few LHC turns while phase trips happen almost instantaneously. A phase trip can happen as consequence of a deliberate action from the LLRF or from losing synchronization with the reference signal. This last scenario was observed in KEK, where the residual RF power in the cavity after a quench caused uncontrolled phase jumps. We calculated the maximum phase shift a crab cavity can sustain per turn based on the available power in order to apply it to the crab cavity failure simulations, presented Chapter 5, as well as other relevant quantities such as the crab cavity kick and voltage.

Chapter No.5

Crab Cavity Failure Simulations

This chapter presents the collimation studies performed with SixTrack using the newly implemented DYNK module, a new functionality developed in the context of this thesis that allows to carry out failure simulations, further explained in Section 5.1. The crab cavity failure scenarios considered in this chapter are described in Section 4.7 and are further discussed in Section 5.2.3. The results are presented in Section 5.3 and comprise a classification of failures per fraction of beam lost, the spatial and temporal distribution of the particles absorbed by the collimation system for different failure cases, the estimation of the trigger of the beam abort and the study of collimator damage for each failure case. The results are analyzed in Section 5.4, where the optimization of the phase advance between crab cavity and primary collimator is proposed as a mitigation technique. Finally, the scope of the study is put into perspective in Section 5.5, where the results are summarized and discussed.

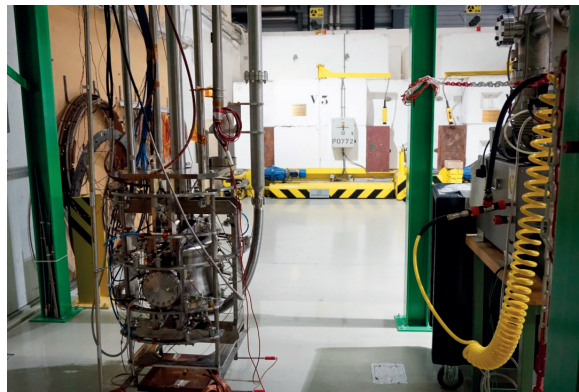


Figure 5.1. A DQW crab cavity on the test bench in the SM18 facility at CERN. Taken the 30th of August, 2016.

5.1 *Crab cavity failures with SixTrack*

SixTrack is a 6D single particle symplectic tracking code used to compute the individual trajectories of relativistic charged particles in circular accelerators. It is, in particular, one of the most speed optimized particle tracking codes for accelerators. The main program comprises around 77000 lines of FORTRAN code that has been developed and improved for more than two decades by several people at CERN [103, 104, 105, 106, 107]. During this time the code has been experimentally benchmarked and many functionalities have been added [108]. SixTrack was used in the design phase of the LHC and is currently being used for HL-LHC studies, such as the one presented in this thesis. SixTrack is used in long term tracking to determine the boundary of unstable motion through the prediction of the dynamic aperture of the machine, simulation of particle losses in the machine for collimation studies, and study of nonlinearities such as the beam-beam effect. Additionally, it is now a standard tool for failure simulations thanks to the dynamic kick functionality called DYNK, developed in the context of this thesis [109, 110].

5.1.1 *The dynamic kick module*

The SixTrack code was modified twice to include a dynamic kick functionality, i.e. the option to change the attributes of an accelerator element on a turn-by-turn basis, which is an essential feature to simulate failure scenarios. This was done for some magnetic elements in 2013 [111] and in a private version for crab cavities in 2014 [112]. Since both codes were never fully developed, maintained or unified, they could not be properly used for the crab cavity failure simulations envisaged for this thesis. This is why work took place to develop an official dynamic kick functionality that could be applied to all the elements of the accelerator, called the DYNK module. A conference paper was published on this topic, and can be found in Appendix E.2. Currently DYNK allows modifying the attributes of the accelerator's elements on a turn-by-turn basis and is part of the official SixTrack version [113, Chapter 3.3.4]. A detail of the DYNK module integration in the SixTrack code is given in figures D.1 and D.2 of Appendix D. The DYNK module has not only been used for the simulations presented in this thesis, but also for simulations of off-momentum collimation through RF detuning, studies of electron lens intensity modulation and studies of losses during energy ramping [110]. It has now become a standard tool for failure simulations.

DYNK is used as a block in the main SixTrack input file, called `fort.3`. In this block the user can specify which attribute of which element to change and when, achieved through the `SET` statement. The evolution of the attribute through time can be described with the `FUN` statement using a function or reading it from an external file. The `GET` function can be used in `FUN` to

retrieve the original value of the attribute from the lattice input file (`fort.2`). An example is shown below, where the voltage and phase of crab cavities ACFCA.AR1.B1 and ACFCA.AL1.B1 are modified with the DYNK block.

```

1  DYNK
2  FUN zero CONST 0.0
3  SET ACFCA.AR1.B1 voltage zero 1 1 0
4  FUN cc_init GET ACFCA.AR1.B1 voltage
5  SET ACFCA.AR1.B1 voltage cc_init 2 -1 0
6  FUN jump FILELIN phases.txt
7  SET ACFCA.AL1.B1 phase jump 1 200 0
8  NEXT

```

In line 2 a constant value of 0 is stored in the function `zero`, which is later used in line 3 to switch off the downstream crab cavity ACFCA.AR1.B1 (see Fig. 5.2) for the first turn of the simulation, i.e. from turn 1 to turn 1. The 0 at the end of the line is an integer added to the actual turn number before evaluating `zero`. The `GET` function is used in line 4 to retrieve the original voltage value of the cavity, which is stored into the `cc_init` function. The crab cavity voltage is then set to `cc_init` from turn 2 to the end of the simulation indicated by -1. In line 6 the content of the file `phases.txt` is stored in the function `jump` through the `FILELIN` function, which is later applied in line 7 to change the phase attribute of the upstream cavity ACFCA.AL1.B1. The DYNK block has many more functionalities that are described in the SixTrack manual [113, Chapter 3.3.4].

5.1.2 Collimation studies with SixTrack

Collimation studies for the LHC and the HL-LHC are carried out with the collimation version of SixTrack. This version allows to load external particle distributions up to $312 \times 64 = 19968$ particles per simulation. Halo distributions can also be created within the program to reduce computation time. The collimation version contains a proton scattering routine [114], based on the K2 code [115], that simulates the interaction of the proton with the collimator material. The interactions are classified into nuclear interactions, Coulomb scattering and ionization. Nuclear interactions include elastic and inelastic scattering with the atomic nucleus of the material, as well as single diffractive scattering. Coulomb scattering comprises large and small angle deflections, implemented as Rutherford scattering and multiple Coulomb scattering.

Collimators are implemented in the input lattice as markers of zero length and their properties such as length, material or jaw opening are read from a collimator database. During the particle tracking the particle's position and angle are evaluated at the collimator jaw. If the position is greater

than the collimator half gap the particle will enter the scattering routines directly. If the position is smaller than the collimator half gap but an angle exists, the longitudinal entry point to the collimator needs to be calculated. The code then follows a Monte Carlo method where the distance travelled by the particle before undergoing inelastic nuclear interaction is randomly generated until the particle is absorbed or leaves the collimator jaw. During the passage through the collimator the particle receives kicks from multiple Coulomb scattering and loses energy from ionization. The results are then given in the form of particle coordinates at the turn where the interaction with the collimator happened, divided into elastic and inelastic interactions.

The particles that undergo elastic scattering continue to travel through the machine with a different angle and might interact inelastically with the collimator in further passages. Due to their change in angle, these particles have a chance of hitting the machine aperture and being lost there. Not taking this fact into account means an overestimation of the number of inelastic absorptions in the collimator system. In order to account for the losses in the aperture the programs `BeamLossPattern` and `CleanInelastic` were developed as a post-processing tool for `SixTrack` output [116, 117], where

BeamLossPattern interpolates the trajectory of particles that interacted elastically with a collimator and finds the location where a given trajectory intercepts the machine aperture within a 10 cm resolution.

CleanInelastic removes the particles that are lost in the machine aperture from the inelastic interactions given by `SixTrack`.

Fig. D.3, in Appendix D, illustrates how `BeamLossPattern` and `CleanInelastic` work with the output from `SixTrack` and the needed input files for a full collimation study. In order to reduce the complexity and improve the accuracy of this process, efforts have been made in the past years to introduce an online aperture check in `SixTrack` coupled `FLUKA`, a more advanced Monte Carlo code [118].

5.2 Simulation set-up

Collimation studies were carried out with SixTrack using the HLLHCV1.2 optics. Since crab cavities will only operate during stable beams the simulations were done at collision energy. This section presents the crab cavity layout, collimation configuration, and particle distribution used.

5.2.1 Crab cavities

The crab cavity layout used in the simulations is shown in Fig. 5.2, using the following naming convention:

ACFCA : denotes the crab cavity element in SixTrack.

A, B, C or D : crab cavity position with respect to the others, A indicating the closest to the IP.

L or R : left or right side of the IP (as seen from inside the ring).

1 or 5 : IP number.

B1 or B2 : beam 1 or beam 2.

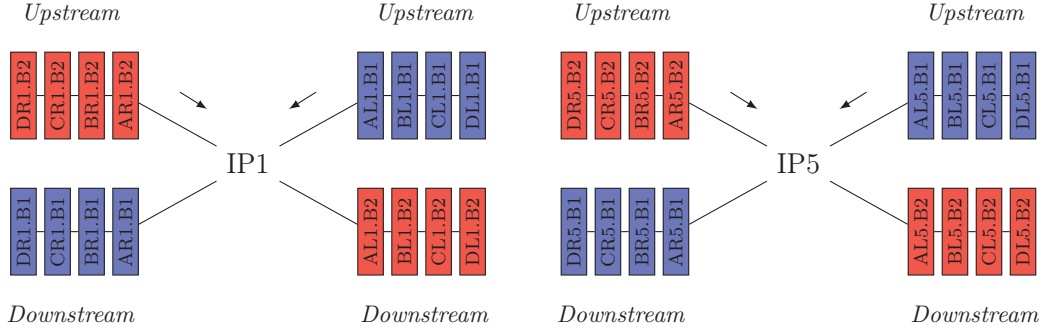


Figure 5.2. Layout of the crab cavities used in the SixTrack simulations, for ATLAS (left) and CMS (right).

Additional details concerning the location and optics functions of the simulated crab cavities can be found in Appendix C. Eq. (4.45) could not be used in this case to calculate the voltage since the phase advance and alpha function are not equal for the upstream and downstream cavities, as shown in Table C.1. Instead, the voltage of the crab cavities upstream of the IP was set to the cavity's maximum, i.e. 3.4 MV, and the voltage of the downstream crab cavities was calculated by MAD-X through matching with the constraint that no additional angle is added to the particles at the IP location (see Table 5.1). The frequency of the crab cavities is 400 MHz and their phase with respect to the arrival of the center of the bunch is zero.

Table 5.1. Voltage per crab cavity used in the simulations.

Experiment	Upstream [MV]	Downstream [MV]
ATLAS	3.4	3.37
CMS	3.4	3.18

5.2.2 Collimation

The collimator openings defined for the HL-LHC are listed in Table 5.2. Additional details concerning the location and optics functions of the simulated collimators can be found in Appendix C.

Table 5.2. HL-LHC collimator openings in terms of σ for emittances of 2.5 μm and 3.5 μm .

Collimator	Opening [$\sigma_{2.5}$] [$\sigma_{3.5}$]	
Primary IR7	6.74	5.7
Secondary IR7	9.11	7.7
Absorber IR7	11.83	10
Primary IR3	17.75	15
Secondary IR3	21.3	18
Absorber IR3	23.66	20
Secondary IR6	10.06	8.5
Dump protection IR6	10.65	9
Tertiary IR2	35.5	30
Tertiary IR8	17.75	15
Tertiary IR1/5	12.9	10.9

5.2.3 Chosen failure cases

As discussed in Chapter 4, the behavior of RF cavities can be summarized as an interplay between the EM fields sustained inside the cavity and the cavity itself, where all the crab cavity parameters (frequency, phase and voltage) are correlated through the physical structure of the cavity. Section 4.3.2 introduced a simplified model that takes into account this behavior, namely a driven damped harmonic oscillator. Simulations were carried out using this model and were published in a conference paper, which can be found in Appendix E.4. On the other hand, the failure scenarios selected for this study correspond to a power source failure and a LLRF malfunction, introduced in Section 4.7, where the voltage and phase evolve independently from each other. Additionally, the interaction of the beam with the cavity was

considered to be negligible [119]. During a power source failure the voltage of the cavity drains exponentially. While a decrease in the cavity fields leads to a frequency detuning and therefore to a change in phase, the amplitude of the kick induced by the phase change is proportional to the amplitude of the fields. This means that if the voltage decay is not compensated, the kick amplitude will exponentially decrease with it, and the effect will be negligible. The second scenario considered is when the voltage remains constant by compensation from the LLRF, or just normal operation, and the wrong phase is fed to the system. This can happen if the synchronization with the reference phase signal is lost or as an operation mistake. These two scenarios were chosen since they can be easily modeled and serve as reference to extrapolate information for any other crab cavity failure. It should be noted that the aim of these simulations is to identify failure cases that are a limit for the machine protection system and to study if they can be easily interlocked or mitigated. Since currently there exists no data concerning the real behavior of the crab cavity prototypes, from the machine protection point of view studying corner cases provides the best input for a safe operation with crab cavities.

The results presented in this chapter deal with three types of failures, already explored in Chapter 4.7, namely

Voltage decay (V) power source failure as described in Subsection 4.7.2, where $\tau_{\text{decay}} = 4$ LHC turns,

Phase jump (PJ) jump in the crab cavity phase from 0 to 60° in one turn and maintained constant,

Phase slip (PS) change of 60° in phase per turn.

A phase slip is equivalent to a linear frequency detuning Δf induced by the change in phase $\Delta\phi$ given by $\Delta\phi = \int_0^t 2\pi\Delta f t \, dt$. For the HL-LHC crab cavities the phase slip would be equivalent to a detuning of $\Delta f = 1.7$ kHz. The maximum phase change per turn of 60° used in the phase jump and phase slip cases is an overestimation of the value calculated with Eq. (4.57) in Chapter 4. In the simulation the particle distribution is tracked for 150 turns before the failure and 50 turns after the failure. This is done for the upstream cavities of ATLAS and CMS, where the failure affects either two or four crab cavities. It is important to note that it is not the number of cavities that matters but the total effective voltage of the crab cavity set-up: an effective voltage of 10 MV can be achieved with two crab cavities at 5 MV or three crab cavities at ~ 3.3 MV. The simulations presented here consider two and four crab cavities with a voltage of 3.4 MV each, i.e. a set-up with an effective voltage of 6.8 MV and 13.6 MV respectively. Results for other effective voltages can be easily extrapolated from those two.

5.2.4 Particle distribution

The presence of non-Gaussian tails has been systematically observed in beam profile measurements at the LHC [120]. In simulations these tails can be accounted for with double Gaussian distributions, where one Gaussian describes the core and the other one the tails. The subject of realistic particle distributions has been tackled in previous crab cavity failure studies, where LHC profile measurements were fitted to double Gaussians [112]. In particular the data from Van der Meer scans at CMS [121] and scraping measurements [122] were used, where

Van der Meer scan $\sigma_{\text{core}} = 1.0$, $\sigma_{\text{tail}} = 1.7957$

Scraping $\sigma_{\text{core}} = 1.3860$, $\sigma_{\text{tail}} = 2.6076$.

In both cases $\sigma_{\text{tail}} = 1.8\sigma_{\text{core}}$. This is why the parameters from the Van der Meer scans were chosen for this study, where the core makes up 95% of the beam and the tail 5% (detail in Fig. 3.4). This constitutes a moderately pessimistic case.

In accelerator physics the 4D beam matrix describes the transverse statistical properties of the beam, i.e. how the transverse coordinates are correlated with each other. If the vertical and horizontal motions are uncoupled a 2D beam matrix is enough to characterize the beam in one plane, given by

$$\sigma^{2\text{D}} = \begin{pmatrix} \sigma_{xx} & \sigma_{xx'} \\ \sigma_{x'x} & \sigma_{x'x'} \end{pmatrix} = \text{Cov}(\vec{x}) , \quad (5.1)$$

where Cov indicates the covariance, $\vec{x} = (x_n, x'_n)$, n is the number of particles, and $\epsilon = \sqrt{\det(\sigma^{2\text{D}})}$. It is often more convenient to express the beam matrix in terms of the Twiss parameters, which are themselves correlation coefficients

$$\sigma^{2\text{D}} = \epsilon \begin{pmatrix} \beta & -\alpha \\ -\alpha & \gamma \end{pmatrix} . \quad (5.2)$$

In order to generate correlated random variables \vec{x} from uncorrelated ones \vec{u} , we must find a transformation matrix \hat{M} such that

$$\vec{x} = \hat{M} \cdot \vec{u} , \quad (5.3)$$

where Eq. (5.1) is true. Remembering that

$$\text{Cov}(a, b) = \langle ab^\top \rangle - \langle a \rangle \langle b \rangle^\top , \quad (5.4)$$

considering that our uncorrelated random variables have zero means $\langle \vec{u} \rangle = \vec{0}$, unit variances $\langle \vec{u} \cdot \vec{u}^\top \rangle = \hat{I}$, and substituting Eq. (5.3) in Eq. (5.1) we get

$$\begin{aligned} \sigma^{2D} &= \text{Cov}(\hat{M} \cdot \vec{u}) = \langle \hat{M} \cdot \vec{u} \cdot \vec{u}^\top \cdot \hat{M}^\top \rangle = \hat{M} \langle \vec{u} \cdot \vec{u}^\top \rangle \hat{M}^\top \\ \sigma^{2D} &= \hat{M} \hat{M}^\top. \end{aligned} \quad (5.5)$$

It is common to computationally calculate the \hat{M} matrix through Cholesky decomposition for its numerical efficiency, where \hat{M} is a lower triangular matrix. In order to have a complete description of the beam at a certain location the dispersive contribution $D\delta$ needs to be added to the coordinates.

The simulations presented in this Chapter start at an IP, where by design β is small, $\alpha \approx 0$, and $D \approx 0$, giving very little correlation among coordinates. The longitudinal profile was created using rejection sampling on an uncorrelated bivariate Gaussian distribution. The separatrix given by the Hamiltonian of the synchrotron motion was set as the limit for the rejection sampling. This method does not provide a perfectly matched longitudinal distribution since it is not completely uniform in phase space, creating small oscillations in bunch length. However, since the synchrotron period is much longer than the timescale for the simulated failures this effect is negligible.

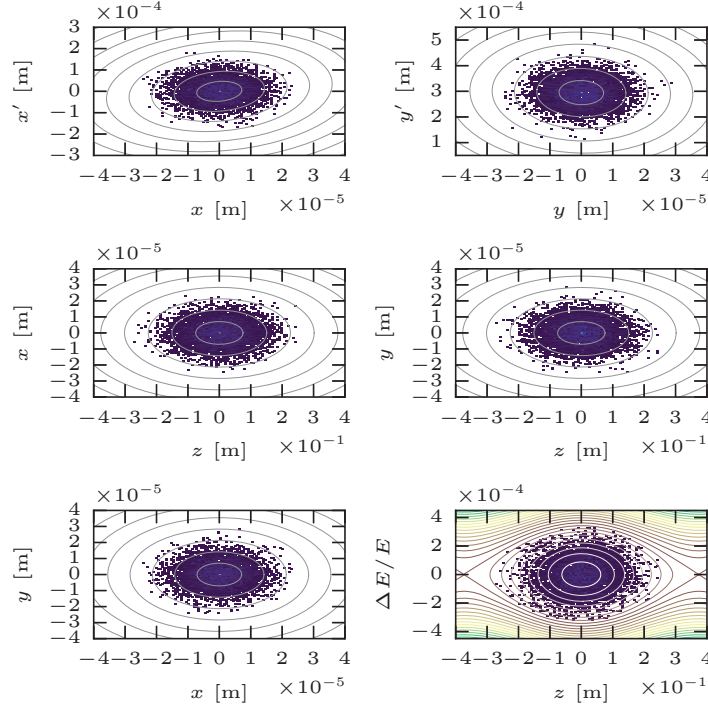


Figure 5.3. Initial particle distribution at IP1, where the gray ellipses indicate areas of constant sigma. We can observe a small, non-zero alpha in the horizontal plane.

5.2.5 *Computational considerations*

Collimation studies were carried out with SixTrack on a single particle bunch, divided into a core and tail population that were tracked separately. The final particle distribution was reconstructed by assigning the correct weights to core and tail, as discussed in Section 5.2.4. Instead of using the total number of particles per HL-LHC bunch, i.e. 2.2×10^{11} protons, a macroparticle representation was used. A macroparticle is a numerical representation of a cluster of neighbouring physical particles and allows to reduce the computational resources needed to run a simulation. This method can increase the granularity of the system and introduce noise if the number of simulated macroparticles is too small. These effects are negligible for the simulations presented here, where ~ 3 million macroparticles were tracked on average per SixTrack run. As mentioned in Section 5.1.2, the current tracking limit of the collimation routine is of $312 \times 64 = 19968$ particles per simulation, resulting in ~ 150 simulations per failure scenario. Considering that 24 different failure scenarios were simulated and that they were divided into core and tail, a total of 7200 simulations was needed. Since the SixTrack collimation runs are long and the output files can end up weighting several gigabytes they had to be carried out using the CERN Batch System. This system offers a centrally-managed cluster of 190000 CPU cores designed to run computing jobs as of early 2018. This is achieved by having a group of computers working together as a single unit, combining computing power and sharing workload and resources [123].

In order to better compare the results for different failure scenarios the same particle distribution was used for each failure case, divided in different jobs. Additionally, the random seed used in the Monte Carlo method that simulates the scattering of the particles through matter, discussed in Section 5.1.2, was set to be the same across failure cases, but different for each job.

5.3 Results from SixTrack simulations

5.3.1 Single particle simulations

In order to clearly observe the effect that the failure scenarios have on the beam we first simulate them with SixTrack for a single particle. The variation of the voltage and phase of the crab cavities is done as described in Fig. 5.4 through the DYNK block, introduced in Chapter 5.1.1.

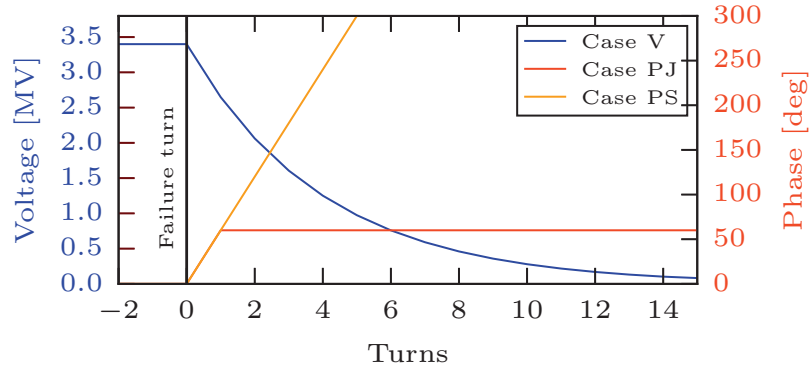


Figure 5.4. Crab cavity parameters modified for each failure case. The phase remains constant at zero value in the V (voltage decay) scenario and the voltage remains constant in the PJ (phase jump) and PS (phase slip) scenarios.

The results are shown in Fig. 5.5, where the position of the particle is shown for each turn in phase space and the transverse plane. The particle's movement is observed at a primary collimator to see if the particle would reach the collimator jaws. For this, the collimator jaws were kept open during this simulation.

We can see from Fig. 5.5 that the V scenario only causes a smear in the particle's orbit, while in the PJ scenario the kick sends the particle to a higher amplitude orbit. In the PS case the particle is kicked differently for each turn, so the amplitude of the particle's orbit grows with time. The collimator jaws are easily hit with four crab cavities failing in the PS case. The impact of simultaneous failures can also be observed, where the effect of a failure is cumulative with the number of crab cavities failing.

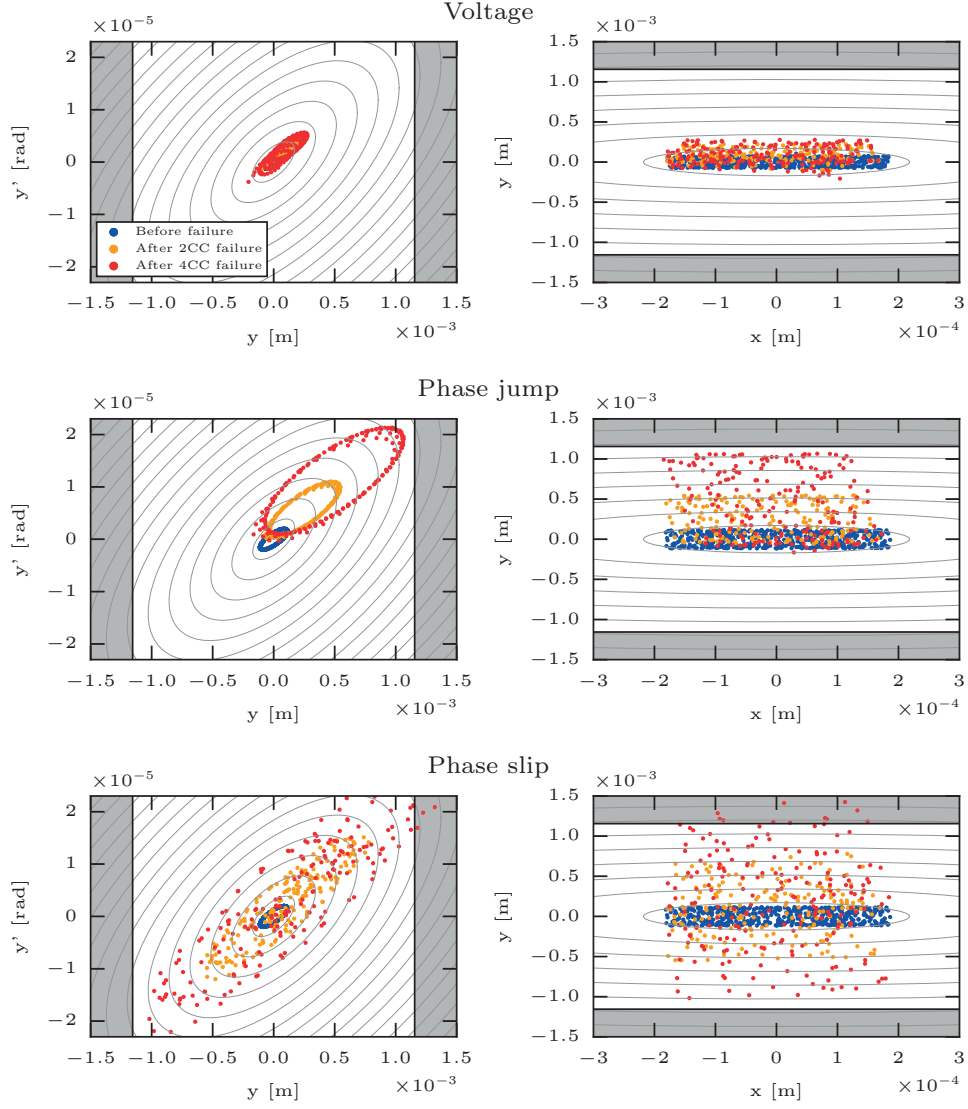


Figure 5.5. Single particle tracking for the three selected failure scenarios, where each point corresponds to one turn. The failures happen in IP1 and the distribution is observed at a vertical primary collimator. The position of the collimator jaws is shown in gray color. In the legend **CC** stands for crab cavity.

5.3.2 Collimation studies

The results presented in this section correspond to simulations carried out for one single particle bunch. The particles absorbed in the collimation system before the failure, or *cleaning*, were removed from the losses presented in this section. In this way we can observe the losses created exclusively by the failure. Before the failure, the beam was tracked for 150 turns, and 0.7% of the simulated halo particles for beam 1 were lost, and 0.6% for beam 2. We assume that all the bunches that make up the beam will see a similar effect as the one simulated, which allows scaling the losses observed in the simulations to the whole beam.

Table 5.3 shows the fraction of beam lost for each failure scenario depending on the maximum average displacement of the beam, observed at the most hit primary collimator within the first 50 turns after the failure. The fraction of beam lost is also given at 10 turns after the failure. Fig. 5.6 shows a visual representation of the data given in Table 5.3 in a semi-logarithmic scale, where we can immediately observe two trends that separate the voltage decay failures (represented in green) from the phase jump and the phase slip failures (represented in orange and red). During a voltage decay the particle bunch is not transversely displaced, which can be seen in the plot from the lack of correlation between losses and transverse displacement. On the other hand, the points corresponding to phase-related failures follow the shape of a cumulative distribution function for a Gaussian profile. This trend is explained by the densely populated beam core gradually reaching the collimator jaws, where the losses will increase with the density of the double Gaussian profile. We can see that the losses start being non-negligible from 4σ displacements onwards, which means that core particles start being intercepted by the primary collimators at that point. For average displacements bigger than the primary collimator opening, i.e. 6.74σ , we observe that the majority of the beam is lost.

We can observe from Fig. 5.6 that the most dramatic losses, clustered in the upper quadrant of the plot, correspond to a phase-related failure of four crab cavities. This allows concluding that the losses created during a phase-related crab cavity failure greatly increase with the number of simultaneous crab cavities failing. Not only phase-related failures are shown to create considerable losses in the collimation system but they also happen very fast, as the majority of the losses take place within the first 10 turns of failure. Concerning the voltage decay scenarios we can see that the losses are generally lower compared to the phase related ones. The biggest losses in the voltage decay case are of the same order of magnitude as the lowest losses observed for phase-related failures of two crab cavities. Looking back at Fig. 5.5 we observed that a crab cavity voltage decay only smeared the particle's orbit, which means that the losses mainly come from halo particles. Concerning

Table 5.3. Losses in the collimation system 10 and 50 turns after the failure, given in fraction of beam lost, and the maximum displacement of the bunch observed in terms of sigma. In the table **V** stands for voltage decay, **PJ** for phase jump, **PS** for phase slip and **CC** for crab cavity.

Failure	Beam 1			Beam 2		
	10 turns	50 turns	σ_{\max}	10 turns	50 turns	σ_{\max}
V IP1 2CC	5.24×10^{-5}	2.82×10^{-4}	-	3.83×10^{-6}	1.31×10^{-5}	-
V IP5 2CC	1.44×10^{-4}	5.67×10^{-4}	-	9.38×10^{-5}	3.71×10^{-4}	-
V IP1 4CC	3.12×10^{-4}	1.44×10^{-3}	-	9.06×10^{-6}	3.27×10^{-5}	-
V IP5 4CC	1.48×10^{-3}	6.56×10^{-3}	-	6.78×10^{-4}	2.62×10^{-3}	-
PJ IP1 2CC	1.29×10^{-3}	2.16×10^{-3}	2.48	1.98×10^{-4}	3.64×10^{-4}	1.32
PJ IP5 2CC	2.17×10^{-3}	3.57×10^{-3}	2.65	1.43×10^{-3}	2.33×10^{-3}	2.38
PJ IP1 4CC	1.33×10^{-1}	1.53×10^{-1}	4.13	2.61×10^{-3}	3.58×10^{-3}	2.47
PJ IP5 4CC	3.06×10^{-1}	3.59×10^{-1}	4.71	1.92×10^{-1}	2.68×10^{-1}	4.43
PS IP1 2CC	4.23×10^{-3}	8.52×10^{-3}	2.79	4.17×10^{-4}	8.46×10^{-4}	1.84
PS IP5 2CC	3.09×10^{-2}	5.87×10^{-2}	3.45	1.16×10^{-2}	2.23×10^{-2}	2.50
PS IP1 4CC	5.72×10^{-1}	7.22×10^{-1}	4.04	3.22×10^{-2}	4.96×10^{-2}	3.62
PS IP5 4CC	9.34×10^{-1}	9.90×10^{-1}	6.98	7.33×10^{-1}	9.51×10^{-1}	6.34

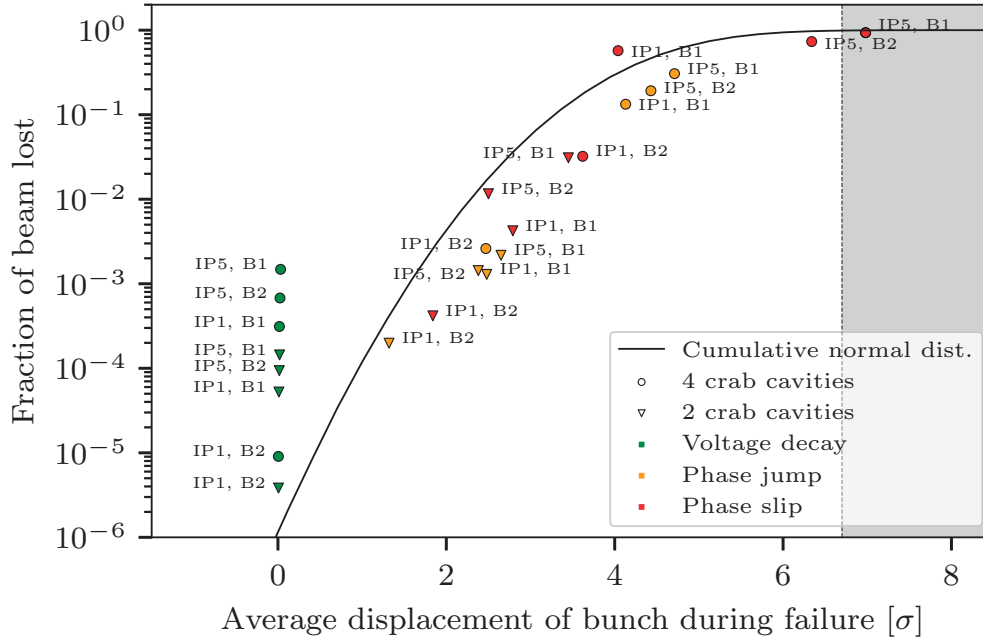


Figure 5.6. Visual representation of the data given in Table 5.3 50 turns after the failure. The gray area represents the opening of the primary collimator.

the timescale for the losses in a voltage decay failure case, we see from Table 5.3 that they happen in a steady way, unlike in the case of a phase-related failure. This suggests that this type of scenario could be mitigated by a halo depletion method, such as the hollow electron lens [124]. In general, we can see that for the same failure scenario the losses change depending on the beam and IP. Particularly, the scenarios corresponding to beam 2 in IP1 are consistently lower than the other cases for the same failure scenario. This is further studied in Section 5.4.1.

The spatial and temporal distributions of the losses are shown in the following pages for the most dangerous failure scenario, i.e. the simultaneous phase slip of four crab cavities, for both IPs and beams. The top plots of figures 5.7, 5.8, 5.9, and 5.10 show that the majority of the losses happen in the betatron cleaning insertion located in IR7, with few other losses around the ring. Particle losses in the machine aperture appear to happen in more locations for crab cavity failures happening in IP5, especially for beam 1. This can be clearly seen in Fig. 5.9, where the particles impact the aperture of the magnets located between IR6 and IR7 during the simulation. We can observe in the bottom figure that the losses in the Target Collimator Dump Quadrupole (TCDQ), a dump protection collimator, increase dramatically in this case. The TCDQ is located in front of a Q4 magnet, which would be at a high risk of quench in this case [125]. The fact that this behavior is not observed for failures happening in IP1, which occur in the vertical plane, suggest that the increase in aperture losses is due to impact with the TCDQ collimator.

The temporal distributions of the losses are shown in the bottom plots of figures 5.7, 5.8, 5.9 and 5.10. We can see that the majority of the losses happen very fast, within the first three turns after the failure. It is important to note that the collimation hierarchy $TCP \rightarrow TCSG \rightarrow TCL \rightarrow TCT$ is not conserved for all cases. Fig. 5.8, which corresponds to a phase slip of four crab cavities in IP1 for beam 2, shows how the secondary collimators receive considerably more losses than the primary collimators. We can also see that for a phase slip of four crab cavities in IP5 for beam 2, shown in Fig. 5.10, the majority of the tertiary halo is stopped by the TCT and not the TCLA. These asymmetries across IPs and beams are further explored in Section 5.4.1.

The time structure of losses during a voltage decay failure is shown in Figs. 5.11 and 5.12 for both IPs and both beams. We can see that the losses happen at a slower rate and in a more steady way than the losses observed during a phase-related crab cavity failure. The losses are consistently higher for the failures happening in IP5, where we observe again losses intercepted by the TCDQ. Additionally, the collimation hierarchy is not broken in this scenario.

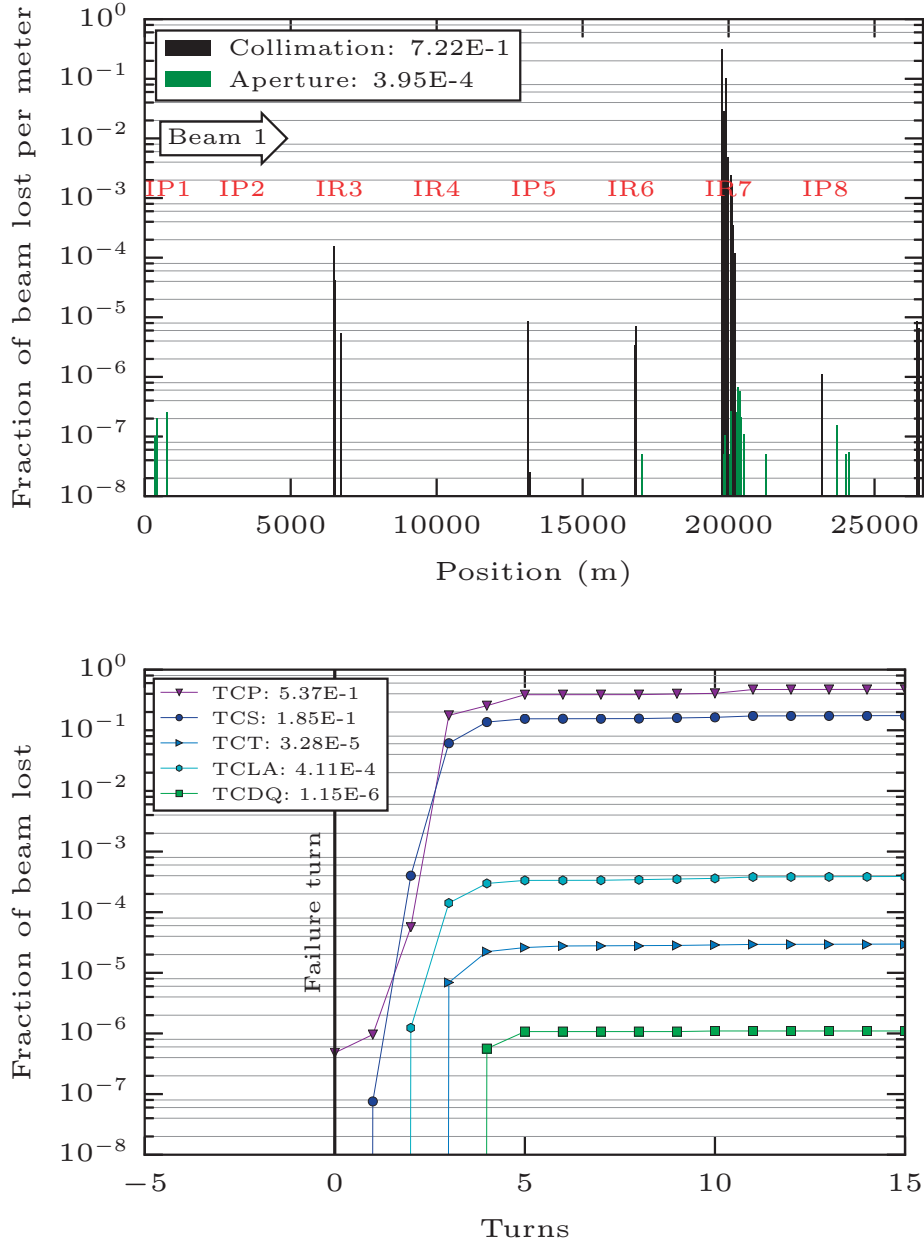


Figure 5.7. **Top:** loss map for the phase slip of four crab cavities in IP1 for beam 1 (PS IP1 4CC failure case). **Bottom:** cumulative losses per turn grouped per collimator type for the same failure scenario. The legends show the fraction of beam lost 50 turns after the failure.

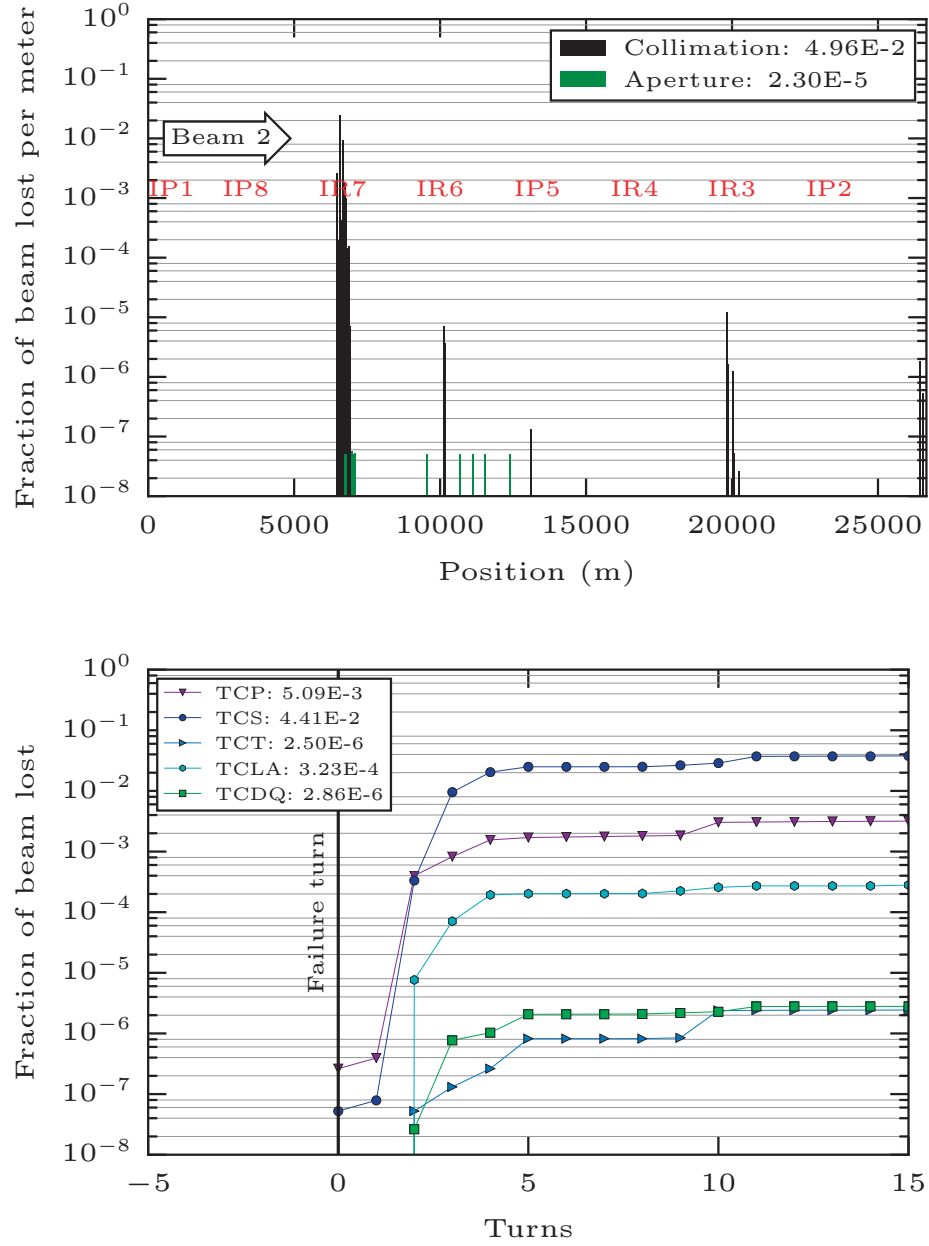


Figure 5.8. **Top:** loss map for the phase slip of four crab cavities in IP1 for beam 2 (PS IP1 4CC failure case). **Bottom:** cumulative losses per turn grouped per collimator type for the same failure scenario. The legends show the fraction of beam lost 50 turns after the failure.

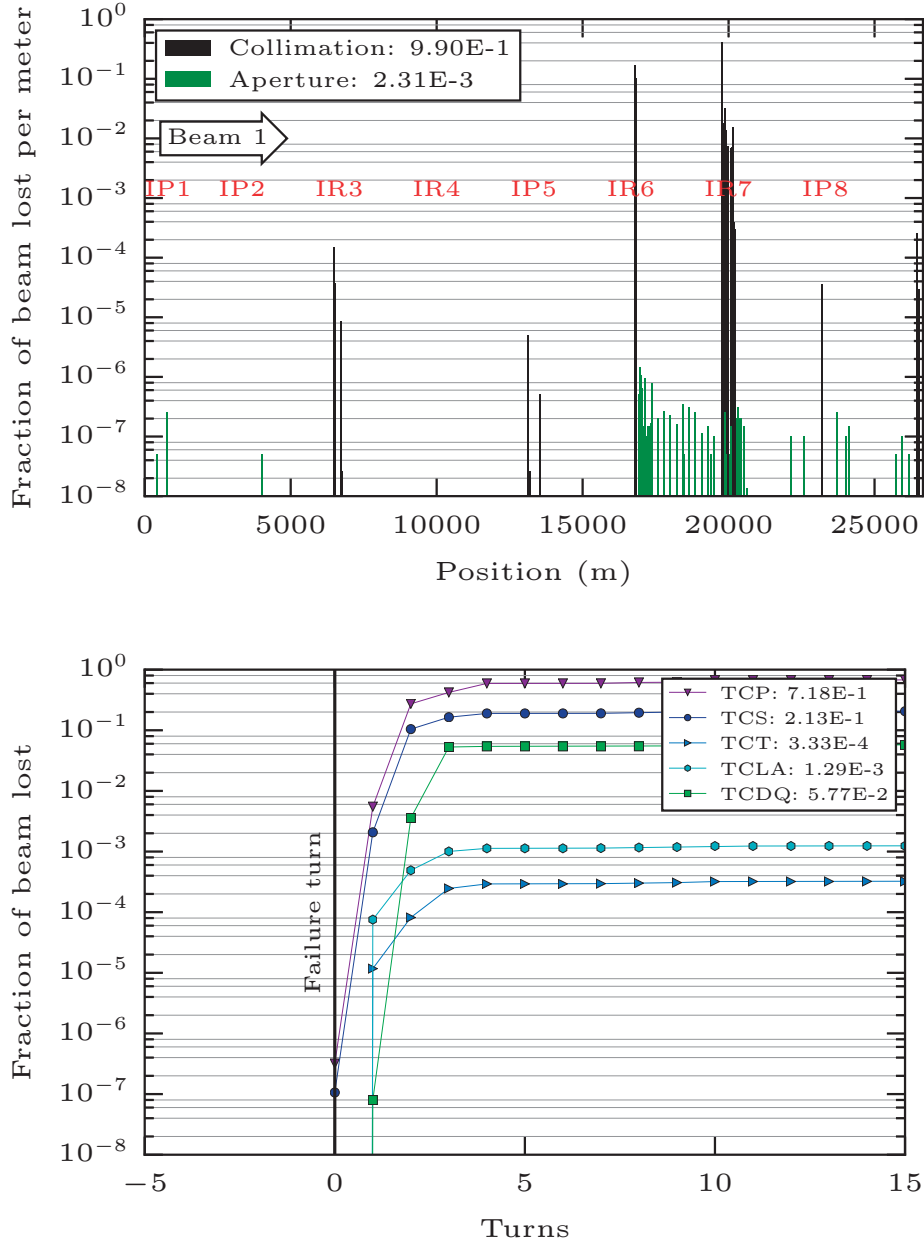


Figure 5.9. **Top:** loss map for the phase slip of four crab cavities in IP5 for beam 1 (PS IP5 4CC failure case.) **Bottom:** cumulative losses per turn grouped per collimator type for the same failure scenario. The legends show the fraction of beam lost 50 turns after the failure.

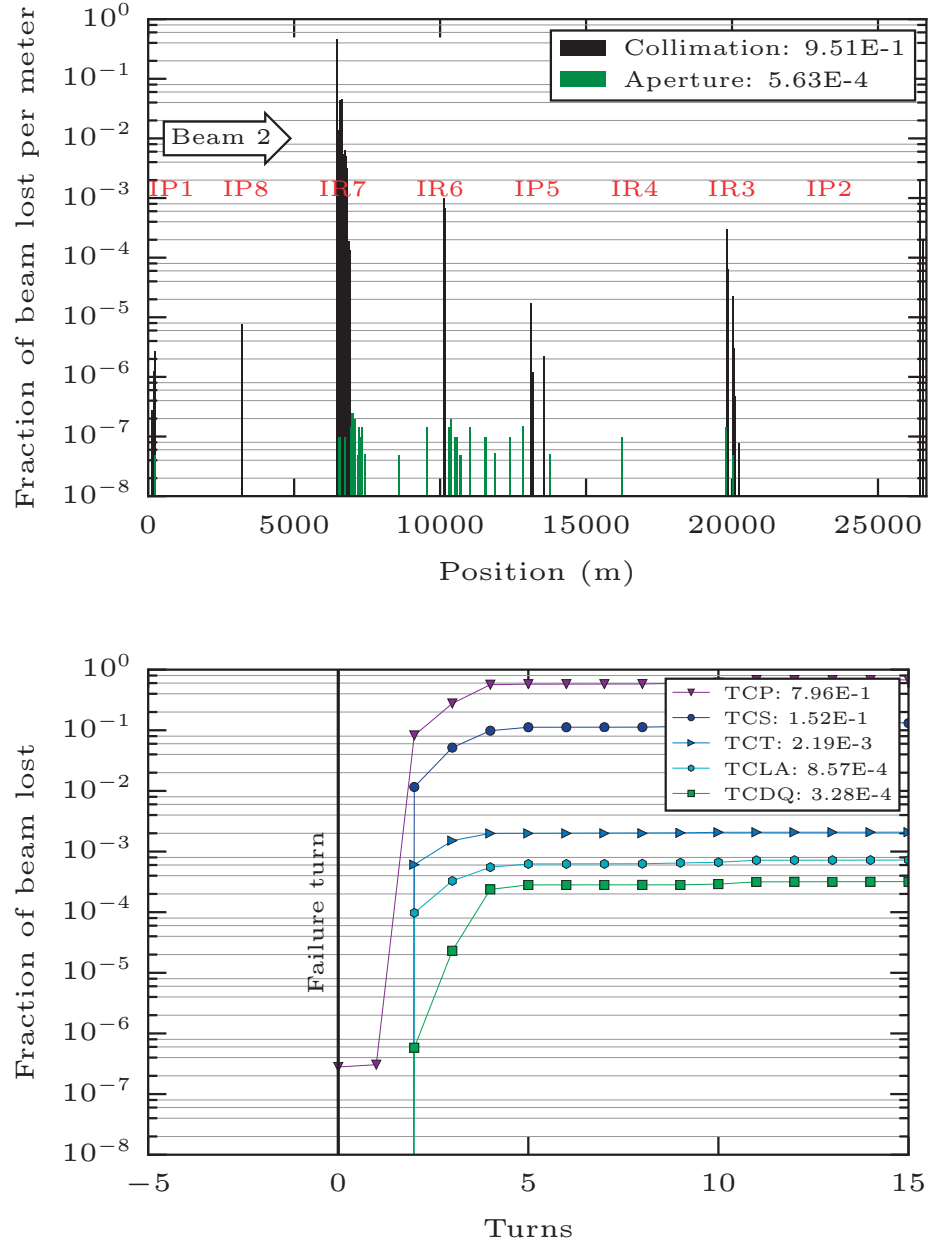


Figure 5.10. **Top:** loss map for the phase slip of four crab cavities in IP5 for beam 2 (PS IP5 4CC failure case). **Bottom:** cumulative losses per turn grouped per collimator type for the same failure scenario. The legends show the fraction of beam lost 50 turns after the failure.

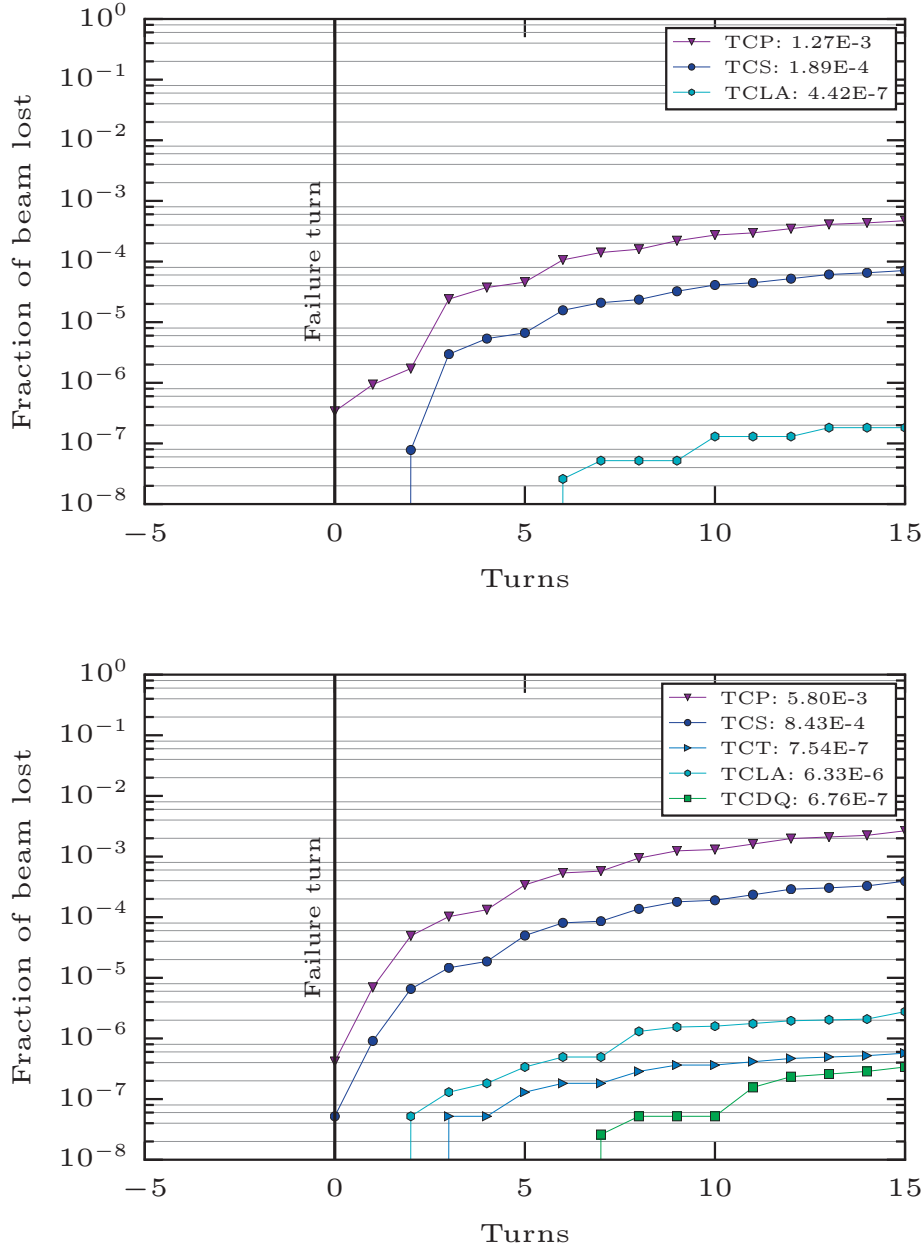


Figure 5.11. Cumulative losses per turn grouped per collimator type for ATLAS (top) and CMS (bottom) for the voltage decay of four crab cavities, beam 1 (V 4CC failure case). The legends show the fraction of beam lost 50 turns after the failure.

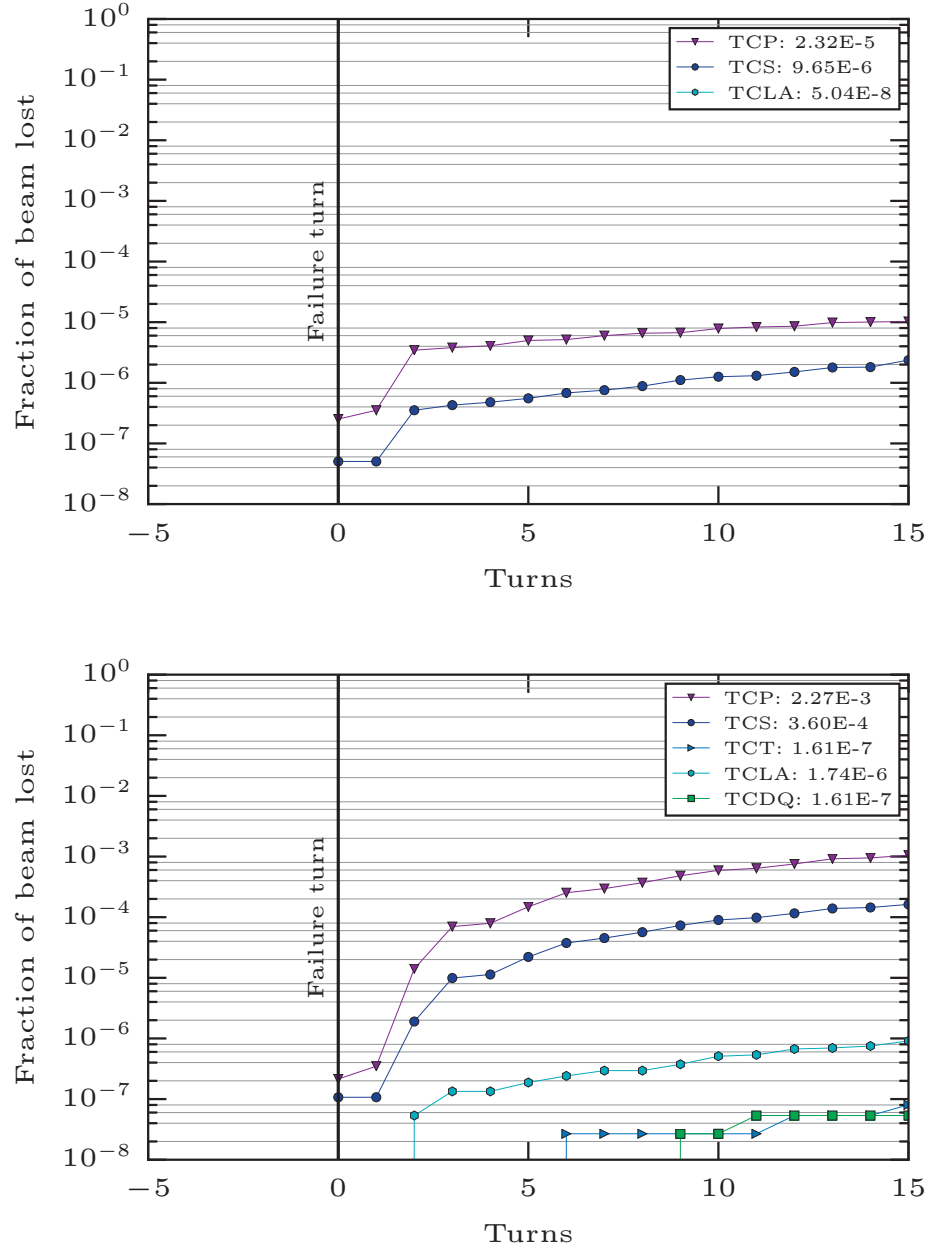


Figure 5.12. Cumulative losses per turn grouped per collimator type for ATLAS (top) and CMS (bottom) for the voltage decay of four crab cavities, beam 2 (V 4CC failure case). The legends show the fraction of beam lost 50 turns after the failure.

5.3.3 Machine protection considerations

We have seen that crab cavity failures happen abruptly and in a very short timescale, so we want to assess the impact these failures have on the collimation system. Despite being among the most robust components in the LHC collimators need to be protected from uncontrolled losses that might deform the jaws or cause jaw fragments to be ejected, which is why each collimator is equipped with Beam Loss Monitors (BLMs). BLMs are ionization chambers that measure the rates of proton loss at the collimator location. If the loss rate reaches a certain threshold that is considered dangerous the BLMs will send a beam dump request that will be completed within two or three turns. At the LHC the beam abort signal will be triggered if 3×10^{10} protons or more are lost in half a turn or less at a TCP [126], as shown in Fig. 5.13.

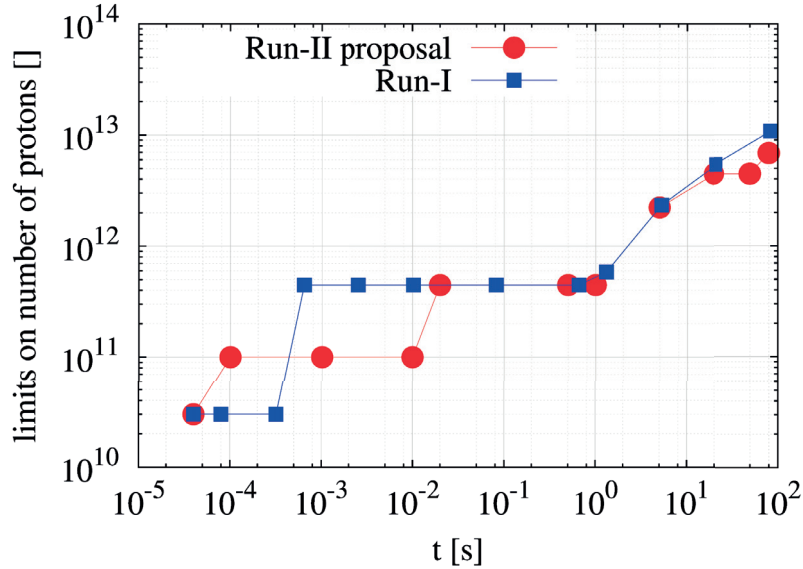


Figure 5.13. Limits on the number of 7 TeV protons impacting on TCP collimators as a function of BLM integration time [127].

Taking this into account, the beam abort trigger was calculated for each failure case and is presented in Table 5.4, which also shows the collimator corresponding to the BLM that triggered it, and the number of protons it received in that half turn. The number of protons is calculated by scaling the fraction of beam lost obtained from the simulations to a full HL-LHC beam, composed of 2748 bunches of 2.2×10^{11} protons each.

We can observe that for the majority of cases the beam abort is initiated right away. Except for one case, the losses during a voltage decay failure are too low to trigger the beam dump process. Considering that the beam is dumped three turns after the beam abort we can estimate that the failure goes on for five turns on average. During this time the collimators are completely exposed to the failure and constitute the only passive protection of

Table 5.4. Trigger of the beam abort for each failure case where **V** stands for voltage decay, **PJ** for phase jump, **PS** for phase slip and **CC** for crab cavity.

Failure	Turn	Beam 1		Turn	Beam 2	
		Collimator	N° protons		Collimator	N° protons
V IP1 2CC	-	-	-	-	-	-
V IP5 2CC	-	-	-	-	-	-
V IP1 4CC	-	-	-	-	-	-
V IP5 4CC	5	TCP.C6L7	5.55×10^{10}	13	TCP.C6R7	4.49×10^{10}
PJ IP1 2CC	3	TCP.D6L7	1.60×10^{11}	-	-	-
PJ IP5 2CC	1	TCP.C6L7	3.72×10^{10}	2	TCP.C6R7	1.39×10^{11}
PJ IP1 4CC	2	TCSG.D4L7	9.49×10^{10}	2	TCP.D6R7	1.05×10^{11}
PJ IP5 4CC	1	TCP.C6L7	1.59×10^{12}	2	TCP.C6R7	2.45×10^{13}
PS IP1 2CC	3	TCP.D6L7	3.25×10^{11}	-	-	-
PS IP5 2CC	1	TCP.C6L7	3.74×10^{10}	2	TCP.C6R7	1.39×10^{11}
PS IP1 4CC	2	TCSG.D4L7	9.41×10^{10}	2	TCP.D6R7	1.06×10^{11}
PS IP5 4CC	1	TCP.C6L7	1.59×10^{12}	2	TCP.C6R7	2.45×10^{13}

the machine. The jaws of the primary and secondary collimators are made of robust carbon-fibre carbon composites (CFC) and are designed to withstand beam impacts without significant permanent damage up to eight bunches of 1.15×10^{11} protons at 7 TeV [25, Chapter 5], as tested for the study of asynchronous beam dumps. Such tests have not yet been performed for the HL-LHC, but assuming a safety factor of 10 the collimators should be able to withstand the impact of eight bunches of 10^{12} protons [128]. In order to easily assess the damage sustained by the collimators during crab cavity failures Tables 5.5 and 5.6 present the most hit collimator during the failure within the primary, secondary and tertiary collimator families and the number of protons absorbed by each collimator in five turns after the failure. The cases where the number of absorbed protons surpasses 8×10^{12} are marked in bold. We can see that the failure scenarios where the collimators could be damaged always correspond to the simultaneous phase-related failure of four crab cavities, except for the phase slip of two crab cavities in IP5 for beam 1. We can also observe that the voltage decay failure cases remain within safe limits.

Table 5.5. Number of protons lost in different scenarios where **V** stands for voltage jump, **PJ** for phase jump, **PS** for phase slip and **CC** for crab cavity. The data is given five turns after the failure scaled to the full HL beam, for the most hit collimators, and for Beam 1. The values in bold letters correspond to values around or above 8×10^{12} protons [128].

Failure	TCP		TCS		TCT	
	Name	Protons	Name	Protons	Name	Protons
V IP1 2CC	TCP.D6L7	3.71×10^9	TCSG.A6L7	3.58×10^8	No hits	$< 7.6 \times 10^6$
V IP5 2CC	TCP.C6L7	1.77×10^{10}	TCSG.B5L7	1.17×10^9	TCTH.6L1	7.63×10^6
V IP1 4CC	TCP.D6L7	1.85×10^{10}	TCSG.A6L7	1.48×10^9	No hits	$< 7.6 \times 10^6$
V IP5 4CC	TCP.C6L7	1.77×10^{11}	TCSG.B5L7	9.63×10^9	TCTH.6L1	4.72×10^7
PJ IP1 2CC	TCP.D6L7	3.27×10^{11}	TCSG.A6L7	1.46×10^{10}	TCTPH.4L8	7.63×10^6
PJ IP5 2CC	TCP.C6L7	6.22×10^{11}	TCSG.B5L7	3.60×10^{10}	TCTH.6L1	5.34×10^7
PJ IP1 4CC	TCP.D6L7	4.84×10^{13}	TCSG.A6L7	2.05×10^{12}	TCTV.6L5	1.81×10^9
PJ IP5 4CC	TCP.C6L7	1.33×10^{14}	TCSG.B5L7	6.68×10^{12}	TCTH.6L1	1.78×10^{10}
PS IP1 2CC	TCP.D6L7	1.61×10^{12}	TCSG.D4L7	8.37×10^{10}	TCTPH4L1	4.58×10^7
PS IP5 2CC	TCP.C6L7	1.04×10^{13}	TCSG.B5L7	5.15×10^{11}	TCTPH4L1	1.21×10^9
PS IP1 4CC	TCP.D6L7	2.24×10^{14}	TCSG.D4L7	5.71×10^{13}	TCTH.6L1	4.75×10^9
PS IP5 4CC	TCP.C6L7	3.41×10^{14}	TCSPA.4R6	5.88×10^{13}	TCTH.6L1	1.41×10^{11}

Table 5.6. Number of protons lost in different scenarios where **V** stands for voltage decay, **PJ** for phase jump, **PS** for phase slip and **CC** for crab cavity. The data is given five turns after the failure scaled to the full HL beam, for the most hit collimators, and for Beam 2. The values in bold letters correspond to values around or above 8×10^{12} protons [128]. The underlined values indicate that the collimator hierarchy is broken.

Failure	TCP		TCS		TCT	
	Name	Protons	Name	Protons	Name	Protons
V IP1 2CC	TCP.B6R7	6.93×10^8	TCSG.B5R7	5.33×10^7	No hits	$< 7.6 \times 10^6$
V IP5 2CC	TCP.C6R7	1.21×10^{10}	TCSG.B5R7	8.60×10^8	No hits	$< 7.6 \times 10^6$
V IP1 4CC	TCP.D6R7	1.61×10^9	TCSG.A6R7	1.07×10^8	No hits	$< 7.6 \times 10^6$
V IP5 4CC	TCP.C6R7	7.38×10^{10}	TCSG.B5R7	4.56×10^9	No hits	$< 7.6 \times 10^6$
PJ IP1 2CC	TCP.D6R7	5.20×10^{10}	TCSG.A6R7	3.11×10^9	No hits	$< 7.6 \times 10^6$
PJ IP5 2CC	TCP.C6R7	4.09×10^{11}	TCSG.B5R7	2.27×10^{10}	TCTPH.4R1	7.62×10^6
PJ IP1 4CC	TCP.D6R7	3.73×10^{11}	TCSG.D4R7	4.38×10^{11}	TCTV.6R1	1.54×10^7
PJ IP5 4CC	TCP.C6R7	5.35×10^{13}	TCSG.B5R7	2.73×10^{12}	TCTH.6R1	7.12×10^9
PS IP1 2CC	TCP.D6R7	9.58×10^{10}	TCSG.D4R7	1.08×10^{10}	No hits	$< 7.6 \times 10^6$
PS IP5 2CC	TCP.C6R7	4.29×10^{12}	TCSG.B5R7	2.32×10^{11}	TCTV.6R5	3.03×10^8
PS IP1 4CC	TCP.D6R7	8.93×10^{11}	TCSG.D4R7	7.49×10^{12}	TCTV.6R1	4.17×10^8
PS IP5 4CC	TCP.C6R7	3.31×10^{14}	TCSG.B4R7	2.16×10^{13}	TCTH.6R1	1.08×10^{12}

5.4 Analysis

5.4.1 Study of the asymmetry in beam losses

The data presented in the previous section showed an asymmetry in the losses intercepted by the collimation system. It was found that, for the same failure case, the number of particles lost greatly varied depending on the beam and the IP where the failure happened. A variation in the number of intercepted particles by the collimators points to a difference in orbit at the collimator, which needs to be studied. To this end, we calculate the change in closed orbit induced by the crab cavity phase kick at the most hit collimator for each failure case. The orbit distortion seen at a point s created by a kick angle θ at a point s_0 can be expressed as the product of the Green function of Hill's equation and the kick angle [28, Chapter 2.III.1.A], given by

$$\Delta y(s) = \theta \frac{\sqrt{\beta(s)\beta(s_0)}}{2 \sin \pi \nu} \cos(\pi \nu - \Delta \mu), \quad (5.6)$$

where β is the beta function, ν is the betatron tune, and $\Delta \mu = |\mu(s) - \mu(s_0)|$, μ being the phase advance. The kick angle for a crab cavity was previously derived and given in Eqs. 4.29 and 4.31 as

$$\theta = -\frac{qV_0}{E} \sin(\phi_{cc} + \omega_{cc}t), \quad (5.7)$$

where V_0 is the voltage of the cavity, E is the energy of the particle, ϕ_{cc} is the phase of the cavity, and ω_{cc} the angular frequency of the cavity. Considering a change of $\phi_{cc} = 60^\circ$ in the crab cavity phase, the LHC tunes $\nu_x = 62.31$, $\nu_y = 60.32$, and the relevant optics parameters from Appendix C we can calculate the orbit distortion, presented in Table 5.7.

Table 5.7. Orbit distortion created at the primary collimators from the kick of four crab cavities and the phase advance between them.

Origin of kick Observation point	ACFCA.AL1.B1 TCP.D6L7.B1	ACFCA.AL5.B1 TCP.C6L7.B1
Orbit change [mm] / [σ]	0.41 / 2.55	-0.74 / -3.30
$\Delta\mu$ [°]	7.88	46.94

Origin of kick Observation point	ACFCA.AR1.B2 TCP.D6R7.B2	ACFCA.AR1.B2 TCSG.D4R7.B2	ACFCA.AR5.B2 TCP.C6R7.B2
Orbit change [mm] / [σ]	0.018 / 0.11	0.37 / 2.48	-0.63 / -2.80
$\Delta\mu$ [°]	55.66	9.68	22.79

We can see that depending on each IP and beam the phase advance between the crab cavities and the primary collimators varies, translating into different particle amplitudes and, therefore, a different number of particles lost in the collimation system. In the failures happening in ATLAS for beam 2 the primary collimator TCP.D6R7.B2 is completely missed and the particles are absorbed in the secondary collimator TCSG.D4R7.B2, breaking the collimator hierarchy that was observed in the previous section.

To better visualize the orbit distortions at the collimators we simulate the crab cavity kick in the HL-LHC lattice with the MAD-X program. The results are shown in Fig. 5.14 for four crab cavities, i.e. an effective voltage of 13.6 MV.

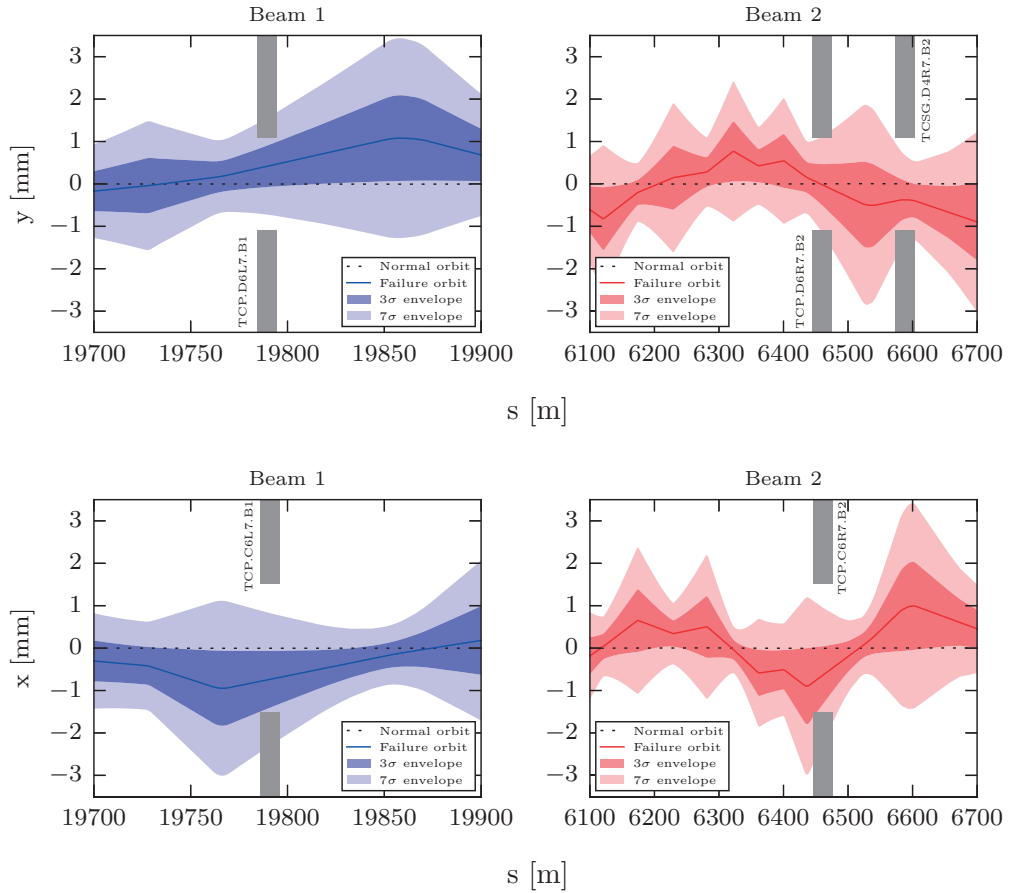


Figure 5.14. Closed orbit calculated by MAD-X in the case of a phase jump of 60° of four crab cavities upstream of ATLAS (top row) and CMS (bottom row) in IR7.

We can observe that the orbit distortions listed in Table 5.7 match the MAD-X simulations. The top, right-side plot of Fig. 5.14 shows how the closed orbit passes through the center of the primary collimator TCP.D6R7.B2, its amplitude increasing as it reaches the secondary collimator TCSG.D4R7.B2.

The secondary collimator is, therefore, receiving primary impacts and acting as a primary collimator. Since the secondary collimators have a bigger aperture than the primary collimators (as shown in Table 5.2) the total losses in the collimation system are reduced. Indeed, looking at Fig. 5.6, we can observe that the cases corresponding to IP1, beam 2, have considerably fewer losses than the rest of the cases. These results show that avoiding the primary collimators can significantly reduce the losses around the accelerator before the beam is dumped in case of a crab cavity failure. This approach is further explored in the next section.

5.4.2 Phase advance optimization as mitigation

We have looked at the impact that an angular kick has on the closed orbit using Eq. (5.6). The closed orbit represents an average path of a particle during multiple passages. Since crab cavity failures happen in a very short timescale, we are also interested in looking at the trajectory of the particle, i.e the path followed by the particle in one passage. We can derive the expression for the change in trajectory using the transport matrix from point s_0 to point s given in Eq. (4.33)

$$M_{s_0 \rightarrow s} = \begin{pmatrix} \sqrt{\frac{\beta(s)}{\beta(s_0)}} (\cos \Delta\mu + \alpha(s_0) \sin \Delta\mu) & \sqrt{\beta(s_0)\beta(s)} \sin \Delta\mu \\ -\frac{(1+\alpha(s_0)\alpha(s)) \sin \Delta\mu + (\alpha(s) - \alpha(s_0)) \cos \Delta\mu}{\sqrt{\beta(s_0)\beta(s)}} & \sqrt{\frac{\beta(s_0)}{\beta(s)}} (\cos \Delta\mu - \alpha(s) \sin \Delta\mu) \end{pmatrix}, \quad (5.8)$$

where $\Delta\mu$ is the phase advance between point s_0 and point s and α and β are the Twiss functions. Let's consider two trajectories, y and y_{kick} , given by

$$y(s) = M_{11} \cdot y(s_0) + M_{12} \cdot y'(s_0), \quad (5.9)$$

where the angular kick θ is defined as the difference in angle of both trajectories $\theta = y'_{\text{kick}} - y'$. We can then express the difference in trajectory as

$$y_{\text{kick}}(s) - y(s) = \Delta y = \theta \cdot \sqrt{\beta(s)\beta(s_0)} \sin \Delta\mu. \quad (5.10)$$

When the particles receive the crab cavity kick they are not traveling on the closed orbit given in Eq. (5.6), so they are mis-injected onto that new orbit. The resulting trajectory is given by Eq. (5.10), which averaged over many turns defines the closed orbit given in Eq. (5.6). We want to know if there is a case where both the trajectory and orbit have zero-crossing at a primary collimator. For this we consider only the terms dependent on the phase advance

$$\begin{aligned}
\cos(\pi\nu - \Delta\mu) &= 0 \quad \text{if} \quad \pi\nu - \Delta\mu = n\pi \\
\sin \Delta\mu &= 0 \quad \text{if} \quad \Delta\mu = (2n+1)\frac{\pi}{2}
\end{aligned} \tag{5.11}$$

where $n \in \mathbb{N}$,

from where

$$\pi\nu - (2n+1)\frac{\pi}{2} = n\pi \quad \rightarrow \quad \nu = 2n + \frac{\pi}{2}. \tag{5.12}$$

We can see from Eq. (5.12) that the only case where both trajectory and orbit have zero crossing at a given point is if the accelerator is working at the half-integer resonance, which is not foreseen for the LHC nor the HL-LHC due to beam instabilities. We can, therefore, conclude that the primary collimator is never completely avoided. The first few turns after the failure will be described by Eq. (5.10) creating some losses at the primary collimator, then averaging out to Eq. (5.6) and limiting the impacts the collimation system receives.

This effect can be observed in the failure case where the collimator hierarchy is broken, i.e. the phase jump in ATLAS for beam 2 (cases labeled PJ IP1 2CC and PS IP1 4CC). In these cases the orbit is minimum at the primary collimator, but grows at the location of the secondary collimator, as shown in the top right plot in Fig. 5.14. We can observe in Table 5.6 that the primary collimator receives an amount of impacts that is in the same order of magnitude of the ones received by the secondary collimator, showing that the primary is not avoided. We can also see in Table 5.5 that for beam 1, where the orbit has been distorted at the primary collimator, the primary receives a number of impacts two orders of magnitude higher compared to beam 2. In terms of fraction of beam intercepted by the collimation system, shown in Table 5.3, we can see a reduction of one order of magnitude for the broken hierarchy case, i.e. PJ IP1 4CC and PS IP1 4CC for beam 2. These results show that optimizing the phase advance between the crab cavities and the primary collimator such that the cosine term of the orbit distortion expression is minimal has the potential to significantly reduce the losses during a crab cavity phase failure. We can also see that the maximum of the orbit distortion happens at a secondary collimator, keeping the machine aperture protected. This will always be the case since secondary collimators in the LHC cover all phase advances. It should be ensured that the secondary collimators are robust enough to sustain this type of failure case.

The concept of optimizing the phase advance to avoid damage to the collimators has also been considered for other failure scenarios, such as the asynchronous beam dump [129]. This scenario has the potential to damage the tertiary collimators, which are not designed to absorb many particles.

In order to avoid damage, the phase advance is adjusted so that it misses the tertiary collimators. At the time this approach was proposed, there was no system that would ensure that the phase advance is stable and that it is kept in a safe regime. This is why a new interlocking layer that constrains changes in phase advance was put in place in 2016 [130], making phase advance optimization also a possibility for crab cavity failure mitigation.

5.4.3 *Impact on the experiments*

In Chapter 3 the possibility of damaging the experiments was raised due to the proximity of the crab cavities to the IPs and the opening of the physics debris shields, the TAN and TAS, which could have acted as passive protection during a failure. In the HL-LHC the tertiary collimators are the only limiting aperture standing between the crab cavities and the experiments for the incoming beam, as shown in Fig. 3.16. This means that in case of failure the tertiary collimator will act as a spoiler, scattering particles and creating showers in the direction of the experimental cavern. These showers have the potential to quench the magnets situated downstream, which can lead to the misteering of the beam and cause irreparable damage.

In order to assess the impact that the failures have on the tertiary collimators we can look at the number of proton impacts they receive before the beam is dumped from Tables 5.5 and 5.6. Considering that the damage limit for HL-LHC tertiary collimators at collision energy is estimated to be 1.2×10^{11} secondary proton impacts [131], we can see that only two failure scenarios surpass this limit: the phase slip of four crab cavities in IP5, for both beams. In particular, the case corresponding to beam 2 reaches 1.08×10^{12} impacts which surpasses the fragment ejection limit. From all the simulated failure scenarios, only this one could potentially pose a real threat to the experiments. As discussed in Section 5.2.3, the failure scenarios considered in this study are deliberately pessimistic. Notably, this particular scenario assumes a continuous maximum phase jump of four crab cavities simultaneously. While technically possible, it is a highly unlikely occurrence.

It was decided that a more realistic case, such as the failure of two crab cavities instead of four, would be chosen to perform a FLUKA [132, 133] simulation on the tertiary collimator. FLUKA is a general purpose tool for calculations of particle transport and interactions with matter. It is used at CERN through detailed 3D models of the components that make up the accelerator, being able to simulate entire beamlines. A FLUKA simulation was carried out based on the loss distribution predicted by SixTrack on the tertiary collimator. Knowing the position, angle, and energy of the particles that impacted the collimator, FLUKA can transport them through the jaw material and estimate the particle showers on the neighbouring magnets. The chosen failure scenario was a phase slip of two crab cavities instead of

four. At the time the simulation was made, only the data for failures in ATLAS and beam 1 existed. It was found that the maximum energy density deposited in the D1 coils from the particle shower was 7×10^{-10} mJ/cm³ per inelastic proton collision in the tertiary collimator. Assuming a transient quench level of a few 10 mJ/cm³, one can therefore expect a quench of the D1 if losses on the TCT would exceed a few 10^{10} protons. Since the number of impacts for this scenario is of the order of 10^7 it poses no risk for quenching or damaging downstream magnets, nor the experiments. It is important to note that these results cannot be scaled directly across different scenarios since the energy density deposited in the neighboring magnets depends on the distribution of the impacts in the tertiary collimator. This study was published in a conference paper, and can be found in Appendix E.3.

A similar study was performed in [134] for an asynchronous beam dump failure, which is considered to be more dangerous than a crab cavity failure. Asynchronous beam dump simulations in the HL-LHC show that the TCT in IP5 receives the impact of a full bunch or half a bunch in less than half a turn, unlike in a crab cavity failure where the number of impacts is distributed over approximately five turns. It was found that the peak energy density values in the triplet remained well below the damage limit, but quenches would happen in all investigated scenarios. The radiation leakage to the experiments changed by one order of magnitude depending on the TCT material, which has not yet been selected. The selection of the TCT material should minimize damage to both the experiments and the TCT itself, which is why an intermediate density option, copper-diamond, is currently being considered.

On the other hand, tests on the ATLAS silicon detectors have been recently performed in the High-Radiation to Materials (HiRadMat) facility to test the survival of the detector in case of accidental beam losses [135]. It was found that the damage threshold is substantially higher than the lower limit published in 2006 and that many others aspects have to be taken into account before claiming that the ATLAS detector is safe.

In conclusion, many components of the HL-LHC are still in the design and construction phase and further studies are needed from the detector side and from collimation to realistically estimate the damage to the experiments.

5.5 *Summary and discussion*

The data presented in this chapter corresponds to simulations of different crab cavity failure scenarios, namely a sudden voltage decay caused by a power source failure and two different types of phase jump coming from the malfunction of the LLRF or human error. We calculated the maximum phase jump per turn taking into account the available source power and the cavity parameters, which was later used in the simulations. We considered that two or four crab cavities would fail simultaneously, which is equivalent to a total voltage of 6.8 MV and 13.6 MV respectively.

The results showed extremely high losses for the phase-related failures of four crab cavities, especially for the phase slip case. These losses have the potential to damage the primary, secondary and tertiary collimators, as well as creating showers in the tertiary important enough to quench the magnets downstream. Nevertheless, a phase slip is a very unlikely scenario since it implies the crab cavity phase changing by its maximum per turn, every turn. Localized phase jumps also have the potential of creating considerable losses, but only for the failure of four crab cavities simultaneously. In the case of only two crab cavities failing, some of the losses are comparable to the ones created by a sudden voltage decay. We showed that the losses in phase-related failures happen extremely fast and that the collimation system will be exposed to uncontrollable losses for at least five turns. The losses related to voltage decay failures happened in a more steady way and were less important, making them manageable by the machine protection system. The difference in damage potential between the phase and voltage failure scenarios comes from the fact that during a phase jump the beam is transversely kicked. In some cases, this causes the collimation system to start intercepting particles from the bunch core, which is much more densely populated than the halo. The losses from a voltage decay scenario come exclusively from the halo, which suggests that the losses from this type of failure could be reduced through a halo depleting method such as the hollow electron lens.

We found that the number of particles intercepted by the collimator system varied considerably depending on the beam and IP simulated in the phase-related failures. This was explained by a different orbit distortion for each case due to the different phase advances between crab cavity and primary collimator. In particular, we observed that a favorable phase advance can reduce the number of impacts in the most hit primary collimator by two orders of magnitude. This led to the proposal of phase advance optimization as a mitigation technique. We proved that despite implementing a phase advance such that the orbit distortion is minimal at the primary collimator, the primary will never be completely avoided. Additionally, the maximum of the orbit distortion will always happen at a secondary collimator, keeping

the machine aperture protected.

From these results, we can conclude that most crab cavity failures are survivable and manageable. The failure that was found to have the potential of inducing irreparable damage to the machine, namely a phase slip of four crab cavities, is a worst-case scenario that should be reliably avoided by the LLRF system. In general, the simultaneous failure of crab cavities should be strictly avoided by the Low Level RF (LLRF) system. Since the importance of the failures is directly related to the total voltage of the crab cavity set-up, reducing the voltage per crab cavity would also serve as mitigation.

Other failures such as crab cavity quenches have also been recently studied in [119], where the computing tools developed in the context of this thesis were used. Combined failure scenarios are also a concern and should be studied in the future. In such a scenario a crab cavity failure would be induced by another, independent failure. One example is the simultaneous quench of crab cavities from particle showers happening nearby.

To conclude, it is worth mentioning that the results presented here depend on many factors such as the optics used, the collimator opening, the weight of the tails of the particle distribution, the total voltage of the cavity system, the Q factor of the cavities, the available power, etc. The study provides a detailed reference for future studies that would need to take crab cavity failures into account. In particular, this study can be a guide for future machine protection studies to define the new interlock system for the HL-LHC and for a possible phase advance locking strategy between crab cavities and primary collimators.

Chapter No.6

Summary, conclusion, and outlook

The HL-LHC is a new configuration of the LHC that will push the limits of accelerator technology to increase the total number of produced collisions by a factor of 10 compared to the current LHC. This will allow gathering an unprecedented data sample that will be key to tackle some of the most important open questions in particle physics. The integrated luminosity, i.e. the quantity of data gathered in the lifetime of the collider, depends on how much time the beams are colliding and the experiments recording data, also called *physics availability*. The challenging goal of reaching 3000 fb^{-1} of integrated luminosity in the HL-LHC is based on the assumption of stable operation and very good physics availability during the lifetime of the project. This is why even a small increase in failure rates could negatively affect the physics research programmes and the ultimate HL-LHC goal.

One of the innovative technologies introduced in the HL-LHC is crab cavities. Crab cavities are devices designed to transversely rotate the beam and help increase the rate at which collisions happen. They have only been used in one e^+e^- collider so far, under conditions very different from the ones of the HL-LHC. Moreover, the HL-LHC crab cavities have been redesigned to be more compact and fit the available space in the LHC tunnel, and the prototypes have never been tested in operating conditions. Additionally, crab cavity failures can be very fast and have the potential of kicking the beam core, leaving the collimators as the only protection from beam losses until the beam is dumped. These new failure scenarios are hard to cover by the current machine protection system, which motivates the detailed study of this topic.

The timescale of this large project is such that crucial decisions related to the configuration of the accelerator have to be determined with simulations based on optics models, well before the actual HL-LHC is built. By the time of writing this thesis, the LHC has been successfully operating at full energy for eight years and the optics of the machine are very well understood, demonstrated by the accuracy achieved in optics measurements and corrections [136]. Optics models are used as input by several simulation tools to carry out advanced simulations, such as MAD-X and SixTrack. These programs have been extensively used to simulate the LHC, and are now also being used to simulate future machines such as the HL-LHC. SixTrack not only allows tracking particles in the HL-LHC lattice but also to simulate the interaction of particles with the collimator system, making it the perfect tool to study particle losses from crab cavity failures in the HL-LHC. Nevertheless, in order to simulate the dynamic change in parameters that happens during a failure a new feature needed to be developed. This new feature called the DYNK (DYNamic Kick) module was developed in the context of this thesis and became a standardized tool for the simulation of failure scenarios.

Different crab cavity failures were studied and narrowed down to a power source failure and a malfunction of the Low Level RF (LLRF) system, where the wrong phase is fed to the crab cavity. An estimation of the maximum possible phase change per turn based on the available power was done and used as input for the simulations. The voltage and phase-related failures were simulated separately to better observe the effects each one would have on the beam. Effects that involve the interaction of the electromagnetic fields of the cavity with the physical structure of the cavity, such as the Lorentz force detuning, were neglected. This is because the mechanical deformation of the cavity happens at a slower rate and this study focuses on ultrafast failures that can challenge the machine protection system. Additionally, beam loading effects were considered to be negligible, as found in a recent study done by another team with the same tools [119].

Collimation studies were carried out with SixTrack on 24 different failure scenarios. These include voltage decay, phase jump, and phase slip scenarios on two and four crab cavities around the high luminosity experiments (ATLAS and CMS), for both beams (beam 1 and beam 2). A phase jump consists of a sudden change in phase happening in one turn and maintained constant, while a phase slip is a change in phase happening every turn. In both cases the phase changes by its maximum per turn. A double Gaussian particle distribution was used to account for the tails observed in the LHC profile measurements [120]. The results showed that the losses in phase-related failures happen extremely fast and that the collimation system will be exposed to uncontrollable losses for at least five turns. The losses related to voltage decay failures happened in a more steady way and were less important, mak-

ing them manageable by the machine protection system. Very high losses were observed for the phase-related failures of four crab cavities, especially for the phase slip case. This is due to the fact that the collimation system starts intercepting particles from the beam core. These losses have the potential to damage the primary, secondary and tertiary collimators, as well as creating showers in the tertiary important enough to quench the magnets downstream. Localized phase jumps also have the potential of creating considerable losses, but only for the failure of four crab cavities simultaneously. In the case of only two crab cavities failing, some of the losses are comparable to the ones created by a sudden voltage decay, which is manageable by the machine protection system. We found that the number of particles intercepted by the collimator system varied considerably depending on the beam and IP simulated in the phase-related failures. This was explained by a different orbit distortion for each case due to the different phase advances between crab cavity and primary collimator. In particular, we observed that a favorable phase advance can reduce the number of impacts in the most hit primary collimator by two orders of magnitude. This led to the proposal of phase advance optimization as a mitigation technique. We have shown that despite implementing a phase advance such that the orbit distortion is minimal at the primary collimator, the primary will never be completely avoided. Additionally, the maximum of the orbit distortion will always happen at a secondary collimator, which leaves the machine aperture protected.

The impact of a selected crab cavity failure on the experiments was investigated through FLUKA simulations [137]. Similar studies were performed by another team on asynchronous beam dump failure cases [134], a scenario in which the losses happen faster than in crab cavity failures. It is, therefore, considered to be more dangerous for the experiments. The study found an order of magnitude difference in radiation leakage to the experiments depending on the material of the TCT collimator, which has not yet been downselected. Moreover, recent radiation tests on ATLAS silicon detectors [135] showed a considerably higher threshold than other tests done in the past, suggesting that further tests are needed.

The work presented in this thesis is the first study to have simulated in detail a variety of crab cavity failure scenarios at different voltages for both high luminosity experiments and both beams with a full particle distribution. In particular, it has allowed identifying which crab cavity failure cases are a limit for the current machine protection system. These corner cases could technically happen but are extremely pessimistic. The worst cases happened for a total crab cavity voltage of 13.6 MV, the equivalent of four crab cavities failing simultaneously, and a maximum phase shift per turn. This scenario can be very easily avoided with the correct interlocks on the crab cavity phase and a reduction of the total voltage. It was also found that the beam losses from any crab cavity failure can increase considerably

due to a disadvantageous phase advance between the crab cavities and the primary collimators. A complete machine protection strategy would, therefore, include both prevention by interlocking and mitigation with an optimal phase advance.

It is important to note that even if the LLRF system does not malfunction in any way, other failures can also trigger crab cavity failures. For example, the presence of micrometer-sized dust particles in the beampipe has been observed in the LHC [138], creating very fast beam losses. Any such event happening near the crab cavities can create particle showers capable of quenching two crab cavities in the same cryomodule. Further study of the impact of correlated failure scenarios is therefore recommended. Additionally, the phase advance locking between the crab cavities and the primary collimators should be studied in detail, as it would significantly reduce the beam losses in case of crab cavity failures.

In conclusion, this study serves as a quantitative reference for crab cavity failures and as a guide for further improvements.

Appendix A

Modes in a cylindrical cavity

Radiofrequency cavities can resonate at an infinite number of frequencies or modes. The shape of a cavity is tailored such that they mainly work at a certain resonant mode or *fundamental mode*, damping the rest of the modes that could be excited by the beam. The chosen fundamental mode depends on the function of the cavity in the machine, which can range from accelerating the beam to shaping bunches longitudinally or simply tilting them. Regardless of the shape of the cavity the resonant modes can be classified into different groups, which are used to label and identify different types of cavities.

Let's consider that the waves in a cavity propagate only along the longitudinal direction z . Remembering that the electric (\vec{E}) and magnetic (\vec{H}) fields are always perpendicular to each other in space and time, we find two independent types of solution to Maxwell's equations called the *transverse magnetic modes* (TM) and the *transverse electric modes* (TE) [84, Chapter 2, Section 1], where:

Transverse magnetic : a longitudinal component of \vec{E} exists, while \vec{H} is transverse everywhere (with respect to the z axis, i.e. $H_z = 0$).

Transverse electric : a longitudinal component of \vec{H} exists, while \vec{E} is transverse everywhere (with respect to the z axis, i.e. $E_z = 0$).

To better understand the different resonant modes, let's consider a simple case such as a cylindrical cavity of length l_0 and radius r_0 . As previously mentioned, we can express the spatial and temporal variations of the electric and magnetic fields as standing waves

$$\begin{aligned} E(r, \theta, z, t) &= E(r, \theta) e^{i(kz - \omega t)} \\ H(r, \theta, z, t) &= H(r, \theta) e^{i(kz - \omega t)}, \end{aligned} \tag{A.1}$$

where (r, θ, z) are the cylindrical coordinates, k the wave number, and ω the angular frequency. In order to calculate the electric fields we consider the wave equation, derived from Maxwell's equations, in cylindrical coordinates:

$$\frac{\partial^2 E_z}{\partial z^2} + \frac{1}{r} \frac{\partial E_z}{\partial r} + \frac{1}{r^2} \frac{\partial^2 E_z}{\partial \theta^2} + \frac{\partial^2 E_z}{\partial r^2} - \frac{1}{c^2} \frac{\partial^2 E_z}{\partial t^2} = 0. \quad (\text{A.2})$$

Separating the space and time contributions in Eq. (A.1), and considering an azimuthally symmetric field (no variations in θ), we obtain the following trial solution:

$$E_z(r, z, t) = R(r) e^{-i\omega t}. \quad (\text{A.3})$$

Substituting the trial solution A.3 in Eq. (A.2) we obtain

$$\frac{\partial^2 R(r)}{\partial r^2} + \frac{1}{r} \frac{\partial R(r)}{\partial r} + \frac{\omega^2}{c^2} R(r) = 0, \quad (\text{A.4})$$

which is a Bessel equation of order 0. We can find the magnetic field using Ampère's law, yielding a Bessel equation of order 1. Since we deal with second order differential equations there are two linearly independent solutions, which are the Bessel functions of first J_n and second kind Y_n . However, the Bessel functions of the second kind have a singularity at the origin, resulting in non-physical solutions.

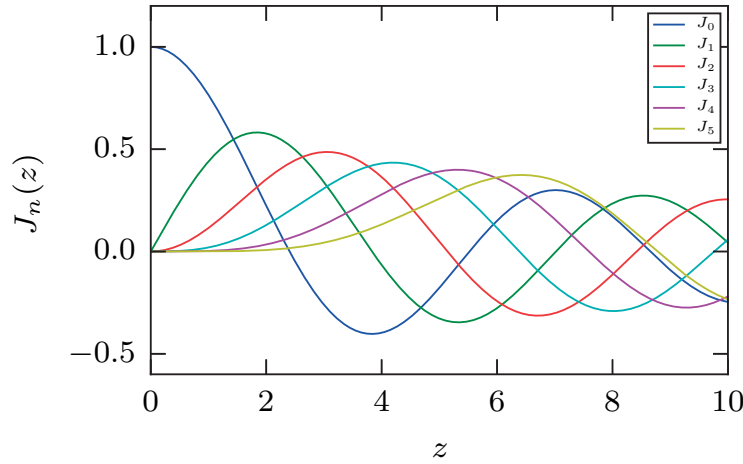


Figure A.1. The first 5 Bessel functions of the first kind.

We can then simply express the radial part of the solution as a Bessel function of the first kind

$$\begin{aligned} E_z &= E_0 J_n(k_{nm}r) e^{i(n\theta + kz - \omega t)} \\ B_z &= B_0 J_n(k_{nm}r) e^{i(n\theta + kz - \omega t)}, \end{aligned} \quad (\text{A.5})$$

where E_0 and B_0 are the amplitude of the fields. According to Maxwell's equations, the electric field is perpendicular to the surface of a conductor, whereas the magnetic field must be parallel to the surface. On the other hand, outside of the cylinder itself, both fields must be zero. Combining both, we can deduce the boundary conditions for each case at the cylindrical boundary $r = r_0$:

$$\begin{aligned} E_z &= 0 && \text{TM modes} \\ \frac{\partial B_z}{\partial r} &= 0 && \text{TE modes} . \end{aligned} \quad (\text{A.6})$$

Applying the boundary conditions given by Eq. (A.6) to Eq. (A.5) we can see that $J_n(k_{mn}r_0) = 0$ satisfies the equation for the TM modes and $J'_n(k_{mn}r_0) = 0$ for the TE modes. The wave number k_{mn} can then be expressed as

$$k_{mn} = \begin{cases} \frac{z_{mn}}{r_0} & \text{TM modes} \\ \frac{z'_{mn}}{r_0} & \text{TE modes} \end{cases} , \quad (\text{A.7})$$

where z_{mn} is the n^{th} zero of the m^{th} Bessel function and z'_{mn} is the n^{th} zero of the derivative of the m^{th} Bessel function. The longitudinal wavenumber k_z can be obtained in a similar way by assuming a sinusoidal form for the longitudinal solution and applying the boundary conditions at the end of the cylinder

$$k_z = \frac{p\pi}{l_0} , \quad (\text{A.8})$$

where l_0 is the length of the cavity and p is an integer. Remembering the dispersion relation

$$k^2 = \frac{\omega^2}{c^2} = k_{mn}^2 + k_z^2 , \quad (\text{A.9})$$

we can derive the resonant frequencies for each set of eigenmodes

$$\omega_{mnp} = \begin{cases} c \sqrt{\left(\frac{z_{mn}}{r_0}\right)^2 + \left(\frac{p\pi}{l_0}\right)^2} & \text{TM modes} \\ c \sqrt{\left(\frac{z'_{mn}}{r_0}\right)^2 + \left(\frac{p\pi}{l_0}\right)^2} & \text{TE modes} \end{cases} , \quad (\text{A.10})$$

where the indices m, n and p correspond to different azimuthal θ , radial r , and longitudinal z solutions:

m : represents the number of full period variations in θ of the field components.

$m = 0$: corresponds to the *monopole mode*. These modes accelerate and decelerate the beam.

$m = 1$: corresponds to the *dipole mode*. These modes are the only ones that can kick the beam transversely and have a distinct polarization, the field points in a given direction and the kick is in one plane.

$m = 2$: corresponds to the *quadrupole mode*. They can also kick the beam, but they are weak near the axis.

n : represents the number of zeros in the axial field component in the radial direction, in the range $0 < r \leq a$ (excluding $r = 0$).

p : represents the number of half period variations in z of the field components.

As previously mentioned, we can see from Eq. (A.10) that cavities have an infinite number of eigenmodes or resonant frequencies.

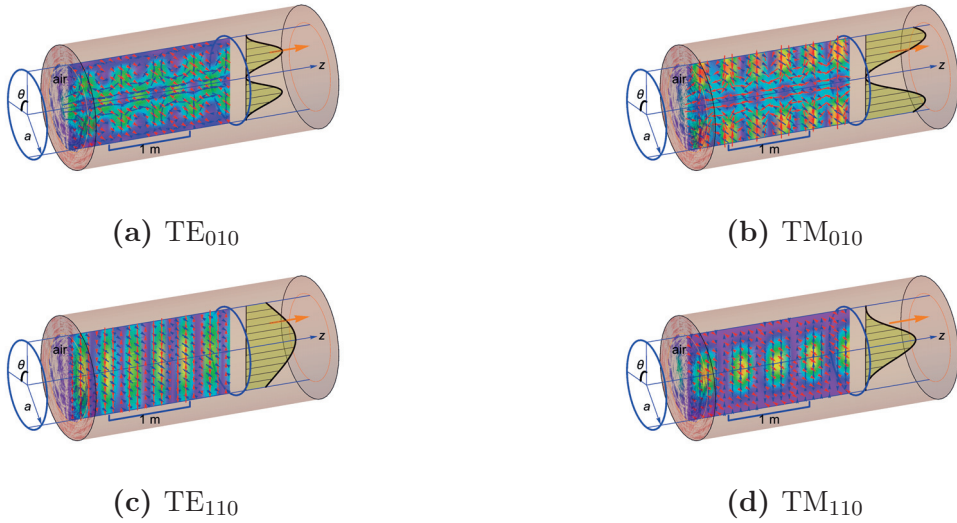


Figure A.2. Different magnetic and electric transverse modes in a cylindrical cavity with a radius of 0.5 m at a frequency of 0.5 GHz. The red arrows represent the \vec{E} field, while the blue ones represent the \vec{H} field. The Poynting vector is shown in orange [139].

Other cavities, such as crab cavities, have often a more complex geometry. Their modes are not purely TE or TM but rather “TE-like” or “TM-like”, since the corresponding fields are not strictly transverse at every point. Apart from these two modes, a third mode exists called the *transverse electric and magnetic mode* (TEM), where both \vec{E} and \vec{H} are transverse everywhere.

Appendix B

Beam loading and the lumped circuit model

The cavity-beam system can be approximated by a resonant circuit (RLC circuit), which allows deriving easily cavity-related expressions.

B.1 Beam loading

The beam is composed of equidistant, ultrarelativistic bunches that traverse the cavity at a certain rate. Since the speed of the particles barely changes when passing through the cavity, the beam can be considered a time-dependent current. In other words, the beam behaves as an RF source that is capable of exciting the fundamental mode of the cavity and other modes. After the passage of the beam through the cavity, a beam-induced voltage remains in each cavity mode, exciting the fields of different resonant modes.

Depending on the beam offset with respect to the center of the cavity the beam can interfere constructively or destructively with the beam-induced field, also called *wakefield*. This means that the beam has the potential of draining or transmitting energy to the cavity. In both cases, the RF source can compensate for the energy disequilibrium by providing more or less power, within the limits of the power supply. We call this interaction of the beam with the cavity *beam loading*.

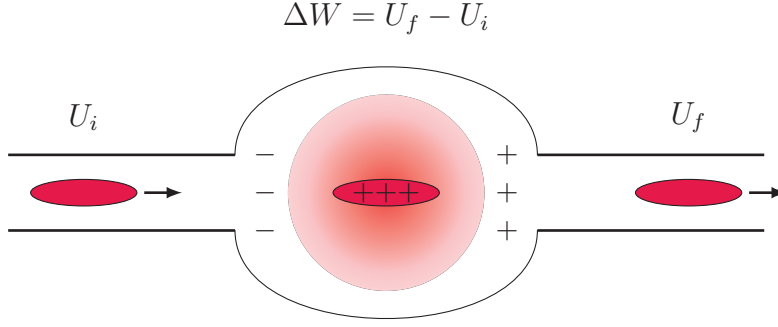


Figure B.1. A positively charged bunch passing through a cavity. As the bunch passes it leaves a negative image current at the upstream end of the cavity gap. By charge conservation a positive image current is created downstream of the cavity gap, generating an electric field and, therefore, a beam-induced voltage. The energy change in the cavity ΔW is equal to the energy variation in the bunch.

B.2 The lumped circuit model

The resonant mode of a beam-loaded cavity can be modeled by a parallel RLC circuit. An RLC circuit acts as a harmonic oscillator for current, where the damping is introduced by the presence of a resistance, as shown in Fig. B.2. The oscillations in the electric field are represented by the charge in the capacitor, and the oscillations in the magnetic field by the current flowing through the inductor. The energy is transferred from the capacitor to the inductor and vice versa, mimicking the oscillatory behavior of the system's stored energy as described in Eq 4.1.

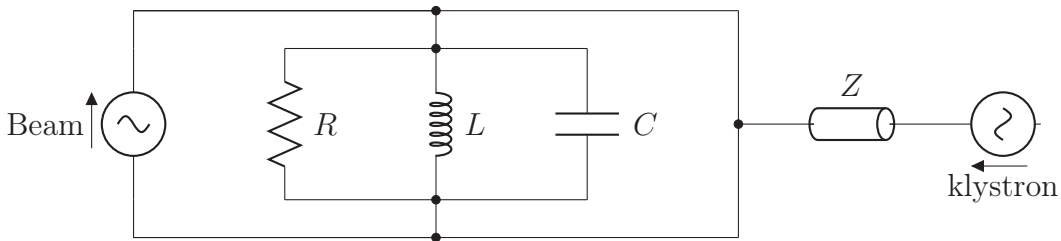


Figure B.2. A circuit model of a beam loaded cavity, where the *klystron* is the source of radio waves, the input coupler is represented by a transmitter of impedance Z , and the cavity resonator by an RLC circuit. The beam is represented by a source of current.

In this circuit the resonant frequency ω_0 and the quality factor Q can be expressed as a function of the resistance R , inductance L , and capacitance C :

$$\omega_0 = \frac{1}{\sqrt{LC}} \quad ; \quad Q = \frac{1}{R} \sqrt{\frac{L}{C}}. \quad (\text{B.1})$$

Capacitors and inductors introduce $\pm 90^\circ$ changes in phase, which allows us to model the behavior of EM fields. It is customary to account for this phase change by adding an imaginary part to the circuit parameters: voltage, resistance, and current. In the case of the voltage, we can rewrite Eq. 4.28 as

$$V(t) = V_0 \cos(\omega t + \phi_V) + i \sin(\omega t + \phi_V) = V_0 e^{i(\omega t + \phi_V)}, \quad (\text{B.2})$$

where the physical voltage is the real part of the equation. In the same way, one can express the current as $I = I_0 e^{i(\omega t + \phi_I)}$. Following the superposition principle we can express the net cavity voltage as the sum of the RF generator voltage V_g and the beam-induced voltage V_b :

$$V = V_g + V_b. \quad (\text{B.3})$$

The concept of resistance, as understood for Direct Current (DC) circuits, needs to also be extended for Alternating Current (AC) circuits. *Impedance* acts as a resistance in AC circuits, having the properties of magnitude and phase instead of just magnitude. It can, therefore, be also expressed as a complex quantity.

All the passive elements of the RLC circuit sketched in Fig. B.2, i.e. anything that is not a current source, can be treated as an impedance

$$\begin{aligned} \text{Resistor:} \quad & Z_R = R \\ \text{Capacitor:} \quad & Z_C = 1/i\omega C \quad , \\ \text{Inductor:} \quad & Z_L = i\omega L \end{aligned} \quad (\text{B.4})$$

where the total impedance of the system can be expressed by Ohm's law for parallel resistors:

$$\frac{1}{Z} = \frac{1}{Z_R} + \frac{1}{Z_C} + \frac{1}{Z_L}. \quad (\text{B.5})$$

In cavity modelizations, the resistance R of the RLC circuit is called the *shunt impedance* and it represents the surface resistance of the cavity walls, defined as

$$R = \frac{V^2}{P}, \quad (\text{B.6})$$

where V is the cavity voltage and P is the power dissipated through the cavity walls. Considering Eq. 4.14, we can express the shunt impedance also

as "R upon Q", which is a purely geometric quantity of a given cavity:

$$\frac{R}{Q} = \frac{V^2}{\omega U}. \quad (\text{B.7})$$

In general, we can interpret the impedance of the circuit as the strength in which the resonant mode of the cavity interacts with the charged particles of the beam.

Appendix C

Crab cavity and collimator configuration

This appendix includes the optics details of the crab cavities and collimators used in the simulations presented in this thesis.

Table C.1. Position, phase advance, Twiss parameters and dispersion for the crab cavities used in the simulations.

Name	s [m]	μ_x (2π)	μ_y (2π)	β_x [m]	β_y [m]	α_x [m]	α_y [m]	D_x [m]
ACFCA.AR1.B1	154.82	0.2521	0.2521	4184.76	3735.1	58.84	19.98	0.39
ACFCA.BR1.B1	155.87	0.2521	0.2521	4062.1	3693.27	57.97	19.86	0.39
ACFCA.CR1.B1	162.26	0.2524	0.2524	3354.99	3443.79	52.69	19.18	0.36
ACFCA.DR1.B1	163.31	0.2524	0.2524	3245.26	3403.63	51.82	19.07	0.36
ACFCA.AL5.B1	13170.65	30.8478	29.6954	3606.02	3777.01	-19.69	-56.12	0.55
ACFCA.BL5.B1	13169.6	30.8477	29.6954	3564.79	3660.08	-19.58	-55.24	0.54
ACFCA.CL5.B1	13163.21	30.8474	29.6951	3318.99	2988.14	-18.89	-49.91	0.52
ACFCA.DL5.B1	13162.16	30.8474	29.695	3279.44	2884.24	-18.78	-49.04	0.51
ACFCA.AR5.B1	13484.11	31.3516	30.1992	4224.81	3751.9	59.41	20.07	0.66
ACFCA.BR5.B1	13485.16	31.3516	30.1993	4100.97	3709.88	58.53	19.95	0.65
ACFCA.CR5.B1	13491.55	31.3519	30.1996	3387.07	3459.29	53.19	19.26	0.59
ACFCA.DR5.B1	13492.6	31.352	30.1996	3276.28	3418.95	52.31	19.15	0.58
ACFCA.AL1.B1	26500.25	62.0584	60.0683	3571.45	3760.15	-19.5	-55.87	0.36
ACFCA.BL1.B1	26499.2	62.0583	60.0682	3530.61	3643.74	-19.39	-55.0	0.36
ACFCA.CL1.B1	26492.81	62.058	60.0679	3287.14	2974.81	-18.71	-49.69	0.35
ACFCA.DL1.B1	26491.76	62.058	60.0678	3247.97	2871.37	-18.6	-48.82	0.34
ACFCA.AL1.B2	154.82	0.251	0.2527	4175.75	3729.77	58.72	19.94	0.72
ACFCA.BL1.B2	155.87	0.251	0.2527	4053.34	3688.01	57.86	19.83	0.72
ACFCA.CL1.B2	162.26	0.2513	0.253	3347.68	3438.94	52.58	19.15	0.66
ACFCA.DL1.B2	163.31	0.2513	0.253	3238.18	3398.84	51.71	19.04	0.65
ACFCA.AR5.B2	13170.65	30.9567	30.121	3611.47	3772.48	-19.71	-56.06	0.31
ACFCA.BR5.B2	13169.6	30.9567	30.121	3570.19	3655.68	-19.6	-55.18	0.3
ACFCA.CR5.B2	13163.21	30.9564	30.1207	3324.08	2984.5	-18.91	-49.86	0.28
ACFCA.DR5.B2	13162.16	30.9563	30.1206	3284.49	2880.72	-18.8	-48.98	0.28
ACFCA.AL5.B2	13484.11	31.4605	30.6248	4230.05	3748.22	59.49	20.04	0.4
ACFCA.BL5.B2	13485.16	31.4606	30.6249	4106.05	3706.25	58.61	19.93	0.4
ACFCA.CL5.B2	13491.55	31.4608	30.6252	3391.19	3455.96	53.26	19.24	0.36
ACFCA.DL5.B2	13492.6	31.4609	30.6252	3280.27	3415.67	52.38	19.13	0.36
ACFCA.AR1.B2	26500.25	62.0571	60.0688	3564.95	3754.1	-19.46	-55.78	0.67
ACFCA.BR1.B2	26499.2	62.0571	60.0687	3524.2	3637.88	-19.35	-54.91	0.67
ACFCA.CR1.B2	26492.81	62.0568	60.0684	3281.26	2969.98	-18.67	-49.61	0.65
ACFCA.DR1.B2	26491.76	62.0567	60.0684	3242.17	2866.7	-18.56	-48.74	0.64

Table C.2. Position, phase advance, Twiss parameters and dispersion for the primary and secondary collimators in IR7.

Name	s [m]	μ_x (2π)	μ_y (2π)	β_x [m]	β_y [m]	α_x [m]	α_y [m]	D_x [m]
TCP.D6L7.B1	19789.18	45.9761	44.2964	158.42	78.5	2.12	-1.1	0.52
TCP.C6L7.B1	19791.18	45.9782	44.3004	150.09	83.01	2.05	-1.15	0.5
TCP.B6L7.B1	19793.18	45.9804	44.3041	142.03	87.74	1.98	-1.21	0.49
TCSG.A6L7.B1	19832.68	46.0685	44.3492	39.7	227.26	0.61	-2.32	0.21
TCSG.B5L7.B1	19891.91	46.2788	44.3846	160.72	166.52	-3.13	2.67	0.16
TCSG.A5L7.B1	19895.91	46.2825	44.3887	186.82	145.91	-3.4	2.48	0.18
TCSG.D4L7.B1	19917.24	46.2957	44.424	334.47	68.76	-2.02	0.9	0.3
TCSG.B4L7.B1	19987.16	46.3415	44.5799	140.3	130.71	1.44	-1.25	0.31
TCSG.A4L7.B1	19991.16	46.3462	44.5846	129.15	141.01	1.35	-1.33	0.31
TCSG.A4R7.B1	19995.16	46.3513	44.589	118.7	151.94	1.26	-1.4	0.31
TCSG.B5R7.B1	20086.42	46.5777	44.6427	121.34	267.65	-2.42	3.89	0.36
TCSG.D5R7.B1	20102.42	46.5935	44.655	213.07	158.68	-3.32	2.92	0.44
TCSG.E5R7.B1	20106.42	46.5963	44.6594	240.51	136.25	-3.54	2.68	0.46
TCSG.6R7.B1	20141.02	46.6132	44.7414	334.72	47.51	2.82	0.02	0.49
TCP.D6R7.B2	6459.74	15.8914	15.1642	159.44	78.4	2.12	-1.1	0.02
TCP.C6R7.B2	6461.74	15.8934	15.1681	151.09	82.9	2.05	-1.15	0.02
TCP.B6R7.B2	6463.74	15.8956	15.1719	143.02	87.62	1.98	-1.21	0.02
TCSG.A6R7.B2	6503.24	15.9828	15.2171	40.18	226.86	0.62	-2.32	0.05
TCSG.B5R7.B2	6562.46	16.1928	15.2526	158.89	166.24	-3.09	2.67	0.12
TCSG.A5R7.B2	6566.46	16.1966	15.2567	184.65	145.67	-3.35	2.47	0.12
TCSG.D4R7.B2	6587.79	16.2099	15.2919	330.43	68.67	-2.0	0.9	0.16
TCSG.B4R7.B2	6653.72	16.2518	15.4428	150.41	121.23	1.5	-1.17	0.08
TCSG.A4R7.B2	6657.72	16.2562	15.4479	138.73	130.93	1.42	-1.25	0.07
TCSG.A4L7.B2	6673.72	16.278	15.4647	98.96	175.97	1.07	-1.56	0.05
TCSG.B5L7.B2	6756.98	16.4918	15.5105	122.8	268.1	-2.44	3.89	0.09
TCSG.D5L7.B2	6772.98	16.5075	15.5228	215.45	158.92	-3.35	2.93	0.13
TCSG.E5L7.B2	6776.98	16.5103	15.5272	243.15	136.45	-3.58	2.69	0.14
TCSG.6L7.B2	6811.58	16.5269	15.6091	337.92	47.51	2.86	0.02	0.18

Appendix D

SixTrack flowcharts

This appendix shows the general program flow of SixTrack with the DYNK module, described in Section 5.1.1, as well as a more detailed program flow when running one of the main subroutines. The file flow between SixTrack output and the collimation post-processing programs is also shown.

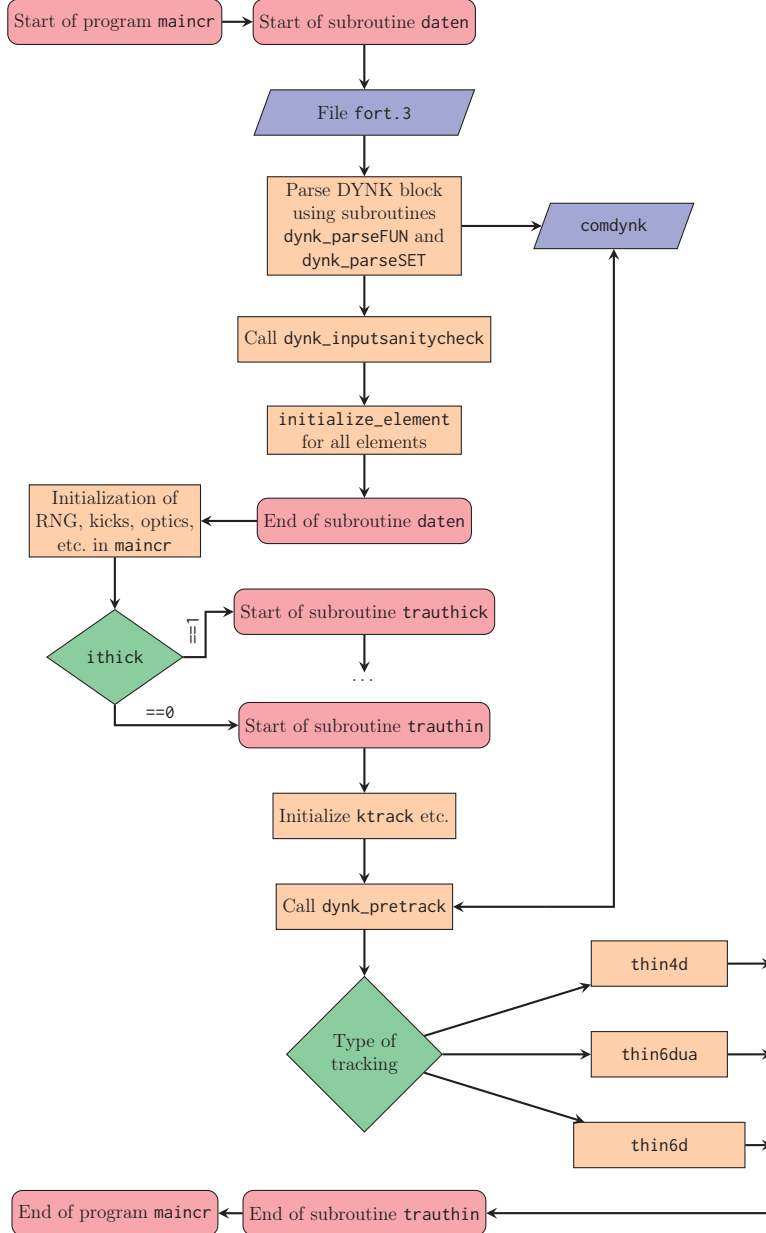


Figure D.1. Program flow in SixTrack with DYNK, where `comdynk` contains all the variables needed for DYNK to run. A more detailed description can be found in [110]. The `thin6d` subroutine is further described in Fig. D.2

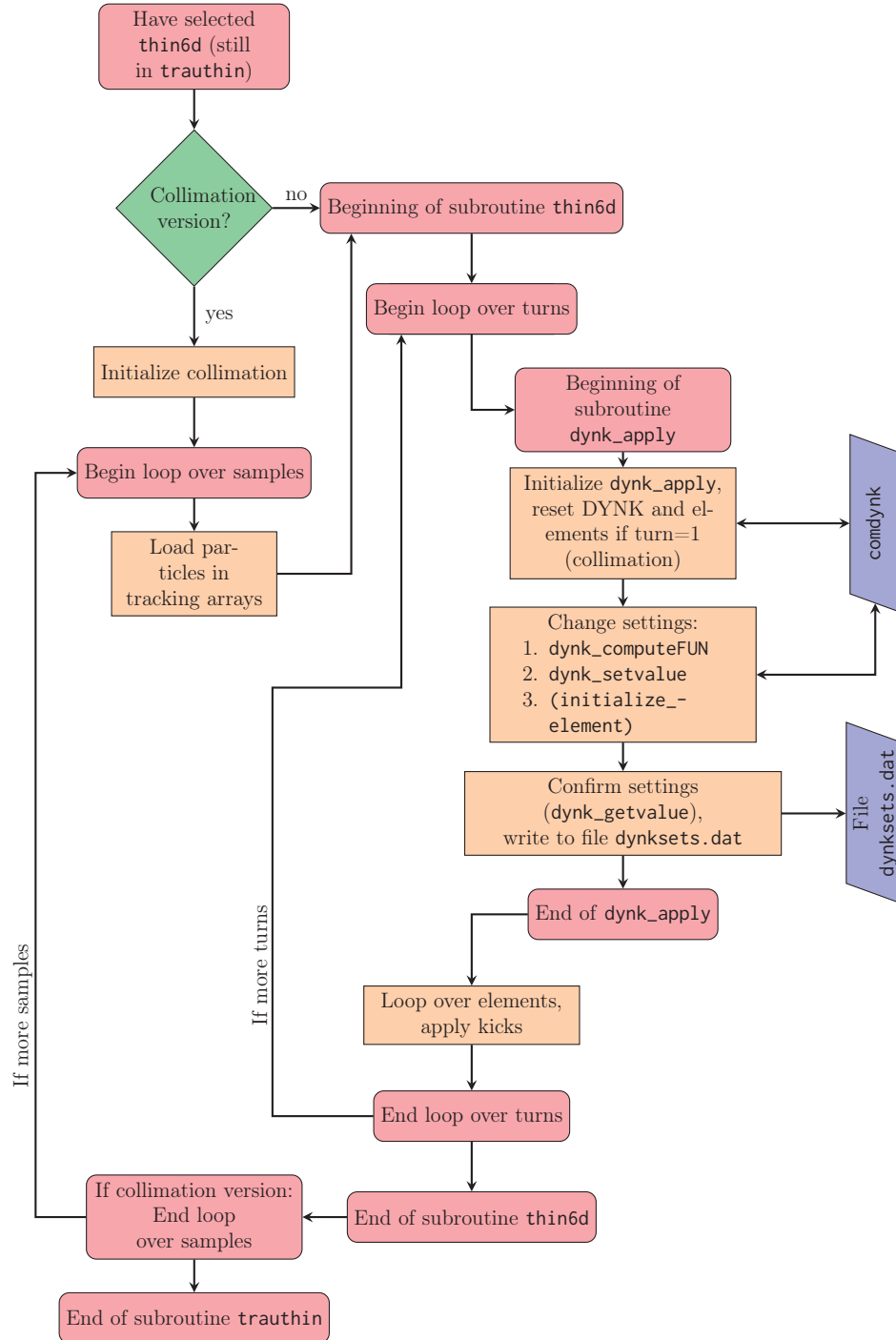


Figure D.2. Details of program flow when running subroutine `thin6d` [110].

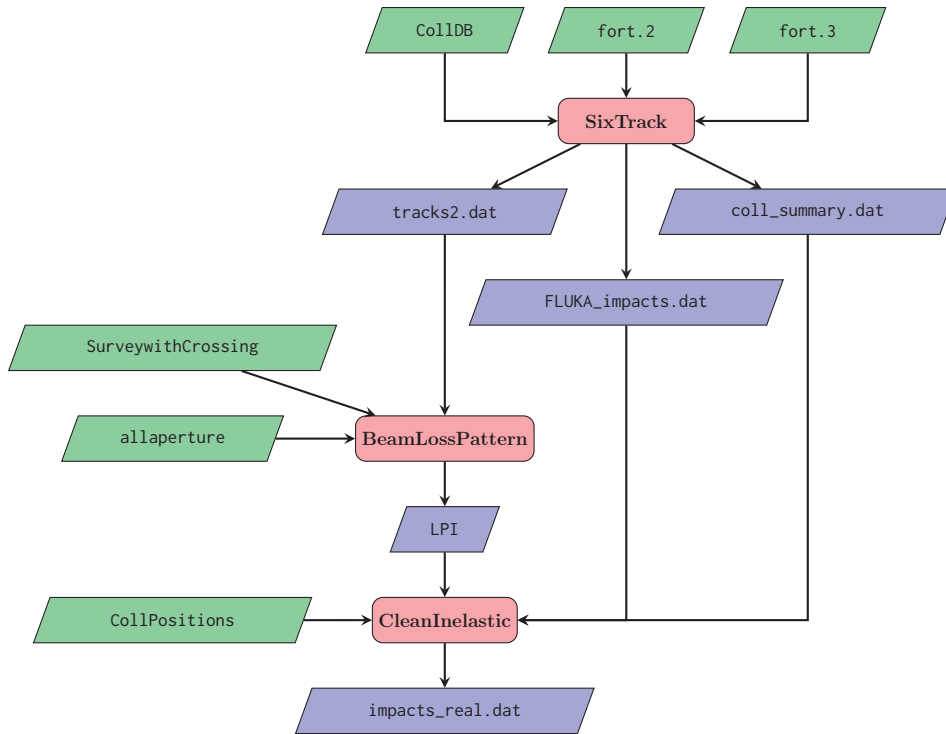


Figure D.3. Collimation version of SixTrack and collimation post-processing file flow chart. The green nodes represent external input files while the blue ones represent the relevant files produced in the process.

The files defined in Fig. D.3 are:

CollDB collimation database that contains the name of the installed collimators, their opening, material, length, orientation, offset and beta functions at their location.

fort.2 lattice file produced by MAD-X from the official optics files. Contains the different accelerator thin elements that form the lattice in order of appearance and the values of their attributes. The point chosen for the beginning of the lattice is the starting point of the simulation.

fort.3 simulation settings file. It contains the number of simulated turns, beam characteristics and additional blocks like DYNK, DUMP, BEAM BEAM or COLLIMATION.

tracks2.dat contains the coordinates of all the particles that interacted with a collimator (elastically or inelastically) and at which turn.

FLUKA_impacts.dat contains the coordinates of the particles that interacted only inelastically with a collimator and at which turn.

coll_summary.dat file containing a summary of the hits received by each collimator, divided in total interactions and inelastic interactions.

SurveywithCrossing file containing orbit offsets as a function of the longitudinal coordinate along the accelerator. This file is needed due to the separation dipoles D1, D2, D3 and D4 where the orbit does not pass through the aperture center of the magnets.

allaperture file generated by MAD-X containing the aperture for each accelerator element.

LPI file containing the location of the particles lost in the aperture and the number of turns before being lost.

CollPositions file containing the longitudinal position of each collimator.

impacts_real.dat file containing the coordinates of the particles that interacted inelastically with a collimator and at which turn after removing the particles that should have been lost in the aperture during the SixTrack simulation. This file serves as input for energy deposition studies.

Appendix E

Publications

This appendix includes a copy of publications the author has contributed to as a part of this thesis work. Before each article, the information about title, authors, abstract, kind of publication and detailed information about what the author has contributed is included. The articles are added in a chronological order, with the original formatting as it was published.

E.1 Limits on Failure Scenarios for Crab Cavities in the HL-LHC

- **Title:** Limits on Failure Scenarios for Crab Cavities in the HL-LHC.
- **Authors:** A. Santamaría García, H. Burkhardt, K. Hernández Chahín, A. Macpherson, K. Sjobak, D. Wollmann, B. Yee-Rendón.
- **Abstract:** The High Luminosity (HL) LHC upgrade aims for a tenfold increase in integrated luminosity compared to the nominal LHC, and for operation at a levelled luminosity of $5 \times 10^{34} \text{ cm}^{-2} \text{ s}^{-1}$, which is five times higher than the nominal LHC peak luminosity. Crab Cavities (CCs) are planned to compensate the geometric luminosity loss created by the increased crossing angle by rotating the bunch, allowing quasi head-on collisions at the Interaction Points (IP). The CCs work by creating transverse kicks, and their failure may have short time constants comparable to the reaction time of the Machine Protection System (MPS), producing significant coherent betatron oscillations and fast emittance growth. Simulations of CC failure modes have been carried out with the tracking code SixTrack, using the newly added functionality called DYNK, which allows to dynamically change the attributes of the CCs. We describe these simulations and discuss early, preliminary results.
- **Where:** IPAC 2015, Richmond VA, USA.
- **Contribution:** A. Santamaría García did the simulations, analysis, and wrote most of the paper.
- **Bibliography entry:** [140]

LIMITS ON FAILURE SCENARIOS FOR CRAB CAVITIES IN THE HL-LHC *

A. Santamaría García, H. Burkhardt, K. Hernández Chahín, A. Macpherson,
K. Sjobak, D. Wollmann, B. Yee-Rendón, CERN, Geneva, Switzerland

Abstract

The High Luminosity (HL) LHC upgrade aims for a tenfold increase in integrated luminosity compared to the nominal LHC, and for operation at a levelled luminosity of $5 \times 10^{34} \text{ cm}^{-2} \text{ s}^{-1}$, which is five times higher than the nominal LHC peak luminosity. Crab Cavities (CCs) are planned to compensate the geometric luminosity loss created by the increased crossing angle by rotating the bunch, allowing quasi head-on collisions at the Interaction Points (IP). The CCs work by creating transverse kicks, and their failure may have short time constants comparable to the reaction time of the Machine Protection System (MPS), producing significant coherent betatron oscillations and fast emittance growth. Simulations of CC failure modes have been carried out with the tracking code SIXTRACK [1], using the newly added functionality called DYNK [2], which allows to dynamically change the attributes of the CCs. We describe these simulations and discuss early, preliminary results.

INTRODUCTION

In order to produce ten times more collisions during the HL-LHC lifetime, the nominal levelled luminosity will be $5 \times 10^{34} \text{ cm}^{-2} \text{ s}^{-1}$. An increase in luminosity entails an increase in proton collisions per bunch crossing (pile-up) and a rapid decay of the beam current due to proton burning. In order to optimize the experimental detectors' efficiency, the pile-up has to be maintained at an acceptable level and the luminosity should remain constant over the length of the fill. It has been proposed to maintain the luminosity constant by reducing the transverse beam size by means of reducing β^* , called β^* levelling. A smaller beam size at the IP implies larger beam sizes in the triplet quadrupole magnets, which will need a larger aperture. The implementation of low β^* collision optics will be carried out with the Achromatic Telescopic Squeeze (ATS) scheme [3]. A smaller β^* requires a larger crossing angle θ , which in turn causes a reduction of the geometrical luminosity. The crossing angle will be increased by a factor of two for HL-LHC, causing a significant loss in luminosity and therefore delaying the integrated luminosity goal. CCs have been proposed to counteract this effect. They generate transverse electromagnetic fields, which rotate each bunch longitudinally by $\frac{\theta}{2}$ such that the bunches collide effectively head-on, compensating the geometric luminosity loss. CCs allow access to the full performance reach of the small β^* values offered by the ATS scheme and the larger triplet quadrupole magnets [4, Chapter 1].

* Research supported by the High Luminosity LHC project.

THE MPS AND CRAB CAVITY FAILURES

A variety of processes can cause unavoidable beam losses during normal and abnormal operation. Because of the high stored energy of the HL-LHC beams, above 700 MJ, the beams can be highly destructive. Even a local beam loss of a tiny fraction of the full beam into a superconducting magnet can cause a quench, and large beam losses can cause damage to accelerator components. Because of this, the MPS is designed with very high reliability to prevent an uncontrolled release of the energy and damage due to beam losses [4, Chapter 7].

With the installation of CCs, new failure scenarios that could cause beam losses have to be considered. Voltage or phase changes of the CCs will happen with a time constant τ , which is proportional to the time it takes to dissipate the energy stored in the cavity through the coupler when the RF sources are turned off (external Q factor):

$$\tau = \frac{2 \cdot Q_{\text{ext}}}{\omega},$$

where ω is the angular frequency of the CCs. For the HL-LHC parameters of $f_{\text{cc}} = 400.79 \text{ MHz}$ and $Q_{\text{ext}} = 3 \times 10^5 - 5 \times 10^5$, CC failures could happen with a time constant as fast as $\tau = 238 - 397 \text{ } \mu\text{s} \approx 2 - 4 \text{ LHC turns}$. These ultrafast failures are potentially dangerous, which motivates detailed studies as there may not be enough time to extract the beam in a controlled way [5].

SIMULATION SETTINGS

Tracking simulations have been carried out with the collimation version of SIXTRACK and the DYNK module, in order to estimate the beam loss distribution around the ring in case of CC failures. These simulations were carried out for Beam 1 and IP1, considering one bunch represented by 9.6×10^5 particles at collision energy. The relevant HL-LHC parameters considered are summarized in Table 1. Further studies including IP5 are foreseen.

Baseline Optics and Layout

The optics used for the whole machine is the HLLHCV1.0 collision optics, which includes the new Nb₃Sn triplet (140 T/m, 150 mm) with all the additional magnets needed to be compatible with $\beta^* = 0.15 \text{ m}$ and implementing the ATS scheme [6].

Crab Cavities

The HLLHCV1.0 optics include the installation of three CCs per IP, per side and per beam (n_{cc}). To simplify the opening and closing of the crab bump, the groups of $n_{\text{cc}} = 3$

Table 1: Relevant HL-LHC Nom. Parameters (25 ns)

Parameter	Symbol	Value
Beam energy at collision	E [TeV]	7
Particles per bunch	N	2.2×10^{11}
Bunches per beam	n_b	2748
Crossing angle (IP1 & IP5)	θ [μ rad]	590
Minimum β^*	β^* [m]	0.15
Norm. transverse emittance	ϵ_n [μ m]	2.50
RMS energy spread	σ_s [0.0001]	1.13
RMS bunch length	σ_l [cm]	7.55
CC RF frequency	f_{cc} [MHz]	400.79

CCs were installed next to each other at the same location. The parameters of the simulated CCs are summarized in Table 2. Further simulations using the current baseline optics HLLHCv1.1 [7] with $n_{cc} = 4$ is foreseen. The phase advance between the CCs and the IP is optimized to be $\Delta\phi = \frac{\pi}{2}$, and the voltage of the CCs is the one required to open the crab bump and produce an effective head-on collision [8], given by

$$V_{cc} = \frac{c \cdot E \cdot \tan(\varphi)}{q \cdot \omega_{cc} \cdot \sqrt{\beta^* \beta_{cc}} \cdot \sin(\Delta\phi) \cdot n_{cc}},$$

where ω_{cc} is the angular frequency of the CCs in [$\text{rad} \cdot \text{s}^{-1}$], β_{cc} is the value of the beta function at the location of the CC in [m], c is the speed of light and q the proton charge. Since the crossing angle in IP1 is in the vertical plane, the kick provided by the simulated CCs is also in the vertical plane.

Table 2: CC Parameters Used in the Simulation for IP1

Side	n_{cc}	s [m]	Voltage [MV]	β_{cc} [m]
Right	3	-147	3.19	4395
Left	3	149	3.23	4281

Collimation and Aperture

The collimation system [9, 10] is installed to safely dispose of unavoidable beam losses, but it also represents a passive protection for the machine during the dumping time (3 LHC turns = 266 μ s) in case of a fast failure. The collimation system was included in the tracking simulations [11] in order to assess the limit in which the machine can cope with CC failures. The settings used in the simulations are summarized in Table 3.

The losses in the aperture are computed from the results of the tracking simulations of the full particle distribution, using a detailed aperture model of the full LHC ring. The spatial resolution of the model is 10 cm over the total length of 27 km [12].

Beam Distributions

For the transverse phase space, a 2D Gaussian distribution was generated for each plane. For the longitudinal plane, the

Table 3: Nominal Settings in Terms of σ ($\epsilon_n = 3.75 \mu\text{m}$)

Collimator	Opening [σ]
Primary IR7	6
Secondary IR7	7
Absorber IR7	10
Primary IR3	12
Secondary IR3	15.6
Absorber IR3	17.6
Secondary IR6	7.5
Dump protection IR6	8
Tertiary IR2/8	12
Tertiary IR1/5	8.3

2D Gaussian distribution was truncated in order to match the RF bucket (Fig. 1). The parameters of the gaussian distributions are given in Table 1. The same initial distribution was used for all the simulations.

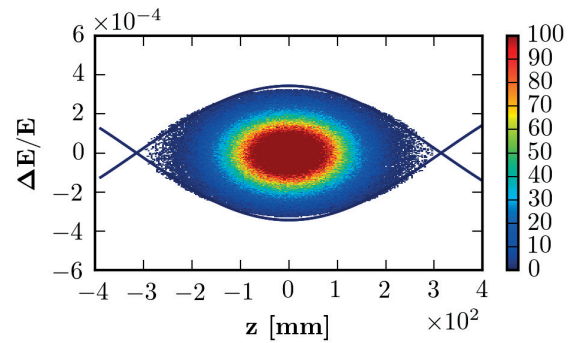


Figure 1: Initial distribution in the longitudinal plane. Arbitrary density units were used.

Simulated Cases

Five scenarios are considered:

- **No failure:** the particles are tracked for 51 turns in normal conditions.
- **Voltage failure of 3 CCs:** the voltage drops exponentially towards 0 V following $V(t) = V_0 \cdot e^{-t}$, where t is the turn number after onset of failure. The phase remains constant with a value of 0° .
- **Phase failure of 1, 2 & 3 CCs:** the phase jumps from 0° to 90° in one turn, while the voltage remains constant.

The failures are applied only to the group of CCs situated downstream, leaving the CCs upstream working normally. The particles are initially tracked for 10 turns. The failure takes place in the 11th turn, and the particles are tracked for 40 additional turns. Nevertheless, since the beam dumping time is of 3 turns, the losses after 3 turns are also considered.

4: Hadron Accelerators

A17 - High Intensity Accelerators

FIRST RESULTS FROM DETAILED SIMULATIONS

Full simulations based on SIXTRACK with the newly implemented general dynamic kick module have started recently. We discuss here our first observations, which extend earlier studies [13–15].

A summary of the number of particles lost in the collimation system, in the aperture and the percentage of the total particles lost from the beam is shown in Table 4.

Table 4: Particle Losses Out of 9.6×10^5 Tracked Particles After 3 Turns After the Fault, and After 40 Turns After the Fault (Between Parenthesis).

Failure	Coll.	Aperture	[%]
None	102	0	0.01
Volt. (3/3 CCs)	689	0 (0)	0.07 (0.3)
Ph. (1/3 CC)	501	0 (0)	0.05 (0.2)
Ph. (2/3 CCs)	44118	4 (5)	4 (8)
Ph. (3/3 CCs)	311596	166 (186)	32 (39)

A simultaneous voltage failure of all CCs on one side results in a loss of 0.07% of the particles tracked.

Phase jumps of 90° in a single turn were considered in our simulations as worst case scenarios. They would result in a significant transverse kick of the densely populated bunch center (see Fig. 2). Studies are still ongoing in order to assess the real phase and voltage decay time of the CCs.

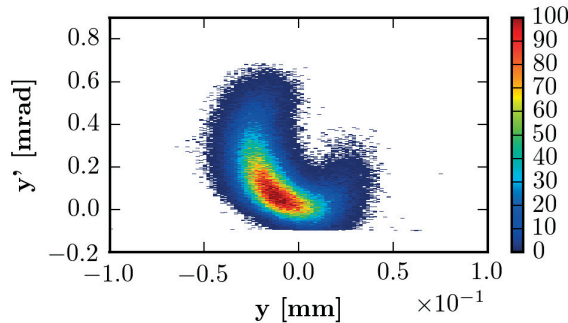


Figure 2: Transverse beam distribution in the crossing plane at IP1, after a phase trip of the 3 CCs downstream (after 1 turn). Arbitrary density units were used.

For a single CC, we observe a loss of 0.05% of the tracked particles, which is in good agreement with earlier studies [13–15]. For a phase jump of 2 CCs this increases to 4% and for 3 CCs to 32%. For this last case, we can see from Fig. 3 (top) that significant losses would start in the 11th turn, which corresponds to the turn of the phase failure. We can also see from Table 4 that almost all the losses occur within the first 3 turns. We see from Fig. 3 (bottom) that the primary IR7 collimators are the main aperture bottleneck which intercepts most losses, and only a small fraction hits the tertiary collimators.

This worst case scenario is considered to be unlikely, as the CC related hardware and control system can be designed

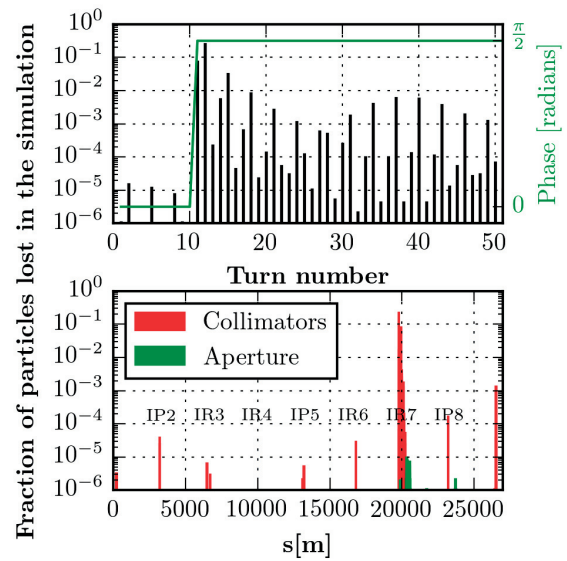


Figure 3: Losses around the ring for the simultaneous phase failure of 3 CCs (9.6×10^5 tracked particles) for 51 turns.

such that a simultaneous failure of these three independent modules is extremely unlikely. Mitigation techniques are also foreseen, in which the Multi-Cavity Feedback controller will adjust the field in the other cavities on both sides of the IP if the field starts changing in one of the CCs. This way the orbit distortions will remain local [4, Chapter 4]. Simulations indicate that if this technique is applied, the losses are reduced by 95 %.

The losses are much less critical for the failure of a single CC, and could be mitigated by the introduction of devices such as hollow electron lenses [16].

SUMMARY AND OUTLOOK

We describe the simulation of CC failures using the new DYNK module within SIXTRACK. We also discuss first results for worst case voltage and phase failures, and observe that these could result in rather fast losses. The studies described here will be continued in close collaboration with the hardware side and in preparation of CC tests in the SPS, to make sure that any dangerous failure scenarios can be avoided to allow for a safe integration of CCs in LHC operation.

ACKNOWLEDGMENTS

The author would like to thank R. Bruce, M. Fiascaris and A. Rossi for their help and collaboration with the collimation files, M. Giovannozzi for the useful discussions about the aperture and A. Avilés for the computing suggestions.

REFERENCES

- [1] F. Schmidt. Single particle tracking code treating transverse motion with synchrotron oscillations in a symplectic manner. CERN/SL/9456 (AP), 2012.

- [2] K. Sjobak et al. General functionality for turn-dependent element properties in SixTrack. In *these proceedings, MOPJE069, IPAC'15, Richmond, VA, USA*, 2015.
- [3] S. Fartoukh. Achromatic telescopic squeezing scheme and application to the LHC and its luminosity upgrade. *Phys. Rev. ST Accel. Beams*, 16:111002, Nov 2013.
- [4] *HL-LHC Preliminary Design Report*, volume V07. CERN, 2015.
- [5] R. Schmidt et al. Machine protection challenges for HL-LHC. In *Proceedings of IPAC'14, TUPRO016, Dresden, Germany*, 2014.
- [6] R.D. Maria et al. HLLHCV1.0: HL-LHC layout and optics models for 150 mm Nb3Sn triplets and local crab-cavities. In *Proceedings of IPAC'13, TUPFI014, Shanghai, China*, 2013.
- [7] R.D. Maria et al. HLLHCV1.1 optics version for the HLLHC upgrade. In *these proceedings, TUPTY037, IPAC'15, Richmond, VA, USA*, 2015.
- [8] Y-P. Sun et al. Beam dynamics aspects of crab cavities in the CERN large hadron collider. *Phys. Rev. ST Accel. Beams*, 12:101002, Oct 2009.
- [9] R.W. Assmann. Collimators and beam absorbers for cleaning and machine protection. In *Proceedings of the LHC Project Workshop - Chamonix XIV, Chamonix, France*, 261, 2005.
- [10] R.W. Assmann. The final collimation system for the LHC. In *Proc. of the European Particle Accelerator Conference, Edinburgh, Scotland*, 986, 2006.
- [11] G. Robert-Demolaize et al. A new version of sixtrack with collimation and aperture interface. In *Proceedings CERN-AB-2005-033, PAC-2005-FPAT081*, 2005.
- [12] S. Redaelli et al. LHC aperture and commissioning of the collimation system. In *Workshop Chamonix XIV*, 2005.
- [13] T. Baer et al. LHC machine protection against very fast crab cavity failures. In *Proceedings of IPAC'11, TUPZ009, San Sebastián, Spain*, 2011.
- [14] F. Bouly et al. Preliminary study of constraints, risks and failure scenarios for the High-Luminosity insertions at HL-LHC. In *Proceedings of IPAC'14, TUPRO016, Dresden, Germany*, 2014.
- [15] B. Yee-Rendon et al. Simulations of fast crab cavity failures in the high luminosity Large Hadron Collider. *Phys. Rev. ST Accel. Beams*, 17:051001, May 2014.
- [16] G. Stancari et al. Electron lenses for the Large Hadron Collider. In *Proceedings of IPAC'14, TUOBA01, Dresden, Germany*, 2014.

E.2 General Functionality for Turn Dependent Element Properties in SixTrack

- **Title:** General Functionality for Turn-Dependent Element Properties in SixTrack.
- **Authors:** K. Sjobak, H. Burkhardt, R. De Maria, A. Mereghetti, A. Santamaría García.
- **Abstract:** In order to facilitate studies of how dynamically changing element attributes affect the dynamics of the beam and beam losses, the functionality for dynamic kicks (DYNK) of SixTrack has been significantly extended. This functionality can be used for the simulation of dynamic scenarios, such as when crab cavities are switched on, orbit bumps are applied, optics are changed, or failures occur. The functionality has been extended with a more general and flexible implementation, such that arbitrary time-dependent functions can be defined and applied to different attributes of families or individual elements, directly from the user input files. This removes the need for source code manipulation, and it is compatible with LHC@Home which offers substantial computing resources from volunteers. In this paper, the functionality and implementation of DYNK is discussed, along with examples of application to the HL-LHC crab cavities.
- **Where:** IPAC 2015, Richmond VA, USA.
- **Contribution:** A. Santamaría García took part in the design of the DYNK software and wrote some of the core parts of the code.
- **Bibliography entry:** [109]

GENERAL FUNCTIONALITY FOR TURN-DEPENDENT ELEMENT PROPERTIES IN SIXTRACK*

K. Sjobak[†], H. Burkhardt, R. De Maria, A. Mereghetti, A. Santamaría García
CERN, Geneva, Switzerland

Abstract

In order to facilitate studies of how dynamically changing element attributes affect the dynamics of the beam and beam losses, the functionality for dynamic kicks (DYNK) of SixTrack has been significantly extended. This functionality can be used for the simulation of dynamic scenarios, such as when crab cavities are switched on, orbit bumps are applied, optics are changed, or failures occur. The functionality has been extended with a more general and flexible implementation, such that arbitrary time-dependent functions can be defined and applied to different attributes of families or individual elements, directly from the user input files. This removes the need for source code manipulation, and it is compatible with LHC@Home which offers substantial computing resources from volunteers. In this paper, the functionality and implementation of DYNK is discussed, along with examples of application to the HL-LHC crab cavities.

INTRODUCTION

SixTrack is a 6D single particle tracking code [1,2], which is routinely used at CERN to study the dynamic aperture and collimation system in high-energy circular machines like the LHC. There are also a large number of tools built around SixTrack, both for analyzing the results and for handling very large numbers of initial conditions. For this reason, SixTrack is the natural tool to use for studying fast failure scenarios at the HL-LHC, and for other transient phenomena at other similar machines.

Functionality for applying dynamic kicks (DYNK) – i.e. time-dependent machine element parameters – was therefore added to the code [3,4] and significantly extended. It makes it possible for the user to specify the functional form of these parameters directly in the input file, or to load them from a file. This eliminated the need for multiple private code forks, freeing up and focusing developer resources. The specification of the functions, to which elements they should be applied, and when they should be applied, is done using a simple mini-language. Some examples of this language are given below, and a full description is given on the TWIKI page [5].

DYNK currently supports setting the strength of all the standard thin elements, and also setting the voltage, phase, and frequency of crab cavities. It also supports a wide variety of functions, which may use the turn number or the output of other functions as input. It is also possible for the functions to store and retrieve data from memory, as is

used for pseudo random number generating functions that stores the random seed between turns, and when loading the functions as tables from files. There is also an option to output the setting of the affected elements at every turn to a file. In order to work with LHC@Home [6], which is used for large tracking campaigns, DYNK supports checkpointing and restarting from a checkpoint. It interacts correctly with the collimation routines, including resetting the elements and generating exactly the same values for each pass of 64 particles. The ripple module is made redundant by DYNK, which can exactly reproduce its results, and is therefore removed.

IMPLEMENTATION

In order to make DYNK work, there are two main components: a function parser and evaluator, and a setter and getter for the element properties. Additionally, there are hooks for calling DYNK in the tracking loops, and for initialization before the start of tracking. The data storage for the functions are provided by one master table (one row per function) and a “free memory” for each of the major data types (integers, floats and strings).

This architecture is very easily extendable, making adding support for new types of functions a matter of adding a few lines to the parser and evaluator. Similarly, new elements or element attributes can be supported by adding them to the setter and getter functions – the difficulty of this is determined by the complexity of the memory structures and initialization scheme used for that element.

EXAMPLE USE CASES

Some examples for the use of DYNK are provided below. All of these are ran using the HL-LHC v1.1 lattice [7] with vertical crab cavities around the first interaction point (IP1, ATLAS). The beam was sampled at IP1 as a Gaussian distribution using the nominal HL-LHC parameters, cropped so to only include particles inside of the RF bucket.

The crab cavities closing the bump (at $s=153.6, 154.6, 160.2$ and 161.2 m, relative to IP1) are in this simulation called CRAB_IP1_R1...4, while the cavities creating the bump (at $s=26494.3, 26495.3, 26500.9$ and 26501.9 m) are called CRAB_IP1_L1...4. Their frequencies are set to 400.8 MHz, i.e. the same as for the accelerating cavities. The standard voltages of the closing- and opening cavities opening cavities are calculated using Eq. 4 from [8]. For the opening cavities, it is assumed that the transverse betatron β -function and phase advance is the same for all the cavities, while the voltage of each of the closing cavities are chosen such that they cancel the symmetrically positioned opening

* Research supported by EU FP7 HiLumi LHC – Grant Agreement 284404
[†] kyrre.ness.sjobaek@cern.ch

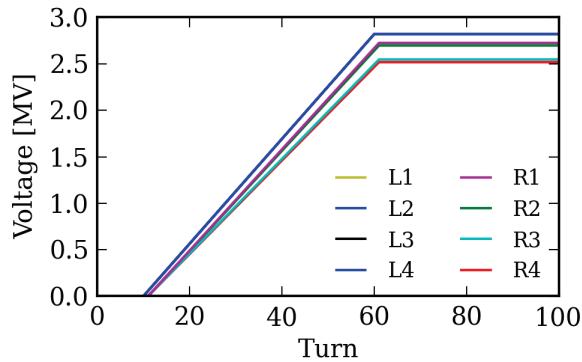


Figure 1: Ramping of crab cavity voltages.

cavity. For these examples, the crab cavities around IP5 (CMS) are switched off.

Starting a Tracking Run with Crabs Switched On

If the tracking is started with a uncrabbed beam inside a bump, such as produced by a crab cavity, the bump must be temporarily disabled during injection. To achieve this, the following DYNK block can be used:

```
DYNK
FUN zero CONST 0.0
FUN CV_1R1 GET CRAB_IP1_R1 voltage
FUN CV_1R2 GET CRAB_IP1_R2 voltage
FUN CV_1R3 GET CRAB_IP1_R3 voltage
FUN CV_1R4 GET CRAB_IP1_R4 voltage
SET CRAB_IP1_R1 voltage zero 1 1 0
SET CRAB_IP1_R2 voltage zero 1 1 0
SET CRAB_IP1_R3 voltage zero 1 1 0
SET CRAB_IP1_R4 voltage zero 1 1 0
SET CRAB_IP1_R1 voltage CV_1R1 2 2 0
SET CRAB_IP1_R2 voltage CV_1R2 2 2 0
SET CRAB_IP1_R3 voltage CV_1R3 2 2 0
SET CRAB_IP1_R4 voltage CV_1R4 2 2 0
NEXT
```

This creates a constant function `zero` which always returns 0.0, and four constant functions `CV_1R1...4` which always return the original voltage of the crab cavity (as defined in the lattice description file `fort.2`). The voltage of these cavities are then set equal to zero at turn 1 (ending at 1), and then changed to the original value for turn 2 (ending at 2). Since no further settings are applied, the current settings remain after turn 2.

Linear Ramping of Crab Cavities

Another case is a simulation where the voltage of the crab cavities are linearly ramped up to the maximum voltage in 50 turns, starting at turn 10. The voltage is then flat for 40 turns. This profile is illustrated in Fig. 1, and the input block looks like (shortened by removing duplicate instructions to control multiple elements):

```
DYNK
FUN zero CONST 0.0
FUN CV_R1 GET CRAB_IP1_R1 voltage
(etc. for R2,R3,R4)
```

5: Beam Dynamics and EM Fields

D11 - Code Developments and Simulation Techniques

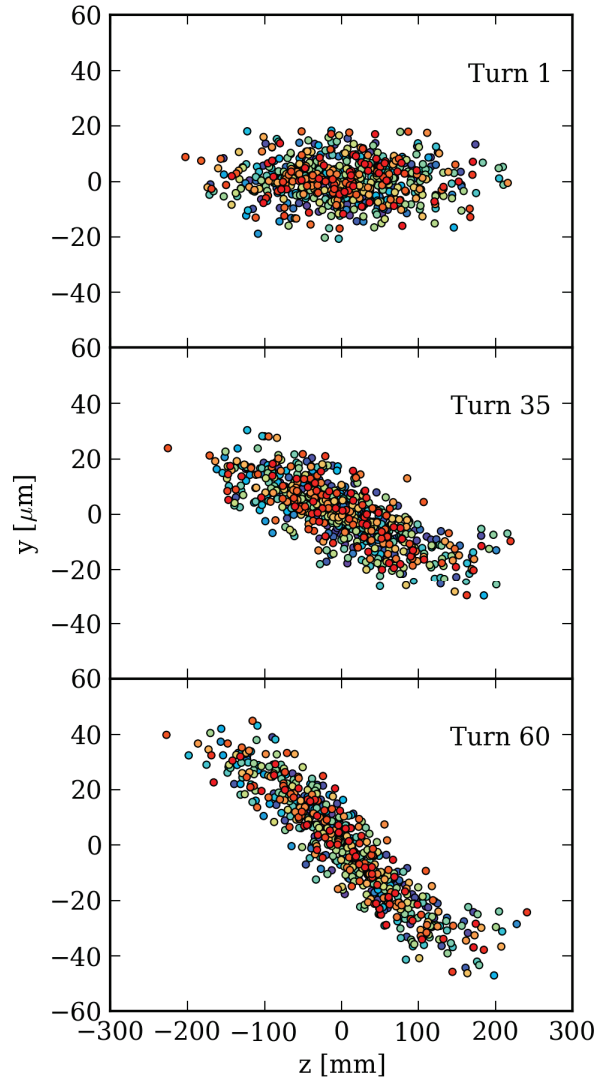


Figure 2: Simulated Z-Y distribution (640 particles) of the beam during ramping of the crab cavity voltages.

```
FUN CV_L GET CRAB_IP1_L1 voltage
FUN ramp LIN 0.02 0
FUN ramp_R1 MUL CV_R1 ramp
(etc. for R2,R3,R4)
FUN ramp_L MUL CV_L ramp
SET CRAB_IP1_R1 voltage zero 1 10 0
(etc. for R2,R3,R4)
SET CRAB_IP1_L1 voltage zero 1 9 0
(etc. for L2,L3,L4)
SET CRAB_IP1_R1 voltage ramp_R1 11 61 -11
(etc. for R2,R3,R4)
SET CRAB_IP1_L1 voltage ramp_L 10 60 -10
(etc. for L2,L3,L4)
NEXT
```

Here the function `ramp` is given as $y(x) = 0.02x + 0.0$, and this normalized ramp is then multiplied by the wanted final voltages. When setting the voltages during the ramp, the point where the functions are evaluated is then shifted

ISBN 978-3-95450-168-7

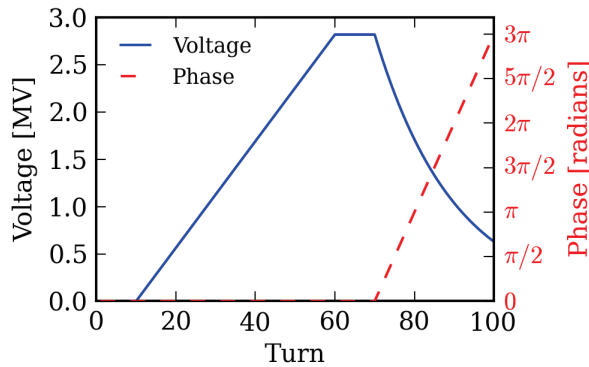


Figure 3: Voltage and phase of crab cavities CRAB_IP1_L1...L4 as function of time, for the exponential decay/linear drift example.

by -11 and -10 turns, as specified in the last column in the SET statement. The resulting beam distributions are shown in Fig. 2, which show the bunch is increasingly tilted as the voltage ramps up.

Exponential Decay of Crab Voltage, Combined with a Linear Drift of Crab Phase

A slightly more complicated case is if the crab cavities on the side upstream of the IP sees an exponential decay in the kick voltage, combined with a linear drift in phase. This failure case corresponds to the cavities being detuned, while also no longer being driven, similarly to what is described in [9]. In this example, the failure starts after 70 turns, following a ramping like in the above example. The extra lines in the DYNK block then looks like:

```
FUN expCore LIN -0.05 0.0
FUN decay EXP expCore
FUN decayScaled MUL decay CV_L
SET CRAB_IP1_L1 voltage decayScaled 70 100 -70
(etc. for L2,L3,L4)
FUN phasedrift LIN 0.3141592654 0.0
SET CRAB_IP1_L1 phase phasedrift 70 100 -70
(etc. for L2,L3,L4)
```

The exponential decay is here given as $V(t') = V_0 \exp(-t'/20)$, where V_0 is the standard voltage and t' is the number of turns after the start of the failure, i.e. $t' = \text{turn} - 70$. The phase drift is given as $\phi(t') = \pi t'/10$. The resulting voltage and phase program is shown in Fig. 3.

REPLACEMENT OF RIPP BLOCK

As the functionality of the ripple module in SixTrack is a subset of what is possible with DYNK, it has been deprecated. The RIPP input block is therefore no longer accepted. A special function COSF_RIPP has therefore been provided in DYNK, exactly mirroring the old RIPP input format. This function is calculated as

$$f(t; A, T, \phi_0) = A \cos \left(2\pi \frac{(t-1)}{T} + \phi_0 \right), \quad (1)$$

where t is the current turn number, A is the specified amplitude, T the period, and ϕ_0 the initial phase.

This was tested against the prob1 and prob3 example cases from sixtest [10], as well as against the results from a recent BOINC campaign. It was confirmed that replacing the RIPP block with a DYNK block exactly reproduced the tracking results, even after 10^6 turns.

As an example, a part of the RIPP block from prob1 is shown below. It specifies a ripple of amplitude $A = \pm 3.2315 \cdot 10^{-10}$ radians/meter and period $T = 244.9$ turns (equivalent to 50 Hz) for the quadrupole elements dmqx1f5015+2 and dmqx2af5015+2, with no start phase or continuation turn number specified:

```
RIPPLE OF POWER SUPPLIES
dmqx1f5015+2      3.2315D-10    224.9
dmqx2af5015+2    -3.2315D-10    224.9
(etc. for more elements)
```

An equivalent DYNK block is:

```
DYNK (autogenerated from RIPP block by ripconverter.py)
NOFILE
FUN RIPP-dmqx1f5015+2 COSF_RIPP 3.2315D-10 224.9 0.0
SET dmqx1f5015+2 average_ms RIPP-dmqx1f5015+2 1 -1 0
FUN RIPP-dmqx2af5015+2 COSF_RIPP -3.2315D-10 224.9 0.0
SET dmqx2af5015+2 average_ms RIPP-dmqx2af5015+2 1 -1 0
(etc. for more elements)
```

Here the final turn number for the SET statement is given as -1, indicating it should be active until the end of the simulation. Also note the NOFILE statement, instructing DYNK to not write a file containing the settings of all elements affected by DYNK in all turns of the simulation, as such a file would in this case be very large. An automatic tool is available for doing the conversion of RIPP blocks to DYNK.

CONCLUSION

The new DYNK functionality allows for extremely flexible definition of time-dependent element settings in SixTrack. It allows the user to choose from and combine more than 25 different function types for computing the wanted setting, or load it from a file. The architecture is extensible, and allows for future additions of element types and functions. DYNK therefore opens many possibilities for future studies of the effect of time-dependent changes of element properties.

ACKNOWLEDGMENT

Thanks to Miriam Fitterer for providing one of the test cases for conversion from the ripple module to DYNK.

REFERENCES

- [1] F. Schmidt, "SixTrack Version 4.2.16 Single Particle Tracking Code Treating Transverse Motion with Synchrotron Oscillations in a Symplectic Manner", CERN/SL/9456, 2012.
- [2] G. Ripken, F. Schmidt, "A symplectic six-dimensional thin-lens formalism for tracking", DESY 95-63 and CERN/SL/95-12(AP), 1995.

- [3] R.D. Maria et al., “Recent developments and future plans for SixTrack”, IPAC’13, Shanghai, May 2013, MOPWO028.
- [4] A. Mereghetti et al., “SixTrack-FLUKA active coupling for the upgrade of the SPS scrapers”, IPAC’13, WEPEA064.
- [5] SixTrack DYNK TWIKI: https://twiki.cern.ch/twiki/bin/viewauth/LHCAtHome/SixTrackDoc#Dynamic_Kicks_DYNK_input_block
- [6] M. Giovannozzi et al., “LHC@HOME: A volunteer computing system for massive numerical simulations of beam dynamics and high energy physics events”, IPAC’12, New Orleans, May 2012, MOPPD061.
- [7] R.D. Maria et al., “HLLHCV1.1 Optics Version for the HL-LHC Upgrade”, TUPTY037, *These Proceedings*, IPAC’15, Richmond, VA, USA (2015).
- [8] Y. Sun, et al., Phys. Rev. ST Accel. Beams 12, 101002 (2009).
- [9] A. Santamaria et al., “Limits on failure scenarios for crab cavities in the HL-LHC”, THPF095, *These Proceedings*.
- [10] E. McIntosh, private communication.

E.3 Machine Protection from Fast Crab Cavity Failures in the High Luminosity LHC

- **Title:** Machine Protection from Fast Crab Cavity Failures in the High Luminosity LHC.
- **Authors:** A. Santamaría García, K. Sjobak, R. Bruce, H. Burkhardt, F. Cerutti, R. Kwee-Hinzmann, A. Lechner, A. Tsinganis.
- **Abstract:** The time constant of a crab cavity (CC) failure can be faster than the reaction time of the active protection system. In such a scenario, the beams cannot be immediately extracted, making the the protection of the machine rely on the passive protection devices. At the same time, the energy stored in the High Luminosity (HL) LHC beams will be doubled with respect to the LHC to more than 700 MJ, which increases the risk of damaging the machine and the experiments in a failure scenario. In this study we estimate the impact that different CC failures have on the collimation system. We also give a first quantitative estimate of the effect of these failures on the elements near the experiments based on FLUKA simulations, using an updated HL-LHC baseline.
- **Where:** IPAC 2016, Busan, Korea.
- **Contribution:** A. Santamaría García defined the scenarios presented in the paper, did the simulations, analysis and wrote most of the paper. She also presented the paper at the poster session of the IPAC 2016 conference.
- **Bibliography entry:** [137]

MACHINE PROTECTION FROM FAST CRAB CAVITY FAILURES IN THE HIGH LUMINOSITY LHC *

A. Santamaría García [†], K. Sjobak, R. Bruce, H. Burkhardt, F. Cerutti,
R. Kwee-Hinzmann¹, A. Lechner, A. Tsinganis, CERN, Geneva, Switzerland

¹also at John Adams Institute at Royal Holloway, University of London, Egham, UK

Abstract

The time constant of a crab cavity (CC) failure can be faster than the reaction time of the active protection system. In such a scenario, the beams cannot be immediately extracted, making the the protection of the machine rely on the passive protection devices.

At the same time, the energy stored in the High Luminosity (HL) LHC beams will be doubled with respect to the LHC to more than 700 MJ, which increases the risk of damaging the machine and the experiments in a failure scenario.

In this study we estimate the impact that different CC failures have on the collimation system. We also give a first quantitative estimate of the effect of these failures on the elements near the experiments based on FLUKA simulations, using an updated HL-LHC baseline.

INTRODUCTION

The HL-LHC [1] will be the first hadron machine to use CCs, for which several prototypes have been developed. The prototype selection has been narrowed down to two designs: the RF dipole and the Double Quarter Wave (DQW) [2, 3]. Prior to their installation in the HL-LHC, these CCs will be tested with proton beams in the SPS to study their behavior in real conditions. In particular, it is planned to study the beam response to three different cases of CC trips: RF trips, beam induced failures and system/operator faults [4]. In this context, a tracking simulation including CC failures helps to identify the most relevant failure cases, to assess their impact on the machine, to give feedback for the future installation and to improve the current mitigation strategies.

CRAB CAVITY FAILURES

CCs act as damped oscillators, in which the loaded quality factor Q_L represents how under-damped the oscillator is and characterizes the oscillator's bandwidth relative to its center frequency. The DQW has a high loaded quality factor of $Q_L = 5.3 \times 10^5$, which indicates a low rate of energy loss relative to the stored energy of the cavity. In the case of a controller failure or arc in the CC coupler, the CC voltage will exponentially decay following

$$V = V_0 \exp\left(-\frac{\omega t}{2Q_L}\right) = V_0 \exp\left(-\frac{t}{\tau}\right), \quad (1)$$

* Research supported by the High Luminosity LHC project.

[†] andrea.santamaria@cern.ch

where ω is the angular frequency of the CC field and V_0 its operating voltage. Considering the baseline CC frequency of $f = 400.79$ MHz, we obtain a time constant for these processes:

$$\tau = 421 \mu\text{s} = 4.73 \text{ LHC turns}. \quad (2)$$

While an abrupt change in voltage of the CC will change the angle between bunches at the collision point, a phase slip will kick the densely populated core of the proton bunch. Nevertheless, a phase slip alone can only happen if the wrong signal is fed to the cavity either by a failure in the control system or by the operator. In the rest of the cases, the three parameters: voltage, frequency and phase are interdependent and closely related to the structure of the cavity. To study these correlations, detailed CC behavior models are being developed [5]. The study presented here focuses only on phase slips happening at constant or decaying voltage.

For a fast phase variation we can expect high power requirements from the CC, which sets a limit on how much the phase can change per time unit [6, 7]:

$$\left.\frac{d\phi(t)}{dt}\right|_{\text{max}} = \frac{\omega}{2Q_L} \sqrt{\frac{8(R/Q_{\perp}) Q_L P_{\text{max}}}{V_0^2} - 1}, \quad (3)$$

where R/Q_{\perp} is the geometric shunt impedance and P_{max} is the maximum power per cavity. Considering the baseline values for the DQW of $R/Q_{\perp} = 429 \Omega$, $P_{\text{max}} = 100$ kW and the CC voltage used in this study $V_0 = 2.84$ MV, one obtains

$$\left.\frac{d\phi(t)}{dt}\right|_{\text{max}} = 56^\circ / \text{turn}, \quad (4)$$

corresponding to a detuning of $\Delta f = 1.7$ kHz. Any such failure risks to cause significant beam losses, which should occur on the LHC collimation system [8] if the received kicks are not large enough to directly reach the machine aperture.

TRACKING SIMULATION SETTINGS

The SixTrack [9] tracking code version 4.5.33 was used in order to study the effect of a linear CC phase slip on the beam. The model of the HL-LHC used in the simulation follows the current baseline layout and optics HLLHCv1.2 [1]. The relevant HL-LHC parameters considered are summarized in Table 1. The phase slip was reproduced with the dynamic kick module [10], and the collimators installed through the collimation routine [11]. The simulations presented here have been performed for Beam 1.

Table 1: Relevant Parameters Used in This Study

Parameter	Symbol	Value
Beam energy at collision	E [TeV]	7
Tot. crossing angle (IP1 & IP5)	θ [μ rad]	590
Minimum β^*	β^* [m]	0.15
Norm. transverse emittance	ϵ_n [μ m]	2.50
RMS energy spread	σ_s [0.0001]	1.13
RMS bunch length	σ_l [cm]	7.55
CC RF frequency	f_{cc} [MHz]	400.79
N $^\circ$ of CCs ¹	n_{cc}	4

¹ per beam, per IP side.

Crab Cavities

The simulated failure scenario affects the downstream CCs of the ATLAS experiment (IP1), where the crossing and CC kick plane is vertical. The CCs are situated between the double aperture dipole D2 and quadrupole Q4.

Failure Scenarios

For this study, the maximum possible phase change per turn found in Eq. (4) was considered. A linear phase change of 56° per turn was applied during 4 turns, then kept constant for 15 additional turns. This phase slip was paired with two different voltage behaviors: constant and decaying voltage as described in Eq. (1), with $\tau = 4$ LHC turns. The different failure cases shown in Fig. 1 were simulated.

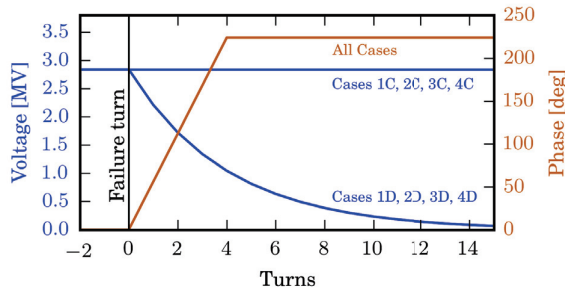


Figure 1: Evolution of the phase and voltage for the different failure cases, where the first digit indicates the number of CCs failing, **C** indicates constant voltage and **D** decaying voltage.

Beam Distribution

Due to the time dependence of the phase slip, each bunch of the beam will see different phases. Separate simulations for each bunch would be needed in order to study this effect, since SixTrack tracks one bunch per run. In this paper, only one bunch is simulated and scaled to the full beam. Further studies are foreseen, in which the time variation of the phase is taken into account for the different bunches.

For the simulations of this study, a double Gaussian beam profile was used as a representation of the bunch in the transverse plane (Fig. 2), which has been found to fit well observed beam distributions [12] and has been used in previous CC failure studies [13]. In the longitudinal plane, a Gaussian distribution was matched to the RF bucket size.

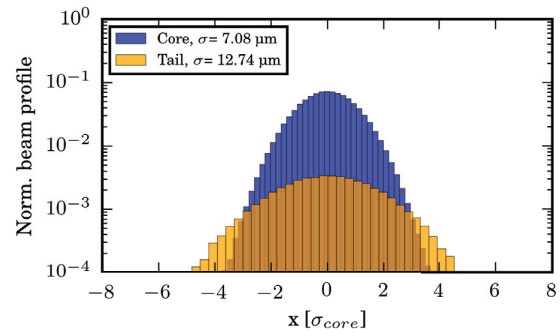


Figure 2: Normalized horizontal beam profile for the simulation, where $\sigma_{tail} = 1.8 \sigma_{core}$. The core represents 95 % of the total bunch and the tail 5%.

Collimation System

The opening of the collimators used in the tracking simulation are summarized in Table 2 [15].

Table 2: Openings in Terms of σ ($\epsilon_n = 3.5 \mu$ m)

Collimator	Opening [σ]
Primary IR7	5.7
Secondary IR7	7.7
Absorber IR7	10
Primary IR3	15
Secondary IR3	18
Absorber IR3	20
Secondary IR6	8.5
Dump protection IR6	9
Tertiary IR2/8	30
Tertiary IR1/5	10.9

RESULTS & DISCUSSION

Losses in the Collimation System

The results from the tracking simulations are summarized in Fig. 3, in terms of losses from the simulated bunch on the collimators. We can observe that in the cases at constant voltage, the losses are almost an order of magnitude higher compared to the cases at decaying voltage after 10 turns. This is expected, since the strength of the kick is proportional to the amplitude of the voltage. For the case of only 1 CC failing, no losses were observed with decaying voltage. The results also show that the losses in general increase an order of magnitude with the number of CCs failing, suggesting that simultaneous failures of CCs should be strictly avoided [16]. Nevertheless, there are no obvious mechanisms that would affect several CCs in the same way in a synchronous manner.

Fig. 4 shows the distribution of losses around the ring. All lost protons have first hit a primary collimator in the betatron cleaning insertion (IR7), which is the main loss location. Here, 0.11 % of the beam was lost in 4 turns. The losses not intercepted by the collimators are very low ($\sim 10^{-5}$ %), which indicates a good cleaning efficiency.

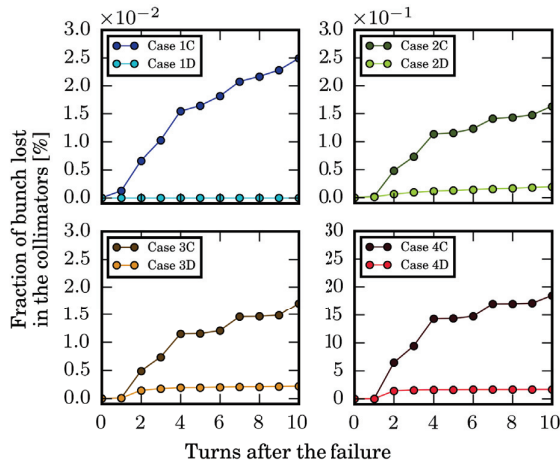


Figure 3: Cumulative fraction of the bunch lost in the collimation system for the cases described in Fig. 1.

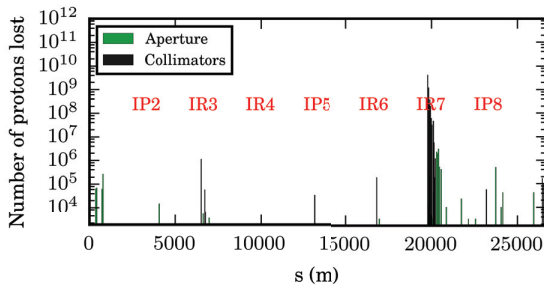


Figure 4: Losses around the ring for Case 2C before dump, in 10 cm bins, scaled to the total beam intensity.

For the current LHC, a beam abort is initiated in case of an abnormal increase of beam loss signal in the collimator BLMs, and will be completed within 2 or 3 turns. This will happen if 3×10^{10} protons or more are lost in half a turn or less [17]. A summary of the number of protons lost in the collimation system before the beam is dumped is presented in Table 3, where the fraction of bunch lost was scaled to the total beam intensity. In all the cases where the beam is dumped, the failure is detected during the first or second turn after the failure.

Table 3: Turn after the failure in which the beam abort is initiated, and the number of protons lost p_{loss} in the collimation system before the beam is dumped, for each failure case.

Case	Turn	p_{loss}	$p_{\text{loss}} [\%]$
1C	2	9.7×10^{10}	0.016
1D	-	No Losses	0
2C	2	6.7×10^{11}	0.11
2D ¹	-	1.2×10^{11}	0.02
3C	2	7.3×10^{12}	1.2
3D	2	1.1×10^{12}	0.19
4C	1	8.6×10^{13}	14.3
4D	2	9.7×10^{12}	1.6

¹ values cumulated for 10 turns. No beam abort is triggered.

It has been estimated that a collimator should survive if 8 bunches, of 1.15×10^{11} protons each, spaced by 25 ns impact on a secondary collimator during an asynchronous beam dump at collision energy [18]. From Table 3 we can conclude that the damage limit of the collimators is reached for any failure of 3 or more CCs, before the beam is dumped. Nevertheless, an accurate assessment of the impact of the obtained losses in the collimation system requires detailed energy deposition studies.

FLUKA Simulations

In case of CC failures, the experiments and superconducting magnets near them are exposed to showers from the tertiary collimators (TCTs), which can be hit by protons outscattered from the collimation insertion. In order to assess the effects of these showers in the experimental insertions, FLUKA [19,20] shower simulations were carried out based on the loss distribution predicted by SixTrack. The most impacted TCT is the horizontal TCT4. Only the case of a phase slip affecting 2 CCs at constant voltage (Case 2C) was considered, being the most unfavorable among the realistic cases. The most impacted magnet is the D1 separation dipole located 50 m downstream of the TCTs. The maximum energy density in the D1 coils is found to be about 7×10^{-10} mJ/cm³ per inelastic proton collision in the TCT4, while it is about an order of magnitude lower in the neighbouring triplet quadrupoles. Assuming a transient quench level of a few 10 mJ/cm³, one can therefore expect a quench of the D1 if losses on the TCT would exceed a few 10^{10} protons. On the other hand, thermo-mechanical studies have shown that already a few 10^9 protons can damage the TCTs depending on the transverse impact distributions on the TCT front face [21]. For the considered case, 2.7×10^7 protons impacted the TCT, which is well below the damage limit of the TCT and poses no risk for quenching or damaging downstream magnets, nor the experiments.

CONCLUSION

A realistic estimation of a CC phase slip and of the time constant of a CC voltage decay was presented, following the current baseline parameters for the DQW and HL-LHC. The results show that for the failure of 1 or 2 CCs, the losses in the collimation system and the downstream magnets before the beam is dumped are below the damage limits. Further studies should assess if several CCs could be simultaneously quenched if they are exposed to particle showers from beam losses, and consider the RF Dipole parameters.

ACKNOWLEDGEMENTS

The authors would like to thank P. Baudrenghien, R. Calaga, K. G. Hernández Chahín, A. Macpherson and S. Verdú Andrés for their valuable help in understanding CCs. We would also like to thank F. Carra, R. Schmidt, M. Valette, D. Wollmann and M. Zerlauth for their feedback and interest in the project.

REFERENCES

- [1] “High-Luminosity Large Hadron Collider (HL-LHC) Technical Design Report V0”, EU Deliverable D1-10, https://edms.cern.ch/ui/file/1558149/1.0/HL_TDR.2015.11.06.V02.pdf
- [2] S. Verdú-Andrés *et al.*, “Design and Prototyping of HL-LHC Double Quarter Wave Crab Cavities for SPS TEST”, in *Proc. IPAC’15*, Richmond, VA, USA, paper MOBD2.
- [3] F. Carra *et al.*, “Crab Cavity and Cryomodule Development for HL-LHC”, in *Proc. SRF2015*, Whistler, BC, Canada, paper FRBA02.
- [4] G. Arduini *et al.*, “Crab Cavity SPS Test Program Day Meeting Report”, presented at: *Crab Cavity SPS Test Day, CERN*, 2016.
- [5] K. Sjobak *et al.*, “Time Scale of Crab Cavity Failures Relevant for High Luminosity LHC”, presented at IPAC’16, Busan, Korea, May 2016, paper THPOY043, this conference.
- [6] J. Tückmantel, “Cavity-Beam-Transmitter Interaction Formula Collection with Derivation”, CERN-ATS-Note-2011-002 TECH, Jan. 2011.
- [7] P. Baudrenghien, private communication, Apr. 2015.
- [8] “HL-LHC Preliminary Design Report”, CERN-ACC-2014-0300, 2014.
- [9] SixTrack, <http://sixtrack.web.cern.ch/SixTrack/>
- [10] K. Sjobak *et al.*, “General Functionality for Turn-Dependent Element Properties in SixTrack”, in *Proc. IPAC’15*, Richmond, VA, USA, paper MOPIE069.
- [11] G. Robert-Demolaize *et al.*, “A New Version of SixTrack with Collimation and Aperture Interface”, in *Proceedings of 2005 PAC, Knoxville, Tennessee*.
- [12] S.M. White *et al.*, “First Luminosity Scans in the LHC”, in *Proc. IPAC’10*, Kyoto, Japan, paper MOPEC014.
- [13] B. Yee-Rendón *et al.*, “Simulations of fast crab cavity failures in the high luminosity Large Hadron Collider”, *Phys. Rev. ST Accel. Beams*, 17:051001, May 2014.
- [14] R. Bruce *et al.*, “Collimator Layouts for HL-LHC in the Experimental Insertions”, in *Proc. IPAC’15*, Richmond, VA, USA, paper TUPTY028.
- [15] R. Bruce *et al.*, “Parameters for HL-LHC aperture calculations and comparison with aperture measurements”, CERN-ACC-2014-0044, 2014.
- [16] A. Santamaría García *et al.*, “Limits on Failure Scenarios for Crab Cavities in the HL-LHC”, in *Proc. IPAC’15*, Richmond, VA, USA, paper THPF095.
- [17] S. Redaelli *et al.*, “Collimator BLM Threshold Strategy”, presented at: *Workshop on Beam-Induced Quenches, CERN*, 2014.
- [18] “LHC Design Report v.1 : the LHC Main Ring”, CERN-2004-003-V-1.
- [19] T.T. Böhlen *et al.*, “The FLUKA Code: Developments and Challenges for High Energy and Medical Applications”, *Nuclear Data Sheets*, Volume 120, June 2014, Pages 211–214.
- [20] A. Ferrari *et al.*, “FLUKA: a multi-particle transport code”, CERN 2005-10, INFN/TC_05/11, SLAC-R-773.
- [21] P. Gradassi, “Updated TCT Damage Limits for Asynchronous Dump Cases”, presented at: *LHC Collimation Working Group #190*, 2015.

E.4 Time Scale of Crab Cavity Failures Relevant for High Luminosity LHC

- **Title:** Time Scale of Crab Cavity Failures Relevant for High Luminosity LHC.
- **Authors:** K. Sjobak, R. Bruce, H. Burkhardt, A. MacPherson, A. Santamaría García, Regina Kwee-Hinzmann.
- **Abstract:** In order to facilitate studies of how dynamically changing element attributes affect the dynamics of the beam and beam losses, the functionality for dynamic kicks (DYNK) of SixTrack has been significantly extended. This functionality can be used for the simulation of dynamic scenarios, such as when crab cavities are switched on, orbit bumps are applied, optics are changed, or failures occur. The functionality has been extended with a more general and flexible implementation, such that arbitrary time-dependent functions can be defined and applied to different attributes of families or individual elements, directly from the user input files. This removes the need for source code manipulation, and it is compatible with LHC@Home which offers substantial computing resources from volunteers. In this paper, the functionality and implementation of DYNK is discussed, along with examples of application to the HL-LHC crab cavities.
- **Where:** IPAC 2016, Busan, Korea.
- **Contribution:** A. Santamaría García took part in the development of the model and the definition of the scenarios studied. She also wrote much of the software used for analyzing the data. She also presented the paper at the poster session at the IPAC 2016 conference.
- **Bibliography entry:** [88]

TIME SCALE OF CRAB CAVITY FAILURES RELEVANT FOR HIGH LUMINOSITY LHC*

K. Sjobak[†], R. Bruce, H. Burkhardt, A. MacPherson, A. Santamaría García,
CERN, Geneva, Switzerland

Regina Kwee-Hinzmann, Royal Holloway, University of London, Surrey, UK

Abstract

A good knowledge of the effects of the crab cavities, required for the baseline High Luminosity LHC (HL-LHC), is needed before the results of the first tests of crab cavity prototypes in the SPS, planned for 2018, will be available. In case of crab cavity failures, we have to make sure that time scales are long enough so that the beams can be cleanly dumped before damage by beam loss occurs. We discuss our present knowledge and modeling of crab cavity induced beam losses, combined with mechanical deformation. We discuss lower limits on the time scales required for safe operation, and possible failure mitigation methods.

INTRODUCTION

In order to reach the target instantaneous luminosity for the HL-LHC baseline design, crab cavities are necessary [1, 2]. There is no prior experience operating such cavities with a high-energy and high current proton beam like that of the HL-LHC, so the same type of devices will be installed for testing at the SPS. Modeling the effect of the cavity during a failure is therefore important in order to plan their installation and operation both at the LHC and the SPS.

This paper describes a model of the phase and voltage seen by the beam during an abrupt shutdown of the cavity input power, and the effect this has on the beam. This is in itself interesting, and is also an important step towards a realistic model for how the cavity will behave during a quench.

CRAB CAVITY MECHANICAL MODEL

In this work, the deformation of the crab cavity is modeled as a single damped harmonic oscillator which is driven by the pressure of the Lorentz force on the inside of the cavity. The deformation then causes a detuning Δf of the RF resonance frequency. This is an approximation; in reality there are several mechanical modes with different frequencies and different couplings to the RF voltage, and different effect of the RF resonance frequency [3].

This model can be described using the ordinary differential equation (ODE)

$$\sigma \frac{d^2 x}{dt^2} + k_D \frac{dx}{dt} + k_R x = k_F V^2(t), \quad (1)$$

where $x(t)$ is the displacement of the cavity surface, σ is the mass per area of the cavity surface, and the coefficients k_R , k_D and k_F scale the pressure from the restoring force,

mechanical damping and the Lorentz force respectively, and $V(t)$ is the deflecting voltage. This can be rewritten as

$$\frac{d^2 x}{dt^2} + 2\xi\omega_m \frac{dx}{dt} + \omega_m^2 x = k_F V^2/\sigma, \quad (2)$$

where $\omega_m = \sqrt{k_R/\sigma}$ is the mechanical resonance frequency and $\xi = \frac{k_D}{2\sqrt{\sigma k_R}}$ is the dimensionless damping coefficient.

Assuming that the shift of the RF resonance frequency $\Delta f(t)$ is proportional to the displacement x such that $\Delta f = K_m x$, Eq. (2) can be written as

$$\frac{d^2 \Delta f}{dt^2} + 2\xi\omega_m \frac{d\Delta f}{dt} + \omega_m^2 \Delta f = K_m k_F V^2/\sigma. \quad (3)$$

In static equilibrium, the Lorentz detuning is given as $\Delta f = K_t V^2$, where K_t is the Lorentz detuning coefficient. Combining this with Eq. (3) yields that

$$K_t = K_m k_F / \omega_m^2 \sigma, \quad (4)$$

and inserting this into the complete Eq. (3) gives an ODE describing the frequency shift

$$\frac{d^2 \Delta f}{dt^2} + 2\xi\omega_m \frac{d\Delta f}{dt} + \omega_m^2 \Delta f = \omega_m^2 K_t V^2, \quad (5)$$

which can be solved to find $\Delta f(t)$. Once $\Delta f(t)$ is known, the phase relative to an oscillator at the reference frequency can be calculated as

$$\phi(t) = \int_0^t 2\pi \Delta f(t') dt' + \phi(0). \quad (6)$$

It is assumed that the cavities are correctly tuned at the beginning of the run, at high voltage. The offset $\Delta f_0 = K_t V^2(0)$ is therefore always subtracted from $\Delta f(t)$.

Parameter Estimates

The main parameters of this model are ω_m , K_t , ξ , and the function $V(t)$. From simulations and measurements [4], the Lorentz detuning coefficient of a double quarter wave (DQW) crab cavity with a realistic stiffener takes a value of $K_t \approx -200 \text{ Hz}/(\text{MV})^2$.

Starting from Eq. (1), we can find an expression for ω_m . Further, by comparing the definitions of K_m and K_t , we get the relation $K_m = K_t V^2/x$. Finally, $k_F V^2$ is the field pressure, which can also be calculated [5] as $(\mu_0 H^2 - \epsilon_0 E^2)/4$, where E and H is the surface electric and magnetic field. At DQW design voltage $V = 3.34 \text{ MV}$, the maximum displacement is $x = -1.73 \mu\text{m}$, and it occurs in a region with low magnetic field and an electric field of roughly 3/4 [4] of the maximum value $\hat{E} = 37 \text{ MV/m}$ [6]. Further, the mass per area can be estimated from the wall thickness and mass

* Research supported by the High Luminosity LHC project.

[†] kyrre.ness.sjobak(at)cern.ch

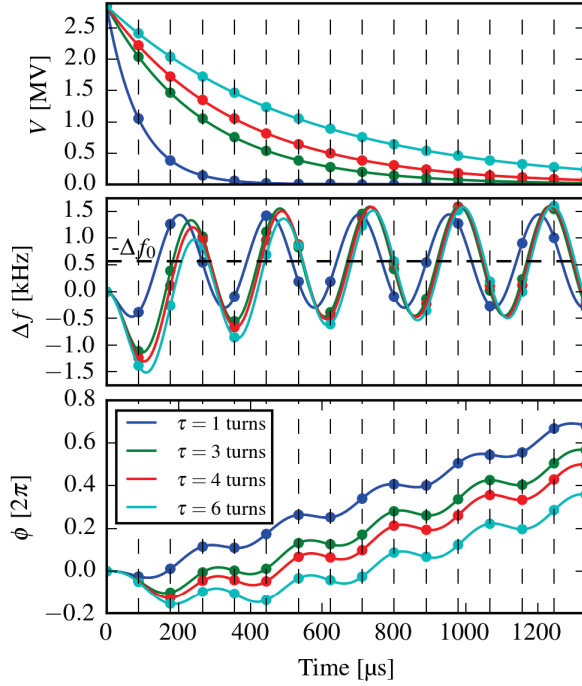


Figure 1: Voltage, RF frequency shift, and phase shift as calculated from Eqs. (5) and (6), with excitation $V(t)$ as given in Eq. (8). The parameter τ is varied, while $f_m = 4000$ Hz, $\xi = 0$ and $V_0 = 2.85$ MV. This high value of the mechanical frequency was selected as it was found in the tracking simulations to produce unusually large losses. The vertical dashed lines indicates the time between LHC turns, and the horizontal line in the Δf plot the equilibrium detuning $-\Delta f_0$ when $V(t) = 0$. The time scale is the same for all the plots. The round markers indicate the values seen by a single bunch passing through the cavity at $t = 0, t_{\text{turn}}, 2t_{\text{turn}}, \dots$, as used in the tracking simulations.

density of Niobium, which yields that $\sigma = 32.3$ kg/m². Combining these expressions yields an expression for the mechanical frequency

$$\omega_m = \sqrt{\frac{K_m k_F}{K_t \sigma}} = \sqrt{\frac{V^2 k_F}{x \sigma}} = \sqrt{\frac{-\epsilon_0 E^2}{4x \sigma}}, \quad (7)$$

which evaluates to $f_m = \omega_m/(2\pi) = 900$ Hz. This approximate estimate of the relevant mechanical resonance frequency indicates that the scale of the frequencies of the interesting eigenmodes is around 1 kHz.

The damping parameter ξ is harder to estimate. However since there are no obvious strong damping effects, it is likely that it is not very large.

The voltage curve $V(t)$ was taken to be

$$V(t) = V_0 \exp(-t/\tau), \quad (8)$$

where the time constant τ can be estimated as $\tau = 2Q_{\text{ext}}/\omega_{\text{RF}} = 421$ $\mu\text{s} = 4.73$ LHC turns. This describes

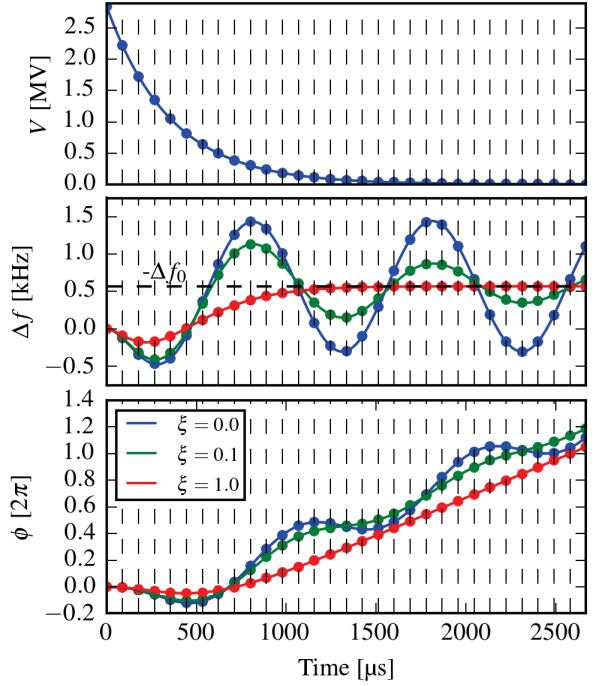


Figure 2: Voltage, RF frequency shift, and phase shift as in Fig. 1. The parameter ξ is varied, while $f_m = 1$ kHz, $\tau = 4$ turns = 356 μs and $V_0 = 2.85$ MV. Note that the vertical scale for Δf and ϕ is not the same as in Fig. 1.

the behavior of the cavity voltage in case it stops receiving input power.

Results and Discussion

Some examples of the behavior of the cavities with different voltage decay time scales and damping parameters are shown in Figs. 1 and 2. The initial voltage is here 2.85 MV and not the 3.34 MV discussed earlier, as this is what is needed to compensate for the crossing angle with the HL-LHCv1.2 optics [1].

From Fig. 2, we see that the main effect of the damping parameter is to reduce the initial undershoot of the frequency, at least in the time period where $V(t)$ is still large enough to affect the beam significantly. Regarding the parameter τ from Eq. (8), Fig. 1 shows that it has both an effect on the phase and amplitude of the mechanical oscillation, and on how long $V(t)$ remains significant.

TRACKING SIMULATIONS

In order to quantify the effects on the beam, tracking simulations were ran for the different parameter sets discussed above using the collimation SixTrack version 4.5.34 [7, 8]. With this, 312×64 particles were tracked for each scenario, using the HL-LHC v1.2 optics [1] for Beam 1. The voltage and phase-shift curves discussed above were then applied to all four crab cavities downstream of IP1 using DYNK [9], and the number of particles absorbed in the collimators

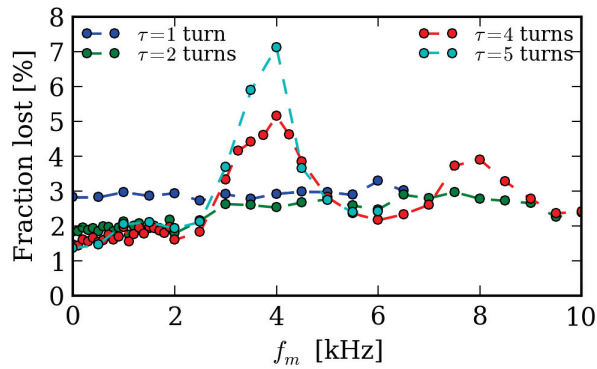


Figure 3: Fraction of beam lost after the onset of failure, as a function of f_m for different voltage fall times τ and $\xi = 0$.

counted for each turn. The loss was then estimated as the number of particles lost after the onset of the failure, and for normalization the number of particles in the simulation at the onset of the failure was used.

In all cases, the simulation was ran for 40 turns, with the 10 first turns unaffected by the failure in order to clean large-amplitude particles. The simulated beam consisted of one bunch with a Gaussian profile in the transverse phase space. As the amount of losses for $f_m \approx 1$ kHz when using the beam width expected from a nominal normalized emittance of $2.5 \mu\text{m}$ were negligible, the transverse width of the beam was increased by a factor 1.8. This distribution is similar to the “tail” part of the double Gaussian distribution discussed in [10, 11], which holds 5% of the beam particles. The longitudinal phase-space distribution of the beam was taken as a multivariate Gaussian, which was then cropped to include only the particles inside of the RF bucket.

Results and Discussion

The tracking results are presented in Figs. 3, 4 and 5. These show that as long as $f_m \lesssim 2$ kHz, the losses are very similar to what is expected from just the voltage drop alone (the 0 Hz points). If the mechanical frequency is further increased, the cavity can respond faster, and at certain frequencies induce quite large losses. As seen in Fig. 3 these losses become more significant for larger τ , as this allows the cavity to affect the beam for a longer time. Finally, it is also seen that when the damping ξ is increased by even a small value, the effect on the beam is noticeably reduced.

The loss positions were checked in a subset of the runs (no detuning and $\tau = 2$ or 4 turns, and $f_m = 4$ kHz and $\tau = 4$ or 5 turns), and virtually all the losses were found to be located in the betatron cleaning insertion (IR7).

The time dependence of the losses for a few characteristic scenarios are shown in Fig. 5. This again shows how the losses normally increase when τ decreases, and how this relationship can be reversed for detuned cavities. Further, it also shows that once the voltage has stopped dropping, a 3-turn pattern in the losses sets in due to the fractional part of the betatron tune, which in the crabbing plane is $Q_y = 60.32$.

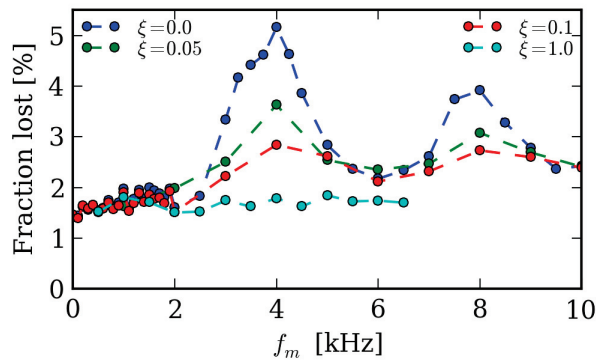


Figure 4: Fraction of beam lost after the onset of failure, as a function of f_m for different ξ and $\tau = 4$ turns.

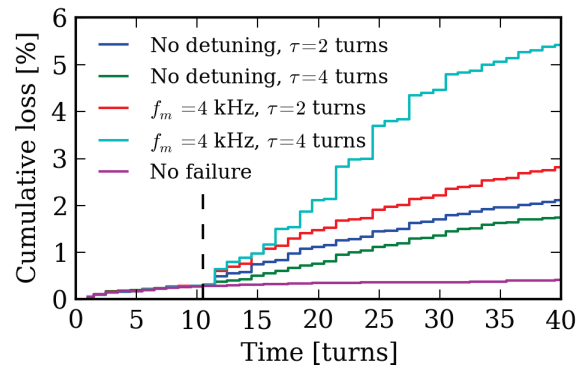


Figure 5: Fraction of beam lost as a function of time for four different simulations. In all cases, $\xi = 0.0$. The vertical line indicates the onset of the failure.

Finally, it shows that the losses are gradual and not abrupt. This means that the losses before the beam is dumped, which should happen within 3 turns after the failure is detected, are smaller than what is indicated in Figs. 3 and 4.

CONCLUSIONS AND OUTLOOK

The model presented in this paper combines dynamical Lorentz force detuning with beam dynamics. This showed that for realistic mechanical frequencies, beam losses induced by RF phase change from the mechanical resonances are not expected to exceed the losses caused by simply draining the cavity. However, this depends on the mechanical frequencies staying below approximately 2 kHz.

Some factors which will modify the shape of $V(t)$ are the RF control system, beam loading, and dynamically changing Q -factor during a quench in a superconducting cavity. Further, a real cavity will have multiple resonance modes with different frequencies and ξ . Including these effects is likely to yield further insights and reduce the uncertainties.

ACKNOWLEDGEMENTS

Many thanks to R. Calaga, O. Kononenko, R. De Maria, D. Wollman, M. Valette, and M. Giovannozzi for valuable feedback and discussions during this work. Also thanks to J. Delaysen for some of the initial ideas for this work.

REFERENCES

- [1] “High-Luminosity Large Hadron Collider (HL-LHC) Technical Design Report V0”, EU Deliverable D1-10, <https://edms.cern.ch/ui/file/1558149/>
- [2] Q. Wu, “Crab cavities: Past, present and future of a challenging device”, in *Proc. 6th Int. Particle Accelerator Conf. (IPAC’16)*, Richmond, VA, USA, May 2015, paper THXB2, pp. 3643-3648, <http://cds.cern.ch/record/2114108/files/CERN-ACC-2015-0189.pdf>
- [3] J. R. Delayen, “Ponderomotive instabilities and microphonics – a tutorial”, In *Proc. of the 12th Int. Workshop on RF Superconductivity (SRF’05)*, Cornell University, Ithaca, NY, USA, Jul. 2005, paper SUP01, pp. 35-39, <https://accelconf.web.cern.ch/accelconf/SRF2005/papers/sup01.pdf>
- [4] S. Verdú-Andrés, S.A. Belomestnykh, J. Wang, Q. Wu, and B. P. Xiao, “Lorentz Detuning for a Double-Quarter Wave Cavity”, in *Proc. 17th Int. Conf. on RF Superconductivity (SRF’15)*, Whistler, BC, Canada, Sep. 2015, paper THPB051, pp. 1215–1218, doi:10.18429/JACoW-SRF2015-THPB051
- [5] E. Haebe and J. Tückmantel, “Electromagnetic surfaces forces in RF cavities”, CERN, Geneva, Switzerland, Rep. CERN-AT-RF-INT-91-99, Dec. 1991, <http://cds.cern.ch/record/950375/files/CM-P00058119.pdf>
- [6] S. Verdú-Andrés, L. Alberty, K. Artoos, S.A. Belomestnykh, I. Ben-Zvi, R. Calaga, O. Capatina, T. Capelli, F. Carra, N. Kuder, R. Leuxe, Z. Li, A. Ratti, J. Skaritka, Q. Wu, B. P. Xiao, and C. Zanoni, “Design and prototyping of HL-LHC double quarter wave crab cavities for SPS test”, in *Proc. 6th Int. Particle Accelerator Conf. (IPAC’16)*, Richmond, VA, USA, May 2015 paper MOBD2, pp. 64-66, <http://jacow.org/IPAC2015/papers/mobd2.pdf>
- [7] SixTrack, <http://sixtrack.web.cern.ch/SixTrack/>
- [8] G. Robert-Demolaize, R. Assmann, S. Redaelli, and F. Schmidt, “A new version of SixTrack with collimation and aperture interface”, In *Proc. 2005 Particle Accelerator Conf. (PAC’05)*, Knoxville, Tennessee, USA, May 2005, paper FRAT081, pp. 4084-4086, <http://accelconf.web.cern.ch/accelconf/p05/PAPERS/FPAT081.PDF>
- [9] K. Sjobak, H. Burkhardt, R. De Maria, A. Mereghetti, and A. Santamaria Garcia, “General functionality for turn-dependent element properties in SixTrack”, in *Proc. 6th Int. Particle Accelerator Conference (IPAC’15)*, Richmond, VA, USA, May 2015, <http://accelconf.web.cern.ch/AccelConf/IPAC2015/papers/mopje069.pdf>
- [10] B. Yee-Rendon, R. Lopez-Fernandez, J. Barranco, R. Calaga, A. Marsili, R. Tomás, F. Zimmermann, and F. Bouly, “Simulations of fast crab cavity failures in the high luminosity Large Hadron Collider”, *Phys. Rev. ST Accel. Beams*, vol. 17, p. 051001, May 2014, <http://link.aps.org/doi/10.1103/PhysRevSTAB.17.051001>
- [11] A. Santamaria Garcia, K. Sjobak, R. Bruce, H. Burkhardt, F. Cerutti, R. Kwee-Hinzmann, and A. Lechner, “Machine and experiment protection from fast crab cavity failures in the HL-LHC”, presented at the 7th Int. Conf. on Particle Accelerators, Busan, Korea, May 2016, paper, this conference.

Bibliography

- [1] CERN. Functional specification of LHC modes, 2015. LHC-OP-ES-0005 rev 1.5.
- [2] M. Solfaroli Camillocci. LHC operation and efficiency in 2015. pages 4–7, 2016.
- [3] L. Rossi and O. Bruning. The High Luminosity Large Hadron Collider: the new machine for illuminating the mysteries of Universe. Advanced series on directions in high energy physics. World Scientific, Hackensack, NJ, 2015.
- [4] 2014 CERN Accelerator Schools: Beam Loss and Accelerator Protection. 2014 CERN Accelerator Schools: Beam Loss and Accelerator Protection. Jun 2014.
- [5] T. Bär. Very Fast Losses of the Circulating LHC Beam, their Mitigation and Machine Protection. PhD thesis, Universität Hamburg, 2013.
- [6] The Large Hadron Collider. <https://home.cern/topics/large-hadron-collider>.
- [7] The ATLAS Collaboration. <http://atlas.cern/discover/physics>.
- [8] E. D. Bloom et al. High-Energy Inelastic e-p Scattering at 6° and 10°. Physical Review Letters, 23:930–934, October 1969.
- [9] M. Breidenbach. Observed Behavior of Highly Inelastic Electron-Proton Scattering. Physical Review Letters, 23:935–939, October 1969.
- [10] J. E. Augustin et al. Discovery of a narrow resonance in e^+e^- annihilation. Phys. Rev. Lett., 33:1406–1408, Dec 1974.
- [11] J. J. Aubert et al. Experimental Observation of a Heavy Particle J. Physical Review Letters, 33:1404–1406, December 1974.
- [12] M. L. Perl et al. Evidence for anomalous lepton production in $e^+ - e^-$

- annihilation. Phys. Rev. Lett., 35:1489–1492, Dec 1975.
- [13] B. R. Stella and H.-J. Meyer. Upsilon (9.46 GeV) and the gluon discovery (a critical recollection of PLUTO results). European Physical Journal H, 36:203–243, April 2011.
 - [14] P. Söding. On the discovery of the gluon. The European Physical Journal H, 35(1):3–28, Jul 2010.
 - [15] UA1 collaboration. Experimental observation of isolated large transverse energy electrons with associated missing energy at $s=540$ GeV. Physics Letters B, 122(1):103 – 116, 1983.
 - [16] UA2 collaboration. Observation of single isolated electrons of high transverse momentum in events with missing transverse energy at the CERN pp collider. Physics Letters B, 122(5):476 – 485, 1983.
 - [17] F. Abe et al. Observation of top quark production in $p\bar{p}$ collisions. Phys. Rev. Lett., 74:2626–2631, 1995.
 - [18] S. Abachi et al. Search for high mass top quark production in $p\bar{p}$ collisions at $\sqrt{s} = 1.8$ TeV. Phys. Rev. Lett., 74:2422–2426, 1995.
 - [19] ATLAS collaboration. Observation of a new particle in the search for the Standard Model Higgs boson with the ATLAS detector at the LHC. Physics Letters B, 716(1):1 – 29, 2012.
 - [20] CMS collaboration. Observation of a new boson at a mass of 125 GeV with the CMS experiment at the LHC. Physics Letters B, 716(1):30 – 61, 2012.
 - [21] LHCb finds new hints of possible Standard Model deviations. <https://home.cern/about/updates/2017/04/lhcb-finds-new-hints-possible-standard-model-deviations>.
 - [22] A. Cakir (CMS and ATLAS Collaboration). Searches for Beyond Standard Model Physics at the LHC: Run1 Summary and Run2 Prospects. PoS, FPCP2015:024, 2015.
 - [23] W. Barletta et al. High Energy Hadron Colliders. Report of the Snowmass 2013 Frontier Capabilities Hadron Collider Study Group, 2013.
 - [24] F. Gianotti. <https://indico.cern.ch/event/660352/>. DG New year’s address 2018.
 - [25] High-Luminosity Large Hadron Collider (HL-LHC): Technical Design Report V. 0.1. CERN Yellow Reports: Monographs. CERN, Geneva, 2017.
 - [26] Images projected on the Globe of Innovation "Light & Luminosity" IYL2015 talks. <https://cds.cern.ch/record/1985263?ln=en>.
 - [27] R. Schmidt et al. Machine Protection challenges for HL-LHC. In IPAC’14, Dresden, Germany, 2014.
 - [28] S. Y. Lee. Accelerator Physics. World Scientific, third edition, 2012.
 - [29] K. Floettmann. Some Basic Features of the Beam Emittance. Phys. Rev.

- ST Accel. Beams, 6:034202, Mar 2003.
- [30] W. Herr and E. Forest. 3 Non-Linear Dynamics in Accelerators, pages 38–61. Springer Berlin Heidelberg, Berlin, Heidelberg, 2013.
 - [31] F. Christoph Iselin. The MAD program (methodical accelerator design): version 8.13 ; Physics Methods Manual. CERN, Geneva, 1992.
 - [32] M. Giovannozzi et al. Parameter Scans and Accuracy Estimates of the Dynamic Aperture of the CERN LHC. In Proceedings of EPAC 2006, WEPOCH093, Edinburgh, Scotland, 2006.
 - [33] R. De Maria et al. Nonlinear Correction Schemes for the Phase 1 LHC Insertion Region Upgrade and Dynamic Aperture Studies. Phys. Rev. Spec. Top. Accel. Beams, 12(CERN-BE-2009-004):011002. 8 p, Jan 2009.
 - [34] R. Bruce et al. Simulations and Measurements of Cleaning with 100 MJ Beams in the LHC. In Proceedings of IPAC’13, MOODB202, Shanghai, China, 2013.
 - [35] L. C. Schachinger and R. Talman. TEAPOT: a thin element accelerator program for optics and tracking. Part. Accel., 22(SSC-52):35. 46 p, Dec 1985.
 - [36] MAD-X Website. <http://madx.web.cern.ch/madx/>.
 - [37] H. Burkhardt et al. Improved TEAPOT Method and Tracking with Thick Quadrupoles for the LHC and its Upgrade. In Proceedings of IPAC’13, MOPWO027, Shanghai, China, 2013.
 - [38] H. Burkhardt et al. Upgrade of Slicing and Tracking in MAD-X. In Proceedings of IPAC’14, TUPRO063, Dresden, Germany, 2014.
 - [39] CERN. <https://cds.cern.ch/record/1621894>.
 - [40] The LHC Design Report, volume Volume I: The LHC Main Ring of CERN-2004-003. CERN, 2004.
 - [41] H. Burkhardt and R. Schmidt. Intensity and Luminosity after Beam Scraping. Technical Report CERN-AB-2004-032-ABP, CERN, Geneva, Jul 2004. revised version submitted on 2004-07-21 15:25:37.
 - [42] B. Yee-Rendón et al. Simulations of Fast Crab Cavity Failures in the High Luminosity Large Hadron Collider. Phys. Rev. ST Accel. Beams, 17:051001, May 2014.
 - [43] The Collimation Project. <http://lhc-collimation-project.web.cern.ch/lhc-collimation-project/pictures.php>.
 - [44] CERN. <https://home.cern/cern-people/updates/2014/03/lhc-collimators-precision-their-nature>.
 - [45] LHC Report: record luminosity, well done LHC. <https://home.cern/cern-people/updates/2017/11/lhc-report-record-luminosity-well-done-lhc>.

- [46] New bunch-production scheme breaks luminosity record. <http://cerncourier.com/cws/article/cern/65796>.
- [47] LHC Report: operation with holes. <https://home.cern/cern-people/updates/2017/09/lhc-report-operation-holes>.
- [48] The ATLAS Collaboration. <https://twiki.cern.ch/twiki/bin/view/AtlasPublic/LuminosityPublicResultsRun2>.
- [49] R. Alemany-Fernandez, E. Bravin, L. Drosdal, A. Gorzawski, V. Kain, M. Lamont, A. Macpherson, G. Papotti, M. Pojer, L. Ponce, S. Redaelli, G. Roy, M. Solfaroli Camillocci, W. Venturini, and J. Wenninger. Operation and Configuration of the LHC in Run 1. Nov 2013.
- [50] L. Rossi. High-Luminosity Large Hadron Collider (HL-LHC) TDR. (December), 2015.
- [51] W. Herr et al. Long-range beam-beam effects in the LHC. In ICFA Mini-Workshop on Beam-Beam Effects in Hadron Colliders, volume 004, pages 18–22, 2014.
- [52] G. Arduini. Down Selection Criteria and MDs prior to LS3. Proceedings of Chamonix 2014 Workshop on LHC Performance, pages 232–238, 2014.
- [53] CERN. <https://cds.cern.ch/record/905940?ln=en>.
- [54] Fermilab. http://www.fnal.gov/pub/today/20070329_page01.html.
- [55] R. Bruce et al. Technical Design IR Collimation. FP7 High Luminosity Large Hadron Collider Design Study Deliverable Report, CERN, 2015. CERN-ACC-2015-0042.
- [56] The ATLAS Collaboration. Performance of pile-up mitigation techniques for jets in pp collisions at $\sqrt{s}=8$ TeV using the ATLAS detector. European Physical Journal C, 76(11), 2016.
- [57] C. Gemme. The ATLAS tracker Pixel detector for HL-LHC. In The 25th International workshop on vertex detectors, pages 0–9, La Biodola, Isola d’Elba, Italy, 2016. ATL-OTK-PROC-2017-001.
- [58] The ATLAS Collaboration. https://twiki.cern.ch/twiki/bin/view/AtlasPublic/EventDisplayStandAlone#Events_with_pile_up.
- [59] A. A. Gorzawski. Luminosity control and beam orbit stability with beta star leveling at LHC and HL-LHC. PhD thesis, École Polytechnique Fédérale de Lausanne, 2016.
- [60] J. Boyd. Feedback from the Experiments on the 2017 run. 8th LHC Operations Evian Workshop, December 2017.
- [61] S. Fartoukh. Pile up management at the high-luminosity LHC and introduction to the crab-kissing concept. Physical Review Special Topics - Accelerators and Beams, 17(11):1–13, 2014.
- [62] Y. I. Levinsen. Machine Induced Experimental Background Conditions in

- the LHC. PhD thesis, University of Oslo, 2012.
- [63] A. Apollonio. Machine Protection : Availability for Particle Accelerators. PhD thesis, Technischen Universität Wien, 2015.
 - [64] F. J. Willeke. Reliability considerations for the operation of large accelerator user facilities. CERN Yellow Reports, 2(0):111, 2016.
 - [65] R. Schmidt. Introduction to machine protection. CERN Yellow Reports, 2(0):1, 2016.
 - [66] M. Valette et al. Requirements for Crab Cavity System Availability in HL-LHC. In Proceedings of IPAC'17, TUPVA022, Copenhagen, Denmark, 2017.
 - [67] R. B. Palmer. Energy Scaling, Crab Crossing, and the Pair Problem. SLAC-PUB-4707, pages 613–619, 1988.
 - [68] K. Oide, K. Yokoya. The Crab-Crossing for Storage-Ring Scheme Colliders. SLAC-PUB-4832, 1989.
 - [69] A. Piwinski. Satellite Resonances due to Beam-Beam Interaction. IEEE Transactions on Nuclear Science, NS-24(3):298–304, 1977.
 - [70] W. Herr and R. Paparella. Landau damping of coherent modes by overlap with synchrotron sidebands. Technical Report 304, 2002.
 - [71] W. Herr. Computer simulation of synchro-betatron resonances induced by a non-zero crossing angle in the LHC. In Proceedings of EPAC 1990, 1624.
 - [72] Joint BNL/US-LARP/CARE-HHH Mini-Workshop on Crab Cavities for the LHC. <https://indico.cern.ch/event/24200/>.
 - [73] H. Koiso, K. Oide. Accelerator Design of the KEK B-Factory: Design of the Lattice for the KEK B-Factory. KEK Report 90-24, pages 32–34, 1991.
 - [74] K. Akai et al. Development of crab cavity for CESR-B. pages 3–5, 1993.
 - [75] LHC Luminosity and Energy Upgrade: A Feasibility Study. Technical report, CERN, 2002. LHC Project Report 626.
 - [76] H. Nakai et al. Research and Development Program on Superconducting Crab Cavities for KEKB. In Proceedings of the 11th Workshop on RF Superconductivity, MOP34, Lübeck/Travemünder, Germany, 2003.
 - [77] CERN. <https://care-hhh.web.cern.ch/care-hhh/HHH-2004/default.html>.
 - [78] Y. Yamamoto et al. Horizontal Tests for Crab Cavities in KEKB. In Proceedings of SRF2007, WEP27, Peking Univ., Beijing, China, 2007.
 - [79] T. Abe et al. Performance and Operation Results of the RF Systems at the KEK B-Factory. Progress of Theoretical and Experimental Physics, 2013(3), 2013.
 - [80] R. Calaga et al. Crab Cavities for the LHC Luminosity Upgrade. CERN Project Document, 2010.

- [81] T. P. Wangler. RF Linear Accelerators. Wiley, Weinheim, 2008.
- [82] H. Rokhsari, T. J. Kippenberg, T. Carmon, and K. J. Vahala. Theoretical and Experimental Study of Radiation Pressure-Induced Mechanical Oscillations (Parametric Instability) in Optical Microcavities. *IEEE Journal on Selected Topics in Quantum Electronics*, 12(1):96–107, 2006.
- [83] H. Padamsee. RF superconductivity. Wiley, Weinheim, 2009.
- [84] H. Padamsee, T. Hays, and J. Knobloch. RF superconductivity for accelerators; 2nd ed. Wiley, Weinheim, 2008.
- [85] B. P. Xiao et al. Mechanical Study of 400MHz Double Quarter Wave Crab Cavity for LHC Luminosity Upgrade. In *Proceedings of IPAC’13, WEPWO050*, Shanghai, China, 2013.
- [86] S. Verdú Andrés et al. Design and Prototyping of HL-LHC Double Quarter Wave Crab Cavities. In *Proceedings of IPAC’15, MOBD2*, Richmond VA, United States, 2015.
- [87] J. R. Delayen. Ponderomotive instabilities and microphonics - a tutorial. In *Proceedings of the 12th International Workshop on RF Superconductivity*, Cornell University, Ithaca, New York, USA, 2005.
- [88] K. Sjobak et al. Time Scale of Crab Cavity Failures Relevant for High Luminosity LHC. In *Proceedings of IPAC’16, THPOY043*, Busan, Korea, 2016.
- [89] National Laboratory for High Energy Physics. Technical Report KEK Report 95-7, 1995.
- [90] K. Hosoyama. Experiences with KEK-B Crab Cavity, presentation.
- [91] S. De Silva. SRF Crabbing Cavity R&D, presentation.
- [92] R. Calaga. Crab Cavities for the LHC Upgrade. In *Proceedings of Chamonix Workshop on LHC Performance*, 2012.
- [93] Z. Li et al. FPC and Hi-Pass Filter HOM Coupler Design for the RF Dipole Crab Cavity for the HL-LHC HiLumi Upgrade. In *Proceedings of IPAC’15, WEPWI004*, Richmond VA, United States, 2015.
- [94] B. Xiao et al. Design, Prototyping, and Testing of a Compact Superconducting Double Quarter Wave Crab Cavity. *Physical Review Special Topics - Accelerators and Beams*, 18(4):1–10, 2015.
- [95] S.U. De Silva et al. Mechanical Analysis of the 400 MHz RF-Dipole Crabbing Cavity Prototype for LHC High Luminosity Upgrade. In *Proceedings of PAC2013, WEPAC40*, Pasadena CA, USA, 2013.
- [96] D. R. Brett, R. B. Appleby, R. De Maria, J. Barranco Garcia, R. Tomas Garcia, B. Hall, and G. Burt. Accurate crab cavity modeling for the high luminosity Large Hadron Collider. *Phys. Rev. Spec. Top. Accel. Beams*, 17(10):104001. 12 p, 2014.

- [97] P. Baudrenghien et al. RF System Conceptual Layout. Technical Report D4.2, 2014.
- [98] J. Tückmantel. Cavity-Beam-Transmitter Interaction Formula Collection with Derivation. Technical Report CERN- ATS-Note-2011-002 TECH, 2011.
- [99] P. Baudrenghien. Private communication, Apr. 23 2015.
- [100] K. Gibrán Hernández Chahín. Private communication, Jan. 19 2016.
- [101] Nakanishi et al. Beam behavior due to crab cavity breakdown. In Proceedings of IPAC’10, WEPEC022, Kyoto, Japan, 2010.
- [102] Y Funakoshi. Operational Experience with Crab Cavities at KEKB. 2014.
- [103] F. Schmidt. SIXTRACK version 1.2: single particle tracking code treating transverse motion with synchrotron oscillations in a symplectic manner; user’s reference manual. Technical Report CERN-SL-94-56. CERN-SL-94-56-AP, CERN, Geneva, Sep 1994.
- [104] G. Ripken and F. Schmidt. A symplectic six-dimensional thin-lens formalism for tracking. Technical Report CERN-SL-95-12. CERN-SL-95-12-AP. DESY-95-063, CERN, Geneva, Apr 1995.
- [105] SixTrack GitHub Repository. <https://github.com/SixTrack/>.
- [106] R. de Maria et al. Recent Developments and Future Plans for SixTrack. In Proceedings of IPAC’13, MOPWO028, Shanghai, China, 2013.
- [107] K. Sjobak et al. New Features of the 2017 SixTrack release. In Proceedings of IPAC’17, THPAB047, Copenhagen, Denmark, 2017.
- [108] R. De Maria, M. Giovannozzi, E. McIntosh, Y. Cai, Y. Nosochkov, and M. H. Wang. Dynamic Aperture Studies for the LHC High Luminosity Lattice. (CERN-ACC-2015-0177):4 p, May 2015.
- [109] K. Sjobak et al. General Functionality for Turn-Dependent Element Properties in SixTrack. In Proceedings of IPAC’15, MOPJE069, Richmond, VA, USA, 2015.
- [110] K. Sjobak et al. Dynamic simulations in SixTrack. In Proceedings of the Tracking for Collimation Workshop, 2015.
- [111] A. Mereghetti et al. Sixtrack-Fluka Active Coupling for the Upgrade of the SPS Scrapers. In Proceedings of IPAC’13, WEPEA064, Shanghai, China, 2013.
- [112] B. Yee-Rendón. Studies of Machine Protections for Fast Crab Cavity Failures in the High Luminosity Large Hadron Collider. PhD thesis, CINVESTAV, 2014.
- [113] F. Schmidt et al. SIXTRACK version 4.6.30: single particle tracking code treating transverse motion with synchrotron oscillations in a symplectic manner; user’s reference manual. Technical Report CERN-SL-94-56. CERN-SL-94-56-AP, CERN, Geneva, April 2017.

- [114] R. W. Assmann, I. S. Baishev, M. Brugger, M. Hayes, J. B. Jeanneret, V. Kain, D. I. Kaltchev, and F. Schmidt. Tools for Predicting Cleaning Efficiency in the LHC. (LHC-Project-Report-639. CERN-LHC-Project-Report-639):4 p, Jun 2003.
- [115] T. Trenkler and J. B. Jeanneret. K2, A software package evaluating collimation systems in circular colliders (manual). Technical Report SL-Note-94-105-AP, CERN, Geneva, Dec 1994.
- [116] G. Robert-Demolaize, R. Assmann, S. Redaelli, and F. Schmidt. A new version of SixTrack with collimation and aperture interface. Conf. Proc., C0505161:4084, 2005. [,4084(2005)].
- [117] Collimation Website. <https://lhc-collimation-project.web.cern.ch/lhc-collimation-project/BeamLossPattern.htm>.
- [118] A. Mereghetti et al. SixTrack for Cleaning Studies: 2017 Updates. In Proceedings of IPAC’17, THPAB046, Copenhagen, Denmark, 2017.
- [119] R. Apsimon et al. Modeling the Low Level RF response on the beam during crab cavity quench. To appear in Phys. Rev. ST Accel. Beams, 2018.
- [120] S. M. White et al. First Luminosity Scans in the LHC. In Proceedings of IPAC’10, MOPEC014, Kyoto, Japan, 2010.
- [121] Absolute Calibration of Luminosity Measurement at CMS: Summer 2011 Update. Technical Report CMS-PAS-EWK-11-001, CERN, Geneva, 2011.
- [122] R. W. Assmann, R. Bruce, F. Burkart, M. Cauchi, D. Deboy, L. Lari, S. Redaelli, A. Rossi, G. Valentino, and D. Wollmann. Beam distribution measurements in the LHC. Jul 2011.
- [123] U. Schwickerath and V. Lefebure. Usage of LSF for batch farms at CERN. Journal of Physics: Conference Series, 119(4):042025, 2008.
- [124] D. Perini and C. Zanoni. Preliminary Design Study of the Hollow Electron Lens for LHC. Technical Report CERN-ACC-NOTE-2017-0004, CERN, Geneva, Jan 2017.
- [125] B. Goddard et al. Beam Halo on the TCDQ Diluter System and Thermal Load on the Downstream Superconducting Magnets. In Proceedings of EPAC 2006, MOPLS008, Edinburgh, Scotland, 2006.
- [126] S. Redaelli et al. Collimator BLM Threshold Strategy. Workshop on Beam-Induced Quenches, CERN, 2014.
- [127] A. Mereghetti, R. Bruce, E. B. Holzer, M. Kalliokoski, S. Redaelli, and B. Salvachua Ferrando. BLM thresholds and damage limits for collimators. pages 197–202. 6 p, 2016.
- [128] F. Carra. Private communication, Nov. 29 2017.
- [129] E. Quaranta, M. Beghi, A. Bertarelli, and S. Redaelli. Investigation of collimator materials for the High Luminosity Large Hadron Collider, Jun 2017. Presented 18 Jul 2017.

- [130] K. Fuchsberger et al. Phase Advance Interlocking throughout the whole LHC Cycle. In Proceedings of IPAC'17, TUPVA022, Copenhagen, Denmark, 2017.
- [131] E. Quaranta et al. Updated Simulation Studies of Damage Limit of LHC Tertiary Collimators. In Proceedings of IPAC'15, THPF095, Richmond, VA, USA, 2015.
- [132] A. Ferrari, Paola R. Sala, A. Fasso, and Johannes Ranft. FLUKA: A multi-particle transport code (program version 2005). CERN Yellow Reports: Monographs. CERN, Geneva, 2005.
- [133] G. Battistoni, F. Cerutti, A. Fasso, A. Ferrari, S. Muraroi, J. Ranft, S. Roesler, and P. R. Sala. The FLUKA code: Description and benchmarking. AIP Conf. Proc., 896(SLAC-REPRINT-2007-184):31–49. 19 p, 2007.
- [134] A. Tsinganis et al. Impact on the HL-LHC Triplet Region and Experiments from Asynchronous Beam Dumps on Tertiary Collimators. In Proceedings of IPAC'17, MOPAB011, Copenhagen, Denmark, 2017.
- [135] A. Sbrizzi et al. Irradiation of ATLAS Silicon Detectors with Fast Extracted and Intense Proton Beams. LBS Meeting #88 (20-11-2017).
- [136] T. Persson et al. LHC optics commissioning: A journey towards 1% optics control. Phys. Rev. Accel. Beams, 20(6):061002. 9 p, 2017.
- [137] A. Santamaría García et al. Machine Protection From Fast Crab Cavity Failures in the High Luminosity LHC. In Proceedings of IPAC'16, TUPMW025, Busan, Korea, 2016.
- [138] E. Nebot del Busto et al. Detection of Unidentified Falling Objects at LHC. In Proceedings of HB2012, TUO1C04, Beijing, China, 2012.
- [139] Wolfram Demonstrations Project. <http://demonstrations.wolfram.com/ElectromagneticWavesInACylindricalWaveguide/>.
- [140] A. Santamaría García et al. Limits on Failure Scenarios for Crab Cavities in the HL-LHC. In Proceedings of IPAC'15, THPF095, Richmond, VA, USA, 2015.

Acronyms

Abbreviations

AC	Alternating Current.
ALICE	A Large Ion Collider Experiment.
ATLAS	A Toroidal LHC Apparatus.
BIS	Beam Interlock System.
BLM	Beam Loss Monitor.
BNL	Brookhaven National Laboratory.
BPM	Beam Position Monitor.
CERN	European Organization for Nuclear Research.
CFC	Carbon Fiber Composite.
CMS	Compact Muon Solenoid.
DC	Direct Current.
DESY	Deutsches Elektronen-Synchrotron.
DQW	Double Quarter Wave.
EM	Electromagnetic.
EWSB	Electroweak Symmetry Breaking.
HEP	High Energy Physics.
HER	High Energy Ring.
HL	High Luminosity.
HOM	Higher Order Mode.
IP	Interaction Point.
IR	Insertion Region.
KEK	The High Energy Accelerator Research Organization.
LEP	Large Electron-Positron Collider.
LER	Low Energy Ring.
LHCb	LHC-beauty.
LHC	Large Hadron Collider.
LINAC	Linear Accelerator.
LLRF	Low Level RF.
LOM	Lower Order Mode.

ACRONYMS

LSS	Long Straight Section.
LS	Long Shutdown.
MAD	Methodological Accelerator Design.
MPS	Machine Protection System.
PSB	Proton Synchrotron Booster.
PS	Proton Synchrotron.
RFD	RF Dipole.
RF	Radio-Frequency.
RMS	Root Mean Square.
SLAC	Stanford Linear Accelerator Center.
SOM	Same Order Mode.
SPS	Super Proton Synchrotron.
TAN	Target Absorber Neutral.
TAS	Target Absorber Secondaries.
TCDQ	Target Collimator Dump Quadruple.
TCLA	Target Collimator Long Absorber.
TCP	Target Collimator Primary.
TCS	Target Collimator Secondary.
TCT	Target Collimator Tertiary.
TDE	Dump for Ejected Beam.
pp	proton-proton.

ANDREA SANTAMARÍA GARCÍA

PHYSICIST / PHD STUDENT

Born the 29th of January 1990 in Madrid, Spain.

KEYWORDS: HL-LHC, crab cavities, SC RF cavities, machine-experiment interface, machine protection, beam losses, collimation, particle tracking, aperture, luminosity, accelerator design, beam dynamics.

CONTACT ME

✉ andrea.stmaria@gmail.com
🌐 <http://kfubuki.github.io/>
in <https://www.linkedin.com/in/ansantam>
🐙 <https://github.com/KFubuki>

SKILLS

Python	● ● ● ● ○
Bash	● ● ● ○ ○
Mathematica	● ● ● ○ ○
SixTrack	● ● ● ● ●
MAD-X	● ● ● ● ○
HTML/CSS/Jekyll	● ● ● ● ○
LaTeX	● ● ● ● ●

LANGUAGES

Spanish	● ● ● ● ●
English	● ● ● ● ●
French	● ● ● ● ●
German	● ● ● ○ ○

PUBLICATIONS

- 📄 Machine Protection from Fast Crab Cavity Failures in the High Luminosity LHC, TUPMW025, IPAC'16
- 📄 Time Scale of Crab Cavity Failures Relevant for High Luminosity LHC, THPOY043, IPAC'16
- 📄 Limits on Failure Scenarios for Crab Cavities in the HL-LHC, THPF095, IPAC'15
- 📄 General Functionality for Turn-Dependent Element Properties in SixTrack, MOPJE069, IPAC'15
- 📄 Integration of a Neutral Absorber for the LHC Point 8, TUPRO020, IPAC'14

EDUCATION

PHD IN ACCELERATOR PHYSICS

EPFL & CERN (Mar 2014 - Mar 2017) 📍 Geneva

I am currently working on my PhD thesis "Experiment and Machine Protection from Fast Losses caused by Crab Cavities in the High Luminosity LHC" under the supervision of Prof. Leonid Rivkin (EPFL) and Dr. Helmut Burkhardt (CERN). This PhD is funded by CERN's Doctoral Program scholarship, associated with EPFL's Doctoral School.

🏆 "My Thesis in 180 Seconds" competition.

LICENCIATURA EN FÍSICA

UAM (Oct 2008 - Jan 2014) 📍 Madrid

The official length of the program is 5 years. The total time of taught classes and practical training is 3000 hours. I took the introductory courses on theoretical physics.

BACCALAURÉAT SCIENTIFIQUE

Lycée St Joseph (May 2008) 📍 Thonon-les-Bains

WORK EXPERIENCE

INTERN

CERN (Sep 2013 - Nov 2013) 📍 Geneva

I worked for three months under the supervision of Dr. Helmut Burkhardt. I studied the integration of a neutral absorber for the LHC point 8, in the framework of High Luminosity LHC. I considered the worst scenarios for the proposed crossing schemes, and estimated the neutral absorber's dimensions and position in the LHC tunnel.

INTERN

Tecnatom, S.A. (Jun 2008 - Jun 2010) 📍 Geneva

During my first two years of undergraduate studies I also worked at Tecnatom under the supervision of Isabel López Cruzado. I researched information in the ITER databases for the VITER project (a vigilance project for the future fusion reactors). I also updated the procedures of the Activated Carbon Laboratory, administrated the Calibration Laboratory and translated technical

reports to English and French for the Testing and Qualification department.

INTERN

CERN (Jun 2006)

📍 Geneva

I spent a month in the Laboratory 27 (group PH-CMA) under the supervision of Dr. Etienne Auffray. This laboratory was charged of testing scintillation crystals for CMS. I made light transmission measurements of LuYAP, LuAP and PbWO₄ crystals with a spectrometer. I also assisted to the different mechanical building phases of the ECAL (Electromagnetic Calorimeter) and took part in the measurement of the light yield of some crystals.

ACCELERATOR SCHOOLS

US PARTICLE ACCELERATOR SCHOOL

Jan 2015

📍 New Brunswick

Two weeks school on intermediate accelerator physics and beam measurements.

INTRODUCTION TO PARTICLE ACCELERATORS

Fall semester 2014/2015

📍 Lausanne

Lectures imparted by Prof. L. Rivkin at EPFL.

JOINT ACCELERATOR PARTICLE SCHOOL

Nov 2014

📍 Newport Beach

Two weeks school on beam loss and accelerator protection.

HADRON COLLIDER SUMMER SCHOOL

Jul 2013

📍 Göttingen

Two weeks school on introductory topics in elementary particle physics and hadron collider physics.

CERN SUMMER STUDENT PROGRAM

Jul 2012 - Aug 2012

📍 Geneva

I worked two months under the supervision of Laurent Deniau and Andrea Latina on creating a new website for the MAD-X code, and started elaborating a document on the formal description of the MAD-X language. I also attended the summer student lectures.

CONFERENCE PRESENTATIONS

IPAC'16

May 2016

📍 Busan

Poster student presentation.

Joint HiLumi LHC-LARP Annual Meeting

Oct 2015

📍 Geneva

Crab Cavity failure modes and IR protection.

RELATED INTERESTS

- Communication in science
- Teaching

